Applications and Noise Properties of High Repetition Rate Ti:Sapphire Frequency Combs

by

Andrew John Benedick

B.S., Mechanical Engineering Technology, Northeastern University, 2001
M.S., Applied Physics, University of Massachusetts Boston, 2006

Submitted to the Department of Electrical Engineering and Computer Science
in partial fulfillment of the requirements for the degree of

Doctor of Philosophy in Electrical Engineering

at the

MASSACHUSETTS INSTITUTE OF TECHNOLOGY

June 2011

Author .....
rtment of Electrical Engineering and Computer Science
April 27, 2011

Certified by .....
Franz X. Kärtner
Professor of Electrical Engineering
Thesis Supervisor

Certified by .....
Erich P. Ippen
Elihu Thomson Professor of Electrical Engineering
and Professor of Physics
Thesis Supervisor

Accepted by .....
Leslie A. Kolodziejski
Professor of Electrical Engineering
Chair, Department Committee on Graduate Theses

THIS PAGE INTENTIONALLY LEFT BLANK

Applications and Noise Properties of High Repetition Rate Ti:Sapphire Frequency Combs

by

Andrew John Benedick

Submitted to the Department of Electrical Engineering and Computer Science
on April 27th, 2011 in partial fulfillment of the requirements for the degree of
Doctor of Philosophy in Electrical Engineering

Abstract

Femtosecond mode-locked lasers are a unique laser technology due to their broad optical bandwidth and potential for linking the optical and radio frequency domains when these lasers are configured as frequency combs. Ti:Sapphire based mode-locked lasers offer considerable advantages over other laser systems by generating both the broadest optical spectrum and highest fundamental pulse repetition rates directly from the laser cavity. Recent advances in laser diode technology have reduced the cost of pump lasers for Ti:Sapphire based frequency combs considerably, and the recent demonstration of direct diode pumping of a narrowband mode-locked Ti:Sapphire laser suggests that Ti:Sapphire frequency combs may finally be ready to make the transition from an indispensible research tool to a wider set of industrial applications.

In this thesis, several applications and fundamental properties of Ti:Sapphire based mode-locked lasers are investigated. To enable more widespread use of Ti:Sapphire based frequency combs, a frequency comb based on an octave spanning 1 GHz Ti:Sapphire laser is demonstrated. The 1 GHz Ti:Sapphire laser is referenced to a methane stabilized HeNe laser, resulting in a frequency comb with a fractional frequency stability of its optical spectrum of 2×10^{-14} on a 20 second timescale.

A recently identified frequency comb application is the calibration of astronomical spectrographs to enable detection of Earth-like planets which are orbiting Sun-like stars. In support of this application, a second frequency comb system was constructed which ultimately was characterized by a 51 GHz pulse repetition rate and 12 nm bandwidth centered at 410 nm. This "astro-comb" system was deployed to the Fred Lawrence Whipple Observatory where preliminary results indicate a 40-fold increase in the spectrograph stability due to calibration by the astro-comb.

Finally, the stability of the optical pulse train emitted from femtosecond mode-locked lasers is expected to exhibit the lowest phase noise of any oscillator, with theoretical predictions of phase noise levels below -190 dBc for offset frequencies exceeding 1 kHz. A comparison between the pulse trains of two nearly identical mode-locked lasers resulted in a measured timing error of less than 13 attoseconds measured over the entire Nyquist bandwidth.

Thesis Supervisor: Franz X. Kärtner
Title: Professor of Electrical Engineering

Acknowledgements

As I say to anyone who will listen, Prof. Kärtner is an amazing person. I've never met anyone with so many ideas, with such a vast knowledge base, who works even half as hard, and has such a positive attitude all the time. I am very lucky that our personalities have meshed as well as they have, since he has truly been a pivotal influence in this process.

My two other committee members, Prof. Ippen and Prof. Kolodziejski fall into the same category. In particular, Prof. Ippen's semi-weekly OAWG meetings forced all of us to keep working and to learn how to explain our work to others clearly and concisely rather than rambling on about the latest minutia. No less influential have been Prof. Kolodziejski's profound comments on this manuscript which have helped result in a far more useful final product.

My fellow graduate students in the OQE group over the years have provided everything from stimulating technical discussions to motivation for excellence in scholarship. In particular, Li-Jin Chen, Jon Birge, and Guoqing Chang, have been most influential on my academic development. I'm lucky to call them friends as well.

Collaboration with Ronald Walsworth's group from Harvard on the "astro-comb" project was also an extremely exciting and unique experience. The examples set by David Phillips, Alex Glenday and especially Chih-Hao Li really challenged me to exceed what I thought I was capable of. I hope I can continue to work with them in the future

There have also been many non-research related people who have helped me through this process in some way. First, I am thankful for the tolerance of the many friends I made in my life prior to beginning this journey. I am very lucky that you are too numerous to mention personally here, but know that I greatly appreciate your patience of my long absence; your ongoing support has not gone unnoticed

Second, it would be a mistake not to mention my Crossfit friends, Yves, Neiko and Dan for pushing me at the gym all those mornings. The endurance developed physically has certainly transferred to increased mental endurance, for which I am grateful. Not to mention that I'd be much slower and weaker without them. Anyone up for Murph or Linda?

Finally, much like the last author on a paper, the last person on the acknowledgement page is the one who made the work possible. Without Erica's continuous and unbounded support, this document would never be written...Thanks E! Let's go hang out with Kenny!

Curriculum Vitae

Education

MIT, Ph.D. in Electrical Engineering, June 2011
University of Massachusetts Boston, M.S. in Applied Physics, June 2006
Northeastern University, B.S. in Mechanical Engineering Technology, June 2001

Refereed Journal Publications

1. A. Benedick, F. X. Kärtner, and J. G. Fujimoto, "Ultrashort laser pulses: Optical flywheels with attosecond jitter," In Preparation (2011).
2. L.-J. Chen, G. Chang, C.-H. Li, A. J. Benedick, D. F. Philips, R. L. Walsworth, and F. X. Kärtner, "Broadband dispersion-free optical cavities based on zero group delay dispersion mirror sets," Opt. Express 18, 23204–23211 (2010).
3. C.-H. Li, A. G. Glenday, A. J. Benedick, G. Chang, L.-J. Chen, C. Cramer, P. Fendel, G. Furesz, F. X. Kärtner, S. Korzennik, D. F. Phillips, D. Sasselov, A. Szentgyorgyi, and R. L. Walsworth, "In-situ determination of astro-comb calibrator lines to better than 10 cm s(-1)," OPTICS EXPRESS 18, 13239-13249 (2010).
4. A. J. Benedick, G. Chang, J. R. Birge, L.-J. Chen, A. G. Glenday, C.-H. Li, D. F. Phillips, A. Szentgyorgyi, S. Korzennik, G. Furesz, R. L. Walsworth, and F. X. Kärtner, "Visible wavelength astro-comb," Opt. Express 18, 19175–19184 (2010).
5. A. Benedick, D. Tyurikov, M. Gubin, R. Shewmon, I. Chuang, and F. X. Kärtner, "Compact, Ti:sapphire-based, methane-stabilized optical molecular frequency comb and clock," Opt. Lett. 34, 2168-2170 (2009).
6. C.-H. Li, A. J. Benedick, P. Fendel, A. G. Glenday, F. X. Kärtner, D. F. Phillips, D. Sasselov, A. Szentgyorgyi, and R. L. Walsworth, "A laser frequency comb that enables radial velocity measurements with a precision of 1 cm s(-1)," Nature 452, 610-612 (2008).
7. M. Y. Sander, J. Birge, A. Benedick, H. M. Crespo, and F. X. Kärtner, "Dynamics of dispersion managed octave-spanning titanium:sapphire lasers," J. Opt. Soc. Am. B 26, 743-749 (2009).
8. J. Moses, S. W. Huang, K. H. Hong, O. D. Mücke, E. L. Falcão-Filho, A. Benedick, F. Ö. Ilday, A. Dergachev, J. A. Bolger, B. J. Eggleton, and F. X. Kärtner, "Highly stable ultrabroadband mid-IR optical parametric chirped-pulse amplifier optimized for superfluorescence suppression," Opt. Lett. 34, 1639-1641 (2009).
9. U. Demirbas, A. Sennaroglu, A. Benedick, A. Siddiqui, F. X. Kärtner, and J. G. Fujimoto, "Diode-pumped, high-average-power femtosecond Cr3+:LiCAF laser," Opt. Lett. 32, 3309–3311 (2007).

Refereed Conference Proceedings

1. A. Benedick, U. Demirbas, D. Li, J. G. Fujimoto, and F. X. Kärtner, "Attosecond Ti:Sapphire Pulse Train Phase Noise," in Conference On Lasers and Electro-Optics (Optical Society of America, 2011), p. CFK4.
2. S.-W. Huang, G. Cirmi, K.-H. Hong, J. Moses, J. Birge, S. Bhardwaj, V.-M. Gkortsas, A. Benedick, L.-J. Chen, E. Li, B. Eggleton, G. Cerullo, and F. Kärtner, "Scalable High-Energy Sub-Cycle Waveform Synthesis for High-Field Physics," in Advanced Solid-State Photonics (Optical Society of America, 2011), p. JWC4.
3. U. Demirbas, A. Benedick, A. Sennaroglu, D. Li, J. Kim, J. G. Fujimoto, and F. X. Kärtner, "Attosecond Resolution Timing Jitter Characterization of Diode Pumped Femtosecond Cr:LiSAF Lasers," in Conference On Lasers and Electro-Optics (Optical Society of America, 2010), p. CTuDD6.
4. J. G. Fujimoto, U. Demirbas, D. Li, A. Benedick, G. S. Petrich, J. R. Birge, J. Wang, S. Nabanja, L. A. Kolodziejski, A. Sennaroglu, and F. X. Kärtner, "Compact and Low-Cost Fs Diode-Pumped

Cr:Colquiriite Laser Technology," in International Conference On Ultrafast Phenomena (Optical Society of America, 2010), p. WC2.
5. L.-J. Chen, G. Chang, C.-H. Li, A. Glenday, A. J. Benedick, D. F. Phillips, R. L. Walsworth, and F. X. Kärtner, "High-Finesse Dispersion-Free Cavities for Broadband Filtration of Laser Comb Lines," in International Conference On Ultrafast Phenomena (Optical Society of America, 2010), p. TuF1.
6. E. Ippen, A. Benedick, J. Birge, H. Byun, L.-J. Chen, G. Chang, D. Chao, J. Morse, A. Motamedi, M. Sander, G. Petrich, L. Kolodziejski, and F. Kärtner, "Optical Arbitrary Waveform Generation," in Conference On Lasers and Electro-Optics (Optical Society of America, 2010), p. JThC4.
7. G. Chang, A. J. Benedick, J. R. Birge, A. Glenday, C.-H. Li, D. F. Phillips, R. L. Walsworth, and F. X. Kärtner, "Tunable Blue Astro-Comb," in Conference On Lasers and Electro-Optics (Optical Society of America, 2010), p. CMHH2.
8. S.-W. Huang, G. Cirmi, J. Moses, K.-H. Hong, A. Benedick, L.-J. Chen, E. Li, B. Eggleton, G. Cerullo, and F. X. Kärtner, "Ultrabroadband Optical Parametric Chirped Pulse Amplifier System for Single-Cycle Waveform Synthesis," in Conference On Lasers and Electro-Optics (Optical Society of America, 2010), p. CWA4.
9. A. Benedick, G. Chang, A. Glenday, C.-H. Li, D. Phillips, R. Walsworth, and F. Kärtner, "Visible Spectrum Frequency Comb for Astronomical Spectrograph Calibration," in Advanced Solid-State Photonics (Optical Society of America, 2010), p. AWC4.
10. C. E. Cramer, C.-h Li, A. G. Glenday, D. F. Phillips, G. Furesz, D. Sasselov, A. Szentgyorgyi, R. L. Walsworth, A. Benedick, and F. X. Kärtner, "ASTRO-COMB: REVOLUTIONIZING PRECISION SPECTROSCOPY IN ASTROPHYSICS," in Proceedings Of the 7th Symposium Frequency Standards and Metrology, L. Maleki, ed. (2009), pp. 166-174.
11. C.-H. Li, A. J. Benedick, C. E. Cramer, G. Chang, L.-J. Chen, P. Fendel, G. Furesz, A. G. Glenday, F. X. Kärtner, D. F. Phillips, D. Sasselov, A. Szentgyorgyi, and R. L. Walsworth, "Femtosecond Laser Frequency Comb for Precision Astrophysical Spectroscopy," in 2009 Conference On Lasers and Electro-optics and Quantum Electronics and Laser Science Conference (cleo/qels 2009), Vols 1-5 (2009), pp. 479-480.
12. C.-H. Li, A. J. Benedick, C. E. Cramer, G. Chang, L.-J. Chen, P. Fendel, G. Furesz, A. G. Glenday, F. X. Kärtner, D. F. Phillips, D. Sasselov, A. Szentgyorgyi, and R. L. Walsworth, "Laser Frequency Combs for Precision Astrophysical Spectroscopy," in CLEO/Europe and EQEC 2009 Conference Digest (Optical Society of America, 2009), p. EG4_3.
13. J. Moses, O. D. Muecke, S.-W. Huang, A. Benedick, E. L. Falcao-Filho, K. H. Hong, A. M. Siddiqui, J. R. Birge, F. O. Ilday, and F. X. Kärtner, "Optimized 2-micron Optical Parametric Chirped Pulse Amplifier for High Harmonic Generation," in Ultrafast Phenomena Xvi, P. Corkum, S. DeSilvestri, K. A. Nelson, and E. Riedle, eds., Springer Series In Chemical Physics (2009), Vol. 92, pp. 786-788.
14. S. W. Huang, J. Moses, K. H. Hong, E. L. Falcao, A. Benedick, J. Bolger, B. Eggleton, and F. X. Kärtner, "High-Power, Few-Cycle, Phase-Stabilized 2.2-mu m Optical Parametric Chirped Pulse Amplifier," 2009 Conference on Lasers and Electro-Optics and Quantum Electronics and Laser Science Conference (Cleo/Qels 2009), Vols 1-5 1791-1792 (2009).
15. U. Demirbas, A. Sennaroglu, A. Benedick, A. Siddiqui, F. X. Kärtner, and J. G. Fujimoto, "High Average-Power Diode-Pumped Femtosecond Cr3+:LiCAF Laser," in Advanced Solid-State Photonics (Optical Society of America, 2008), p. MC38.
16. J. Moses, O. D. Mücke, A. J. Benedick, E. L. Falcao-Filho, S.-W. Huang, K.-H. Hong, A. M. Siddiqui, J. R. Birge, F. Ö. Ilday, and F. X. Kärtner, "Two-Micron Optical Parametric Chirped Pulse Amplifier for Long-Wavelength Driven High Harmonic Generation," in Conference On Lasers and Electro-Optics/Quantum Electronics and Laser Science Conference and Photonic Applications Systems Technologies, OSA Technical Digest (CD) (Optical Society of America, 2008), p. CTuEE2.
17. A. Szentgyorgyi, C. Cramer, A. Benedick, A. G. Glenday, F. X. Kärtner, S. Korzennik, C. H. Li, M. P. Ordway, D. F. Phillips, D. Sasselov, and R. L. Walsworth, "Deploying comb and tunable lasers to enable precision radial velocity surveys - art. no. 70141W," Ground-Based and Airborne Instrumentation for Astronomy Ii, Pts 1-4 7014, W141-W141 (2008).

18. F. X. Kärtner, A. Benedick, J. Birge, and M. Sander, "Carrier-Envelope Phase Controlled Ultrashort Light Pulses for Nonlinear Optics," in Nonlinear Optics: Materials, Fundamentals and Applications (Optical Society of America, 2007), p. MB1.
19. A. Benedick, J. Birge, R. Ell, O. D. Mücke, M. Sander, and F. X. Kärtner, "Octave Spanning 1GHz Ti:sapphire Oscillator For HeNe CH4-based Frequency Combs and Clocks," in CLEO/Europe and IQEC 2007 Conference Digest (Optical Society of America, 2007), p. CF3_1.
20. F. X. Kärtner, A. Benedick, R. Ell, O. D. Mücke, J. Birge, and M. Sander, "Octave Spanning Ti:Sapphire Lasers," in Advanced Solid-State Photonics, OSA Technical Digest Series (CD) (Optical Society of America, 2007), p. WA1.

Invited Presentations

1. "Frequency combs: From the Laboratory to the Mountain," for IEEE Boston Photonics Society, Lexington, Ma, Jan 2011.
2. "Octave Spanning 1GHz Ti:sapphire Oscillator For HeNe CH4-based Frequency Combs and Clocks," for CLEO/Europe, Munich, Germany, June 2007

THIS PAGE INTENTIONALLY LEFT BLANK

Contents

THIS PAGE INTENTIONALLY LEFT BLANK

Chapter 1

Introduction

1.1 Background

Ti:Sapphire mode-locked lasers are a unique laser technology due to their broad bandwidth and potential for wide comb line spacing (high repetition rate) and inherently low noise operation. Maturity of this technology along with the falling cost of the diode-pumped solid state (DPSS) pump lasers has allowed advancement of several applications of frequency combs which would not otherwise be practical. This thesis will pursue compact frequency combs for use as high precision optical clocks, wavelength calibrators for astronomical spectrographs as well as measurement of the fundamental noise limits of these devices with respect to their use as ultra low phase noise RF oscillators. These applications benefit from higher pulse repetition rate lasers (>1GHz) which will also be investigated.

Frequency combs based on octave spanning mode-locked lasers have revolutionized the measurement of time and frequency over the past ten years. The unprecedented precision and accuracy of these systems has enabled measurements of fundamental constants [1], searches for extra solar planets [2-5] as well as enabling development of new technologies such as optical arbitrary waveform generation [6], non-linear biomedical imaging [7,8] and ultra low phase noise master oscillators [9-12]. High repetition rate Ti:Sapphire lasers (>1 GHz) benefit nearly all of these applications by simplifying some aspect of each system's operation.

Increasing the pulse repetition rate of a mode-locked laser has several consequences for the frequency comb user including lower pulse energy, higher power contained in each comb line and larger frequency spacing between each comb line. The benefits of a high repetition rate include less damage in biological tissue for non-linear imaging due to the generally reduced average power. Spectroscopy benefits from the increased power in each comb line through stronger heterodyne beat signals for referencing single frequency continuous wave (CW) lasers. Wider frequency spacing of comb lines simplifies filtering requirements for both optical arbitrary waveform generation and astrophysical spectrograph calibration [5]. The already low phase noise of high frequency microwave signals generated by photo detecting a mode-locked laser's pulse train can be reduced even further by using the fundamental repetition rate tone rather than a harmonic [9].

Building high repetition rate Ti:Sapphire lasers to enable these benefits is challenging. Integrated techniques are not yet available for the Ti:Sapphire material or the common dispersion compensation techniques, so the remaining option is optimizing the free space configuration. However, using this approach it is still possible to achieve mode-locking at 10 GHz [13]. Higher repetition rates may be possible, though new cavity geometries or integration will be necessary which will likely push up the cost of development. While Ti:Sapphire is traditionally one of the most expensive solid state laser systems mainly due to the cost of the pump laser, its optical performance and wavelength coverage has maintained interest in the material. Fortunately, increasing competition in the diode-pumped solid state laser market promises to push the cost of a 10 W pump laser down by more than a factor of three. Combined with continued development of semiconductor laser diodes in the range of 450-550nm [14,15], Ti:Sapphire lasers are poised to become a truly viable commercial and industrial product in addition to their role as an indispensable research tool.

1.2 Overview of thesis

This thesis explores the construction, application and noise properties of Ti:Sapphire based frequency combs and their underlying mode-locked lasers. The constructs used to discuss these broad topics are: the

design and construction of an octave-spanning Ti:Sapphire frequency comb; application of frequency combs to calibration of astronomical spectrographs, specifically a visible wavelength astro-comb; measurement of the intrinsic phase noise of optical pulse trains from Kerr lens mode-locked Ti:Sapphire lasers; an octave spanning Ti:Sapphire laser suitable for optical parametric chirped pulse amplifier (OPCPA) seeding; and high repetition rate Ti:Sapphire lasers with pulse repetition rates exceeding 1 GHz. Specific practical aspects to successful completion of these three experiments are discussed in appendices at the end of the thesis.

1.2.1 Frequency comb and optical clock based on an Octave spanning 1 GHz Ti:Sapphire laser and methane referenced HeNe laser

The growing number of applications for frequency combs can only continue if frequency comb systems can continue to become smaller, cheaper, and easier to use. The third chapter of this thesis will describe construction and testing of a simple Ti:Sapphire frequency comb and optical molecular clock, composed of a commercially-available methane-stabilized helium-neon laser. The resulting stabilized optical spectrum of the Ti:Sapphire laser could then be used as the source for an optical arbitrary waveform generation (OAWG) system, which would have the additional capability for precision spectroscopy. The system as constructed is demonstrated to have a fractional frequency stability of the optical spectrum of $2x10^{-14}$ on a 20 sec time scale. RF domain measurements demonstrate a measurement limited timing jitter of the optical pulse train from the laser of only 10 fs. The optical portion of the system fits within a 1 m^3 volume, with the supporting electronics in half of a standard 19 inch rack. This result demonstrates that broad distribution of Ti:Sapphire based frequency comb technology is limited more by enabling simple operation of broadband Ti:Sapphire lasers rather than the complexity and size of frequency comb systems.

1.2.2 An Octave Spanning Ti:Sapphire laser suitable for OPCPA seeding

A table-top sized source of coherent soft x-rays would enable a wide range of imaging experiments from biology to crystallography [16,17]. One of the leading candidates for achieving this goal is high-

harmonic generation in noble gases using ultra intense light pulses. Several sources [18,19] have predicted that using long wavelength pulses to drive such process will result in a significant decrease in the cutoff wavelength in the resulting harmonic spectrum. A promising route towards generating short pulses at mid-IR wavelengths is optical chirped pulse amplification (OPCPA). Rather than direct generation and amplification of short pulses, OPCPA is a parametric process which uses lower intensity, high average power beams to reduce non-linearity in the amplification process, allowing amplification of broader bandwidths and ultimately shorter and more intense pulses. Seeding such systems requires a laser that can directly generate the seed spectrum at mid-IR wavelengths through difference frequency generation allowing passive stabilization of the f_{CEO} frequency to zero Hertz, which is very important since the high harmonic generation process is electric field dependent rather than intensity dependent. The difference frequency spectrum generated by the Ti:Sapphire laser constructed for this thesis covers nearly 900 nm centered at 2 μm, measured at the -20 dB level.

1.2.3 Frequency combs for astronomical spectrograph calibration

The search for planets in other star systems ("exoplanets") is one of the most exciting areas of research in astronomy today. Currently more than 500 planets have been discovered, with the majority of discoveries occurring through the use of the "radial velocity method", also known as Doppler shift spectroscopy. This technique takes advantage of the fact that stars with planets orbit around the common center of mass of the two objects. For an observer located in the orbital plane, examination of the stellar spectrum will reveal periodic shifts in the stellar spectrum corresponding to the period of the planets orbit. For astronomers interested in finding planets similar to the Earth in orbit around stars similar to the Sun, the resulting spectral shifts are very small and occur on year long time scales. The orbital velocity imparted on the Sun by the Earth is estimated to be 5 cm/s, corresponding to a 125 kHz frequency shift in the stellar spectrum. Current methods for calibrating the spectrographs used for measuring stellar spectra can only provide precisions of 2.5 MHz or 1 m/s, and this level of stability is only available on a one month time period. Using frequency combs as calibrators for these spectrographs was suggested by

Murphy et.al. in 2007, with the initial technical complication being that the resolution of astronomical spectrographs is not high enough to resolve the individual optical components from existing frequency combs. Currently the best solution is to use a Fabry-Perot filter to remove all but every nth comb line; a process which leaves an optical spectrum dubbed as an "astro-comb". A portion of the thesis has resulted in construction of an astro-comb for the visible wavelength region as well as preliminary results from an attempt to calibrate an astronomical spectrograph.

1.2.4 Phase noise of optical pulse trains

Low phase noise oscillators enable a wide range of applications including secure communications, Doppler radar, high speed sampling clock for analog to digital conversion, timing synchronization for synthetic aperture radar observations, and timing systems for next generation free electron laser facilities. Traditionally, microwave oscillators based on large sapphire cavities have been the standard for low phase noise signals. Phase noise levels of -175 dBc/Hz (1 kHz) offset have been reported [20], with even lower levels predicted for next generation systems. Mode-locked lasers on the other hand, specifically when operated as frequency combs, are generally regarded for their frequency stability. This stability is entirely derived from the frequency reference used to construct the frequency comb and is generally only useful at extremely small offset frequencies (<<1 Hz). As low phase noise oscillators, especially at high offset frequencies (>10 kHz), optical pulse trains from unstabilized femtosecond mode-locked lasers should have the lowest phase noise of any oscillator [21,22]. The challenge is to demonstrate these predictions, since at offset frequencies of interest the predicted noise levels are more than 40 dBc below what is possible with RF domain measurement techniques. Balanced optical cross correlation offers the opportunity to measure the phase noise of these optical pulse trains directly in the optical domain without first generating an RF signal by photodetection (which is a non-trivial task [23,24]). Using the balanced optical cross correlation technique to measure the phase noise between two 80 MHz Ti:Sapphire lasers, a measurement floor of -203 dBc/Hz is demonstrated, with an integrated timing error between the two lasers of less than 13 as. As there is still a large portion of the phase error

spectrum consisting of pump laser relative intensity noise converted into pulse train phase noise, this measurement result merely constitutes an upper limit to the actual pulse train phase noise.

1.2.5 High repetition rate Ti:Sapphire lasers: is there life beyond 1 GHz?

For many applications, including the calibration of astrophysical spectrographs, optical arbitrary waveform generation, precision spectroscopy and two-photon microscopy, increasing the spacing between the comb lines or increasing the repetition rate of the mode-locked laser simplifies the design and operation of these systems. Currently the majority of Ti:Sapphire mode-locked lasers are limited to repetition rates of less than 1GHz, with only a few examples operating at higher rates, with the current limit for a laser generating an octave spanning spectrum set at 2.1 GHz [25]. The highest reported pulse repetition rate is 10 GHz [13], though the spectrum of this laser is very far from octave spanning at only 19 nm. As part of this thesis, mode-locked operation at 10 GHz has been demonstrated in two laser configurations, though with very limited bandwidths. Along with details of these results will be a discussion of the current difficulties and some possible ways to increase the bandwidth of such high pulse repetition rate lasers.

Chapter 2

Frequency combs

2.1 Introduction

The original application envisioned for frequency combs was precision spectroscopy [26]. One of the most fundamental methods to probe the structure of matter is to shine light on a sample of material and analyze what is transmitted and reflected. Increasing knowledge of the incident light can only increase the amount of information to be gathered from the resulting reflection and transmission spectra. As late as 1996 however, the best technique yet conceived to measure optical frequencies was to build frequency chains [27]. These are devices which could phase coherently link a low frequency oscillator (100 MHz) to a microwave transition in Cesium near 9 GHz and then proceed to up-convert this 100 MHz quartz oscillator to as high as 400 THz. While these systems were able to achieve fractional frequency accuracies of 10^{-12} at the ultimate optical frequency, the resulting signal typically could not be tuned more than a few GHz. Performing an experiment only a few nanometers away could require a major redesign of the chain.

Theodore Hänsch's revelation [28] was that the mode-locked laser could be used as a ruler in the frequency domain where knowing the absolute frequency of each mode could allow a link from radio frequencies to optical frequencies in one step. As will be described in greater detail in the next section, it turns out that the discrete components of the mode-locked lasers optical spectrum can be described by a very simple relation,

$$f_n = f_{CEO} + nf_R \tag{2.1}$$

where f_R is the pulse repetition rate of the mode-locked laser, f_{CEO} is the carrier-envelope offset frequency, and n is a large integer. By detecting and defining both f_R and f_{CEO}, every optical frequency in the mode-locked laser spectrum is defined and the mode-locked laser can be referred to as a frequency comb. While detection of f_R is very straightforward, determining f_{CEO} proved much more challenging. It took until 1997 [29,30] to simply figure out a way to detect the f_{CEO} frequency. The ideas reported in these publications determined that it was necessary for a laser to emit an optical spectrum of over one octave in bandwidth to allow detection of the f_{CEO} frequency. Another 2 years was required until in 1999 [31-33] both Theodore Hänsch's group in Garching Germany as well as John Hall's group at JILA both demonstrated frequency comb systems. The breakthrough was provided by the development of highly non-linear optical fibers [34], which allowed a relatively narrowband laser output spectrum (<10 nm) to be non-linearly broadened to more than 1000 nm, giving the bandwidth necessary to access the f_{CEO} frequency. Following this breakthrough, there was a barrage of experiments [35-37] aimed at determining the exactness of Eq. (2.1), several of which were able to provide verification of the regularity of comb line spacing to a precision of 10^{-17}.

The following years have seen an incredible expansion of applications for frequency comb technology. Originally envisioned for precision spectroscopy as a way to reference single frequency lasers, the current list of applications includes: direct frequency comb spectroscopy, dual comb spectroscopy, cavity ringdown spectroscopy, optical clocks for precision timekeeping, precision range finding, astronomical spectrograph calibration, low phase noise microwave generation, frequency translators for tests of fundamental physics, time and frequency transfer, attosecond physics enabled by direct control of f_{CEO}, and optical arbitrary waveform generation (OAWG). Because of the wide range of applications currently supported by frequency comb technology after only ten years of life, discovery of a suite of applications similar to that of the standard CW laser over the next 10 year is highly likely.

2.2 Femtosecond mode-locked lasers

The basic building block for a frequency comb is a mode-locked laser. In principle, any type of mode-locked laser can be made into a frequency comb, provided f_{CEO} frequency can be determined. As mentioned previously, this is a non-trivial requirement which currently limits construction of frequency combs to lasers based on generally three types of gain material: Erbium(Er) doped fiber lasers, Ytterbium(Yb) doped fiber lasers and Ti:Sapphire free space lasers. Other materials have been demonstrated; however the vast majority of frequency comb systems have been constructed using these three material systems. The reason for using these particular materials are the short pulses which can be generated directly from both Er fiber lasers and Ti:Sapphire allow detection of f_{CEO} directly (Ti:Sapphire) or after nonlinear broadening (Er fiber). Ytterbium fiber lasers are typically much more narrowband than either Ti:Sapphire or Er fiber lasers; however generating extremely high powers from Yb lasers is much more straightforward, allowing Yb lasers to reach high intensity for supercontinuum generation through high average powers rather than short pulse durations.

All three technologies, however, follow the same general rules for operation. On a round trip basis, the laser cavity has low dispersion allowing propagation of an optical pulse with very little temporal spreading, as well as a mechanism for forcing the laser to operate in pulsed mode rather than continuous wave. Additional nonlinear effects can also be included to broaden the optical spectrum beyond what the gain bandwidth of the laser would normally provide. The mathematical basis for this process was originally described by Haus in 1991 [38], and has subsequently been used as the foundation for essentially all work in the mode-locked laser field. This section will review the formalism outlined by Haus and other to describe the mode-locking process to provide a basis for understanding the operation of mode-locked lasers as frequency combs. Because the work in this thesis is based on Kerr lens mode-locked Ti:Sapphire lasers, the following section will focus on the Kerr lens mechanism. However, many of the concepts are general and can be applied to many other laser systems.

2.2.1 Linear pulse propagation - Dispersion

A reasonable place to start the discussion of mode-locked laser operation is with linear pulse propagation through dispersive media. An optical pulse can be described by a carrier wave and a complex envelope function such as

$$E(z,t) = \Re\left[A(t)\exp\left(i\left(\omega_0 t - k_0 z\right)\right)\right] \tag{2.2}$$

$$A(t) = \frac{1}{2\pi}\int_{-\infty}^{\infty} A(\Omega)\exp(i\Omega t)\,d\Omega \tag{2.3}$$

where in this description ω_0 is the carrier frequency of the optical spectrum, and the spectrum of the envelope function has been shifted to zero frequency such that $\Omega=\omega-\omega_0$, and $|A|^2$ is the pulse power . Propagation of the envelope function in space is achieved through multiplying by a complex phase factor to account for the index of refraction of the intervening media.

$$A(z,t) = \frac{1}{2\pi}\int_{-\infty}^{\infty} A(\Omega)\exp(i\left(\Omega t - k(\Omega)z\right)d\Omega \tag{2.4}$$

$$k(\omega-\omega_0) = \frac{\Omega n(\Omega)}{c} = \frac{2\pi n(\Omega)}{\lambda} \tag{2.5}$$

with $k(\Omega)$ known as the wave number, $n(\Omega)$ as the refractive index and λ as the wavelength in vacuum. From these expressions, it is already possible to see that some sort of distortion will occur to the envelope of the pulse during propagation through a given medium depending on the shape of the index of refraction function, $n(\omega)$.

Because $n(\omega)$, and ultimately $k(\omega)$ are generally frequency dependent, it is standard practice to approximate them as Taylor expansions around the pulse center frequency ω_0.

$$k(\omega) = k(\omega_0) + \frac{\partial k}{\partial \omega}\omega + \frac{1}{2}\frac{\partial^2 k}{\partial \omega^2}\omega^2 + \frac{1}{6}\frac{\partial^3 k}{\partial \omega^3}\omega^3 + O\left(\omega^4\right) \tag{2.6}$$

This expansion allows an opportunity to explore the effect of each term on the pulse propagation. By using the standard Fourier Transform relationships, $k - k(\omega_0) \Leftrightarrow -i\frac{\partial}{\partial z}$ and $\omega \Leftrightarrow i\frac{\partial}{\partial t}$, and inserting $A(z,t)$ as an operand, the Taylor series can be re-written as a propagation equation for the pulse envelope.

$$i\frac{\partial A(z,t)}{\partial z} = -ik'\frac{\partial A(z,t)}{\partial t} + \frac{k''}{2}\frac{\partial^2 A(z,t)}{\partial t^2} - i\frac{k'''}{6}\frac{\partial^3 A(z,t)}{\partial t^3} \tag{2.7}$$

This equation describes the evolution of a pulse under the influence of linear dispersion in isotropic media. Examining each term on the right side of equation (2.7), and transforming back to the frequency domain as necessary:

$$\frac{\partial A(z,\omega)}{\partial z} = -ik'\omega A(z,\omega) \tag{2.8}$$

The first term on the right side of equation (2.7) generates a linear phase change as a function of frequency. Using the shift theorem of Fourier transforms, Eq. (2.8) results in a shift in pulse position in the time domain. This shift is known as the group velocity of the pulse defined as

$$v_{g0} = \left(\left.\frac{\partial k}{\partial \omega}\right|_{\omega=\omega_0} \right)^{-1} \tag{2.9}$$

The second term on the right side of equation (2.7), describes a parabolic phase modulation on the pulse spectrum.

$$\frac{\partial A(z,\omega)}{\partial z} = i\frac{k''}{2}\omega^2 A(z,\omega) \tag{2.10}$$

A chirped pulse can be interpreted as a super-position of many narrowband sections of the pulse spectrum, each experiencing its own linear phase. In such a framework it is straightforward to understand that various sub sections of the pulse will be travelling at different speeds in the time domain, resulting in a net broadening of the pulse, assuming initially that the pulse phase was linear. Broadening of a pulse due to the second order frequency dependent phase is known as group delay dispersion (GDD)

$$GDD = \frac{1}{2}\frac{\partial^2 k}{\partial \omega^2}L \tag{2.11}$$

with L as the length of material through which the pulse has propagated.

The third term on the right hand side of equation (2.7) also generates a non-linear phase across the pulse spectrum.

$$\frac{\partial A(z,\omega)}{\partial z} = i\frac{k'''}{6}\omega^3 A(z,\omega) \qquad (2.12)$$

Notice that Eq. (2.12) term is anti-symmetric in frequency, requiring that the resulting frequency chirp of the pulse also be nonlinear. It is straightforward to understand now that any contribution to the phase of a pulse which is not linear in frequency is considered dispersion.

Dispersion terms can be both positive or negative, though all optically transparent materials exhibit positive dispersion(i.e. Eq. (2.11) is positive in all transparent materials) . To compensate this normal material dispersion, several techniques have been developed, specifically techniques utilizing prism pairs [39] and chirped mirrors [40,41]. The method for dispersion compensation most applicable for construction of high repetition rate Ti:Sapphire mode-locked lasers is the use of chirped mirror pairs.

Chirped mirrors are dielectric Bragg reflector type mirrors where the Bragg wavelength is slowly varied through the layer structure, typically in a monotonic fashion. The variation in Bragg wavelength gives two results. First, extremely broad reflectivity bandwidths are possible by satisfying the Bragg condition for many different wavelengths. Second, because the Bragg condition is varied, the penetration depth of light into the mirror coating is a function of its frequency. By carefully engineering the rate at which the Bragg wavelength is varied, it is possible to generate dispersion profiles which are the exact opposites of those experienced by light travelling through different materials.

Design and construction of chirped mirrors is very challenging due mainly to the large numbers of layers necessary (70-110) to achieve the desired reflectivity and phase response. Recently a new technique [42] was developed to streamline the design process; however, due to the complexity of the mirror structure, having a good starting design to optimize is still necessary. For this thesis, chirped mirrors will be used as a tool for constructing mode-locked lasers and for pulse compression.

2.2.2 Non-Linear pulse Propagation – Self Phase Modulation

A naïve solution to the problem of dispersion in a laser cavity or an optical fiber would be to suggest that the dispersion be completely compensated by chirped mirrors, prism pairs, etc. As with all manufactured items however, the compensation provided by all available linear methods is not exact, and cannot

completely remove the effects of dispersion. This becomes a serious problem in a laser cavity where millions of round trips occur every second, quickly leading to significant pulse spreading for any finite amount of residual dispersion.

Nonlinear phase modulation of the pulse spectrum can be the inverse phase correction necessary for exact dispersion balance in a laser cavity. The phase modulation mechanism theory originates from the optical Kerr effect [43] and is termed self phase modulation(SPM). The Kerr effect describes the intensity dependent refractive index of a medium as,

$$n \approx n_0(\omega) + n_2 I \tag{2.13}$$

where n_2 is the intensity dependent refractive index, I is the incident light intensity, and there is no linear dependence on the electric field of the pulse because the medium is isotropic. This causes an important redefinition of the propagation vector, which is now written as

$$k(\omega, I) = \frac{\omega n}{c} = \frac{\omega}{c} n_0 + \frac{\omega}{c} n_2 I \tag{2.14}$$

The effect on the envelope propagation can be determined by considering the derivative of the propagation constant k with respect to the pulse intensity

$$\frac{\partial k}{\partial I} = \frac{\omega}{c} n_2 \tag{2.15}$$

Because the refractive index is essentially an instantaneous response to the power in the pulse, the response of a pulse during propagation when considering self phase modulation is

$$\frac{\partial A(z,t)}{\partial z} = -ik(\omega_0) n_2 \left| A(z,t) \right|^2 A(z,t) \tag{2.16}$$

where $|A|^2$ is pulse intensity, and noting that SPM is most easily represented in the time domain. As the pulse intensity is highest at the peak of the pulse and most pulse shapes (sech, Gaussian, Lorentzian, etc.) are well approximated by quadratics around the center of the pulse, the phase induced by SPM is also quadratic. This quadratic phase variation in time is the same as a linear frequency variation with red wavelengths in the front of the pulse and blue wavelengths at the trailing edge of the pulse. The quadratic phase provided by self phase modulation has the opposite sign from the GDD accumulated by linear

propagation through the remainder of the laser cavity. Because of the difference in sign, self phase modulation acts as a dynamic mechanism for balancing the round trip laser cavity dispersion. The amount of frequency shift which occurs due to self phase modulation can be estimated using the following relationships derived in part from Eq.(2.16)

$$\begin{aligned} \phi_0 &= nk(\omega_0)z = nk_0 z \\ \phi &= (n_0 + n_2|A|^2)k_0 z \\ \omega &= \frac{\partial\phi}{\partial t} = n_2 k_0 \frac{\partial|A|^2}{\partial t} z \end{aligned} \qquad (2.17)$$

Expressions (2.17) can be used to estimate the bandwidth of frequency components generated in the self phase modulation process.

Combination of the self phase modulation term and the GDD term from Eq. (2.10) describes propagation of a pulse through a dispersive medium in a reference frame that is moving with the pulse, i.e. the effect of the group velocity term in Eq. (2.8) has been subtracted off since there is no contribution to pulse width.

$$i\frac{\partial A(z,t)}{\partial z} = -GDD\frac{\partial^2 A(z,t)}{\partial t^2} + \delta|A(z,t)|^2 A(z,t) \qquad (2.18)$$

Equation (2.18) has the form of a non-linear Schrödinger equation and can be used as a zero order description of pulse propagation in a laser cavity. To understand pulse propagation further, a solution is required which drives the left side of Eq. (2.18) to zero implying a pulse which propagates without spreading. The traditional method for finding the solution to Eq. (2.18) equation is to use an inverse scattering transform [44]. Rather than derive the solution using this method, the generally accepted solution will be used which is a sech shaped pulse

$$A(z,t) = A_0 \operatorname{sech}\left(\frac{t}{\tau}\right)\exp(-i\theta) \qquad (2.19)$$

with the full width at half maximum of the pulse defined as $\tau_{1/2}=1.76\tau$, and the nonlinear phase shift $\theta = \frac{1}{2}\delta A_0^2 z$, where a constant phase shift across the pulse is assumed for simplicity. A few parameters which will be useful in later discussions are the pulse energy

$$\omega_p = \int_{-\infty}^{\infty}|A(z,t)|^2 dt = 2A_0^2\tau \qquad (2.20)$$

as well as the relationship between Eq.(2.20) and the definition of θ

$$\tau = \frac{4|GDD|}{\delta\omega_p} \tag{2.21}$$

where if the pulse is to propagate without dispersing, i.e. for the left side of Eq.(2.18) to equal zero, $\theta = \frac{GDD}{\tau^2} z$.

The fact that the amount of phase modulation provided by SPM is dependent on the pulse shape itself allows this mechanism to balance dispersion described by functions more complex than parabolas. In the simplest case, only the GDD contribution is assumed to be compensated by SPM, but empirically during the course of this thesis I have found that lasers which are mode-locked with the Kerr effect are tolerant of much higher order phase errors contributed by residual high-order dispersion as long as either the amplitude of these errors is small compared to those from the non-zero average GDD over the pulse bandwidth, or if the fluctuations of the phase errors are very fast on the pulse bandwidth basis.

2.2.3 Self-Steepening effect

As discussed previously, the frequencies of individual components in the optical spectrum of a mode-locked laser are exactly described by $f_n = f_{CEO} + nf_R$. The pulse repetition rate is easily controlled through changes in the length of the optical cavity; however, control of the carrier envelope offset frequency and an explanation of why such control is possible is more involved. An excellent description about the dynamics of f_{CEO} control has been presented in several places [45,46], so here only a summary of these results will be presented to allow clear understanding of the results later in the thesis.

The carrier envelope offset frequency is caused by a mismatch between the overall group and phase velocity in the laser cavity as well as the non-linear phase shift of the pulse envelope in the Ti:Sapphire crystal. The result is that the electric field of each pulse exiting the laser cavity has a different phase alignment with the pulse envelope, which evolves at a rate defined as f_{CEO}. Because of the capability to modulate the pump power to the laser using an acousto-optic modulator, controlling the f_{CEO} frequency through changes in the intracavity pulse energy is of great interest. The contribution to

changes in f_{CEO} from changing group and phase velocities in linear propagation due to shifts in the center of gravity of the optical spectrum will be ignored. Further, for the octave spanning spectra typically necessary to simply detect the f_{CEO} signal, the laser spectrum is completely filling both the laser and mirror bandwidths. Since this filling prevents frequency shifts in the center of gravity of the optical spectrum, any effect which would attempt to change the relationship between group and phase velocity by changing the center frequency of the spectrum is significantly reduced.

In deriving the non-linear phase shift described in section 2.2.2 above, the contribution to the pulse group velocity due to the peak power of the pulse is neglected. Using the definition of k which includes the peak pulse intensity, Eq. (2.14), the inverse group velocity as a function of peak pulse intensity can be defined as

$$\frac{\partial k\left(\omega,|A|^2\right)}{\partial \omega} = \frac{n_0}{c} + \frac{\omega}{c}\frac{\partial n_0}{\partial \omega} + \frac{n_2|A|^2}{c} + \frac{\omega}{c}\frac{\partial n_2}{\partial \omega}|A|^2 \qquad (2.22)$$

The first two terms in Eq.(2.22) comprise the inverse group delay from Eq.(2.9). The second two terms are the first order correction to the group delay due to the Kerr effect. Dispersion of n_2 has been found experimentally to be very small [43] so the last term in Eq.(2.22) can be ignored, leaving only the third term as the main contributor.

Summing this result into Eq.(2.6) and using the same Fourier transform relationship which generated Eq. (2.7) yields

$$\frac{\partial A(z,t)}{\partial z} = -\frac{n_2}{c}\frac{\partial}{\partial t}|A|^2 A(z,t) \qquad (2.23)$$

which describes self steepening of an optical pulse. The self steepening term redistributes the power of the pulse in the time domain, putting more of the pulse energy at the back of the pulse resulting in a steepening of the trailing edge of the pulse and an overall shift in the center of gravity.

2.2.4 Gain and loss in mode-locked lasers

The previous sections dealt only with phase effects on the pulse envelope due to propagation through dispersive media or due to a power dependent refractive index. To build a laser, gain and loss effects must be considered to determine the output power, spectral bandwidth, dynamics of the laser power, pulse train phase noise, etc. The simplest model for both gain and loss during propagation of a pulse through any material can be expressed as

$$\frac{\partial A(z,\omega)}{\partial z} = (g - l) A(z,\omega) \qquad (2.24)$$

where g is the gain experienced by the pulse and l is the loss. Both terms (g and l) as written above assume no optical frequency dependence, and no saturation (reduction of either term with increasing pulse intensity), both of which are fairly imperfect assumptions for a free space solid state laser similar to those used in this thesis. A better approximation for the finite bandwidth of the laser gain is

$$\frac{\partial A(z,t)}{\partial z} = \left[g - D_f \frac{\partial^2}{\partial t^2} \right] A(z,t) \qquad (2.25)$$

where the gain in the frequency domain is limited by approximating the Lorentzian gain line as a parabola.

In most narrowband mode-locked lasers, the gain bandwidth is the limiting element, and all other optical components can be assumed to have constant reflectivity (loss) as a function of frequency. In cases where the laser bandwidth exceeds a certain range, it is necessary to consider the exact reflectivity profile of all optics as they will have a significant effect on the final pulse shape. Generally accounting for a frequency dependent reflectivity can only be accomplished numerically; however the above expressions are still valid for understanding the basic dynamics of mode-locked lasers.

2.2.5 Spatial Kerr effect

In section 2.2.2, a temporal intensity dependent refractive index effect was discussed which generated new frequency components for the pulse. Here, the spatial aspect of the intensity dependent refractive index is discussed. In Ti:Sapphire lasers, generally the effect is only important in the Ti:Sapphire crystal

itself since this is the only location where the intensity is high enough to consider an intensity dependent refractive index. It will be found that the intensity dependent refractive index and resulting self focusing creates the discrimination necessary for determining if the laser operates in a CW or pulsed regime as well as the lasing bandwidth of the mode-locked laser.

In a real laser resonator, the spatial description of the laser mode in the gain material is different in the two axes normal to the direction of propagation. For simplicity the beam can be assumed to have a radially symmetric Gaussian beam whose transverse electric filed can be described by

$$U(r,z) = \frac{U_0}{q(z)} \exp\left(-ik\frac{r^2}{2q(z)}\right) \tag{2.26}$$

where U_0 is the peak electric field divided by the material impedance, r is the radial location on the face of the beam and $q(z)$ is a complex valued parameter describing the beam waist and wavefront radius of curvature as

$$\frac{1}{q(z)} = \frac{1}{R(z)} - i\frac{\lambda}{n\pi w^2(z)} \tag{2.27}$$

The spatial description of the resulting beam intensity can be described by

$$I(r,z) = \frac{2P}{\pi w^2(z)} \exp\left(-\frac{2r^2}{w^2(z)}\right) \tag{2.28}$$

(2.29)

Definitions for the beam waist, $w(z)$, and the wavefront radius, $R(z)$, have been developed in many places throughout the literature, and are defined as

$$w(z) = w_0\left[1+\left(\frac{\lambda z}{n\pi w_0^2}\right)^2\right]^{1/2} \tag{2.30}$$

$$R(z) = z\left[1+\left(\frac{n\pi w_0^2}{\lambda z}\right)^2\right] \tag{2.31}$$

Both w_0 and the location where R becomes infinite are one in the same and these three facts serve to anchor any description of the propagation of a Gaussian beam.

Within the framework of an intensity dependent refractive index and the spatial description of a Gaussian beam, the action of the Kerr effect on the beam becomes clear. The refractive index of a material is modified by an incident beam of suitably high intensity as

$$\delta n(r,z) = n_2 \frac{2P}{\pi w^2(z)} \exp\left(-\frac{2r^2}{w^2(z)}\right) \qquad (2.32)$$

Approximating the spatial intensity profile of the beam as a parabola and the beam intensity as a constant across the length of the crystal, the distance traveled by the beam through the laser crystal of length *Lc* as a function of the spatial power distribution described in Eq. (2.32) and the intensity dependent refractive index Eq. (2.13) can be defined as

$$L(r) = \left(1 - \frac{4r^2}{\omega_0^2}\right)\left(n + n_2 \frac{2P}{\pi\omega_0^2}\right) L_c \qquad (2.33)$$

From this expression, the effect of the spatial Kerr effect can be compared to that of a thin lens. The central portion of the beam is phase shifted with respect to the outer edges of the beam due to the slightly longer optical path, causing a weak focusing of the beam as during propagation with high intensity.

By making the diameter of the laser beam used to pump the Ti:Sapphire gain material slightly smaller than the calculated diameter of the intracavity laser mode when in CW operation, it is possible to force the laser to operate in a mode which attempts to match the more tightly focused pump beam. With the correct ratio of beam sizes, a slight perturbation in laser mode intensity will cause a slight increase in the overlap of the laser mode and the pump mode in the laser crystal due to the non-linear focusing of the Kerr effect, and more gain for the higher intensity time window. On the following round trip the intensity will be slightly higher, allowing an even better overlap of the intensity fluctuation with the pumped volume than on the previous pass. The reduction in mode size continues until the overlap of the pump mode and laser mode is nearly perfect, Fig 2.1, and in fact cannot become unstable to drive the pulse energy to a very large value since eventually additional focusing will begin to degrade the overlap of the pump and laser mode. The dependence of laser intensity on overlap of the laser and pumped crystal volume is therefore a self stabilizing process.

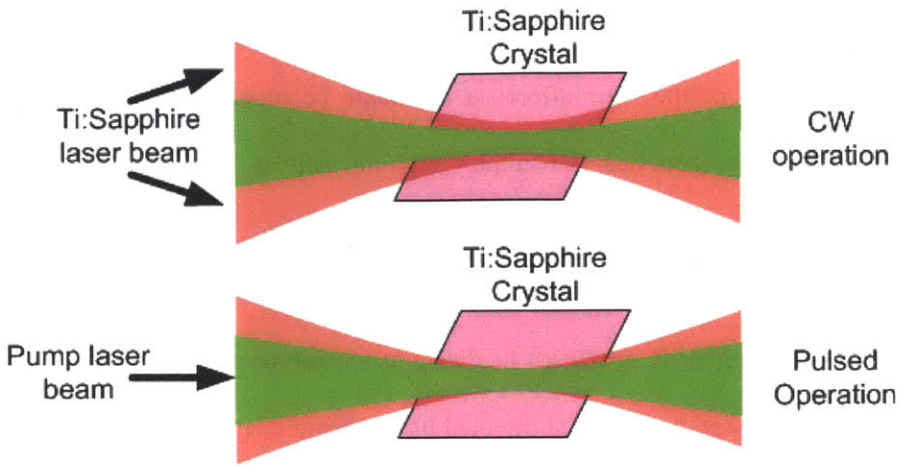

Figure 2.1 -- Sketch of the spatial overlap between the pumped crystal volume and the crystal volume occupied by the Ti:Sapphire laser mode. In the CW case the overlap is poor, and the mode intensity is not high enough to utilize all of the available gain. The additional focusing provided by the high intensity pulse improves the overlap, utilizing more of the available gain.

The evolution of the spot size change due to increasing pulse energy accumulated through improved overlap of the pump and laser mode occurs slowly over many round trips because the pulse energy in short pulse Ti:Sapphire lasers is not large enough to saturate the gain in a single pass. The evolution of the overlap of the laser and pump beams is accounted for using a saturable absorber which reduces the loss affecting the cavity as the pulse energy increases.

$$q(A) = \frac{q_0}{1 + \frac{|A|^2}{P_A}} \tag{2.34}$$

where q_0 is the non-saturable loss of the absorber (i.e. the effect of a poor initial mode overlap) and P_A is the saturation power of the absorber. Typically the saturable absorber response is approximated as

$$q(A) = q_0 - \frac{q_0}{P_A}|A|^2 \tag{2.35}$$

to allow analytic solutions to be drawn from the master equation of mode-locking, described in Section 2.2.6. This description is consistent with the discussion in the preceding paragraphs if instead of increasing the gain for the pulsed case, the loss is decreased. As long as a solid understanding of the limitations of each representation is maintained, either description is acceptable.

2.2.6 Mode-locked laser analysis

Hermann Haus is credited with generating and popularizing the following representation of steady state pulse propagation in a mode-locked laser [38]. An extensive literature exists for both analytic and numeric interpretations of linear and non-linear pulse propagation, only a few of which were discussed in the preceding sections. The general results will only be stated here, leaving specific discussion for the sections of the thesis where they are necessary.

A pulse circulating in a mode-locked laser will experience all of the effects described above on each round trip through the laser cavity. The individual terms can be summed together as lumped effects to achieve a master equation which describes pulse propagation on a round trip basis, while still allowing each term to be analyzed in turn as necessary to achieve an accurate lumped element effect. The final equation will be

$$T_R \frac{\partial A(T,t)}{\partial T} = \left[i\frac{k''}{2}\frac{\partial^2}{\partial t^2} - ik(\omega_0)n_2|A|^2 + \frac{q_0}{P_A}|A|^2 + \left[g - D_f \frac{\partial^2}{\partial t^2} \right] - l - \frac{n_2}{c}\frac{\partial}{\partial t}|A|^2 \right] A(T,t) \tag{2.36}$$

which includes terms, from left to right, for linear group delay dispersion, self phase modulation, self amplitude modulation, gain and gain bandwidth, frequency independent linear loss and the self steepening effect. Since each term is now essentially a lumped element to be summed each round trip, the time basis is now T, representing the round trip time. The timescale associated with the duration of the pulse, t, is retained to allow analysis of the effect of each component as the pulse passes through. Analytic solutions to Eq. (2.36) are typically found by assuming steady state operation, which allows simplification to

$$\left[i\frac{k''}{2}\frac{\partial^2}{\partial t^2} - ik(\omega_0)n_2|A|^2 + \frac{q_0}{P_A}|A|^2 + \left[D_f \frac{\partial^2}{\partial t^2} \right] - \frac{n_2}{c}\frac{\partial}{\partial t}|A|^2 \right] A(T,t) = 0 \tag{2.37}$$

In the simplest case, where only self phase modulation and dispersion play a role, the solution can be shown as a sech shaped pulse, as discussed in the previous section. The additional terms generally lead to slightly more complex pulse shapes, chirped pulses, etc.

The simplest solution [47] to (2.37) is a repeating pulse shape

$$A(T,t)=\sum_{m=-\infty}^{\infty} a(T=mT_R,t)\exp\left(i\left[\omega_0\left(t-mT_R+\left(\tfrac{1}{v_g}-\tfrac{1}{v_p}\right)2mL\right)-\theta\right]\right) \tag{2.38}$$

where a is a function representing the pulse shape(sech, Gaussian, etc.) with a certain round trip average group velocity, v_g, and phase velocity, v_p, and soliton phase shift θ which is defined through Eq.(2.19) as

$$\theta=\frac{1}{2}\delta|A|^2 z=\frac{GDD}{\tau^2}z \tag{2.39}$$

Eq. (2.38) also reports the phase shift between the carrier wave and the envelope of each pulse defined as

$$\Delta\phi_{CE}=\omega_0 2L\left(\tfrac{1}{v_g}-\tfrac{1}{v_p}\right)-\theta+\mathrm{mod}(2\pi) \tag{2.40}$$

For $\omega_0=\omega_c$ which is the center frequency of the resulting optical spectrum. The Fourier transformation of Eq.(2.38) gives

$$\begin{aligned}
A(\omega)&=a(\omega-\omega_c)\sum_{m=-\infty}^{\infty}\exp\left(-i\left[\frac{(\omega-\omega_c)}{f_R}-\Delta\phi_{CE}\right]m\right)\\
A(\omega)&=a(\omega-\omega_c)\sum_{m=-\infty}^{\infty}\exp\left(-i\frac{m}{f_R}[\omega-f_R\Delta\phi_{CE}]\right)\\
A(\omega)&=a(\omega-\omega_c)\sum_{m=-\infty}^{\infty}\frac{1}{f_R}\delta\left(\omega-\left(m2\pi f_R+\Delta\phi_{CE}f_R\right)\right)
\end{aligned} \tag{2.41}$$

The main result of Eq. (2.41) is the relationship

$$f_m=mf_R+\frac{\Delta\phi_{CE}}{2\pi}f_R=mf_R+f_{CEO} \tag{2.42}$$

which is of great importance because Eq. (2.42) enables a direct connection between the frequency of each mode of the optical spectrum and two RF frequencies, f_R and f_{CEO}. By defining f_R and f_{CEO} through stabilization methods to be discussed throughout this thesis, a phase coherent link is established between the RF domain and the optical domain in a single step.

To understand the startup dynamics of a mode-locked laser, as well as include the frequency dependent properties of each element in the laser cavity, it is generally necessary to solve Eq.(2.36) numerically. Solutions are generally found with a split-step Fourier method which allows the propagation and evaluation of each term in both the time and frequency domain. Switching domains is advantageous

since some terms in Eq. (2.36) are more easily implemented in the time domain and others in the frequency domain. By slowly stepping through a given piece of material, each of the appropriate nonlinear terms can be applied in turn for a small propagation distance and incur very little error.

2.3 Free space versus fiber based mode-locked lasers

An equally important question when designing a frequency comb system is what type of laser material to use. To date, Ti:Sapphire, Er fiber and Yb fiber lasers are the most commonly used laser materials for frequency combs. There are important general trends in performance and specification between the fiber and free space lasers which are summarized in the table below.

Unfortunately, it is not yet possible to for any one laser system to display all of the positive traits listed below. This simply means it is necessary to choose the laser material based on the frequency comb application and not the other way around.

Ti:Sapphire / Cr:LiCaF / Solid State Lasers	**Er:fiber / Yb:fiber / Solid State Fiber Lasers**
PRO	**PRO**
Broadband	Nearly alignment free
Narrow linewidth	Insensitive to environment (temp., humidity)
Low timing jitter	High output power (narrowband)
High repetition rate (fundamental)	Excellent output spatial mode quality
Visible wavelength output	Good wall plug efficiency
CON	**CON**
Low wall plug efficiency	Low output power (broadband)
Large pump laser (physical)	Narrowband
Large pump laser (total power required)	Linewidth
Large pump laser (Cost)	Timing jitter
Alignment sensitivity	Low repetition rate
Output spatial mode quality	Infrared output only
Sensitive to environment (temp., humidity)	

2.4 Frequency comb stabilization techniques

Once the laser material has been chosen, the method of stabilizing the comb must be selected. For a mode-locked laser to be referred to as a frequency comb, both the pulse repetition rate and the carrier envelope offset frequency must be controlled. Similar to the previous section, there is no one best way to achieve stabilization of the mode-locked laser's optical spectrum since the best method will depend on both the final application for the comb as well as the mode-locked laser used. Below is a brief discussion of several methods for stabilizing the pulse repetition rate, f_R, and the carrier envelope offset frequency, f_{CEO}, along with some advantages and disadvantages of each method.

f_R stabilization: Method 1 – The most straightforward way to stabilize the pulse repetition rate of a mode-locked laser is to simply photodetect the pulse train, and phase lock one of the harmonics to an RF oscillator by feeding back to the cavity length using a movable mirror (piezo mounted or moveable stage). While this method is simple, the general problem is that it can easily add significant amounts of phase noise to the optical spectrum [48]. Within the feedback loop bandwidth, the phase noise of the RF oscillator will be transferred to the pulse train of the mode-locked laser. The phase noise spectrum of the reference oscillator will be scaled up by a factor of N^2 in the transition from the locking harmonic to an optical harmonic of interest. Since the harmonic number of the optical components in the laser spectrum is typically 10^5, and results in a 100 dBc increase in the phase noise spectrum of the optical line, potentially increasing the linewidth to several MHz. Careful selection of the feedback loop bandwidth is therefore necessary to prevent degradation of the optical spectrum.

A significant advantage to this method is that the reference oscillator used in the phase lock can itself be referenced to a GPS receiver. Assuming the f_{CEO} frequency has been stabilized as well, repetition rate stabilization by direct photodetection allows all of the optical frequencies of the laser to be defined by leveraging the existing infrastructure for defining the duration of one second and by virtue of the frequency comb, any optical frequency. This type of referencing scheme can greatly simplify comparisons of results from different laboratories [1,3,49] when absolute values are being measured.

f_R stabilization: Method 2 – Using intrapulse difference frequency generation (DFG) it is possible to generate an optical spectrum with no f_{CEO} component. Stabilization of the resulting difference frequency comb results directly in stabilization of the line to line frequency spacing of the original optical spectrum. Typically the difference frequency generated is in the mid IR region, with the best known optical reference in that wavelength region being methane referenced helium-neon lasers operating at 3.39 um [50-54]. This method is also advantageous because it separates detection and control loops for f_R and f_{CEO}, reducing cross coupling between the control loops.

f_{CEO} stabilization: Method 1 – Currently the simplest and most sensitive way to stabilize the carrier envelope offset frequency of a mode-locked laser is to use the *f-2f* method [30]. In this technique, the low frequency portion of the laser spectrum is frequency doubled and heterodyned against the high frequency portion.

$$f_{CEO} = 2f_n - f_m = 2f_{CEO} + 2nf_R - f_{CEO} - mf_R \qquad (2.43)$$

If the optical components being mixed on the photodiode were originally separated by an octave of frequency ($m=2n$), the RF signal appearing at the output of the photodiode will be the carrier envelope offset frequency. The challenge for *f-2f* method is the requirement of having more than one octave of optical bandwidth to begin with. For Ti:Sapphire lasers, this method has been successfully demonstrated using the spectrum generated directly from the laser for repetition rates up to 2.16 GHz [25]. Ti:Sapphire is the only material capable of generating an octave of bandwidth directly from the laser cavity, though broadening the output spectrum of other types of lasers allows use of the *f-2f* method independent of laser material. For frequency domain measurements, the broadening process imparts very little noise [55]. In the time domain, a study is ongoing to determine the possible impact of excess phase noise due to relative intensity noise converted into phase noise.

Another alternative method similar to the *f-2f* approach is *2f-3f* detection [30,56]. This method leverages the wavelength dependent power distribution of the laser output to generate spectra at *2f* and *3f*

to detect the carrier envelope offset frequency. As the *2f-3f* process has two non-linear steps rather than one, the amount of power necessary is not insignificant, limiting the applicability of this method.

Simultaneous f_R and f_{CEO} stabilization – Several methods are possible for stabilizing both f_R and f_{CEO} simultaneously. One is to reference the laser spectrum to an optical cavity [57,58]. By modulating the optical spectrum of the laser using a method such as Pound-Drever-Hall [59,60], it is possible to determine the degree of misalignment of the comb lines from the mode-locked laser with the transmission fringes of the reference cavity. Excellent levels of stability can be achieved by locking to a reference cavity; however the absolute frequency of the resulting stabilized spectrum will be unknown and will drift with the reference cavity, which may not be a problem depending on the application.

Simultaneously locking the mode-locked laser spectrum to two stable single frequency lasers will achieve essentially the same effect as locking the entire spectrum to a reference cavity. The two single frequency lasers are both heterodyned against the mode-locked laser spectrum, with the resulting RF beat signal phase locked to low noise RF oscillators. Similar to referencing the mode-locked laser spectrum to an optical cavity, the frequency of the optical components are still undefined limiting the usefulness of this approach.

The other difficulty with stabilizing a mode-locked laser's optical spectrum to a cavity is crosstalk between control channels. The error signal from both the cavity method and the dual reference laser method give only weak discrimination between a shift in f_{CEO} and a change in f_R. Fortunately, small changes in f_R can compensate for f_{CEO} shifts, though depending on the long term dynamic range needed to stabilize the laser, the cross coupling between these signals will likely be too large. Stabilizing to an optical cavity does have some advantage as the transmission through the cavity can be used as a discriminator for f_{CEO} drift detection, but this signal is quite susceptible to corruption from relative intensity noise [61]. No analog exists yet for the dual laser technique.

Chapter 3

Octave Spanning Ti:Sapphire Frequency comb using a methane stabilized helium-neon reference laser

3.1 Motivation

Over the last ten years, frequency combs have emerged as powerful tools for molecular and atomic spectroscopy [62-64], astronomical spectrograph calibration [3,4], and as low phase noise radio frequency master oscillators [11]. The purpose of this work is to construct a light source suitable for high precision optical arbitrary waveform generation (OAWG), long distance reflection mode spectroscopy and precision laser radar and imaging. Spectroscopy requires high accuracy in the frequency comb spectrum, while fine range resolution is achieved through high stability of the optical spectrum used to generate and time gate the distance measurement signals. The ultimate precision in frequency comb stability is achieved using a single trapped ion as the frequency reference [64], though these are the most sophisticated but least compact types of systems. While it has been shown possible to distribute frequency stability to the 10^{-14} level over moderate distances using existing, unstabilized fiber optic networks [65], widespread distribution is still years away. Further, stabilization to more readily available standards such as GPS or cesium only gives high stability on timescales much longer than those presented

here. Because of this, development of compact high stability frequency references such as those based on methane, and to a lesser extent iodine and acetylene, enables high stability frequency combs to be used both in research and industrial settings. The frequency comb system described here uses a commercially available methane stabilized HeNe laser [53] along with a home built 1GHz repetition rate octave spanning Ti:Sapphire laser similar to the one constructed in [66] which in principle can be replaced by a commercially available laser of equivalent performance, resulting in a nearly turn-key system.

This chapter will review the construction of a frequency comb system based on an octave spanning 1 GHz Ti:Sapphire laser referenced to a helium-neon laser which has itself been referenced to an absorption feature in methane. Several methods for designing optical cavities for mode-locked lasers will be discussed. The operation of the frequency combs system will follow, with a description of how the final system was characterized.

3.2 Octave-spanning 1 GHz Ti:Sapphire laser

Access to the full capabilities of the frequency comb was limited until 2000 when nearly simultaneously Theodor Hänsch and John Hall both demonstrated full stabilization of the frequency comb. These early systems were typically of lower repetition rate, 80-200 MHz, as lower repetition rates afford higher pulse energies for a given average power reducing the average power threshold to achieve mode-locking and specifically broadband mode-locking. The first octave spanning spectrum directly from a laser cavity was demonstrated by Richard Ell [67] who was able to generate an f-$2f$ beat signal using only the spectrum generated by the laser. This was achieved using a 65 MHz laser, not a repetition rate suitable for applications requiring high power in each optical mode and large frequency separation between modes such as optical arbitrary waveform generation (OAWG).

The following sub-sections will review the design process for broadband Kerr lens mode-locked (KLM) Ti:Sapphire lasers, specifically optical cavity design for soft aperture KLM as well as design of the temporal optics. A general discussion of KLM will be followed by descriptions of two methods for analyzing cavities to optimize KLM operation: the nonlinear ABCD matrix, and a method for rescaling

the beam propagation parameter q. Note that both of these approaches are rather phenomenological, and don't address the underlying physics directly other than to linearize the material response so it can be accounted for in an ABCD type analysis of the beam propagation in the cavity. A more complex analysis than those to be presented here may give more insight into the actual mechanisms bounding operation of KLM lasers; however here the goal is to develop design parameters which allow rapid construction of lasers for use in larger systems. Concluding this section will be a discussion of a method for selecting the optics for control of the temporal portion of laser operation.

3.2.1 Kerr lens mode-locking

Within the realm of solid state lasers, there are three main mode-locking techniques: Saturable absorber mode-locking, active mode-locking, and Kerr lens mode-locking [68-75]. Mode-locking using the Kerr lens mechanism produces the shortest pulses of the three methods and therefore is the best choice for generating a broad optical spectrum necessary for an OAWG system. A survey of the literature will turn up, among others, at least three themes in the design of optical resonators for Kerr lens mode-locking (KLM), the first being a non-linear ABCD matrix method [73,74], where utilizing the standard methods for designing optical cavities [76], a power dependent focusing element is added to the normal ABCD propagation matrices to find a self-consistent solution. Another method uses a slightly simpler approach by using feasibility arguments to rescale the beam parameter for propagation through a power dependent nonlinear element [69,71,72]. By isolating the nonlinear element from the remainder of the cavity it is possible to modularize the design of the laser into linear and nonlinear elements.

As described in section 2.25 above, the refractive index of all materials shows an intensity dependent refractive index for suitably high intensity. This dependence can be expressed as

$$n = n_0 + n_2 I \tag{3.1}$$

where n_0 is the linear refractive index ,n_2 is the nonlinear refractive index and I is the laser intensity. Considering now the transverse spatial intensity profile of a TEM_{00} beam,

$$I(r,z) = I_0 e^{-2\left(\frac{r}{w(z)}\right)^2} \tag{3.2}$$

The variation in refractive index due to the incident intensity can be linearized to

$$n(r,z) = n_0 + \frac{2n_2 P}{\pi w(z)^2} e^{-2(r/w(z))^2} \approx n_0 \left(1 - \frac{r^2}{2h_{sf}^2}\right) \tag{3.3}$$

$$h_{sf} = \frac{w(z)^2}{2}\sqrt{\frac{\pi a n_0}{2n_2 P}} \tag{3.4}$$

where a is an experimental variable between 2 and 6 used to tune the value of P_c to match experimental values [70]. Inspection of equation (3.3) reveals it to be very similar to the description of the phase shift produced by a parabolic lens [77]

$$-\varphi = \frac{k}{2f} r^2 = \frac{w n_0}{2c h_{sf}^2} r^2 \delta z \tag{3.5}$$

where δz describes the thickness of the medium and $-\phi$ is the radially varying phase shift caused by the medium.

Kerr lens mode-locking (KLM) refers to using this intensity dependent change in the refractive index [78] and the resultant change in the beam parameter q to cause a preferential increase in gain or decrease in loss in the cavity for high power pulses rather than lower power CW operation. In the case of decreased loss, the usual method is to place an aperture on one of the mirrors to define the size and or shape of laser mode which will experience reduced loss. Because of the well defined boundary between high and low loss beam sizes this mode of operation is referred to as hard aperture KLM. In the case of longitudinally laser pumped media, the Kerr lens action can be arranged to cause an improvement in the overlap of the laser and pump mode to cause an increase in gain. Since the shape and size of the pump mode does not have well defined limits, this technique is called soft aperture KLM.

Because the effectiveness of the mode-locking element is directly dependent on changes in the shape and size of the laser beam in the cavity, the arrangement and alignment of the cavity is very important. This sensitivity should be contrasted against the other two main mode-locking methods (active

and semiconductor saturable absorber mirror, SESAM) which are not dependent on the configuration of the laser cavity as long as normal cavity stability requirements are met. Sensitivity to the environment is a disadvantage since it requires a more careful and thorough optical design, as well as increased sensitivity to environmental factors and laser construction. The advantage of KLM is the nearly instantaneous response of the non-linear element to the increased intensity of an optical pulse. The refractive index changes and recovers directly with the passing of the optical pulse. Much shorter optical pulses are possible using the KLM technique than with any other mode-locking mechanism. In contrast, saturable absorbers and active mode-locking mechanisms, both have finite response bandwidths which limit their ability to window the pulse gain or loss in time, subsequently putting an upper limit on the possible bandwidth and a lower limit on the duration of the resulting pulses.

3.2.2 The non-linear ABCD matrix

Traditional laser cavity design is based on the ABCD matrix method of beam propagation [76,77]. To analyze a cavity using ABCD matrices, a reference plane is selected somewhere in the cavity and a matrix is constructed to represent propagation through the elements in the cavity during one round trip. Using the round trip matrix and the ABCD rules of Gaussian beam propagation it is possible to determine the laser beam parameters (beam waist w, or wavefront radius R) anywhere in the laser cavity as well as whether or not the laser cavity is optically stable, i.e. whether or not a ray launched within the cavity at an angle nearly parallel to the axis of the resonator will be trapped in the resonator. Further, based on design parameters such as desired output power, beam size, laser crystal absorption and figure of merit, as well as available pumping power, among others, the designer can rather readily determine the best configuration which will give the desired results for a CW laser.

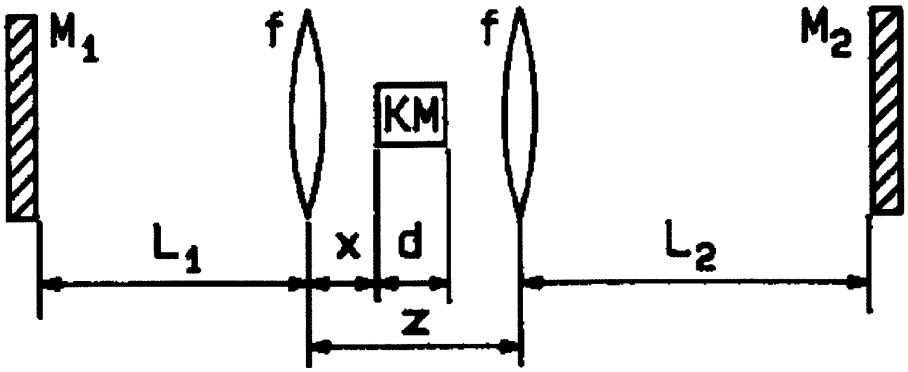

Figure 3.1—Above is the generalized representation of a resonator for KLM using solid state gain media. M_1 and M_2 are plane mirrors, f are lenses, and KM is the gain media which is also used as the Kerr medium. With appropriate scaling it is possible to replace f with curved mirrors with no loss of generality. Figure adapted from [74].

When designing a laser for KLM operation, in addition to the previous parameters, it is also necessary to maximize the non-linear element's ability to differentiate pulsed from CW operation. To date, most KLM lasers have had a topology which can be represented by that in Fig.3.1. In this standard configuration, the laser crystal serves as both a gain medium and the non-linear Kerr element. The first KLM optimization method to be discussed, described by Magni et al in [73,74], uses a matrix in the description of a laser cavity whose parameters depend on the laser power to describe a non-linear lens element which will be inserted into the laser cavity (located in the center of the gain medium for Ti:Sapphire lasers).

To describe the construction of the nonlinear matrix, a formalism similar to the result in Eq. (3.2) will be used where the transverse spatial intensity profile in the crystal is approximated as a parabola, Eq. (3.6) and (3.7), and is used to solve the wave equation , Eq.(3.8).

$$u(r,z) = (U/w)\exp[-(r/w(z))^2 - ikr^2/2R(z) + i\varphi(z)] \tag{3.6}$$

$$|u|^2 \approx \frac{3U^2}{4w^2}\left(1-\frac{2r^2}{3w^2}\right) \tag{3.7}$$

$$\nabla_T u - 2ik\frac{\partial u}{\partial z} + k^2\frac{n_2}{n_0}|u|^2 u = 0 \tag{3.8}$$

In the above expressions, u is the complex field amplitude, and U is a constant to maintain the beam power P through $U^2=4P/\pi c\varepsilon_0 n_0$. The solution of the wave equation is achieved by breaking Eq.(3.8) into four differential equations which can be solved to account for propagation through the non-linear medium. The two differential equations related to beam propagation are solved to give

$$w^2(z) = w_1^2\left[\left(1+\frac{z}{R_1}\right)^2+\left(\frac{\lambda z}{\pi n_0 w_1^2}\right)^2\left(1-\frac{P}{P_c}\right)\right] \tag{3.9}$$

$$\frac{1}{R(z)} = \left(\frac{w_1}{w(z)}\right)^2\left[\frac{1}{R_1}+\frac{z}{R_1^2}+z\left(\frac{\lambda}{\pi n_0 w_1^2}\right)^2\left(1-\frac{P}{P_c}\right)\right] \tag{3.10}$$

Equations (3.9) and (3.10) assume a beam waist and initial wavefront radius of w_1 and R_1 respectively and are scaled by the parameter $(1-P/P_c)$ where P/P_c is the ratio of beam power to the critical power for self focusing. Using the standard q parameter and the ABCD law of beam propagation, it is possible to use equations Eq.(3.9) and (3.10) to define a ray transfer matrix for the nonlinear element in the laser crystal as

$$M_k = \sqrt{1-\gamma}\begin{pmatrix} 1 & de \\ -\gamma/\left[(1-\gamma)\,de\right] & 1 \end{pmatrix} \tag{3.11}$$

$$\gamma = \left[1+\frac{1}{4}\left(\frac{2\pi w_c^2}{\lambda de}-\frac{\lambda de}{2\pi w_0^2}\right)^2\right]^{-1}\frac{P}{P_c} \tag{3.12}$$

In the above equations, w_c is the spot size in the center of the crystal at the Kerr matrix (where R is not necessarily infinite) calculated using the entire cavity round trip matrix when $P=0$, and w_0 is the size of the beam waist outside of the Kerr matrix M_k if the beam is propagated away from the Kerr medium in free space assuming an initial spot size of w_c and an associated R_c. So initially a solution is found for w_0 with $P=0$, and then this result is used in Eq.(3.9) to determine the waist at some point away from the Kerr matrix as if it were in free space, Fig 3.2. With w_0 and w_c, γ can be specified which allows the final step to describe the M_k matrix.

$$M = \begin{pmatrix} 1 & de/2 \\ 0 & 1 \end{pmatrix} M_k \begin{pmatrix} 1 & de/2 \\ 0 & 1 \end{pmatrix} \tag{3.13}$$

where the Kerr material has been placed between equal length pieces of dielectric material and now taking the first order expansion in gamma of the above result gives

$$M_k \approx \begin{pmatrix} 1 & -\gamma de/4 \\ -\gamma/de & 1 \end{pmatrix} \tag{3.14}$$

This matrix can be understood directly as the combination of a lens and a negative distance. Consider the matrix product below of a lens inserted between two negative distances,

$$M = \begin{pmatrix} 1 & -\frac{D}{2} \\ 0 & 1 \end{pmatrix} \begin{pmatrix} 1 & 0 \\ \frac{-1}{f} & 1 \end{pmatrix} \begin{pmatrix} 1 & -\frac{D}{2} \\ 0 & 1 \end{pmatrix} = \begin{pmatrix} 1+\frac{D}{2f} & -D-\left(\frac{D}{2}\right)^2 \frac{1}{f} \\ -\frac{1}{f} & 1+\frac{D}{2f} \end{pmatrix} \approx \begin{pmatrix} 1 & -D \\ -\frac{1}{f} & 1 \end{pmatrix} \tag{3.15}$$

in the limit of a weak lens (large f), the form of this expression is the same as that of Eq. (3.14), remembering that γ is a dimensionless parameter. From the original discussion, the inclusion of a focusing element is somewhat expected due to the change in wavefront curvature by the nonlinear

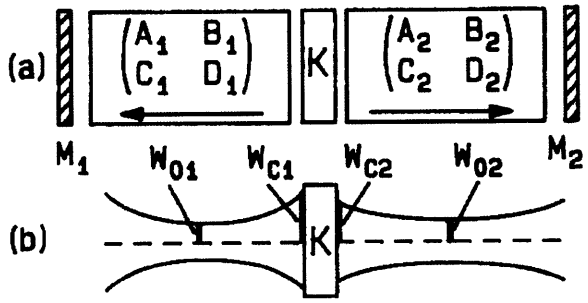

Figure 3.2—(a) Matrix description of the resonator: the arrows indicate the direction to which the matrices refer, K is the thin element with the lumped Kerr nonlinearity in the middle. (b) Gaussian beam profiles outside the nonlinear element K: w_{c1} and w_{c2} are the spot sizes at the entrances of K and w_{01} and w_{02} are the beam waists assuming free space propagation. Figure adapted from [74].

element. The idea of a negative distance can be understood with a physical argument. In the case of $P=P_c$, the beam travels through the medium without diffraction because M_k becomes a unity transformation. The beam emerges on the far side as if the focus had been shifted to coincide with the far

end of the material. The fact that the focus has been shifted does not imply that the physical path length has been drastically changed, only that the total path over which diffraction can occur has been changed. In a simpler example, inspection of Eq.(3.10) with $P=P_c$ causes the beam to propagate without change. For cases when $P<P_c$, it is reasonable to expect proportionally less self contained propagation through the material, or stated another way, proportionally more diffraction.

With the nonlinear matrix defined, the beam spot size can be calculated at the desired plane within the resonator for various values of P. Note that because of the discrete nature of the approximation of the Kerr media, it is not possible to calculate a meaningful value for the beam parameter during propagation through the laser crystal. While the discrete nature of the non-linear lens limits the applicability of the method with respect to analyzing the detailed changed in pump laser overlap in soft aperture mode-locking, quantifying the changed in waist size due to intensity is still possible. This limitation is also not a serious handicap for calculations of hard aperture mode-locking since such apertures are usually placed well away from the nonlinear element.

To analyze the change in laser cavity spot size for very small changes in intracavity power to determine the best laser configuration for self starting of mode-locking a new parameter will be defined. The change in beam waist size is used as a proxy for quantifying the overlap of the pump laser beam with the mode-locked laser beam inside the laser crystal. By defining the change in spot size of the beam inside the laser crystal as

$$\delta = \left(\frac{1}{w} \frac{\partial w}{\partial P} \right)_{P=0} \tag{3.16}$$

the designer can create plots of δ as a function of up to two parameters, providing immediate insight into the mode-locking process for different cavity alignments suggesting a relative level of alignment complexity between cavity configurations. Two important observations will be made from plotting the result of expression (3.16); first, the beam diameter can be made to change quite quickly at $P/P_c=0$ for careful choice of cavity parameters. Specifically, if the slope of the change in beam waist is negative with respect to increasing laser power the use of a hard aperture on M_1 will result in reduced loss for pulsed

operation. From a practical standpoint, because of the small difference in location of the crystal x, between the stable and possibly bi-stable configuration serves to highlight the empirically determined sensitivity of the KLM process to the cavity alignment. From inspection of the map of relative spot size changes for a given laser, Fig. 3.4, it is immediately apparent that the plot contains several of the empirically understood behaviors of mode-locked lasers: The blank areas in the middle of the plot and on the sides show the optically unstable regions of the parameter space. The areas where $|\delta|$ is largest are closest to the edges of the stability region as recorded anecdotally in many experimental references. Each stability region has its own preferred crystal location for optimal mode-locking stability. Finally, it is possible though quite difficult to achieve mode-locking at the outer edges of both stability regions.

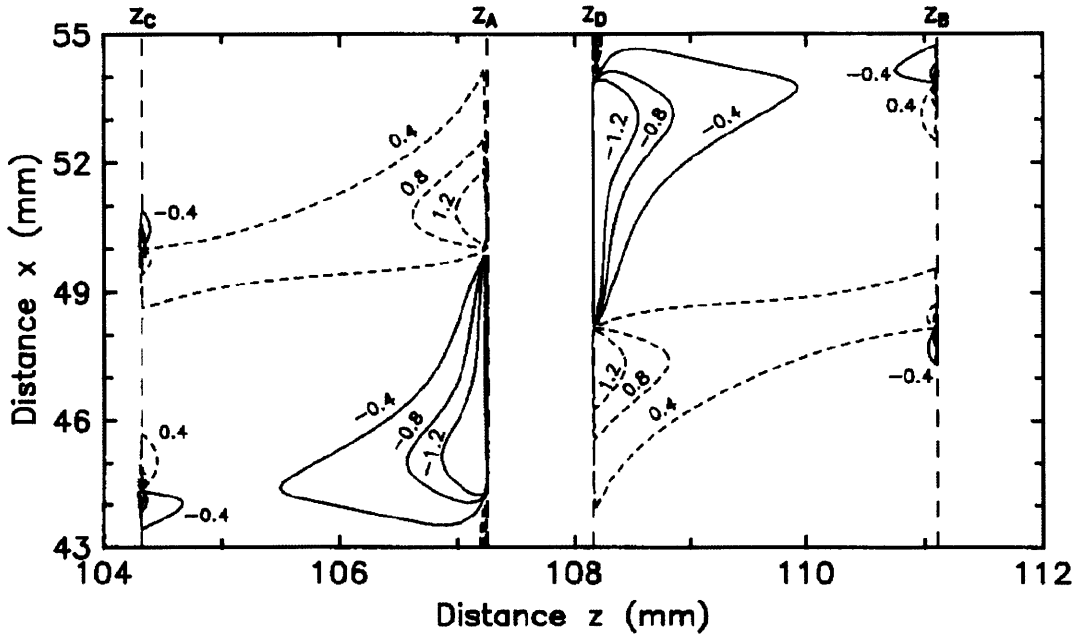

Figure 3.4—Contour line plot of δ on mirror 1 as a function of lens separation, z, and relative crystal position, x, as defined in Fig. 3.1. Dashed contour lines are positive values and solid lines are negative. The stability region with respect to lens separation is defined by the dashed vertical lines. The remaining cavity values with respect to Fig. 3.1 are—$L1$=700 mm, $L2$=900 mm, f=50 mm, d=10 mm, $n0$=1.76. Figure adapted from [74].

Of special note is what is not revealed by Fig. 3.5. Most interesting is a lack of distortion of the stability region due to the nonlinearity. As described earlier in this chapter, it is expected that for certain non zero values of P the stability region will be distorted. Since δ is currently only defined for $P=0$, it

would likely be of some value to re-derive P for some non zero value and compare the two plots. Re-evaluating the model at a pair of higher power levels would allow the designer to immediately choose the position which would give both the best startup alignment and the best operating alignment. In [68,69], experimental results are plotted on a figure similar to the one above as locations in the parameter space where mode-locking was achieved and to what level of intervention was required to initiate mode-locking. These plots indicate a good correlation between the areas of large negative δ_l and areas where self starting of mode-locking was observed, in agreement with the described basis for the definition of δ.

3.2.3 Rescaling the q-parameter

Using a discrete matrix to describe the non-linearity of a Kerr medium within a resonator as presented above highlights the complexity of such a solution in a self similar fashion over a wide parameter space. In contrast, the approach taken by Huang et al in [70] and in [71,72] is to simply perform a rescaling of the q parameter upon entry and exit of the Kerr medium normalized to the critical power for self focusing P/P_c. As both approaches are formed on a similar basis, Huang's formalism will be used to suggest the idea for rescaling. Beginning with the parabolic index profile created by the Gaussian transverse spatial intensity profile of the laser beam in Eq.(3.3) above and assuming a differential section of nonlinear media as a lens between two pieces of dielectric, a matrix can be constructed as

$$M = \begin{pmatrix} A & B \\ C & D \end{pmatrix} = \begin{pmatrix} 1 & \dfrac{\delta z}{n_0} \\ -\dfrac{n_0}{h_{sf}^2} & 1 \end{pmatrix} \tag{3.17}$$

With the matrix above, the ABCD law of beam propagation, and defining q' as $q'+dq'$, a differential equation for the q parameter is obtained

$$\frac{dq}{dz} = \frac{1}{n_0} + \frac{q^2 n_0}{h_{sf}^2} \tag{3.18}$$

$$\frac{1}{q}=\frac{1}{R}-i\frac{\lambda}{\pi n_0 w^2} \tag{3.19}$$

Since the q parameter is a complex quantity, Eq.(3.17) obscures some of the dynamics of interest, specifically the evolution of the wavefront radius, i.e. diffraction. Performing the same calculation again but making a few substitutions will help clarify the desired mechanism. Mapping $p=1/q$, p' as $p'+dp'$ and most importantly breaking p into its real and imaginary parts yields

$$\frac{dp_r}{dz}=-\frac{p_r^2}{n_0}+\frac{(\xi p_i)^2}{n_0} \tag{3.20}$$

$$\xi\frac{dp_i}{dz}=-\xi p_i\frac{2p_r}{n_0} \tag{3.21}$$

$$\xi=\sqrt{1-\frac{P}{P_c}} \tag{3.22}$$

Inspection of Eq. (3.20) and (3.21) reveals that the factor ξ can be accounted for as a simple scale factor of the imaginary part of the q parameter. Since p_i serves to control diffraction in Eq. (3.20) it can be immediately understood that such a rescaling would allow the beam to focus tighter than would normally be possible. Because this is a perturbative analysis, values of P approaching P_c begin to provide incorrect results and once $P>P_c$ the approximations in the analysis are completely invalid. However, for $P/P_c=0.33$, Huang et al reports good agreement with experimental z-scan measurements which directly measure the amount of self focusing experienced by a beam in a non-linear material.

To use the mapping $p_i\rightarrow\xi p_i$, a simple scaling transform, Ξ, is developed in reference [70] to be applied at the input and output of a material. The procedure is to determine the q parameter at the input to the nonlinear material then apply the forward transform, propagate the beam through the nonlinear material as if it were linear, and finally apply the inverse transform to the q parameter at the output of the material.

$$q'=\hat{\Xi}^{-1}\hat{M}\hat{\Xi}q \tag{3.23}$$

$$\hat{\Xi}q \equiv \frac{1}{\mathrm{Re}(1/q) + j\xi \mathrm{Im}(1/\mathrm{q})} \tag{3.24}$$

$$\hat{\Xi}^{-1}q \equiv \frac{1}{\mathrm{Re}(1/q) + j\xi^{-1} \mathrm{Im}(1/\mathrm{q})} \tag{3.25}$$

The resulting q parameter can then be manipulated through the rest of the propagation in the usual manner. The transformation in the non-linear material has been somewhat separated from the rest of the beam propagation calculation at the cost of having to determine the q parameter at two extra points in any given calculation. Because the nonlinearity of the medium is accounted for across the entire medium, it is possible to use the Ξ transform to calculate the spot size of the laser across the entire non-linear medium in addition to all planes of interest outside of the nonlinear medium, which allows both hard and soft aperture mode-locking to be analyzed with this method.

In both hard aperture and soft aperture mode-locking, as mentioned above, the amount of spot size modulation as a function of beam power determines the amount of gain or loss modulation. Huang et al determined that the modulation experienced by a hard or soft aperture mode-locked laser would be the same using the rescaled q-parameter, allowing further separation of the design of the laser cavity and the nonlinear medium. Using the arrangement in Fig 3.4(a) and 3.4(b) and simple ABCD matrices it is possible to determine the expected modulation depth as a function of the normalized beam power and the normalized thickness of the nonlinear material, Fig 3.4(d). Of special note is Fig 3.4(d) which illustrates saturation of the nonlinear modulation for a confocal parameter larger than half the length of the nonlinear media, $l/2<Z_R$.

The reduction in self focusing can be understood intuitively since the confocal parameter is defined as the point where the beam intensity has reduced to ½ of the value at the waist, meaning that adding more material outside of the high intensity region will not add to the effect. The result of Fig 3.4(d) can be used as the

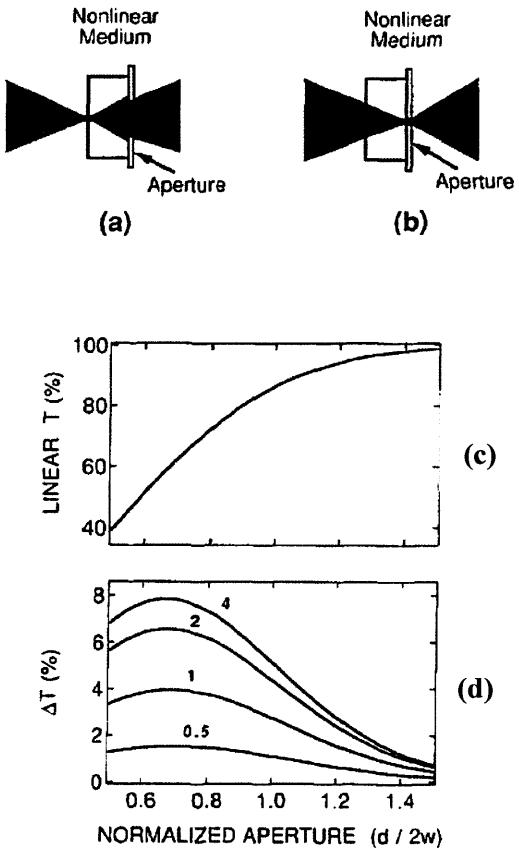

Figure 3.5—(a) and (b) are self focusing modulator designs which are roughly equivalent to hard and soft aperture arrangements, respectively. (c) Calculated linear transmission and (d) the nonlinear loss modulation versus normalized aperture size. Given the same parameters, the two modulators in (a) and (b) perform identically. The four curves in (d) are plotted with nonlinear medium thicknesses of $0.5n_0b$, $1n_0b$, $2n_0b$ and $4n_0b$. The normalized beam power is set to P/P_c=0.2, which is equivalent to the following parameters: λ=800 nm, n_0=1.51, n_2=3.45x10^{-20}m^2/W (BK7 glass), a=5.35, P_{CR}=2.62 MW, and P=525 kW. Figure adapted from [70].

basis for more detailed analysis to be performed with greater confidence knowing that initial values are close to the final solution. In contrast to the matrix method presented by Magni et al, Huang's method does not allow direct determination of the effect of beam power on the stability regions of the optical cavity. Stability must be determined by interpretation of the q parameter at carefully selected planes within the cavity, which means a full beam propagation calculation including all elements.

3.2.4 Final design methodology

Of the two methods presented above, rescaling of the q parameter seems to be best suited to propagation simulations such as a first order simulation of the spatial propagation of a pulse in the laser cavity on an

element-by-element basis. As a dual to the rescaling method, the lumped element method is not suited to investigations of the evolution of the laser spot size during propagation through the non-linear media. Some finite distance of propagation is necessary for the discrete nature of the lumped matrix to become less apparent. The lumped element method though, and specifically the δ parameter may give the best practical information with the least complexity arguably considering the ability of waist size modulation to predict mode overlap change. By making such an analysis near zero intracavity beam power, self starting can also be analyzed which is arguably more important than steady state operation.

To understand the optics selection for the 1 GHz Ti:Sapphire laser, an analysis of the cavity has been performed using the delta parameter analysis outlined above, but using a lumped element model similar to that described in section 3.2.2. The modeled cavity is drawn in Fig. 3.6, which is an expanded version of an x-folded ring cavity. At the time this laser was designed, the dispersion compensating mirrors (described in the next sub-section) were only available in two different ROC values suitable for building a 1 GHz repetition rate laser, 3 cm and 5 cm. To choose between these two options, a delta parameter analysis was performed to determine which ROC would provide the best

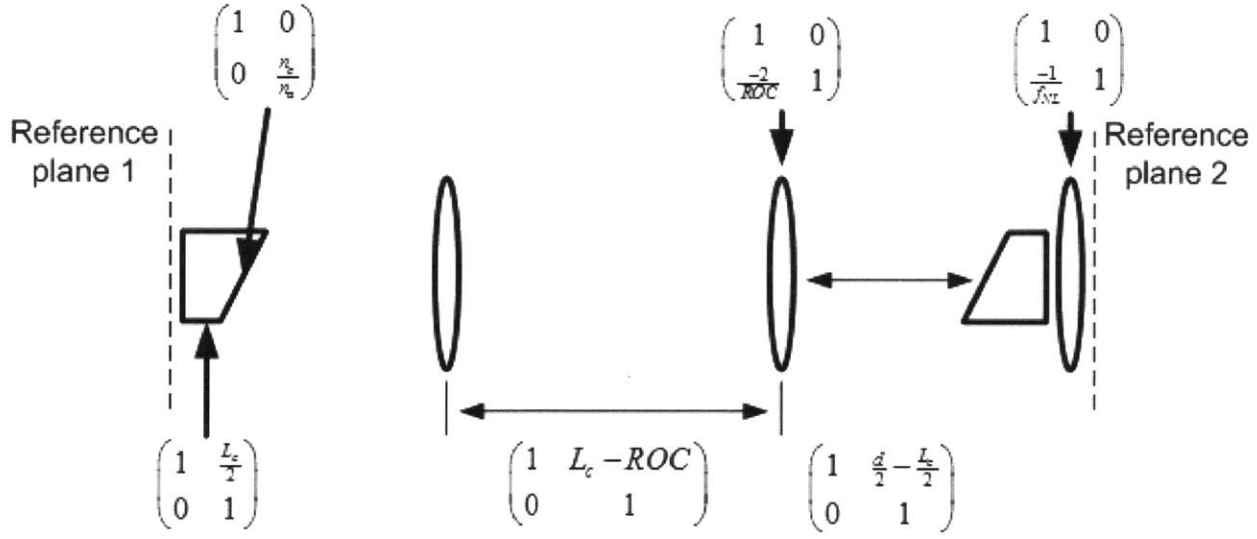

Figure 3.6 – Schematic of the cavity model used to determine the delta parameter for the 1 GHz laser. The ABCD matrices above and below are the same as those used to generate Fig. 3.7. f_{NL} is determined using Eq. (3.4) and (3.5) assuming a 1 mm nonlinear region in a 2.2mm long crystal. Duplicate matrices have been omitted for figure clarity.

self starting characteristics. In the delta analysis, the laser spot size was determined at the center of the Ti:Sapphire crystal, and then propagated to either end of the crystal. This assumes that the beam propagates linearly, at high intensity and that only the final spot size is modulated due to high intensity.

From the two plots in Fig. 3.7 which report the change in beam size in the Ti:Sapphire crystal for average powers of 0 and 100 mW, it is clear that the 3 cm ROC mirrors experience similar fractional waist size modulation to that of the 5 cm ROC mirrors for the same change in peak power. The resulting larder delta parameter for the 3 cm ROC mirrors is fortunate since these mirrors will allow for a longer linear propagation length than the 5 cm ROC mirrors would. The extra length of linear propagation means that addition of necessary intracavity elements for dispersion compensation, as discussed in the next sub-section, is much simpler.

One other parameter which warrants mentioning is astigmatism compensation. Beams which are either focused through tilted plates or reflected from curved mirrors at non-normal incidence experience a shift in both location and size of the resulting focus in one axis of the beam. This is known as astigmatism and it can significantly reduce the peak intensity in the resulting focus. Fortunately, for the two examples just given, the focal length shift occurs in opposite directions for the configuration which occurs in Fig. 3.12 [79]. It is possible to derive a formula for the incident angle which achieves astigmatism compensation [80]

$$\theta_a = \pi - \arccos\left(\frac{L_c}{2Rn_c^3}\left[n_c^2 - 1 - \sqrt{n_c^4 - 2n_c^2 + 1 + 4R^2 n_c^6 / L_c^2}\right]\right) \qquad (3.26)$$

where the crystal length and refractive index are L_c and n_c, and R is the focusing mirror ROC. Using the incident angles determined by Eq. (3.26) the focus of the laser beam will occur at the same point in the laser crystal, though the focus will still be slightly elliptic due to the Brewster angled interface of the Ti:Sapphire crystal. Regardless, astigmatism compensation provided by the curved mirrors is a great improvement, allowing greatly increased overlap with the pumped mode of the crystal.

3.2.5 Temporal optical design

In addition to the geometric optics design, mode-locked laser design requires consideration of the laser cavity dispersion to allow buildup of short duration, wide bandwidth pulses. Traditional analysis of soliton propagation and mode-locked laser operation assumes continuous dispersion and non-linearity, resulting in zero net dispersion per unit length of propagation. In solid state lasers, the dispersive elements are distributed, such that the condition of zero net dispersion is only satisfied on a round trip basis resulting in type of operation known as dispersion managed mode-locking [81].

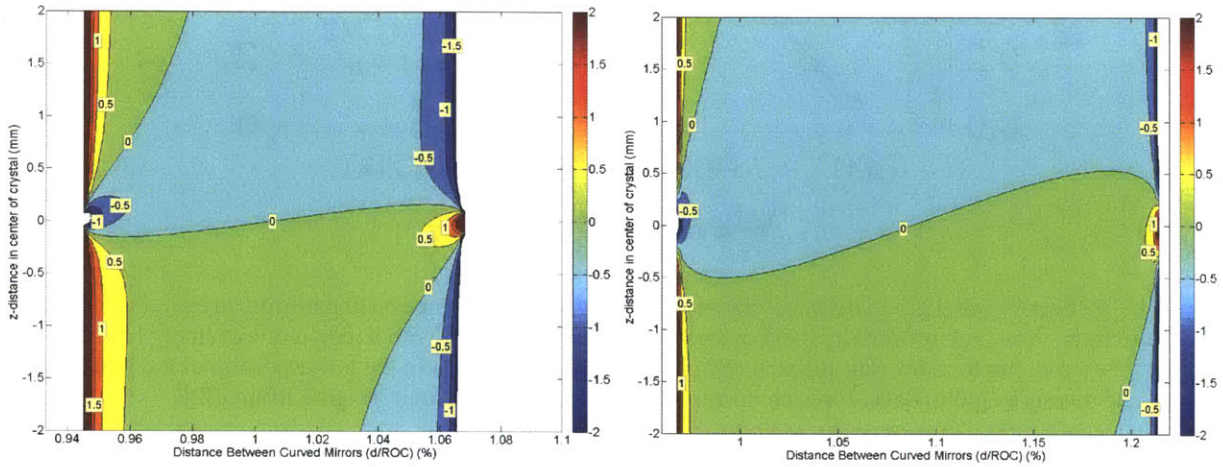

Figure 3.7 – Results of a delta parameter type analysis assuming output powers of *Pavg*=0 and *Pavg*=100mW with 100 fs pulses and 5 % output coupling. Close inspection of both plots reveals that the fractional regions of *d/ROC* where the delta parameter is maximized are actually quite similar. This suggests that both ROC mirrors should give similar mode-locking initiation characteristics. While regions of negative delta exist on both sides of the stability region, experimentally the smaller region at small values of *d/ROC* seems to work best.

Both types of propagation support mode-locking, but dispersion managed mode-locking puts an additional requirement on the design that the pulse be properly compressed prior to entering the lumped nonlinear material. This is not a stringent requirement though, and in the case of ring cavity lasers, it is automatically satisfied by ensuring the round trip linear dispersion is slightly negative (~10-20 fs^2). Traditionally, methods such as prisms [39], or even grating pairs have been used to compensate for dispersion in laser cavities. Given that the cavity of a 1 GHz mode-locked laser is only 30 cm long, there simply is not enough space to incorporate traditional dispersion compensating elements. The solution is to use chirped mirrors.

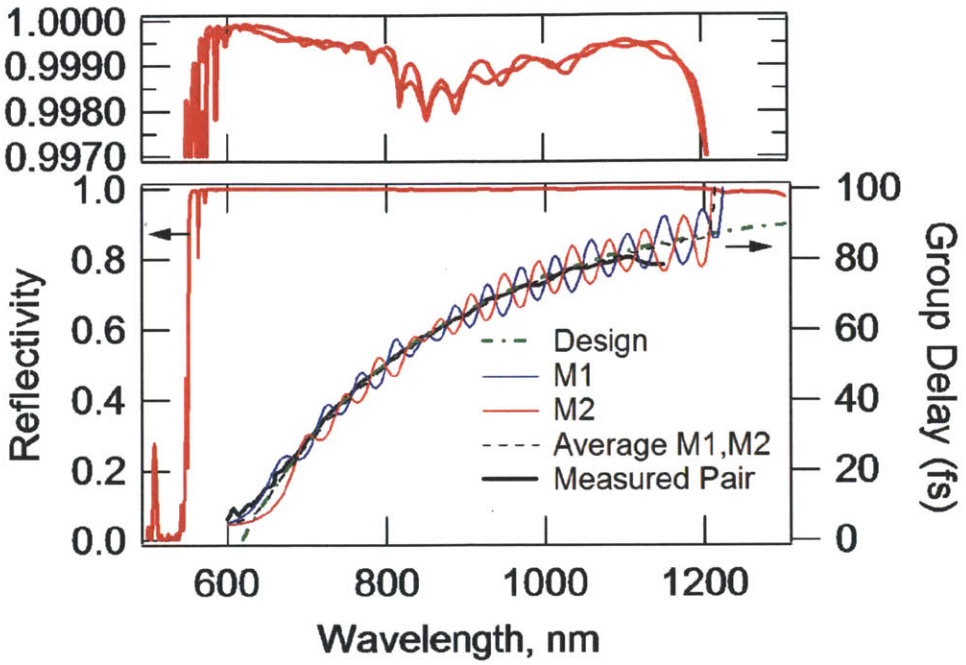

Figure 3.8 – Reflectivity and group delay for double-chirped dispersion compensating mirrors used in the 1 GHz Ti:Sapphire laser. The high reflectivity band extends from 600 – 1200 nm, with a region of extremely low reflectivity near 532 nm to allow transmission of light from the pump laser. In the lower portion of the graph is the designed and measured group delay for each mirror as well as the average value. Figure from [82].

Dispersion compensating chirped mirrors are similar to dielectric Bragg type reflectors in that they both use quarter-wave thickness layers of dielectric materials for generating multiple reflections to ultimately achieve a high reflectivity. While Bragg reflectors have layers with only one (optical) thickness through the material, the layer thickness in a dispersion compensating mirror is slowly changed or "chirped" for each layer, resulting in a wavelength dependent penetration depth into the mirror coating, Fig 3.8. A subtlety of the mirror design requires that the mirrors be used in pairs. The requirement that the mirrors be used in pairs is a result of a design modification necessary for broadband operation. Most wavelengths must penetrate into the layer stack a finite distance before being reflected, so it turns out to be necessary [41] to use an anti reflection (AR) coating on the front surface of the chirped layer stack. The AR coating prevents small spurious reflections generated by the impedance mismatch between air

and the first layer from destabilizing the mode-locking process. An elegant solution to the problem of imperfect AR coatings

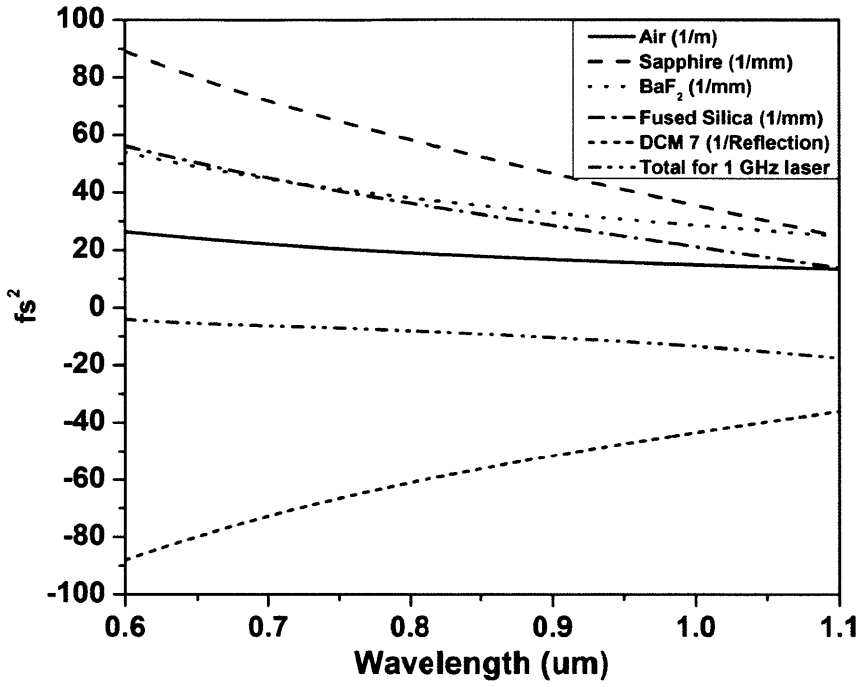

Figure 3.9 – Group delay dispersion of common materials used in mode-locked laser cavities as well as the compensation capability of a single DCM mirror from the 7th generation. The curve for the DCM 7 mirror is a design goal curve, and so does not show the residual ripples from the imperfect AR coating. The curve also assumes that the mirror will be used as part of a pair. For the plot of residual dispersion in the 1 GHz cavity, the following assumptions were used: 30 cm cavity length, 2.12 mm Sapphire crystal, 0.7 +1.6 mm BaF_2 tuning wedge and 4 DCM 7 mirrors.

is to insert a quarter wave thickness layer for the central wavelength between the AR coating and the chirped layer stack. In the frequency domain, these spurious reflections are equivalent to an oscillating group delay. The addition of the quarter wave layer shifts the oscillations by a phase of π, allowing cancellation of the reflections when such mirrors are used in pairs. Mirrors designed with the extra quarter wave layer are referred to as a double chirped dispersion compensating mirror (DCM). Having determined the method for compensating the normal dispersion in the laser cavity caused by air and the Sapphire crystal, determining the exact dispersion compensating scheme is simply a matter of summing the contribution from each element. Figure 3.9 plots the final dispersion compensation scheme used for the 1 GHz laser. The goal value for the summation process should be about -10 to -20 fs^2 residual

dispersion across all wavelengths. Since there is a rather large uncertainty in the summation due to residual oscillations in the group delay of the DCMs it is better to allow for some tuning of the overall cavity dispersion value in the construction of the laser than to try to achieve a particular value. Experience has shown however that summation of the average dispersion values is reasonably reliable for achieving broadband mode-locking.

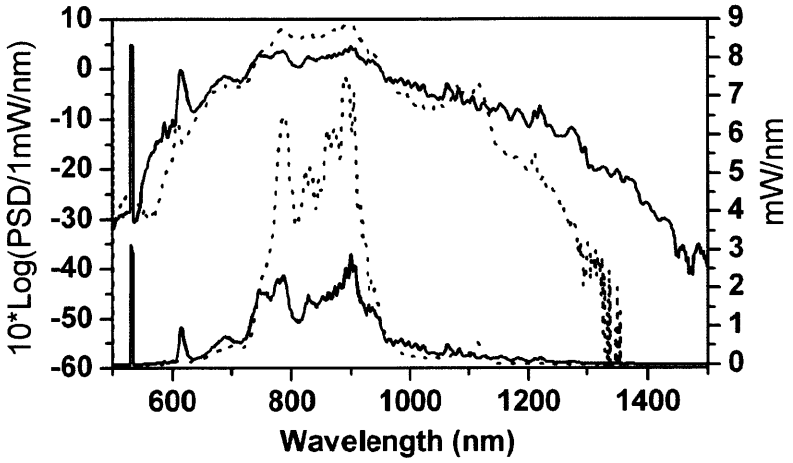

Figure 3.10 -- Output spectrum from the Ti:Sapphire laser using output couplers with Barium Fluoride (600mW avg. output) and Fused Silica(>1W avg. output) substrates in solid and dotted lines, respectively. The difference in width of the two spectra and total output power is attributed to uncompensated TOD of the Fused Silica and lower surface quality of Barium Fluoride.

3.2.6 Construction and performance of final laser design

The final design and constructed configuration of the 1 GHz laser, Fig. 3.12, is as follows. The laser uses a 2.12 mm long crystal which has an absorption coefficient of 2.25 cm^{-1}. All four mirrors are broadband, highly reflective DCMs, which overcompensate for the dispersion of the crystal and air path of the cavity. To correct the overcompensation of group delay dispersion (GDD) provided by the DCMs, two pieces of Barium Fluoride are used at Brewster's angle, a 0.7 mm plate and a shallow angle wedge of 1.7mm center thickness, which allows fine tuning of the overall cavity dispersion. The combination of the sapphire crystal, DCMs and the Barium Fluoride allows tuning of the average overall cold cavity GDD very close to 0 fs^2 between 600 nm and 1100 nm. The wedge is coated on one side to provide nominally 4% output

coupling from 650 nm to 1050 nm, rising to more than 50% for shorter and longer wavelengths. Because the amplitude and phase of a coating in transmission obey Kramers-Kronig relations and since the

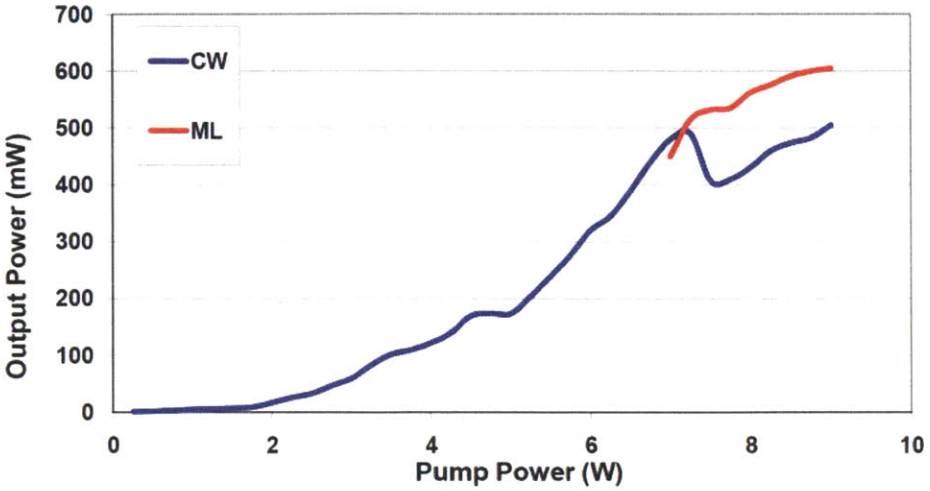

Figure 3.11 – Optical to optical power conversion for both mode-locked and CW operation for the 1 GHz Ti:Sapphire laser. The trace for CW operation is not linear because the pump beam size in the crystal has been optimized for mode-locked operation. Because the pump focus is smaller than optimal for CW operation, at least three spatial modes are excited as the pump power is increased. In mode-locked operation, 7% optical to optical efficiency is observed.

transmission profile is constant over most of the spectral range where the laser spectrum is expected to generate significant power, the GDD introduced by the output coupling is negligible. Mode-locking can be achieved anywhere between 7.25 W and the 10.5 W, and over this range the output spectrum is virtually constant with a maximum output power of 600 mW achieved with 10 W of pump power, Fig.3.11.

For additional stability, the laser cavity is constructed on an optical breadboard separate from the main optical table. The second breadboard was further isolated from the main table using lead filled acoustical foam, the isolating properties of which cannot be understated [83]. Isolation of the laser from air currents and acoustic disturbances was provided by a rectangular box consisting of ½" thick Lexan which was constructed to fit tightly around the laser cavity. A second box of ¼" thick acrylic enclosed the entire breadboard on which was mounted the pump laser, f_{CEO} detection optics and repetition rate stabilization optics in addition to the 1 GHz laser itself.

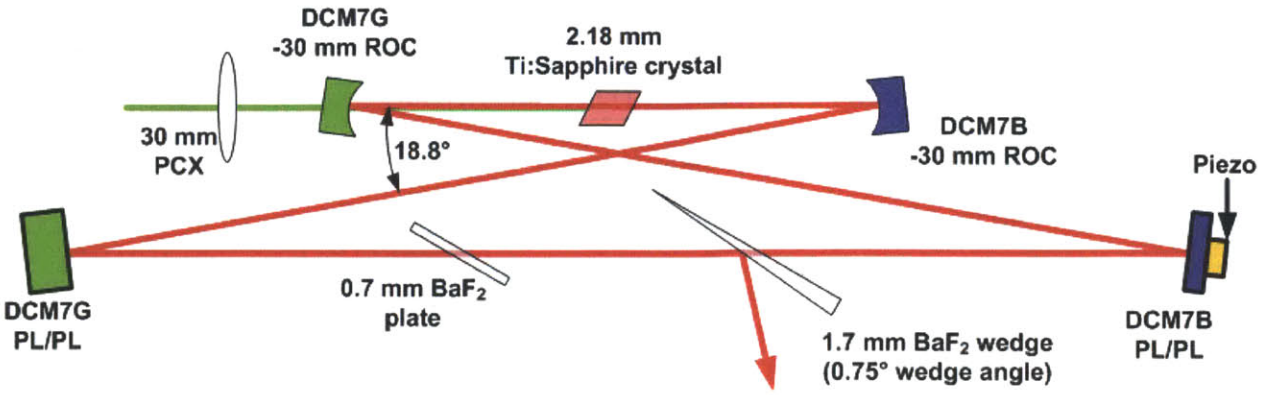

Figure 3.12 – Schematic of the final 1 GHz laser. The DCM mirrors used in this laser were generation 7, which have proven to provide the most ripple free compensation of all succeeding generations. The BaF_2 wedge does introduce some angular dispersion to the beam, though the spatial chirp of the output beam seems to be dominated by the Kerr lens effect. Overall footprint of the laser cavity is ~20 cm by 8 cm.

3.3 Optical molecular clock and frequency comb system description

For achieving an optical clock and stabilized femtosecond laser frequency comb a methane stabilized HeNe laser similar to [53] for stabilization of the repetition rate in [51] was used, and because of the octave spanning spectrum generated directly from the laser the *f*-2*f* self-referencing technique [63] to stabilize the carrier-envelope frequency, f_{ceo}, Fig. 3.13, was employed.

By sending a fraction of the Ti:Sapphire output through a 20 mm long periodically poled Lithium-Niobate crystal with a 21 μm poling period, intrapulse Difference Frequency Generation (DFG) provides an offset free frequency comb at 3.39 um for locking to the reference laser. To achieve good conversion efficiency, the beam is first reflected off of 5 DCM mirrors to ensure good temporal overlap of the 810nm and 1064nm components, which differs from earlier work by Foreman [51] due to the more symmetric output spectrum from the current laser. Because there is no offset frequency in the comb generated in the DFG process, stabilization of the DFG comb corresponds to direct stabilization of the frequency spacing between modes in the Ti:Sapphire output spectrum, i.e. the repetition rate [36], separate from stabilizing the carrier-envelope offset-frequency.

From the DFG process ~200 nW of power is generated as measured in a 50 nm bandwidth, giving ~150 pW per mode assuming a uniform distribution. The DFG signal is sent through a HeNe discharge tube giving a further 20 dB of gain prior to heterodyning with the HeNe laser, resulting in a 30 dB SNR in

a 100 kHz bandwidth. Stabilization of the mode spacing of the Ti:Sapphire laser is achieved by offset locking the DFG comb to the methane stabilized HeNe laser using a second HeNe laser as a transfer oscillator and sending the phase error signal to a piezo mounted mirror in the Ti:Sapphire's cavity. The mirror and piezo are mounted on a small copper cylinder which is massive enough to allow the majority of the displacement force generated by the piezo to result in displacement of the mirror, yet short enough that the lowest order compression mode of the cylinder is greater than 100 kHz yielding a piezo/mount system which can support feedback bandwidths exceeding 60kHz (Appendix B).

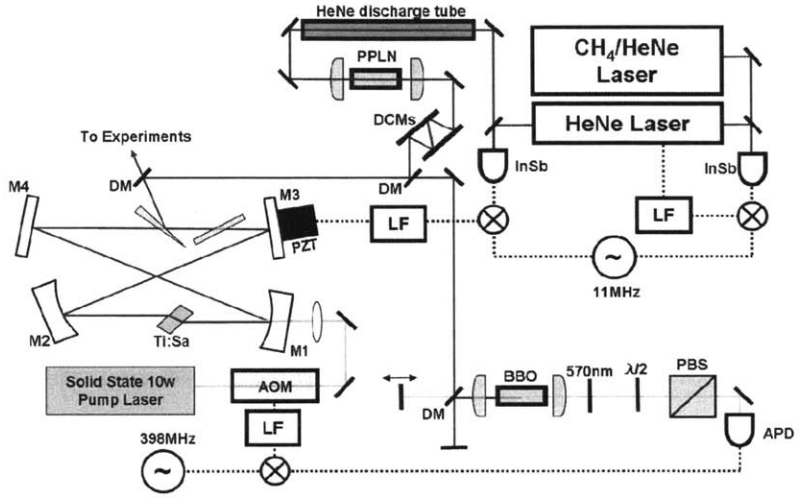

Figure 3.13 -- Schematic of the 1 GHz Ti:Sapphire laser and CH_4/HeNe referenced frequency comb system. Repetition rate control optics are in the upper right corner and f_{ceo} stabilization optics are in the lower right. AOM, Acousto-optic modulator; LF, Loop filter; PZT, Piezo electric transducer; DM, Dichroic mirror.

For carrier-envelope offset frequency stabilization, a Michelson type geometry is used to phase the f and $2f$ components due to the spatial chirp of the output beam from the Ti:Sapphire laser. Because of the extremely broad bandwidth of the Ti:Sapphire laser, a large amount of power is available at 570 nm and 1140 nm, 300 μW and 2.5 mW both in 10 nm bandwidths, respectively. Both components are sent through a 1 mm thick BBO crystal for Type II second harmonic generation, and a 10nm bandpass filter centered at 570nm for generating a beatnote with a signal to noise ratio of 50 dB in a 100kHz bandwidth using an avalanche photodiode (MenloSystems APD210). This signal is phase locked to a high stability RF synthesizer by modulating the Ti:Sapphire's pump power using an AOM which changes the

intracavity pulse energy and subsequently the carrier-envelope frequency through the self-steepening effect.

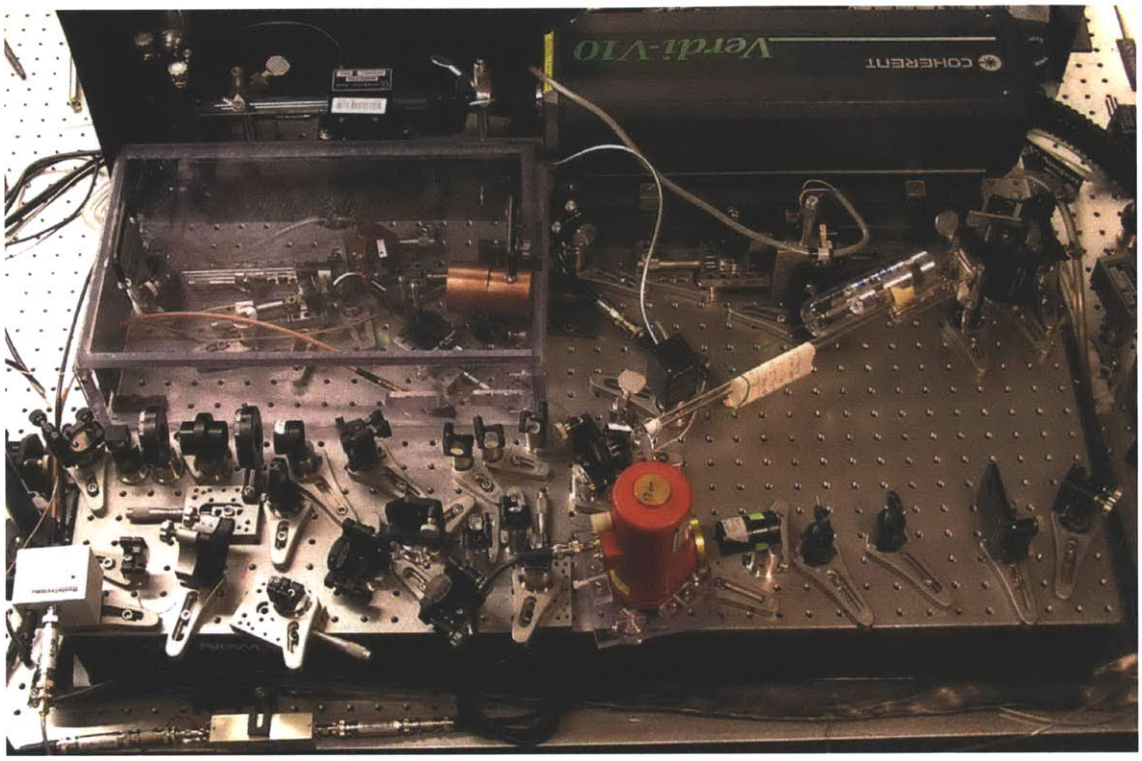

Figure 3.14 -- Picture of the 1 GHz Ti:Sapphire frequency comb. The mode-locked Ti:Sapphire laser is in the upper left hand portion of the picture. Carrier Envelope offset frequency stabilization optics are in the lower left hand portion of the picture. Difference frequency generation and amplification of the DFG signal as well as detection of the beatnote between the reference laser and the DFG comb all occur on the right hand side of the picture. The reference laser is not pictured, however this 2 foot deep and 3 foot wide breadboard is the same size as the board on which the reference laser is mounted.

The entire frequency comb system described above consists of a minimal number of physical components suggesting the possibility of a truly compact system construction. The Ti:Sapphire and all frequency stabilization optics fit comfortably on one 2ft by 3ft breadboard, while the reference laser is contained on another breadboard of the same size. The robust construction of the reference laser should allow stacking of the two optics boards to save table space if necessary with little to no degradation in performance. Electronics necessary for stabilization of the Ti:Sapphire laser along with the pump laser controller and cooling system will fill only half of a standard size electronics rack.

3.4 Characterization of system stability

The reference oscillator used in this work for measuring the Allan Deviation of the frequency comb was a 674 nm laser diode stabilized to a Fabry-Perot cavity using the Pound-Drever Hall locking method [59]. The cavity was constructed using a 10 cm long ultra low expansion glass spacer mounted to its support at the center of the spacer with the optical axis vertical to minimize the effect of ambient mechanical vibrations. Optically contacted mirrors provide a measured cavity finesse of 708,000+/-10,000.

The frequency comb and diode laser sources were located in the same building, but were separated by one floor and ~30 m direct distance. Light generated by the stabilized diode was delivered to the Ti:Sapphire comb by a single mode polarization maintaining fiber which was not stabilized due to the short length of the fiber (60 m) and the expected level of frequency stability to be measured [65]. A 10 nm bandwidth around 674 nm from the stabilized frequency comb gave ~900 μW was heterodyned against ~800 μW of light from the stabilized diode laser generating a 35 dB SNR radio frequency beat note at ~18 MHz. This RF signal was counted using two zero dead time frequency counters (Pendulum CNT-90) to ensure that adequate signal to noise ratio was maintained during the measurement.

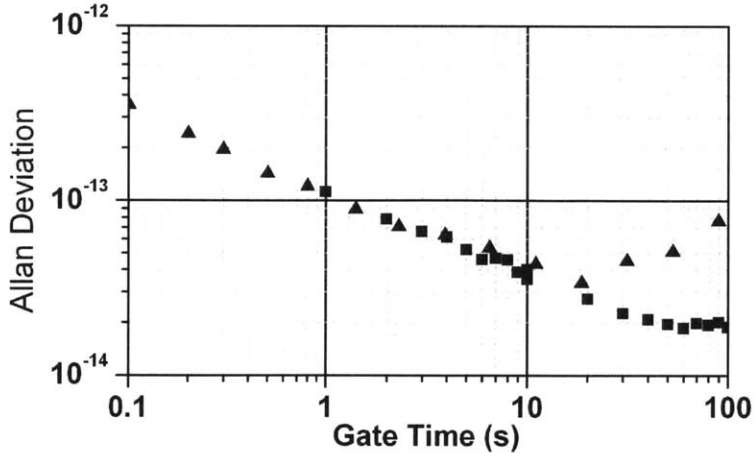

Figure 3.15 -- Measured Allan Deviation of the heterodyne beat note between the cavity stabilized diode laser and the Ti:Sapphire frequency comb plotted in triangles, and squares plot the stability of the methane stabilized HeNe reference laser. The divergence of the two plots at 20 s gate time is due to long term drifts of the cavity stabilized diode laser.

The Allan Deviation plot in Fig.3.15 shows that the measured stability of the diode/frequency comb system as measured at 674 nm directly follows the stability of the methane stabilized reference laser, which was determined by a direct comparison of two identical HeNe lasers. For gate times longer than 20 s the Allan Deviation from the current measurement increases while the expected stability of the methane laser continues to decrease until about 100 s where long term pressure and temperature drifts take over. Drifts in the current measurement beginning at 20 s originate from the uncompensated temperature changes of the 674 nm diode laser's reference cavity.

For using the frequency comb in quantum information science or high speed sampling, pulse repetition rate phase noise is a primary concern. A preliminary characterization of high frequency phase noise of the optical clock was achieved by detecting the pulse repetition rate of the Ti:Sapphire output using a GaAs photodiode, filtering the 6th harmonic and amplifying the signal using a low noise amplifier before analyzing the signal using an Agilent E5052 Signal Source Analyzer. As is evident from Fig.3.16 the major noise contribution is from the white noise floor of the photodetection process and the noise floor of the Agilent signal source analyzer [84]. Despite this heavily instrument limited measurement, the upper bound for the maximum timing jitter when integrating from 10MHz to 40Hz is only 10fs.

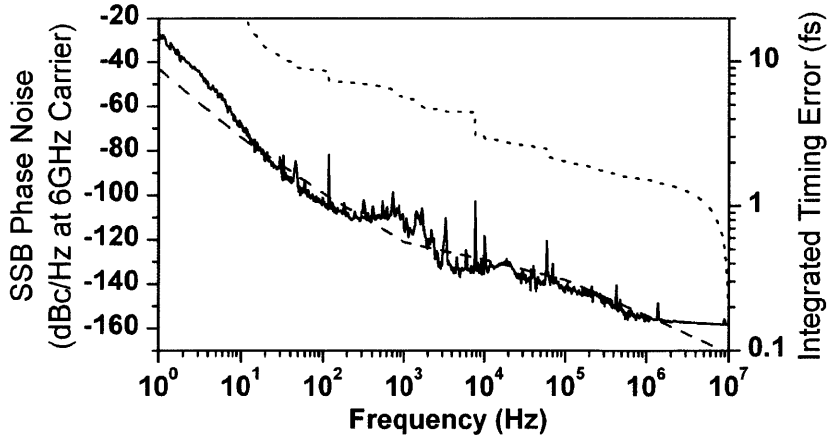

Figure 3.16 -- The solid line plots the single sided phase noise of the 6th harmonic of the Ti:Sapphire laser's pulse repetition rate, and the dotted line is the integrated timing jitter starting at 10MHz. The dashed line is the published noise floor of the Agilent 5052 signal source analyzer used for this measurement.

3.5 Conclusion and future work

A compact, transportable frequency comb system based on a 1 GHz octave spanning Ti:Sapphire laser and a commercially available methane stabilized HeNe laser, using a conceptually simple scheme for comb stabilization has been presented. A fractional frequency stability of the Ti:Sapphire's optical spectrum has been demonstrated to be $3x10^{-14}$ on a 20 second timescale when the Ti:Sapphire laser is stabilized as a frequency comb using the HeNe reference laser. A preliminary measurement of the timing jitter of the Ti:Sapphire laser's pulse train using a simple radio frequency technique suggests an upper limit of 10 fs, considering a bandwidth of 10 MHz. The system simplicity is highlighted by the octave spanning output of the Ti:Sapphire laser, the commercial availability and easy operability of the reference laser, and the separation of control of the Ti:Sapphire's carrier envelope offset frequency and the pulse repetition rate. The high level of frequency stability provided by this compact and still transportable system is a distinct advantage enabling widespread deployment of visible frequency comb technology.

The ability to utilize the entire optical bandwidth of this system in an OAWG system will require significant advances in filter and modulator technology to allow cost efficient construction of massively parallel components. A modest 100 THz bandwidth of an as yet unrealized 40 GHz frequency comb could support in excess of 1000 channels. A recent paper [85] has demonstrated that access to 600 comb lines simultaneously is possible for a 21 GHz comb using a grism based disperser, though such a device will likely need to be constructed as a solid state device for long term deployment.

To increase the penetration of frequency comb technology into other fields, two hurdles need to be overcome: operational complexity/reliability and the physical and electrical footprint. The system presented here is a large step in this direction. With a modest amount of engineering, the optical portion of the system could be reduced in volume to less than 1 m^3 with the supporting electronics occupying less than one half of a standard 19" rack. A dedicated operator is still unfortunately required due to the difficulty in operating a Ti:Sapphire laser on a long term basis. New advances in optical components [86] may reduce the alignment sensitivity related to mode-locking of Ti:Sapphire lasers, however octave

spanning operation will still be challenging since the laser must be operated at such an extreme operating point. Progress on stable octave spanning operation will only come through dedicated study of the spatiotemporal dynamics of the mode-locking process.

On the physical and electrical side, exciting advances in laser diode technology [14,15] suggest that in less than 5 years, laser diodes with spectra centered at 480-490 nm should be commercially available. While the spatial mode quality of the beams from these lasers is not ideal, their vastly decreased physical size and electrical requirements make them extremely attractive alternatives to the pump lasers currently used for octave spanning Ti:Sapphire lasers.

Chapter 4

80 MHz Octave Spanning Ti:Sapphire laser for OPCPA seeding and high harmonic generation

4.1 Introduction

Ultra-short pulse lasers have been suggested as a route to generation of soft-x-ray radiation. Specifically, the use of high energy, short duration and long wavelength pulses has attracted increased attention [18,19] due to the potential to reduce the wavelength at which significant harmonic generation is produced. Optical parametric chirped pulse amplification (OPCPA) is an attractive route for generating the broadband, long wavelength and high power optical spectra necessary to eventually achieve soft-x-ray sources which could be considered tabletop systems. Using Ti:Sapphire as the seed source for such a laser system allows for a broadband, long wavelength seed pulse between 1500 nm and 2500nm through difference frequency generation (DFG). This seed pulse can then be amplified in several stages by as much as 10^8 to generate a pulse suitable for soft-x-ray creation.

4.2 Design decisions specific to supporting OPCPA systems and high harmonic generation

Imaging of biological systems is enabled by generation of light in the 2-4 nm wavelength region. This region is known as the water window because of a reduction in absorption of radiation, allowing finite transmission of light into tissue for direct imaging. Short pulse lasers are capable of generating optical spectra with wavelengths in the water window through a process known as high harmonic generation. Briefly, the idea is to focus an extremely intense laser pulse into a gas jet to create a non-linear interaction which emits high frequency radiation. As the pulse propagates through the gas, the large electric field of the focused laser pulse will partially ionize atoms in the gas, and capture the ionized electrons in the laser's electric field. There is a small probability that when the electric field reverses, the electrons will be accelerated back towards the atom and collide with it, releasing photons with energy proportional to the accumulated kinetic energy. Depending on the strength of the electric field and the time which the electrons spend in the electric field of the laser pulse, different energy photons will be generated.

By increasing the driving laser wavelength the energy level of the photons generated in the interaction process can be extended to higher energy levels at the expense of overall conversion efficiency [87]. Building a high power, short pulse laser system at mid-IR wavelengths can only be achieved through nonlinear processes, as there are no broadband laser materials in this wavelength region. For the system constructed here, an OPCPA process was selected for the ability to scale the pulse energy to very high values with short duration pulses without fear of damage to the pulse generation system. The center wavelength of the optical spectrum for harmonic generation was chosen at 2.1 μm due to the availability of high average power laser sources at 1.064 μm supplied by T.Y. Fan's group at MIT Lincoln Laboratory. An additional benefit of choosing 2.1 μm as a center wavelength is the anomalously low group velocity mismatch between 1.064 μm and 1.9 μm pulses in Lithium Niobate. By operating between 1 μm and 2 μm allows use of relatively long crystals in the OPCPA system, increasing overall efficiency of the system for a given number of pulse amplification stages.

The ideal seed pulse for such a system would be a relatively broadband pulse with a stable or constant envelope to carrier wave relationship. A stable carrier envelope phase, or f_{CEO} frequency is advantageous for isolated attosecond pulse generation via high harmonic generation experiments since as described above, the harmonic generation process is electric field dependent [88]. To satisfy both of these requirements, a broadband Ti:Sapphire laser is a nearly ideal source. The broad optical spectrum from a Ti:Sapphire laser can be used to perform difference frequency generation to generate a seed spectrum for the OPCPA system which has no f_{CEO} component, as well as providing the time base for the remainder of the amplifier chain through photodetection of the pulse repetition rate. A linear cavity, 80MHz repetition rate laser is a good compromise for OPCPA seeding because of the good pulse energy and relatively small size of the laser cavity versus a 5-10 MHz laser. The laser system developed in this chapter ultimately generated 90 mW with a spectrum extending from 625 nm to 1075 nm, as measured at the -10 dB points. Using the output from this laser in a MgO:PPLN crystal, spectrum from 1570 nm to 2470 nm was generated to seed the OPCPA amplifier chain, Fig. 4.1. Three amplification stages in the OPCPA system resulted in an amplification of the 1.5 pJ seed pulse to 200uJ and 23 fs duration.

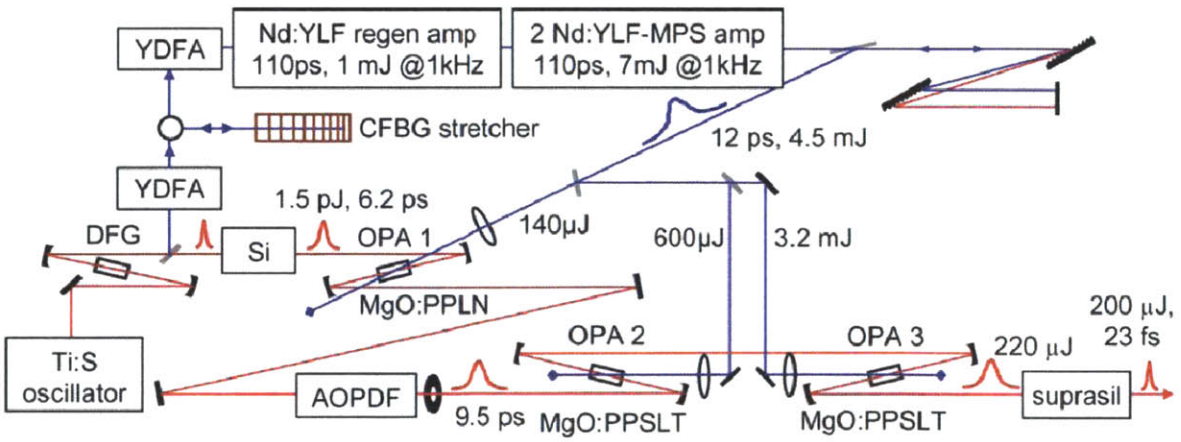

Figure 4.1 -- Schematic of the OPCPA system. OPA1-OPA3 are the three optical parametric amplifier crystals; AOPDF is an acousto-optic programmable dispersive filter for pre-compensating dispersion in the OPAs; YDFA is a Ytterbium doped fiber amplifier for amplifying pump seed pulses at 1 um; CFBG is a chirped fiber Bragg grating for stretching the amplifier pump seed pulses to prevent nonlinearities in the pump lasers; Si is silicon for both spectral filtering and stretching of the seed pulse prior to amplification by ~10^8 in the OPCPA system.

4.3 Laser design

The design of this laser will closely follow the methodology outlined in sections 3.2.1 to 3.2.6. Differences specific to this laser system include the longer cavity length and a requirement for significant power near 1100 nm. For design purposes, generating significant spectrum near 100 nm is equivalent to requiring a spectrum capable of supporting *f-2f* self referencing for f_{CEO} stabilization. The following sections will outline both a delta parameter type analysis for the geometric optical design and a temporal optical design specific to linear cavity lasers.

4.3.1 Geometric optical design

A successful cavity configuration typically used for low repetition rate lasers is a z-folded arrangement similar to that depicted in Fig. 4.3. This type of cavity is used because of the split stability region it generates. The unequal length arms break the symmetry of the cavity, generating the double stability region in Fig. 4.2. The large sensitivity of the beam waist to curved mirror separation distance in the inner edge of the outer stability region is an indicator for a cavity alignment which could favor mode-locking. The arm length ratio used here of 1.7:1 was selected based on research by Uwe Morgner during his Habilitation Thesis.

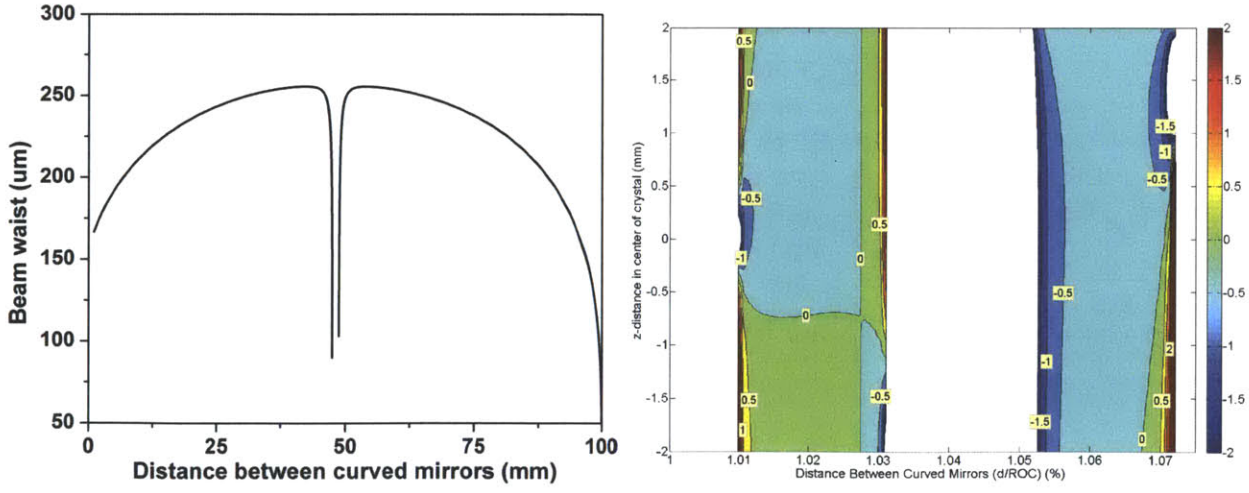

Figure 4.2 -- Plots of the beam waist in the cavity focus as a function of curved mirror separation (left) and delta parameter as a function of the fractional mirror separation (right). The delta parameter was analyzed for the difference between output power P=0 and P=3 mW, for 1% output coupling and 100 fs pulses.

The model used for the delta analysis of the 80 MHz laser is very similar to the one used for the ring laser. The main difference being due to the fact that the nonlinear medium is transited twice in one round trip rather than just once as required by the layout. Otherwise the matrix construction process in identical.

There is an interesting difference between the results of the delta parameter analysis for the 1 GHz ring laser and those found for the 80 MHz linear cavity laser, Fig. 4.2. The portion of the stability region where mode-locking should occur for the ring cavity is on the inner edge (or left side in Fig. 3.7), primarily near the focus. However, for the linear cavity laser it appears that spot size reduction should occur over the entire length of the crystal for the outer stability region. Such a large region of the parameter space which supports a large spot size change suggests that the linear cavity laser should experience a much stronger discrimination between CW and mode-locked operation because of the increased change in overlap between the laser mode and the pumped volume.

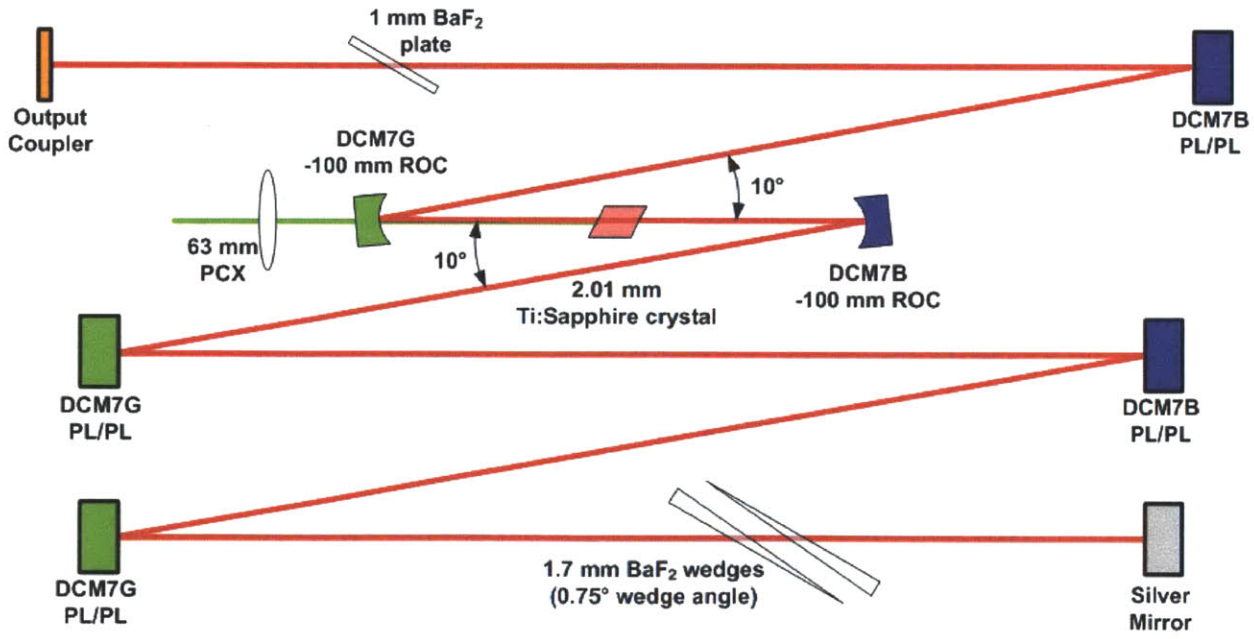

Figure 4.3 – General schematic of the 80 MHz laser. All mirrors are DCM type except for the mirrors at the ends of the cavity. The output coupler is a multilayer dielectric consisting of only a few layers and so has minimal dispersion. The silver mirror also contributes nearly zero dispersion, though with a reflectivity of ~98% there is around 2% loss per round trip. Overall length of the laser cavity is 1.875 m, with the ratio of the length of the two arms set at 1.7. The laser is pumped with 5.5 Watts of 532 nm light from a single frequency Coherent Verdi laser. With this configuration, 90 mW average output power is possible.

4.3.2 Temporal optical design

As discussed in section 3.2.6., careful control over the round trip cavity dispersion is necessary to support the broadband spectrum necessary for generating light at 1100 nm to seed the OPCPA system. As before, dispersion compensation is achieved using discrete dispersion compensating elements, forcing the laser to operate in a dispersion managed mode-locking regime. The main difference between dispersion compensation for a ring laser and a linear cavity laser is the manner in which dispersion is summed. In the ring cavity, there is only one point in the cavity where the cavity dispersion must sum to near zero. In the linear cavity, the dispersion must sum to just below zero twice per round trip: once per entrance to the crystal. Figure 4.4 plots the dispersion of various intracavity elements as well as the round trip dispersion for both the short and long arms, with both summations starting and ending in the center of the crystal.

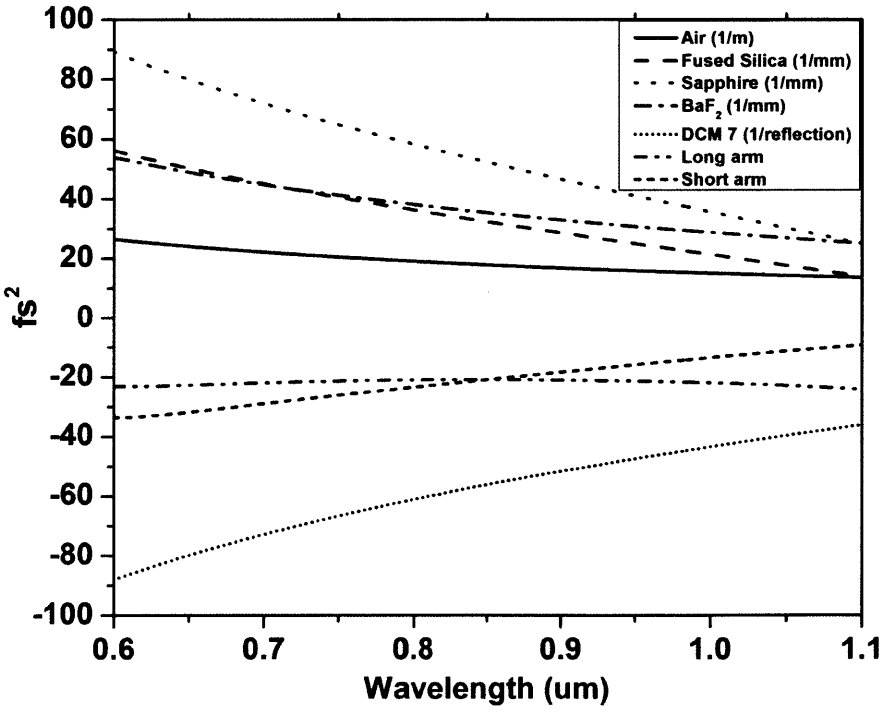

Figure 4.4 – Dispersion of common laser materials as well as round trip dispersion of each arm of the 80 MHz laser. Round trip dispersion experienced for both the long and short arm of the linear cavity laser is plotted to ensure that when the pulse traverses the crystal in both directions it is properly compressed to maximize the Kerr effect.

Finally, the output coupler used for this laser was designed by Richard Ell as part of his work in reference [67], and is also described in the PhD thesis of Lia Matos [89]. The output coupler provides 1% of transmission at 800 nm, with the transmission rising sharply above 900 nm and below 700 nm to more than 50%. The transition between the low and high transmission regions may play an important role in the development of short pulses and the stability of the mode-locking process. After the coating run which created the output coupler used here, several other attempts were made to duplicate this coating design. None were successful in recreating the performance seen with optics from the original run, suggesting the sensitive dependence on rate of change of transmission.

4.4 Operating performance of the resulting Ti:Sapphire laser

The performance of the resulting laser is characterized by its output power, efficiency and optical spectrum. The laser output power was 90 mW average power for 5.5 W pump power, resulting in an optical to optical efficiency of 1.6%. This low level of efficiency can be at least partially attributed to the silver mirror at the end of the laser cavity. A silver mirror is used as an end mirror to prevent generation of uncompensated pre and post pulses which would arise from using a single DCM mirror. An alternative to using a silver mirror would be to use a slightly less broadband DCM mirror in place of the silver mirror. By slightly reducing the reflectivity bandwidth, it might be possible to make a higher quality AR coating thus reducing the amplitude of the pre and post pulses. The optical spectrum from the laser is plotted in Fig. 4.5. The effect of the output coupler is visible in the structure of the output spectrum as evidenced by the slight increase in power at just above 700 nm and just below 900 nm. The very slight M-shape of this spectrum may also indicate that the majority of the optical spectrum beyond the 700-900 nm range is generated in a single pass through the Ti:Sapphire crystal due to the high pulse energy circulating within the cavity.

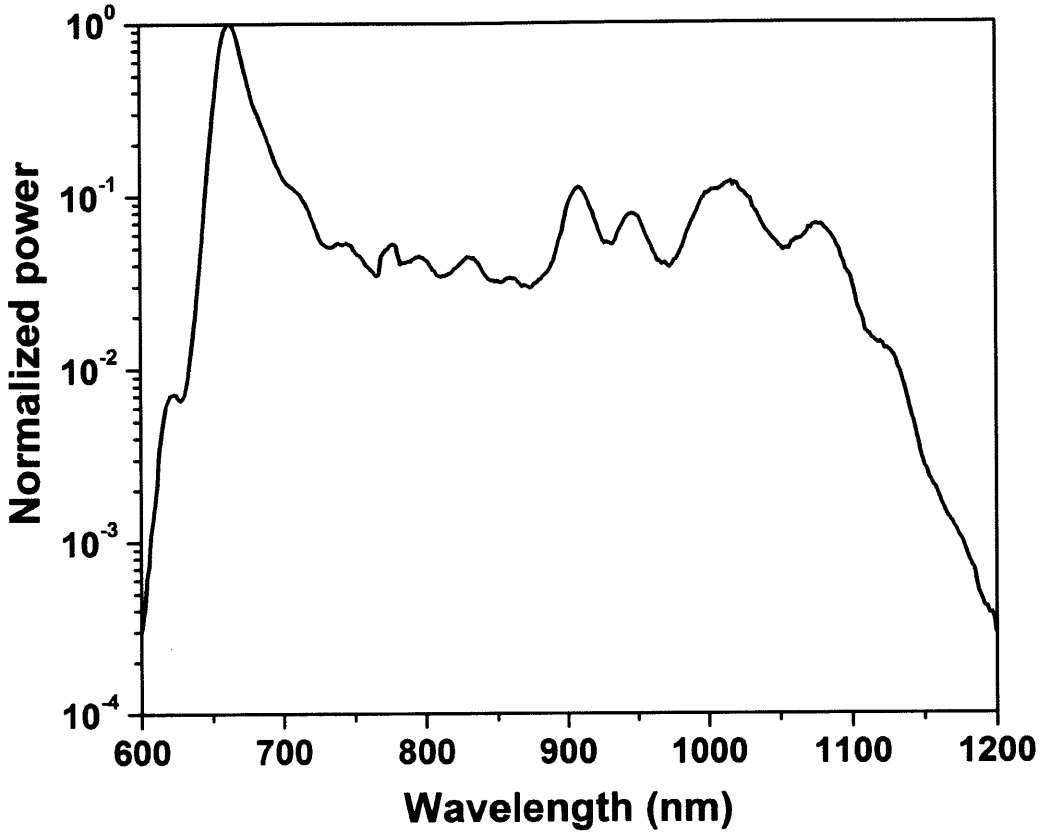

Figure 4.5 – Optical spectrum from the 80 MHz Ti:Sapphire laser. The large peak near 608 nm occurs due to phase matching in the laser cavity caused by dispersion of the output coupler.

4.5 Conclusion

In this section, the design and performance of a broadband Ti:Sapphire laser with 80 MHz repetition rate was described. A design process similar to that used for the 1 GHz laser described in Chapter 3 was used, and differences between the two laser types were highlighted. The resulting laser system generated 90 mW with a spectrum extending from 625 nm to 1075 nm, as measured at the -10 dB points. Using the output from this laser in a MgO:PPLN crystal, spectrum from 1570 nm to 2470 nm was generated to seed the OPCPA amplifier chain, Fig. 4.1. Three amplification stages are required to boost the 1.5 pJ seed pulse to 200uJ and 23 fs duration.

In addition to increasing the optical bandwidth generated by Ti:Sapphire lasers used in such seeding applications, increasing the stability and operability of such systems is quite important. The

current system was constructed using discrete optical and mechanical components on an optical breadboard. Operation of the laser on a daily basis was generally possible with the laser running without intervention for the entire day. On a semi-monthly basis however, the laser would need to either have the Ti:Sapphire crystal cleaned or the optics slightly realigned. Construction of an engineered system to isolate the laser from dust and debris as well as temperature stabilizing all optical components would provide a large increase in the availability of the laser.

THIS PAGE INTENTIONALLY LEFT BLANK

Chapter 5

Visible wavelength frequency comb for astrophysical spectrograph calibration

5.1. Introduction

A successful method for identifying planets in other star systems (exoplanets) is the radial velocity (RV) technique, which exploits small, periodic Doppler shifts in the spectrum of a target star to infer the existence of orbiting planets and determine characteristics such as orbital period and a lower limit to the planet's mass. Utilizing the RV method to find small, rocky exoplanets similar to the Earth in the habitable zone requires wavelength calibration precision and stability ~10 cm/s for the astrophysical spectrograph used to measure the stellar spectrum [5]. Because frequency combs provide a broad spectrum of highly stable and precisely known optical frequencies [90] which can be traced to a common reference such as GPS, they are an ideal wavelength calibration tool for astrophysical spectrographs. Spectral filtering of the frequency comb using a Fabry-Perot cavity [91,92] is generally required for the spectrograph to resolve individual comb lines, Fig. 5.1, though work is progressing to develop frequency combs with repetition rates high enough to eliminate the need for filter cavities [25,93,94]. Measurements of time-variation of the fundamental constants or of the expansion of the universe [95,96] may also be enabled by these types of calibration systems, with expansion of the universe requiring ~1 cm/s sensitivity over decadal timescales. In this work, the focus is on calibrators for the near-term goal of exoplanet detection.

Frequency comb systems optimized for astrophysical spectrograph calibration ("astro-combs") have been demonstrated at several wavelength regions to date [3,4,49,97,98] though recently there is a trend toward demonstrating systems operating in the short wavelength end of the emission spectrum of Sun-like stars (400-700 nm) [97,98]. In addition to providing the largest photon flux, this wavelength region is rich with spectral features of high quality most suitable for use with the RV method [99]. Shorter wavelengths also avoid fringing effects in the spectrograph's charge coupled device (CCD) caused by weak etaloning in the silicon substrate. Etaloning can be a serious complication for data analysis at wavelengths longer than 700 nm since correction of these fringes to a precision better than 1% is challenging.

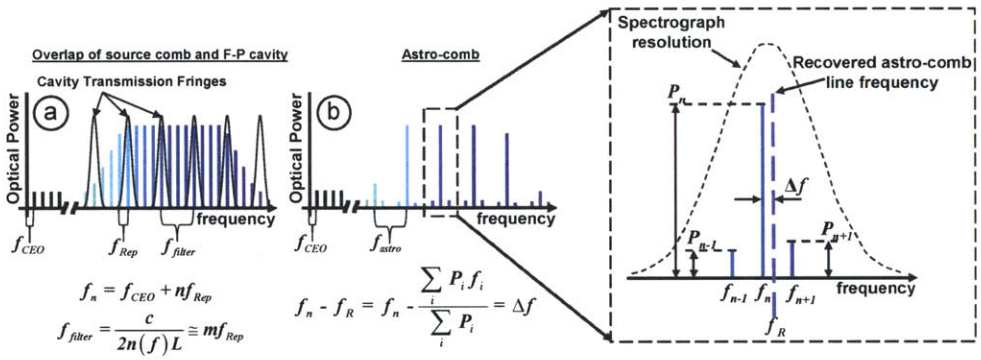

Figure 5.1 – Description of an astro-comb in the frequency domain. (a) Frequency-doubled source comb lines and analytic description of the optical spectrum in terms of the repetition rate, f_{rep}, and the carrier envelope offset frequency, f_{CEO}, of the underlying Ti:Sapphire laser. The frequency doubled spectrum is multiplied by the transmission function of the Fabry-Perot cavity, filtering the source comb spectrum which becomes the astro-comb spectrum shown in graph (b). The free spectral range of the transmission resonances of the filter cavity, f_{filter}, is ideally an integer multiple of the repetition rate of the source laser. However due to dispersion from air and mirror reflections, f_{filter} will generally be a function of frequency. In this example the integer m=4 (typically m=20-50 with our 1 GHz repetition rate laser) such that in (b) every 4th line (referred to as an astro-comb line) is fully transmitted. Because the spectrograph resolution (~>15 GHz) is generally larger than the repetition rate of the source comb, finite suppression of the source comb modes closest every astro-comb line results in a power weighted average frequency, f_R, to be reported by the spectrograph. The difference Δf must be recovered to realize the full accuracy of the astro-comb.

Here, operation of an astro-comb with a center wavelength near 420 nm with FWHM bandwidth of about 15 nm, center wavelength tunable over 20 nm, and spectral line spacing of 22 and 51GHz is demonstrated. Systematics of the calibration system including dispersion, higher order transverse modes of the cavity filter and alignment of the frequency comb and cavity filter transmission resonances have been characterized. Using a scanned-cavity technique [100], the accuracy of the astro-comb system has

been compared to the underlying laser frequency comb. The basic idea of the scanned cavity technique is as follows. A single frequency diode laser is phase locked to one tooth of a stabilized frequency comb. The filter cavity is then phase locked to the diode laser at a length corresponding to an integer multiple of the frequency combs cavity length. By scanning the offset frequency between the diode laser and the frequency comb and monitoring the spectrum which is transmitted through the filter cavity, information about the dispersion of the filter cavity can be gained. The scanned cavity technique requires assumptions about the finesse of the filter cavity and cannot handle dispersion which changes quickly with frequency, though it can provide good calibration for low dispersion cavities.

Broadband characterization of an astro-comb system is necessary to ensure that the optical filtering process has not left unevenly suppressed source comb lines on either side of each astro-comb line. Identifying where uneven suppression has occurred can allow use of a much wider bandwidth than would normally be possible if only exactly even suppression could be tolerated. Analysis of the source frequency comb to filter cavity locking method is also presented with consequences of misalignment of these two spectra. A method for avoiding misalignments is also discussed.

5.2 Limits of spectrograph calibration

Astrophysical spectrographs used for high precision spectroscopy are generally configured as cross-dispersion spectrographs which disperse the input spectrum in two orthogonal directions to increase resolution and optical bandwidth. Focusing the cross-dispersed beam on a CCD creates a two dimensional image which transforms the frequency (or wavelength) of the input light to a physical position on the CCD. The ideal calibrator for such a spectrograph would be a single light source whose spectrum is composed of an ensemble of individual incoherent emitters, each with equal power and separated in frequency by slightly more than the spectrograph resolution [5]. Each emitter should also have a spectral width much less than the spectrograph resolution. Knowing the frequency of each component of the calibration spectrum allows recovery of the spectrograph's mapping of frequency (or wavelength) to CCD position as well as the point spread function of the spectrograph for all frequencies.

Frequency combs based on mode-locked lasers are currently the closest analogue to this ideal calibrator with the exceptions that their optical bandwidth is typically much narrower than the spectrometer's bandwidth and the frequency spacing between spectral features (comb lines) is much less than the resolution of the spectrometer. Overcoming the bandwidth limitation can be partially achieved by broadening the spectrum from the frequency comb in a nonlinear fiber or crystal and/or shifting the spectrum to a different wavelength range using a similar process. A Fabry-Perot cavity can be used to selectively remove all but every m^{th} comb line in the output spectrum of the frequency comb to generate a new comb whose comb lines are resolvable by the spectrograph, Fig. 5.1. The shot noise limited velocity uncertainty of a radial velocity measurement using the Doppler shift of a single spectral feature has previously been discussed as [5,101]

$$\sigma_V = \lambda A \frac{\delta v_{1/2}}{SNR\sqrt{n}} \tag{5.1}$$

where A is a number close to one related to the specific line shape of the feature in question, $\delta v_{1/2}$ is the FWHM of the feature, SNR is the peak signal to noise ratio due to shot noise for the feature usually measured at peak center, n is the number of spectrograph CCD pixels sampling the spectral feature in the grating dispersion direction and λ is the center wavelength of the feature. Using all N emission features of a target star or all the lines from an astro-comb, the value given by Eq. (5.1) may be reduced by $1/N^{1/2}$. By matching the frequency spacing of the astro-comb lines to a value just larger than the resolution of the spectrograph ($\alpha \approx 3$) [5], and defining N as the ratio between the FWHM frequency bandwidth of the calibration spectrum δv_{input} and the astro-comb repetition rate, Eq. (5.1)can be rewritten including the spectrograph resolving power $R=\lambda/\delta\lambda$ as

$$\sigma_V = \frac{Ac}{SNR\sqrt{n}R^{1/2}}\sqrt{\frac{\alpha\lambda}{\delta\lambda_{input}}} \tag{5.2}$$

In addition to the benefits achieved by shifting the center wavelength of the RV measurement to shorter wavelengths as stated in the introduction, there is an additional precision benefit of $\sim 1/\sqrt{2}$ gained from

frequency doubling the Ti:Sapphire laser. However large increases in the bandwidth of the calibration source are necessary to see significant gains in calibration precision for a given spectrograph with resolving power R. The sensitivity gain between calibrating 15 nm and calibrating the full octave spanning spectrum of the Ti:Sapphire laser (>300 nm) is a factor of ~4.5. The difficulty of achieving comb line filtering over 300 nm generates far greater challenges than those presented here [2,4,102].

5.3 Visible frequency comb generation

Our visible wavelength astro-comb (Fig. 5.2) follows the general approach outlined above by using a frequency doubled octave spanning Ti:Sapphire laser which is spatially and spectrally filtered before its spectrum is fiber coupled to the astrophysical spectrograph for calibration of the spectrograph's frequency (or wavelength) to CCD position mapping. Currently, nonlinear frequency conversion is the only method for generating a frequency comb in the 400-600 nm wavelength region, as no broadband laser materials in this region are known. Frequency doubling of a broadband Ti:Sapphire laser, Fig. 3, has been chosen to provide a source comb at 400 nm, because our group has previously [50] constructed stable and high power Ti:Sapphire lasers that are capable of operating unattended on day long timescales. Absolute referencing of such lasers is also more direct than with other systems, as Ti:Sapphire lasers can generate optical spectra directly from the laser cavity that cover more than one octave allowing direct access to the carrier envelope offset frequency, f_{CEO}, control of which is required if all optical frequencies from the frequency comb are to be known.

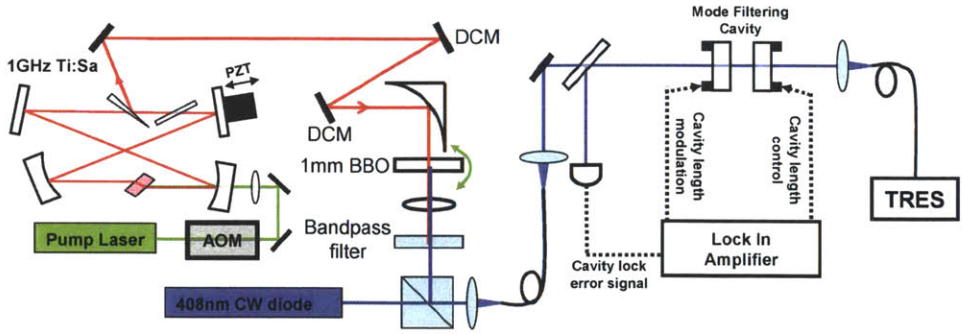

Figure 5.2 -- Layout for visible wavelength astro-comb. Output from an octave-spanning 1 GHz Ti:Sapphire laser frequency comb is pre-chirped using two Dispersion Compensating Mirrors (DCM) and focused with an off-axis parabolic mirror into a BBO crystal. Single mode fiber between the Ti:Sapphire laser and the Fabry-Perot cavity filter ensures that the spatial profile of the beam entering the cavity is of lowest order (TEM_{00}), giving the best possible suppression of transmission by higher order transverse modes. A 408 nm external cavity diode laser allows for identification of the desired Fabry-Perot cavity length as well as side-mode suppression estimation. TRES – Tillinghast Reflector Echelle Spectrograph, AOM – acousto-optic modulator, PZT – piezo electric transducer.

Optical frequencies of comb lines from femtosecond lasers are uniquely described by $f=f_{CEO}+nf_R$, where active control of both f_{CEO} and f_R allows unique definition of the absolute frequency of each comb line. In the system depicted in Fig. 5.2, f_R is detected using a PIN photodiode to recover the pulse repetition rate which is then phase locked to a low noise radio frequency oscillator using a low bandwidth feedback loop to control the length of the laser cavity. Control of the f_{CEO} frequency is achieved by modulation of the pump laser intensity using an AOM. A phase locked loop which generates the control signal for the AOM matches the f_{CEO} frequency detected using the f-2f method with a second low noise frequency synthesizer. Both synthesizers are phase locked to a commercial rubidium frequency reference to enable the entire chain to have a fractional frequency stability $<10^{-11}$ over time scales from seconds to days. Heterodyne measurements with a narrowband diode laser at 408 nm reveal a maximum linewidth of the optical comb lines <5 MHz, limited by the linewidth of the diode laser.

The astro-comb system must be very robust and reliable over many hours for use in an observatory environment. For high reliability operation, a 1mm BBO crystal was chosen for frequency conversion rather than a photonic crystal fiber. Using 300 mW from the Ti:Sapphire laser as input to the BBO crystal, 18 mW average power and 15 nm FWHM spectrum centered at 420 nm is typically generated. Rotation of the BBO crystal in the laser focus allows tuning of the generated spectrum over a

FWHM bandwidth of nearly 50 nm as measured directly after the BBO crystal. For reasons explained below, the tuning bandwidth is reduced to approximately 20 nm after transmission through the Fabry-Perot cavity, Fig. 5.3(A).

For optimal spectral filtering of the source comb, it is necessary to ensure that the intensity distribution of the beam sent to the Fabry-Perot cavity is well described by a fundamental order Hermite-Gaussian mode. Due to both the spatial chirp of the Ti:Sapphire laser output and spatial walk-off which occurs during second harmonic generation in the BBO crystal, the beam at the output of the BBO crystal contains many higher-order spatial terms. A single-mode fiber (mode field diameter ~2.9 μm) placed in the Fourier plane of a 4F lens system leads to a transverse intensity distribution at the output of the 2nd lens which is approximately a lowest order Gaussian. While using a single-mode fiber as a spatial filter reduces the power available after the doubling process by a factor of almost 5, the spatial profile of the output beam becomes a constant and only the spectral content and transmitted fraction can be affected by changes in beam pointing from the laser.

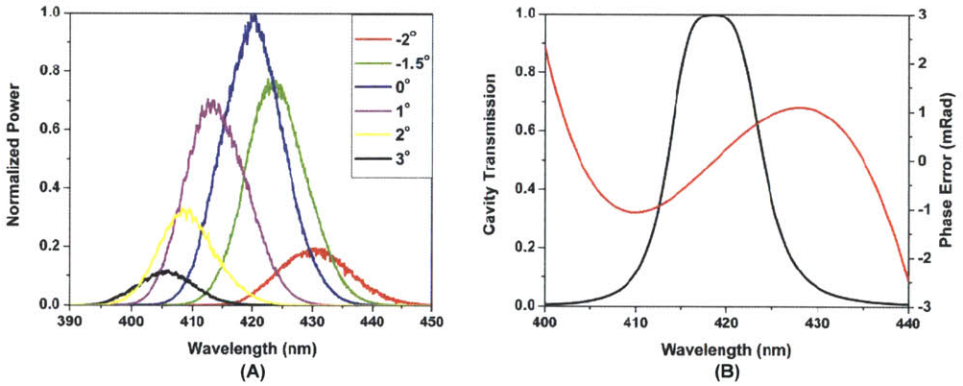

Figure 5.3 -- (A) Measured optical spectra of the visible wavelength astro-comb, after the Fabry-Perot cavity filter, for several angles of the BBO crystal relative to the IR source comb beam. Integrated power for the central spectrum is 25 uW (~25 nW per astro-comb line). Filtered mode spacing is 22 GHz. (B) Calculated characteristics of the Fabry-Perot cavity filter using dispersion-optimized dielectric Bragg reflectors. Round-trip dispersion due to reflection from the Fabry-Perot cavity mirrors is plotted on the right axis, and cavity transmission for an input spectrum centered at 420 nm is plotted on the left axis taking into account air dispersion as well as mirror dispersion and reflectivity.

5.4 Spectral filtering

The highest precision of calibration occurs when the spacing between spectral features in the spectrum used to calibrate a spectrograph is approximately three times the resolution of the spectrograph [5], ensuring high contrast coverage of the spectrograph's CCD. Spectral filtering of the source comb is currently necessary to achieve the ideal spacing since the frequency spacing between comb lines of all current mode-locked lasers suitable for spectrograph calibration is smaller than the resolution of most existing astrophysical spectrographs.

The most straightforward way to achieve filtering is by using a two mirror Fabry-Perot cavity where the distance between the mirrors, L, is set such that the free spectral range of the filter cavity, $c/2L$, is an integer multiple of the source comb repetition rate, Fig. 5.1. Such a filter only transmits every m^{th} source comb line, suppressing the remaining source comb lines to varying degrees resulting in a transmitted spectrum which more closely approximates the ideal. Dispersion from air or mirror reflections causes a deviation from an integer spacing resulting in a change in amplitude of source comb line transmission. The difference in transmitted amplitude is generally small and is manifested primarily as an asymmetry in the suppression of the two source comb lines on either side of the m^{th} transmitted source comb line (astro-comb line), causing an apparent shift in the overall line center recovered by the spectrograph. This shift occurs because the spectrograph's limited resolution causes all three source comb lines to be recovered as a power-weighted sum rather than as individual lines. The shift in frequency of the recovered center of gravity caused by asymmetrical line suppression as $\Delta f=(P_{n+1}-P_{n-1})f_R/(P_{n-1}+P_n+P_{n+1})$ which is a truncated version of the formula described above in Fig. 1. A recently developed scanned cavity technique [100] can be used to identify and remove these systematic shifts from the final calibration which is critical since any dielectric mirror coating will contain both small errors and a systematic divergence of the dispersion at the edges of its working range.

In this work, plane parallel mirrors are used to construct the Fabry-Perot cavity filter to reduce distortion of the astro-comb caused by transmission of source comb light through the filter cavity as a

result of excitation of higher order transverse modes (HOM) at frequencies far from the longitudinal, *c/2L*, resonances. The reduction in transmission via HOM is a result of three factors: First, the frequency offset for the higher order transverse modes is typically <100 MHz for plane parallel cavities. Second, due to the high source comb repetition rate of 1 GHz, transmission of a source comb line adjacent to a desired astro comb line, can only occur via transverse modes with very high mode order (10 or more). Third, the difference in nominal transverse mode size between the $TEM_{(0,0)}$ mode and higher order transverse modes prevents significant coupling into higher order transverse modes once the coupling is optimized for the $TEM_{(0,0)}$ mode. The combination of these three factors reduces the side mode transmission via higher order transverse modes to a level similar to what would be expected from a hypothetical cavity possessing only the longitudinal *c/2L* modes. To verify our chain of arguments experimentally, Fig. 5.4(A) shows the measured transmission of the Fabry-Perot filter cavity using a swept frequency laser diode. Asymmetry of the measured transmission, due to transmission via higher order transverse modes is clearly visible on the high frequency side of the transmission fringe in Fig. 5.4(A). However, it should be emphasized that the benefit of using a plane parallel mirror cavity is the elimination of transmission maxima in a similar sweep spanning the full 22 GHz free spectral range, Fig. 5.4(B). The broadening of

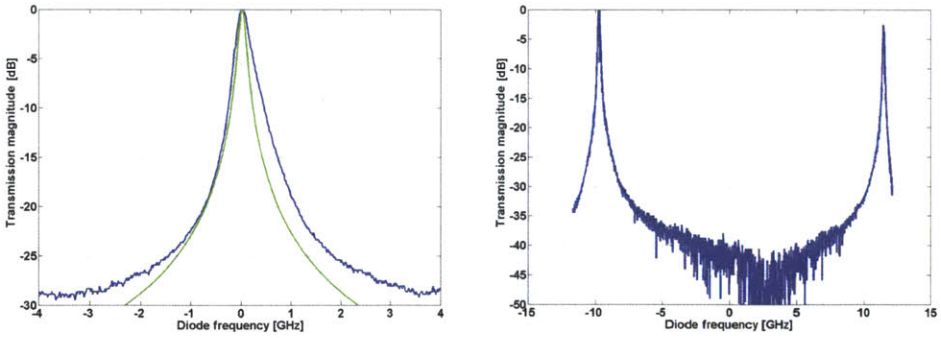

(A) (B)

Figure 5.4 – Transmission of the Fabry-Perot cavity filter measured with a swept frequency laser diode. (A) Comparing measured transmission (blue) and calculated transmission assuming R=98.2% and a free spectral range of 22 GHz (green) shows the asymmetric observed line shape. Coupling of the diode laser into the cavity is identical to that of the frequency comb. (B) No higher order peaks are visible in a sweep spanning the full 22 GHz free spectral range.

the main transmission fringe in Fig. 5(A) occurs mainly because the flatness deviations are not spherical, though the asymmetry of the transmission fringe can be compensated using the technique described in [100].

Misalignment in the frequency domain of the Fabry-Perot cavity filter's transmission resonances and the source comb lines caused by air and mirror dispersion is also a limiting factor for the bandwidth of the source comb which can be successfully filtered. The mirrors used here are dielectric Bragg reflectors with slightly modified layer thicknesses using the numerical routine described in [103]. The layer thicknesses are optimized for minimum accumulated phase on reflection over most of the high reflectivity bandwidth of the initial Bragg layer stack. The resulting phase from reflection as a function of wavelength is plotted in Fig. 5.3(B) with the portion due to a constant group delay removed. Due to the fast variation of round trip phase mainly due to air dispersion [4] at the edges of the reflectivity bandwidth, the bandwidth over which the input comb lines and the Fabry-Perot cavity's transmission resonances are well aligned is limited, reducing the overall transmission and resulting in an astro-comb bandwidth of ~20 nm, Fig 5.3(A).

For calibration of an astrophysical spectrograph, it is not strictly necessary that the absolute frequency of each astro-comb line to be known before the astro-comb light is sent to the spectrograph. The astro-comb spectrum as measured on the spectrograph can be compared to the spectrum from an iodine cell or a thorium argon lamp, the emission lines of which are well tabulated and known to better than 1 GHz. Once one line of the filtered astro-comb is identified by using the thorium argon spectrum, all of the other lines in that spectrograph order can be identified and the full accuracy of each individual astro-comb line can be exercised. In our previous NIR (near infrared) astro-comb studies [3], a single fiducial reference laser was used as a frequency marker to identify the frequency of all astro-comb lines recorded by the spectrograph. However, because the frequency difference between spectrograph orders is not constant, and for some orders the dispersed spectrum extends beyond the collection area of the CCD, the loss of information between orders can prevent indexing of astro-comb lines from one order to the

next. Thus in general a fiducial wavelength marker is required for each order of the spectrograph, which an iodine cell or thorium argon lamp can easily provide.

5.5 Source comb and Fabry-Perot cavity alignment and stabilization

Initially, alignment of the comb lines from the source comb with the transmission resonances of the Fabry-Perot cavity filter is achieved by maximizing the transmission of the source comb through slow change of the filter cavity length. Once the cavity is set to the nominally correct length, the cavity length is modulated by ~3 pm at a rate of 100 kHz, causing modulation of the power transmission of the cavity. Demodulating the detected transmission using a lock in amplifier, one can use the resulting signal to control the length of the cavity with a second piezo mounted mirror. Two piezos are used so that one of the piezos can be optimized for generating a high frequency modulation allowing a higher feedback bandwidth. The second piezo can then be of slightly larger physical size enabling larger deflection and thus correction of larger amplitude cavity length errors at the cost of much larger piezo capacitance and longer response time.

A more mathematical description is warranted to allow consideration of the effects of dispersion, mirror reflectivity and repetition rate multiplication factor. The optical components of the frequency comb are described by

$$f_n = f_{CEO} + nf_R \tag{5.3}$$

with emphasis on the fact that each mode of the comb is separated equally in frequency by f_R. In the final astro-comb system, both f_R and f_{CEO} will be stabilized to GPS disciplined oscillators, the values of f_{CEO} and f_R can be assumed as absolutes. The Fabry-Perot cavity has transmission fringes which occur at frequencies corresponding to

$$\phi = 2\pi\frac{L}{\lambda} = L\frac{\omega}{c} \tag{5.4}$$

allowing us to describe the transmission spectrum of the Fabry-Perot cavity using the familiar Airy function

$$T = \frac{1}{1 + F \sin^2\left(\frac{\phi}{2}\right)} \tag{5.5}$$

$$F = \frac{4R}{(1-R)^2} \tag{5.6}$$

where F is the coefficient of finesse and R the power reflectivity of the mirrors, assuming equal reflectivity of both mirrors. In the current experiment, the bandwidth of the input spectrum from the doubling stage is less than half the reflectivity bandwidth of the current mirrors, so it is reasonable to assume constant reflectivity across the band of interest. The dispersion due reflection and especially round trip dispersion due to air cannot be ignored. To account for phase error in the round trip phase of the cavity, the effects of mirror reflections and air dispersion will considered as additive errors.

$$\phi = L\frac{\omega}{c} + \delta\phi \tag{5.7}$$

Phase error due to air can be straightforwardly determined from the refractive index of air, n_a, as

$$\begin{aligned} \delta\phi_a &= \phi_a - \frac{\partial\phi_a}{\partial\omega_0}(\omega - \omega_0) \\ \delta\phi_a &= L\frac{(\omega-\omega_0)}{c} - \frac{L}{c}\left(-\frac{\partial\lambda}{\partial\omega_0}\frac{\partial n_a}{\partial\lambda}(\omega-\omega_0) + n_a\right)(\omega-\omega_0) \end{aligned} \tag{5.8}$$

Phase error due to reflections from the mirrors used to construct the filter cavity must be determined by measuring the group delay on reflection from the mirror using a white light interferometer [104]. The resulting phase error is determined up to an unknown constant by integration of the measured group delay.

$$2\pi\int\frac{\partial\phi}{d\omega}df \tag{5.9}$$

Since the unknown constant merely changes the length of the cavity, this constant can be set to zero with no consequence. For the mirrors used here, the dispersion from reflection is ~1/10 of that caused by air, and can be ignored for the discussion here.

The dither lock scheme relies on coherent detection of the modulated reflection signal, *E(t)*, from the filter cavity to determine the alignment of the frequency comb lines and Fabry-Perot cavity, figure

5.2. The length of the filter cavity is modulated by applying a sinusoidal voltage signal, *m(t)*, at a frequency of f_m to a piezo on which one of the cavity mirrors is mounted.

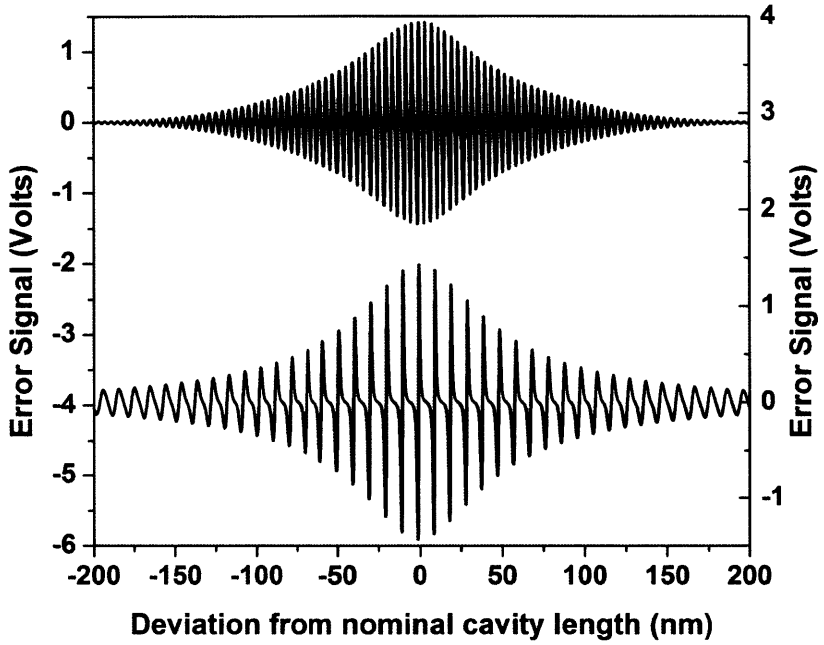

Figure 5.5 – Above is plotted the error signal for a nominal cavity length of 2.9 mm (upper) and 7.1 mm (lower) +/- 200 nm, corresponding to 51 and 21 GHz filter cavities both with a finesse of 312 (R=99%). The system is locked to one of the steep zero crossings. Note the small difference in locking fringe amplitude for adjacent fringes for both cavity configurations.

The cavity reflection signal *E(t)* is mixed with the original modulation signal and low pass filtered to recover the phase and amplitude information.

$$e(t) = \left[E(t)m(t)\right] \otimes \left\{h_{LPF}(f)\right\} \tag{5.10}$$

An analytic description of the resulting signal can be easily constructed from (5.10), however it is of little instructive value. A more intuitive description can be made if the comb and cavity transmission fringe are already well aligned such that the cavity transmission function can be approximates as a parabola. In the parabolic approximation the modulated reflection signal can be described as

$$E(t) \approx R_{\min} + K\delta L \sin\left(2\pi f_m t + \phi(\delta L)\right) \tag{5.11}$$

where $\delta L = L\delta f / f$ is the length misalignment of the Fabry-Perot cavity. Recognizing that the Fourier transform of Eq. (5.11) merely returns the phase and amplitude at the modulation frequency, the

calculation of the expected error signal in Eq.(5.10) can be simplified. Rather than evaluating expression (5.10) the difference in reflection for the two extremes of cavity length modulation for a given alignment condition to determine the error signal can be found as

$$E(L) = \int T(f)\big|_{L=L+\delta L}\, df - \int T(f)\big|_{L=L-\delta L}\, df \qquad (5.12)$$

Evaluating *E(L)* considering the conditions of the astro comb constructed here for two different repetition rate multiplication factors results in Fig. 5.5.

Notice that the error signal has more than one zero crossing. Each locking fringe is generated when central transmission fringe moves from one source comb line to the next, Fig. 5.7, due to a change in filter cavity length. When the filter cavity length is an integer multiple of the source comb cavity, all of the filter cavity transmission peaks line up exactly with the source comb lines. When the filter cavity length

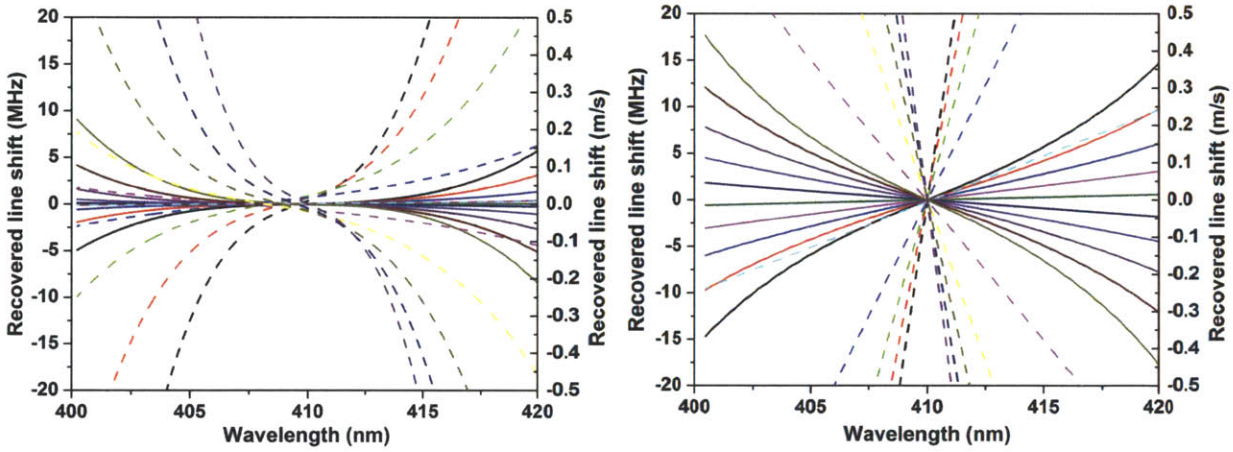

Figure 5.6 – Plots of the recovered astro comb center error for the central 10 lock point described in the previous figure assuming finesse of 312 (R=99%), for both 21 and 51 GHz, left and right respectively. The line center error occurs due to the spectrograph measuring each astro comb line as a power weighted sum of the main astro comb line and the two suppressed first side modes, Fig. 5.1. Solid lines are read from the left axis of each graph and dotted lines are read from the right. While both cavities are capable of precisions better than current calibrators, only the 21 GHz line spacing allows the central 3 fringes to have recovered shifts less than 50 cm/s over the entire astro-comb spectrum.

is in error by an amount required for the central transmission fringe to shift over by one source comb line, the other transmission fringes are shifted slightly off center depending on what side of the spectrum they are located and in which direction the cavity length is in error. The net result is a reduction in the

amplitude of the error signal, *E(t)* resulting in the reduction of the fringe amplitude reported in a sweep of the cavity length by *E(L)* in Fig. 5.5. As discussed in Fig. 5.1 at the beginning of this chapter, misalignment of source comb lines also causes a shift in the recovered astro-comb line center as seen by the spectrograph. Figure 5.6 plots the effect of source comb to filter cavity misalignment for the case of a 21 GHz and a 51 GHz astro-comb, highlighting the need for increased locking fringe discrimination.

5.5.1 Fringe discrimination

As shown in the previous section, the dither locking scheme only reproduces the accuracy of the source comb for one of the available locking fringes. The long term precision of the source comb is available when locking to any of the fringes, but to use the astro-comb to determine the drift of fundamental constants, the astro-comb must retain the accuracy of the underlying frequency comb. However, there will always be a finite optical bandwidth where the astro-comb faithfully maintains the accuracy of the source comb due to filter cavity dispersion. In the two cases from the previous section, the amplitude of each fringe was within 10% of the adjacent fringe, making experimental determination of the central locking fringe difficult. Selection of the correct fringe could be made easier if the difference in locking fringe amplitude between the central fringe and the first adjacent fringe could be made larger than 50%.

For small modulation depths, comparison of the amplitude of locking fringes, can be achieved by comparing the derivative of the transmission function for each transmission fringe of the Fabry-Perot cavity for two different cavity lengths. Specifically, we are interested in the peak amplitude of the derivative of the transmission function

$$\frac{\partial T}{\partial \phi} = \frac{-2\cos(\phi)\sin(\phi)F}{\left[1+F\sin(\phi)^2\right]^2} \tag{5.13}$$

with $\phi = \pi \frac{\Delta f}{f_a}$, where Δf is the local misalignment of a source comb and its transmission fringe. The peak of this function occurs at offset frequencies which satisfy

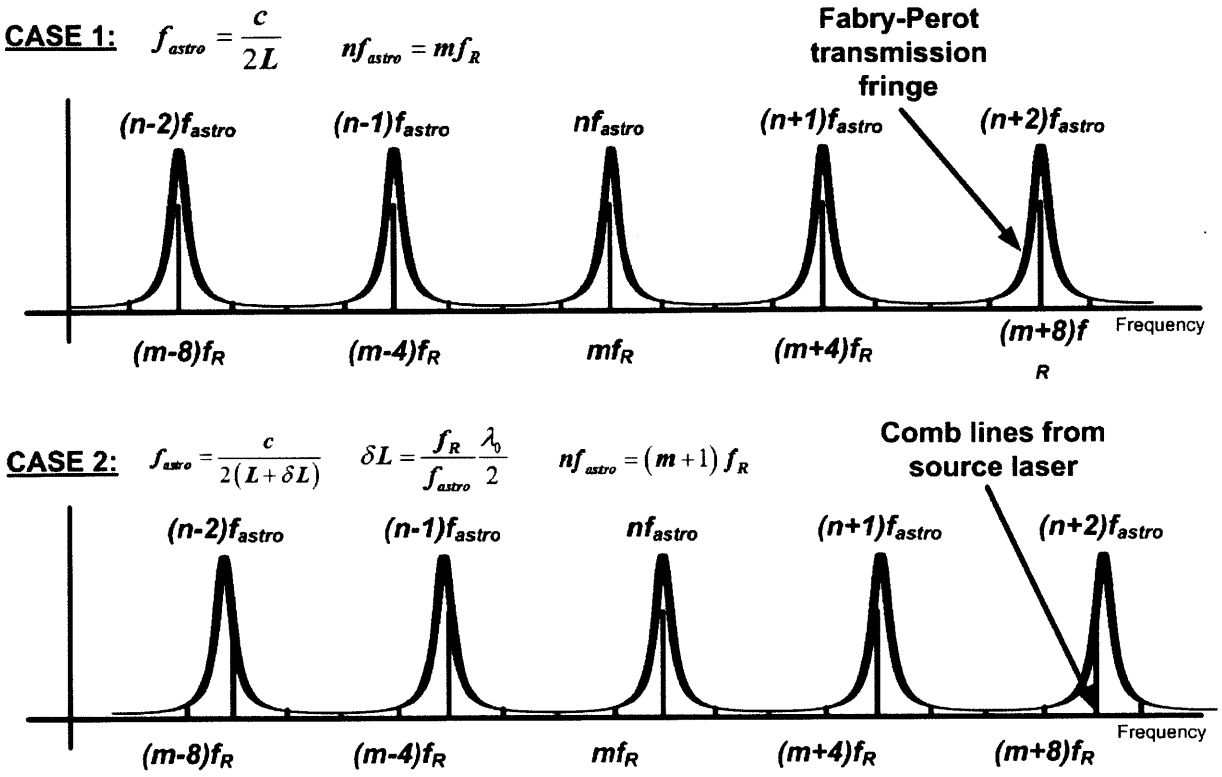

Figure 5.7 -- Case 1 demonstrates the ideal case where the frequency spacing of the Fabry-Perot transmission fringes are an integer multiple of the source comb repetition rate. In this alignment condition the dither lock uses the central locking fringe (Fig. 5.5), and the astro comb lines are recovered by the low resolution spectrograph at the exact locations of the source comb lines. In case 2, the Fabry Perot cavity length has been increased slightly, causing a systematic misalignment of the source comb lines from the transmission fringes. This misalignment has three results: the dither lock uses the first fringe adjacent to the central fringe, the recovered astro comb lines are all shifted towards the central fringe and the overall transmission is reduced.

$$\frac{\partial^2 T}{\partial \phi^2} = \frac{2F\left[1+F\sin(\phi)^2\right]\left(4F\cos(\phi)^2\sin(\phi)^2 - \left[1+F\sin(\phi)^2\right]\left[-\sin(\phi)^2+\cos(\phi)^2\right]\right)}{\left[1+F\sin(\phi)^2\right]^4} = 0 \qquad (5.14)$$

which can be shown to occur for values of $\phi_{1/2}$ which satisfy

$$\frac{1}{F}\left[\cot(\phi_{1/2})^2 - \tan(\phi_{1/2})^2\right] - \tan(\phi_{1/2})^2 = 3 \qquad (5.15)$$

Unfortunately, $\phi_{1/2}$ must be determined numerically, although given the narrow bound over which (5.15) function has a meaningful value, $\phi = 0 \rightarrow \frac{\pi}{2}$ determination of the peak value is fast.

The reduction in locking fringe amplitude occurs due to a systematic misalignment of the FP cavity transmission fringes with the source comb line due to the length of the filter cavity not being an

exact integer multiple of the source comb cavity length, Fig. 5.7. The length mismatch necessary to generate each additional locking fringe can be recovered by realizing that each locking fringe occurs when the central transmission fringe has moved to the adjacent source comb line

$$\frac{\delta L}{L}=\frac{\delta f}{f}\Rightarrow \delta L = L\frac{\delta f}{f}=\frac{c}{2f_a}\frac{f_R}{f_0}=\frac{f_R}{f_a}\frac{\lambda_0}{2} \tag{5.16}$$

with λ_0 the central wavelength of the spectrum and f_R the source comb repetition rate, and f_a as the astro comb line spacing. From the discussion above, each transmission fringe will be shifted from perfect alignment with the source comb by an amount described by

$$f_e = f_a - f_a^{'} = \frac{c}{2L}-\frac{c}{2\left(L+\frac{f_R\lambda_0}{f_a 2}\right)} \tag{5.17}$$

with each transmission fringe shifted by an additional increment of f'_e which is the free spectral range of the filter cavity when the central fringe of the transmission spectrum has been shifted to the adjacent source comb line, Fig. 5.7. Finally, the expression to evaluate is

$$\frac{\sum_{n=0}^{N_L}\left.\frac{\partial T}{\partial \Delta f}\right|_{\Delta f=\frac{\phi_{1/2}}{\pi}f_a}}{\sum_{n=0}^{N_L}\left.\frac{\partial T}{\partial \Delta f}\right|_{\Delta f=\frac{\phi_{1/2}}{\pi}f_a+f_e}} \tag{5.18}$$

where the summation is over half of the symmetric astro-comb spectrum, $N_L=\nu_{1/2}/f_a$.

A useful question related to the design of an astro-comb system is what mirror reflectivity is needed to achieve a 50% locking fringe discrimination, given that there exists a useful optical bandwidth of about 10 nm. Figure 5.8 plots predictions by both Eq. (5.18) and Eq.(5.12) for such an operating point, revealing that reflectivity of ~99.79% should be sufficient to achieve a finesse of 1500.

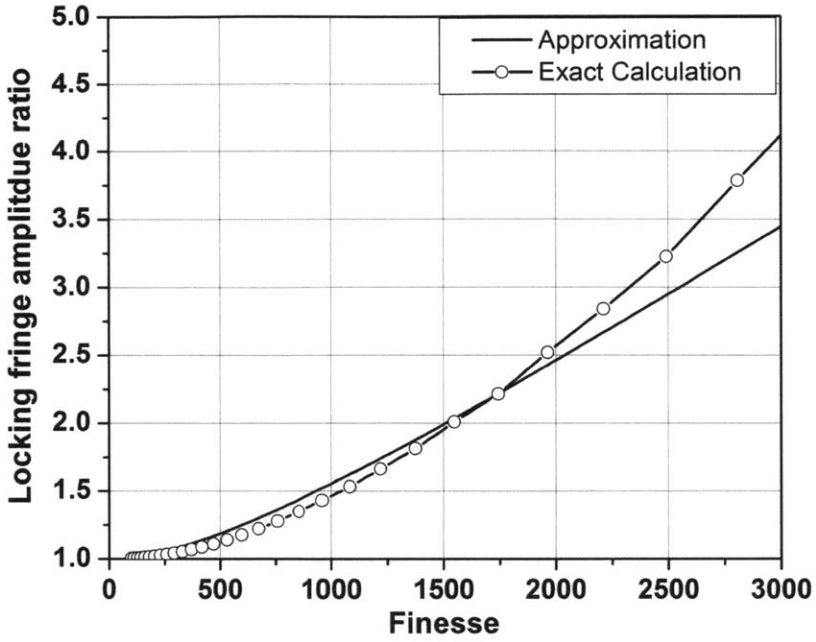

Figure 5.8 – Plot of the result from Eq.(5.18) and Eq.(5.12), to determine the cavity finesse necessary to achieve 50% difference in locking fringe amplitude for a 21 GHz filter cavity and 1 GHz source comb. The optical spectrum in both cases is assumed to be a 10 nm FWHM Gaussian shaped spectrum centered at 410 nm.

The comparison of Eq. (5.18) and Eq.(5.12) plotted in Fig. 5.8 shows good agreement for values of finesse below 2000, although the two curves diverge for higher values. As would be expected, much higher values of finesse are necessary to generate a 51 GHz astro-comb with a similar level of locking fringe discrimination as evidenced by the difference in width of the envelope functions in Fig. 5.5. The divergence between the approximation and the exact calculation is likely due to the fact that the source comb spectrum and Fabry-Perot cavity transmission fringe spectra don't perform a simple convolution. As shown in Fig. 5.7 above, the frequency shift of the Fabry-Perot's transmission fringes occurs because the frequency spacing between the fringes increases, rather than the entire transmission spectrum moving as a whole unit. In Eq.(5.18), two lengths were chosen at which to evaluate the cavity's transmission derivative, and do not account for the phase difference between the error signal generated by each astro-comb line. Despite this approximation, calculation of the approximation takes ~1/3 the time of the full computation.

The best solution for increasing the discrimination is to increase the bandwidth of the astro-comb spectrum. A new type of chirped mirror which was recently introduced [102] should allow filtering of

>100 nm of bandwidth at 500 nm and more than 200 nm at 1 μm. Dispersion due to air will become a serious limitation in these cases, even though it can be partially compensated in the design of the chirped mirrors. The ultimate solution is to put the filter cavity in a very mild vacuum (100-10 Torr) which would reduce the dispersion contribution by a factor of 10-100.

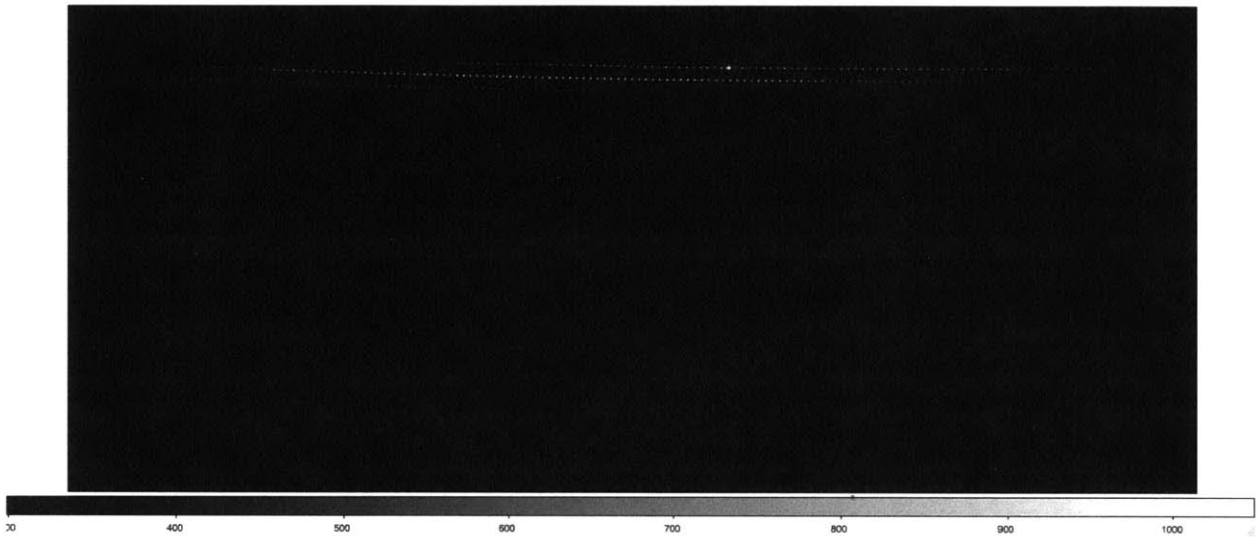

Figure 5.9 – Raw spectrograph CCD output after exposure to the astro-comb spectrum for 30 sec. The spectrograph reports optical power at wavelengths increasing from 390 nm to 910 nm from the upper left hand corner of the CCD to the lower right hand corner. See the text in section 5.6 for a description of the spectrograph functionality. The faint dotted bands in the upper portion of the figure are the individual astro-comb lines. The strong "astro-comb" line in the upper most band is a diode reference laser.

5.6. Astro-comb system characterization

A second astro-comb system nearly identical to the one described above has been installed at the Fred Lawrence Whipple Observatory (FLWO). Using a Menlo Systems 1 GHz octave spanning Ti:Sapphire laser as the source comb source as well as a BBO crystal, Fabry-Perot filter cavity, and filter cavity stabilization scheme identical to that described above, an average output power from the astro-comb of 10-30 μW (~10-30 nW per astro-comb line) is generally possible with a line spacing of 51 GHz. The TRES spectrograph [105] has a resolving power of $R=\lambda/\delta\lambda$=40,000 and spectral coverage from 390-900 nm. A 100 um multimode step-indexed fiber couples light from the calibration system where astro-comb light is injected to the spectrograph optical bench to where the spectrum is dispersed by an echelle grating and a prism to produce a 2-dimensional spectrum consisting of 51 orders of approximately 10 nm each,

figure 5.9. The dispersed light is then re-imaged onto a two dimensional CCD array with a resolution of ~0.01 nm, sampled by ~6 pixels in the dispersion direction. The CCD (E2V 42-90) is read out with added noise of less than 3 counts per pixel. Spectra are arranged as 1 dimensional data through the use of a halogen flat-fielding lamp which maps the spectrograph orders and compensates for pixel to pixel gain variations. Approximately six pixels in the cross-dispersion direction orthogonal to the grating dispersion direction contained counts from each order which are added together to produce one dimensional spectra. In the data presented in Fig. 5.10, the wavelength calibration was provided by a standard thorium argon calibration lamp also attached to the spectrograph calibration system. For exposure times compatible with the spectrograph control software (~30 sec), the output of the astro-comb was attenuated by 20 dB to avoid saturating the CCD.

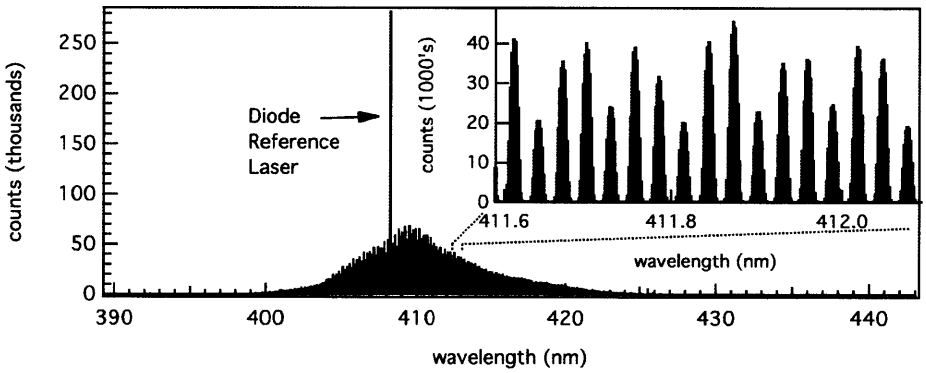

Figure 5.10 -- Extracted one dimensional spectrum of full astro-comb spectrum. The FWHM of the spectrum is approximately 10 nm, with approximately 50,000 peak counts in 10 seconds on the spectrograph. Inset: example of filtered comb lines with mode spacing of 51 GHz. The diode reference laser is used for characterization of the filter cavity transmission profile described in the text.

To achieve ~10 cm/s precision required for detection and characterization of Earth-like exoplanets over several year observation times, an *in-situ* technique may be used to characterize the cavity filter [100] and determine the apparent shift in the center of gravity of each astro-comb line from its nominal position caused by cavity dispersion and transmission resonance asymmetry and thus recover accurate astro-comb calibrations. Briefly, the scanned cavity technique uses a diode laser phase locked to the stabilized source comb to which the cavity filter is then locked using the Pound-Drever-Hall technique. After initially aligning the comb lines from the source comb and the transmission resonances of the cavity filter, the

offset frequency between the diode laser and frequency comb is changed in discrete steps and the spectrum transmitted through the cavity is recorded. Broadband characterization of an astro-comb system is necessary to ensure the astro-comb spectrum is fully understood prior to its use as a calibrator.

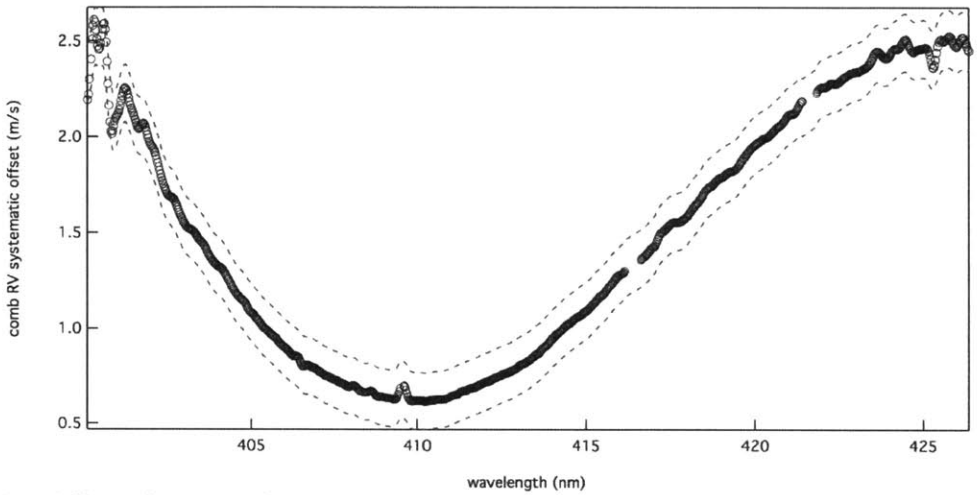

Figure 5.11 – Offset of recovered astro-comb line center caused by misalignment of filter cavity transmission maximum and the source comb lines as measured by the TRES spectrograph (black circles). Error bars at +/-15 cm/s on the recovered offset correspond to the uncertainty of the laser diode frequency used to lock the filter cavity and astro-comb (blue dotted lines). Breaks in the data set at 417 nm and again at 422 nm correspond to transitions between spectrograph orders as recovered from the CCD. The glitch at 408 nm is caused by amplitude to phase conversion by slight saturation of the CCD by the laser diode. Increased fluctuation in the trace above 424 nm and below 402 nm is due to the reduced signal to noise ratio at the edges of the astro-comb spectrum. The offset of recovered astro-comb lines has been low pass filtered to remove oscillations caused by mild etalon effects from the mirror substrates, see text above.

The scanned cavity calibration technique has been employed with the system installed at the FLWO, Fig. 5.11. From the data generated from the scanned cavity measurement data, good agreement is found between the measured group delay dispersion (GDD) and that expected from the mirrors, Fig. 5.3(B), along with few mRad oscillations in the recovered offset due to weak etalon effects between the mirror substrates. Because the etalon effect can be straightforwardly circumvented by using wedged substrates for the cavity filter mirrors, the offset data in Fig. 5.11 has been low pass filtered. A four point binomial filter with a cut-off frequency of 0.1 nm^{-1} was chosen for removal of the high frequency oscillations to reveal the true potential of the system. Incorporation of the calibration data into astronomical observations will also require a robust model of the cavity transmission asymmetry, which was not accounted for in Fig. 5.11, as well as the line to line amplitude variation of the source comb.

Complete analysis of the wavelength to pixel position mapping is a very complex process. A robust model of propagation from the spectrograph fiber inlet to the CCD must be constructed. Construction of the propagation model is in addition to reduction of data from each CCD exposure to one-dimensional data from the original two-dimensional format shown in figure 5.8. At several megabytes per file, this is not a trivial process, though preliminary results from the data reduction are promising.

Plotted in Fig 5.12 are both the average change in radial velocity of the astro-comb spectrum as reported by the spectrograph and the standard deviation. Since apparent radial velocity is the quantity which will be used to eventually find extra-solar planets, it is natural to use it also as the basis for determining the precision of calibration provided by the astro-comb. The upper trace in Fig. 5.12 is generated by comparison of sequential exposures of the astro-comb spectrum, specifically determination of the locations of each comb line in the astro-comb spectrum on the CCD by fitting each peak with a number of Hermite Gaussian functions to determine the peak center. Use of such a high order fit is warranted due to the chromatic aberrations in the spectrographs point spread function. The locations are determined first in terms of their pixel location on the CCD and then in terms of a standard pixel to CCD pixel mapping provided by a Thorium Argon lamp spectrum. Once the astro-comb system has been qualified, the pixel to wavelength mapping will be provided solely by the astro-comb, but for qualification purposes, using a single mapping for all of the exposures allows determination of the movement of each peak in terms of apparent radial velocity. Changes in the peak locations are mapped to an apparent radial velocity over the entire astro-comb spectrum using

$$\delta v = \frac{c}{N}\sum_{n}^{N}\frac{\delta\lambda_n}{\lambda_n} \qquad (5.19)$$

where $\delta\lambda$ is the fractional change in comb line location, λ is the wavelength of each comb line, N is the number of comb lines in the recovered astro comb spectrum, and c is the speed of light. Since the astro-comb spectrum is stabilized to a rubidium reference clock, which provides a level of stability for exceeding that necessary for finding Earth like planets around Sun like stars, the drifts reported in Fig. 5.12 are solely due to drifts in the spectrograph. Typically these drifts are due to temperature and

pressure changes in the spectrograph which cannot be corrected through measurement of temperatures and pressures inside the spectrograph. Based on comparisons with barometric pressure data for the

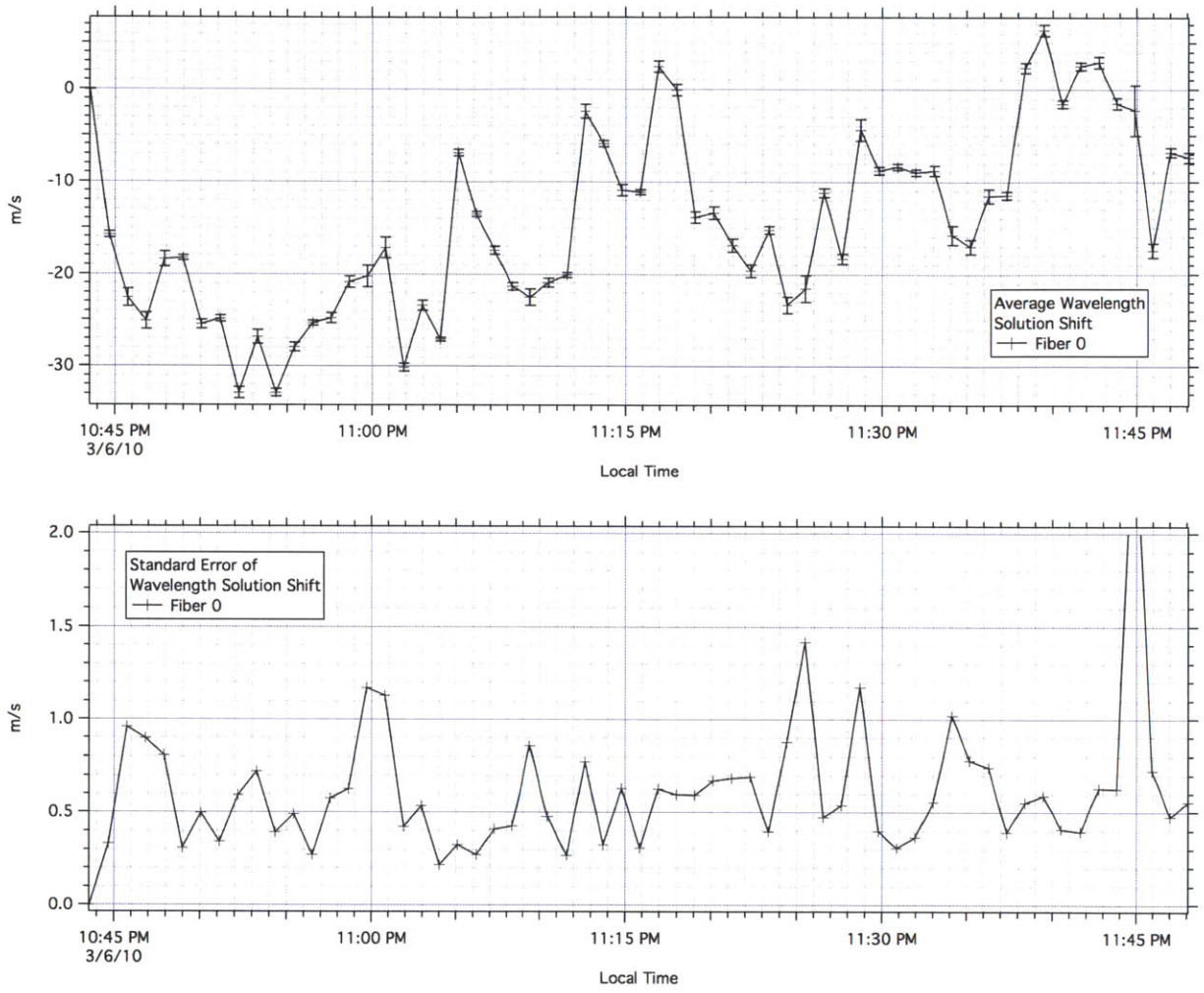

Figure 5.12 – The upper plot reports the average effective radial velocity reported by the TRES spectrograph by exposure to the astro-comb spectrum. The lower bound for calibration precision can be made using (5.2) which reports the standard deviation of the reported radial velocity. The first astro-comb spectrum exposure is chosen as the reference for the comparison.

same time period, the large variations seen in the effective radial velocity are most likely due to pressure variations in the spectrograph enclosure which has no pressure stabilization.

In terms of spectrograph calibration, the standard deviation reported by the lower trace of Fig. 5.12 is a more important indicator of the performance of the astro-comb system. Application of the changes in peak locations reported by the astro comb spectrum to the spectrograph CCD pixel to

wavelength mapping will be in error by an amount indicated by the plot of standard deviation if only the average value of apparent radial velocity is used for correction. For comparison, thorium argon lamps provide approximately 1 m/s calibration precision, while Fig. 5.12 reports nearly 0.6 m/s calibration precision. In comparison with the unstabilized case, reported in the upper trace of figure 5.12, the lower trace in the same figure represents an improvement in calibration precision of approximately 50.

5.7. Conclusion and future work

Development of visible wavelength frequency combs with wide mode spacing will have broad applicability as high-accuracy and high-stability wavelength calibrators for astrophysical spectrographs. The absence of broadband laser materials in the 400-600 nm range leaves nonlinear frequency conversion as the means to realize such wavelength calibrators. A frequency-doubled Ti:Sapphire laser frequency comb was used to provide a tunable visible wavelength astro-comb operating near 420 nm, with a spectral line spacing variable over tens of GHz (up to 51 GHz in the present demonstration), a usable spectrum of 15 nm, and an output power of up to 20 nW per line. Systematic shifts in the resulting astro-comb will not limit the final calibration accuracy [100]. Long term operation of astro combs at telescope installations will also require extremely robust cavity to comb alignment methods. The dither locking scheme outlined in detail above is the most robust method for maintaining this alignment, although careful integration of the locking system with the overall comb line filtering design is necessary.

Since the wavelength region best suited to exoplanet discovery using the radial velocity method is dependent on many factors, the most broadband astro-comb calibrator design will likely receive the most use. Further, since calibration precision and radial velocity shift sensitivity scale with the square root of the calibration source bandwidth, increasing the nonlinear conversion bandwidth is one of the most important upcoming tasks. To generate an optical spectrum useful for spectrograph calibration in the visible band exceeding 200 nm can only be achieved currently using an unreferenced etalon [106]. The ideal solution for using a frequency comb as a calibrator seems to be something similar to the system constructed by Quinlan et al [49]. In essence, a high power narrowband frequency comb is filtered using

two Fabry-Perot filters to achieve >60 dB side mode suppression prior to amplification and broadening in a photonic crystal fiber. Using two filter cavities is attractive because the side mode suppression prior to spectral broadening can be very high. The disadvantage of the approach is the increased system complexity and the possibility of uneven power distribution of power in the spectral broadening process. A recent publication by Chang et al [107] suggested that slight phase errors between the two sidebands of the main transmitted comb lines would be transformed into a much larger power asymmetry during the broadening process. Sensitivity to slight side mode asymmetries in the optical spectrum used for spectral broadening was noted in the experiments by Quinlan, et al, though currently this remains the most promising approach.

THIS PAGE INTENTIONALLY LEFT BLANK

Chapter 6

Optical measurement of mode-locked laser pulse train timing jitter

6.1 Introduction

It has been known for some time that the steady state pulse propagating inside a mode-locked laser is the optical equivalent of a mechanical flywheel. The ultrashort pulse duration, approaching a few optical cycles, drastically reduces high frequency pulse position fluctuations caused by unavoidable spontaneous emission noise resulting in emitted pulse trains with unprecedented homogeneity of their pulse-to-pulse time spacing. Here we show that optical pulse trains from Kerr lens mode-locked Ti:Sapphire lasers exhibit the lowest high frequency phase noise and integrated timing jitter of any oscillator known today. By measuring the phase error between phase locked optical pulse trains from two identical 10-fs Ti:Sapphire lasers, we demonstrate that the pulse train phase noise of each individual laser is below -203 dBc/Hz for offset frequencies greater than 1 MHz. This constitutes the lowest high frequency phase noise ever recorded and results in an integrated timing error between two tightly synchronized Ti:Sapphire lasers of less than 13 attoseconds, measured over the entire Nyquist bandwidth. The dominant noise source is conversion of pump laser relative intensity noise (RIN) into phase noise, suggesting that the currently observed phase noise can be further reduced by improvements in pump laser technology. Such a highly uniform train of pulses from mode-locked lasers enables new science and technology at unprecedented levels, such as synchronization of pump-probe experiments which measure evolution

dynamics of chemical [108,109], biological and atomic processes [17,110] evolving on femtosecond and attosecond timescales. The ultra low timing jitter of such pulse trains also allows photonic analog to digital conversion of mid IR waveforms with up to 6 bits of resolution [111]. Further parameter optimization of the laser dynamics can be used to reduce timing jitter originating from the Gordon-Haus effect [112] and self-steepening [113]. With those improvements the integrated timing error from standard Kerr lens mode-locked Ti:Sapphire lasers may be reduced to the sub-attosecond level.

To understand the impact of the low phase noise measurement result and how it was accomplished, this chapter will begin with a general discussion of mode-locked laser pulse train stability as compared to other highly stable oscillators, as well as two of the main limitations to achieving zero phase noise. Also included is a review and analysis of the non-linear optical processes necessary for balanced optical cross correlation and as well as lower limits on phase noise detection capability. A description of the measurement setup used for this experiment follows with analysis of the results and possible improvements for the future.

6.2 Low phase noise oscillators

The advent of femtosecond laser frequency combs [114] has revolutionized frequency metrology in the last 10 years and with it a wide variety of disciplines ranging from astrophysics and the search for exoplanets [3,4,98] to precision spectroscopy [62,115] and most recently attosecond science [116,117]. Optical atomic clocks have also been realized with fractional frequency instabilities below 10^{-16} in only a few seconds of averaging [1,64]. The existence of a well defined frequency comb is due to the pristine temporal periodicity of the pulse envelope of femtosecond laser pulse trains and a well defined carrier-phase evolution from pulse to pulse, however the latter is not important for this work. As with any oscillator the translation invariance of the steady state oscillation with respect to pulse position or carrier phase leads to a Brownian motion like diffusion of the pulse position and phase. It can be shown [118] that the fundamental spontaneous emission noise of the gain medium compensating for output coupling and internal losses of a Kerr Lens mode-locked laser generating soliton like pulses of under 10 fs duration

is given by

$$\frac{\mathrm{d}}{\mathrm{dt}}\left\langle t^2\right\rangle = \frac{\pi^2}{6}\tau^2\frac{h\nu}{E_P\tau_c} \tag{6.1}$$

where Δt is the offset of the pulses from their nominal time locations which are equal to multiples of the roundtrip time of the pulses in the cavity, τ the full width at half maximum pulse width divided by 1.76, E_P the intracavity pulse energy, τ_c the cavity decay time and $h\nu$ the quantum energy of the laser photons. The phase noise of a harmonic ω of the microwave signal generated by detection of the pulse stream is given by $\Delta\phi=\omega\Delta t$. The lowest phase noise oscillators demonstrated to date have been microwave systems based on large (~5 cm), precisely grown, sapphire crystals operating at 10 GHz to take advantage of the anomalously low absorption of electromagnetic energy in sapphire at that frequency [20]. As a reference for the current state of the art, a single sideband (SSB) phase noise of -190 dBc at 1 kHz offset is predicted for the next generation of cryogenically cooled sapphire loaded microwave cavity oscillators [119].

The rate at which mode-locked lasers emit pulses is related to the inverse length of the optical cavity. As a result, phase noise in the emitted pulse train can be generated not only by spontaneous emission, but also by environmental perturbations of the cavity length including mirror vibrations, as well as slight laser cavity misalignments leading to intracavity power fluctuations. These power fluctuations, in addition to those caused by relative intensity noise from the pump laser, are transformed into phase noise through the self-steepening effect. The Gordon-Haus effect may also lead to increased timing jitter through center frequency fluctuations of the optical spectrum of the laser pulse that which are transformed into timing fluctuations via the intracavity dispersion. Extremely short pulse lasers may be able to minimize the contribution of Gordon-Haus jitter by completely filling the gain bandwidth of the Ti:Sapphire crystal, and careful choice of the laser operating point can minimize the contribution from self steepening. Assuming careful elimination of such noise sources and conversion mechanisms, spontaneous emission from the gain medium directly driving the pulse diffusion according to the discussion above will remain the only noise source resulting in a single-side band phase noise of a

microwave component of the photo-detected pulse train at frequency ω is,

$$L(f) = \omega^2 \frac{\pi^2}{12} \tau^2 \frac{h\nu}{E_p \tau_c (2\pi f)^2} \tag{6.2}$$

Where f is the offset frequency from line center.. Theoretical estimates of the phase noise of pulse trains from solid-state mode-locked lasers were predicted to be below -190 dBc for offset frequencies greater than 1 kHz assuming a harmonic at 10 GHz [21,120] but such low levels of phase noise have never been measured until this work.

6.3 Analysis of the balanced optical cross correlator performance with short pulses

Measurement of phase noise in optical pulse trains can be difficult if the optical pulse train has been converted to a radio frequency signal [121,122], independent of the challenge of making a low noise optical to microwave conversion [23,123]. RF domain techniques are limited by thermal noise in terminating resistors and the signal level available for input to the phase noise measurement system to a level of about -192 dBc with discriminator slopes of nearly 110 V/Rad [20,124]. Balanced optical cross correlation [125-127], Fig. 6.1, avoids the photodetection process, allowing direct measurement of the optical pulse train phase noise with phase noise discrimination slopes usually exceeding 1 kV/Rad. The optical cross correlator performs sum frequency generation (SFG) between orthogonally polarized pulses from the two femtosecond lasers with the efficiency of the up-conversion process dependent on the temporal overlap of the two pulses in a Beta Barium Borate (BBO) crystal. By aligning the extraordinary axis of the BBO crystal to a different input polarization in each arm and noting that the group velocity in the BBO crystal is different in each polarization axis, the two arms of the cross correlator are forced to require different initial time offsets between the orthogonally polarized pulses for optimal conversion, Fig. 6.1.

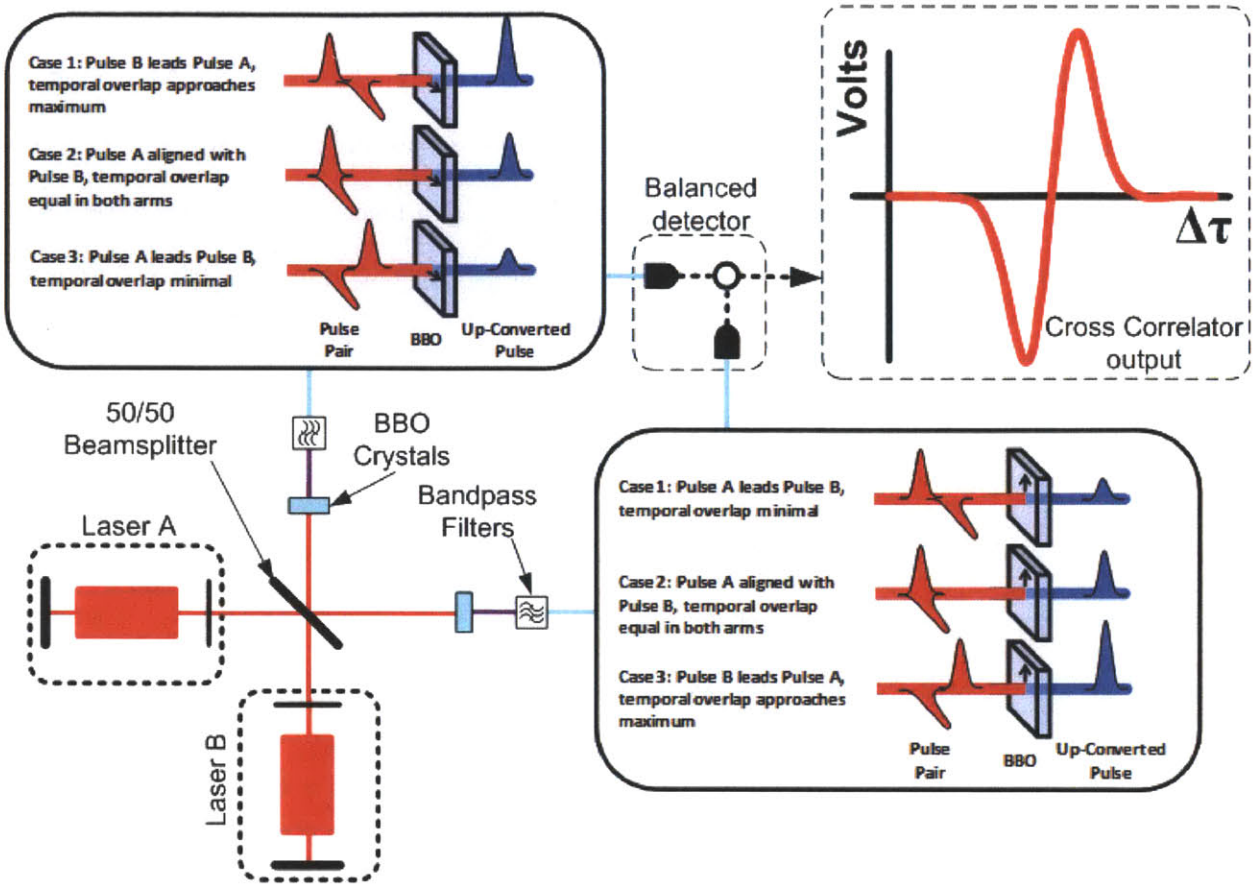

Figure 6.1 – General method for detecting time of arrival difference between optical pulses using Type-II sum frequency generation (SFG) as a cross correlation mechanism. Linearly polarized pulses from lasers A and B are cross polarized prior to combination at the beamsplitter. The pulses then travel to the two BBO crystals where, depending on the difference in the time of their arrival at the BBO crystal, $\Delta\tau$, proportionally more or less sum frequency generation will occur. Note that the orientation of the crystal axis (indicating the polarization which will experience increased index of refraction and lower group velocity) is different in each of the two arms. This difference forces the two arms of the cross correlator to require different initial time offsets for maximum SFG, generating the characteristic timing error detection signal in the upper right hand corner of the diagram.

Using the output of the cross correlator and balanced detector (Thorlabs PDB120A, modified for 36 kΩ transimpedance gain with Hammamatsu S5712 photodiodes) as the phase error discriminator in a phase locked loop, the voltage output of the balanced detector is measured when the loop is locked to determine the relative phase error between the two optical pulse trains. The measurement floor of balanced optical cross correlation is ideally set by shot noise of the incident pulse train converted into apparent phase error by the transimpedance amplifier and discriminator slope, however here the input current noise of the balanced detector limits the noise floor to -203 dBc/Hz.

While the mathematical basis for operation of the balanced optical cross correlator is described

in [127], the operating regime described in that work is one of a long pulse laser and a relatively short crystal where the effect of group velocity mismatch between the two pulses is small. As a result, the cross correlation performed in each BBO crystal is accounted for as static time offset in each arm, allowing the conversion to be evaluated by an overlap integral as a function of the time offset due to phase noise. In this work the pulse durations are much shorter than the time shift caused by the difference in group velocity of the two crystal axes. The group delay provided by the orthogonally oriented crystals is ~140 fs in total and pulses at the input to the crystal are no longer than 50 fs, such that it is no longer an appropriate approximation to take the cross correlation as a static time offset.

Because of the difference in operating regime, a separate analysis is warranted. The first portion of the following analysis will account for the temporal effects of the conversion process. The second portion of the analysis will account for the spatial effects of the conversion. Finally suggestions will be given for how best to optimize the conversion process for highest timing or phase error sensitivity.

6.3.1 Temporal conversion analysis

To begin, below are expressions for the three fields involved in sum frequency generation

$$E_1(z,t) = \frac{1}{2} A_1(z,t) \exp\left[i(k_1 z - \omega_1 t)\right] + c.c. \tag{6.3}$$

$$E_2(z,t) = \frac{1}{2} A_2(z,t) \exp\left[i(k_2 z - \omega_2 t)\right] + c.c. \tag{6.4}$$

$$E_3(z,t) = \frac{1}{2} A_3(z,t) \exp\left[i(k_3 z - \omega_3 t)\right] + c.c. \tag{6.5}$$

where A_i are the complex pulse amplitudes, k_i are the propagation vectors in the BBO crystal and ω_i are the center frequency of each pulse, with $\omega_3 = 2\omega_1 = 2\omega_2$. To have an efficient conversion process the BBO crystal should be cut for phase matched Type-II second harmonic generation (SHG) at the center wavelength of the Ti:Sapphire spectra, ensuring that the refractive index at the fundamental and second harmonic wavelength are equal, $k(\omega) = k(2\omega)$. By assuming perfect phase matching, the coupled wave equations can be written as

$$\frac{\partial A_1(z,t)}{\partial z} = -\frac{i\omega_1 d_{eff}}{cn_1} A_3(z,t) A_2^*(z,t) \tag{6.6}$$

$$\frac{\partial A_2^*(z,t)}{\partial z} = \frac{i\omega_2 d_{eff}}{cn_2} A_1(z,t) A_3^*(z,t) \tag{6.7}$$

$$\frac{\partial A_3(z,t)}{\partial z} = -\frac{i\omega_3 d_{eff}}{cn_3} A_1(z,t) A_2(z,t) \tag{6.8}$$

In the low conversion limit (<1%), the usual assumption is that the input fields are constant allowing elimination of the first two equations and ignoring any back conversion of the SHG field to the two input fields. To account for the different group velocity experienced in each polarization for the input pulses, as well as the bandwidth of the input pulses, the time variable is changed to, $t_{1,2} = t - z/v_{g1,2}$. For simplicity of analysis the pulse width from both lasers and the pulse energy will be assumed to be equal. To simplify notation in the following expressions, the difference in group velocity between the two input fields is

$$\left(\frac{1}{v_{g1}} - \frac{1}{v_{g2}}\right)^{-1} = \Delta v_g \tag{6.9}$$

where there is no account made for the difference between the group velocity of the two input fields and the output field because back conversion is ignored. Again for simplicity of the following analysis the amplitude of pulses from each laser are modeled as Gaussian functions, specifically

$$A_i(z,t) = a_i \exp\left(-\frac{\left(t-\frac{z}{v_g}\right)^2}{4T^2}\right) \tag{6.10}$$

with full width at half maximum pulse widths of $2\sqrt{\ln 2}T$ and amplitudes properly normalized to the pulse energy E_p by

$$a_i = \int \left|A_i(0,t)\right|^2 = \sqrt{\frac{E_p}{T}}\sqrt{\frac{2}{\pi}} \tag{6.11}$$

Rewriting Eq.(6.8) using the differenced group velocity the conversion for both arms of the cross correlator can be expressed as

$$\frac{\partial A_{3L}(z,t')}{\partial z} = -\frac{i\omega_3 d_{eff}}{cn_3} A_1\left(0, t - \frac{z}{\Delta v_g} + \Delta\tau\right) A_2\left(0, t + \frac{z}{\Delta v_g} - \Delta\tau\right) \quad (6.12)$$

$$\frac{\partial A_{3R}(z,t')}{\partial z} = -\frac{i\omega_3 d_{eff}}{cn_3} A_1\left(0, t + \frac{z}{\Delta v_g} + \Delta\tau\right) A_2\left(0, t - \frac{z}{\Delta v_g} - \Delta\tau\right) \quad (6.13)$$

where the time error between the pulses due to phase noise, $\Delta\tau$, has been explicitly included. Integrating with respect to z gives the instantaneous pulse power at the crystal output

$$P_{L,R}(z) = \left| \int_0^{L_c} \frac{\partial A_{3L,R}}{\partial z} dz \right|^2 \frac{n_3}{2\eta} A_{eff} \quad (6.14)$$

including the effective cross sectional area of the beam within the crystal as A_{eff}, refractive index of the crystal at the up converted wavelength, n_3 and the free space impedance η. Integrating again over the entire pulse duration gives the pulse energy of the converted pulse.

$$E_{p(2f)} = \int_{-\infty}^{\infty} P_{L,R} dt \quad (6.15)$$

Evaluating the second integral over a time window much longer than the duration of the two input pulses is reasonable because the detector response time is slow with respect to the duration of the pulse and will only measure the average power of the resulting converted pulse train. Appendix A.4.2 cautions against using the difference in timescales as an excuse for imprecise detector placement.

After passing through the BBO crystal, bandpass filters are used to remove the unconverted portion of the beams at the fundamental wavelength. The resulting power incident on each photodiode of the balanced detector for the left and right channels for a crystal of length L will be

$$P_L(\Delta\tau) = f_R \omega_{p3} = f_R \left\{ -erf\left[\frac{\Delta\tau}{\sqrt{2}T}\right] + erf\left[\frac{\Delta v_g \Delta\tau - L}{\sqrt{2}\Delta v_g T}\right] \right\}^2 \left(\frac{\Delta v_g E_p \omega_3 d_{eff}}{n_1 n_2 c}\right)^2 \frac{T\sqrt{2\pi}\eta}{A_{eff} n_3} \quad (6.16)$$

$$P_R(\Delta\tau) = f_R\omega_{p3} = f_R\left\{erf\left[\frac{\Delta\tau}{\sqrt{2}T}\right] - erf\left[\frac{\Delta v_g\Delta\tau + L}{\sqrt{2}\Delta v_g T}\right]\right\}^2\left(\frac{\Delta v_g E_p\omega_3 d_{eff}}{n_1 n_2 c}\right)^2\frac{T\sqrt{2\pi\eta}}{A_{eff}n_3} \quad (6.17)$$

The balanced photodetector will convert the incident optical power into currents and ultimately an output voltage proportional to the difference in photo-current similar to the inset in Fig. 6.1. The difference in powers is the phase error discriminator function used to phase lock the two pulse trains. The slope of the discriminator near $\Delta\tau=0$ and the time window over which there is a linear voltage to time or phase error relationship is the characteristic quantity of balanced optical cross correlation and is what allows such a highly sensitive measurement of the optical pulse train phase noise. In terms of the incident pulse energy, the discriminator slope is

$$\Gamma = \frac{\partial P}{\partial\Delta\tau} = 8\sqrt{2}\left(\frac{\Delta v_g\omega_3 d_{eff}}{c}\right)^2\frac{\eta E_{p1}E_{p2}f_R}{A_{eff}n_1n_2n_3}\left\{\begin{array}{l}\exp\left(\frac{-\Delta\tau^2}{2T^2}\right)\left[erf\left(\frac{\Delta v_g\Delta\tau + L_c}{\sqrt{2}\Delta v_g T}\right) - erf\left(\frac{\Delta v_g\Delta\tau - L_c}{\sqrt{2}\Delta v_g T}\right)\right] \\ +erf\left(\frac{\Delta\tau}{\sqrt{2}T}\right)\left[\exp\left(-\left(\frac{L_c + \Delta v_g\Delta\tau}{\sqrt{2}T\Delta v_g}\right)^2\right) - \exp\left(-\left(\frac{L_c - \Delta v_g\Delta\tau}{\sqrt{2}T\Delta v_g}\right)^2\right)\right] \\ +\exp\left(-\left(\frac{L_c - \Delta v_g\Delta\tau}{\sqrt{2}T\Delta v_g}\right)^2\right)erf\left(\frac{\Delta v_g\Delta\tau - L_c}{\sqrt{2}\Delta v_g T}\right) - \exp\left(-\left(\frac{L_c + \Delta v_g\Delta\tau}{\sqrt{2}T\Delta v_g}\right)^2\right)erf\left(\frac{\Delta v_g\Delta\tau + L_c}{\sqrt{2}\Delta v_g T}\right)\end{array}\right\} \quad (6.18)$$

Evaluating (6.18) at $\Delta\tau=0$ provides considerable clarity on how to best optimize the cross correlator

$$\Gamma = \frac{\partial P}{\partial\Delta\tau} = 16\left(\frac{\Delta v_g\omega_3 d_{eff}}{c}\right)^2\frac{\eta E_{p1}E_{p2}f_R}{A_{eff}n_1n_2n_3}erf\left(\frac{L_c}{\Delta v_g T}\right)\left[1 - \exp\left(-\left(\frac{L_c}{\Delta v_g T}\right)^2\right)\right] \quad (6.19)$$

The error function and exponential terms in (6.19) limit the benefit of using a non-linear crystal which is significantly longer than the interaction length of the two pulses, $\Delta v_g T$. The expression also indicates that there is no penalty for using a crystal which is longer than the interaction length, other than extra cost, and in fact a longer crystal appears to make full use of the available pulse energy.

6.3.2 Spatial conversion analysis

The previous analysis only considered the temporal walkoff or group velocity mismatch (GVM) of the two input pulses due to the difference in group velocity in the two principal axis of the BBO crystal. GVM takes account of the pulse bandwidth, changing the shape of the cross correlator output. Spatial

walkoff of the two input beams occurs inside the nonlinear crystal as well when the crystal axis is not aligned either with the input beams *k*-vector or in a plane normal to the input beams. If neither of these two conditions is satisfied (which is the definition of a non-critically phase matched crystal), the input beam polarized in the plane of the crystal axis, as well as the converted field will propagate away from one another and away from the second input field at a small angle to the input *k*-vector, which will result in a further reduction in conversion efficiency. Typical walkoff angles, α, are in the range of 100 mRad, with a value of 75 mRad between the two input fields for Type II SFG in BBO at 800 nm.

As before, due to the low conversion efficiency, only the walkoff between the two input fields will be considered. Beginning with the spatial distribution of the field amplitudes written as

$$E_1(x,y,z) = E_1 \frac{w_{01}}{w_1(z)} \exp\left(-\frac{x^2+y^2}{w_{01}^2}\right) \tag{6.20}$$

$$E_2(x,y,z) = E_2 \frac{w_{02}}{w_2(z)} \exp\left(-\frac{x^2+y^2}{w_{02}^2}\right) \tag{6.21}$$

where $w_{01,02}$ are the waists of the two input beams, and $w_{1,2}(z)$ are given by equation (2.30) in the propagation direction, z. Spatial walkoff will be modeled as a transverse motion of one of the beams, d_α, over a propagation distance z

$$d_\alpha = z\alpha \tag{6.22}$$

resulting in an efficiency factor γ over the entire crystal length. In reality, there must also be a reduction in the effective electric field strength, however, this reduction will be directly proportional to the walkoff angle and can be ignored. The evolution of the beam diameter due to diffraction will also be ignored in the following analysis because the confocal parameter, which defines the distance over which a beam will maintain at least half its peak intensity, will generally be much longer than the spatial walkoff distance. The spatial overlap of the two beams in the BBO crystal can be expressed as

$$\gamma = \frac{\iiint E_1 E_2 \exp\left(-\frac{x^2+y^2}{w_0^2}\right)\exp\left(-\frac{x^2+(y-z\alpha)^2}{w_0^2}\right)dxdydz}{\iiint E_1 E_2 \exp\left(-\frac{2(x^2+y^2)}{w_0^2}\right)dxdydz} \tag{6.23}$$

where equal size beam waists have been assumed. Evaluating (6.23) expression yields

$$\gamma = \sqrt{\frac{\pi}{2\alpha}}\frac{w_0}{z} erf\left[\sqrt{\frac{\alpha}{2}}\frac{z}{w_0}\right] \tag{6.24}$$

suggesting an effective length of $2\sqrt{2/\alpha}w_0$ equal to ~20 μm for a 6μm beam waist at the crystal input face. Equation (6.24) serves as an interaction strength factor in the product of the two fields in Eq. (6.12) and (6.13). Unfortunately, these new equations cannot be integrated, so (6.24) will be approximated as

$$\gamma \approx \exp\left(-\frac{\alpha z^2}{\pi^2 w_0^2}\right) \tag{6.25}$$

The resulting difference in converted power is accurate to within ~10% for crystal lengths not exceeding $4\sqrt{2/\alpha}w_0$, beyond which Eq. (6.25) will underestimate the overlap by as much as 75% depending on crystal length (see Figure 6.2).

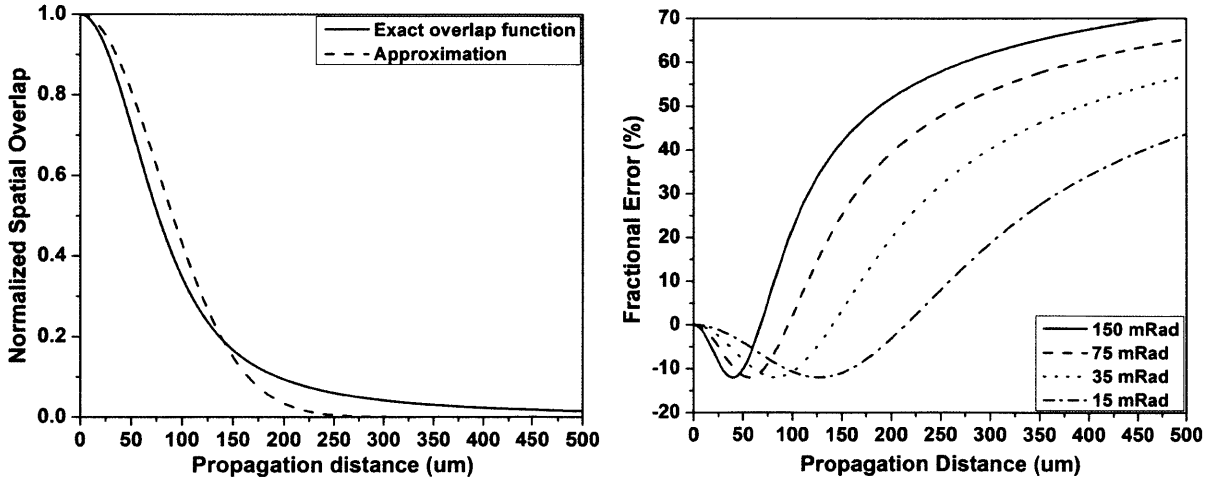

Figure 6.2 – Eq. (6.24) and (6.25) are drawn in the left plot for a beam waist of 6 μm and walk off angle of 15 mRad. After integrating Eq (6.24). and (6.25) with respect to z and squaring the result, the percentage difference between the exact overlap function and the approximation is plotted on the right for several different walk off angles. While the divergence of the error plot may indicate a poor approximation, note that as the error function diverges towards gross underestimation, the product of the two electric fields has been reduced by a factor of 10, resulting in a converted power reduction of ~100.

The output power from each channel of the cross correlator is now

$$P_L(\Delta\tau)=\psi\left\{-erf\left[\frac{\pi\Delta\tau w_0}{T\sqrt{4\alpha T^2\Delta v_g^2+2\pi^2 w_0^2}}\right]+erf\left[\frac{\pi^2\Delta v_g\Delta\tau w_0^2-L_c\left(2\alpha T^2\Delta v_g^2+\pi^2 w_0^2\right)}{\pi\Delta v_g T w_0\sqrt{4\alpha T^2\Delta v_g^2+2\pi^2 w_0^2}}\right]\right\}^2 \quad (6.26)$$

$$P_R(\Delta\tau)=\psi\left\{erf\left[\frac{\pi\Delta\tau w_0}{T\sqrt{4\alpha T^2\Delta v_g^2+2\pi^2 w_0^2}}\right]-erf\left[\frac{\pi^2\Delta v_g\Delta\tau w_0^2+L_c\left(2\alpha T^2\Delta v_g^2+\pi^2 w_0^2\right)}{\pi\Delta v_g T w_0\sqrt{4\alpha T^2\Delta v_g^2+2\pi^2 w_0^2}}\right]\right\}^2 \quad (6.27)$$

$$\psi=8Tf_r\pi^4\sqrt{\pi}\left(\frac{E_p d_{eff}}{n_1 n_2\lambda}\right)^2\frac{\eta}{n_3 A_{eff}}\frac{\Delta v_g^2 w_0^2}{2\alpha T^2\Delta v_g^2+\pi^2 w_0^2}\exp\left(-\frac{2\alpha\Delta\tau^2\Delta v_g^2}{2\alpha T^2\Delta v_g^2+\pi^2 w_0^2}\right) \quad (6.28)$$

with the peak slope of the cross correlator output now

$$\Gamma=\left.\frac{\partial(P_L-P_R)}{\partial\Delta\tau}\right|_{\Delta\tau=0}=-\theta\left[\left[-\frac{4A}{\sqrt{\pi}D}erf\left[\frac{-C}{E}\right]+\frac{4B}{\sqrt{\pi}E}\exp\left(-\frac{C^2}{E^2}\right)erf\left[\frac{-C}{E}\right]+\frac{4A}{\sqrt{\pi}D}erf\left[\frac{C}{E}\right]-\frac{4B}{\sqrt{\pi}E}\exp\left(-\frac{C^2}{E^2}\right)erf\left[\frac{C}{E}\right]\right]\right] \quad (6.29)$$

$$\begin{aligned}A&=\pi w_0\\ B&=\pi^2\Delta v_g w_0^2\\ C&=L_c\left(2\alpha T^2\Delta v_g^2+\pi^2 w_0^2\right)\\ D&=T\sqrt{4\alpha T^2\Delta v_g^2+2\pi^2 w_0^2}\\ E&=\pi T\Delta v_g w_0\sqrt{4\alpha T^2\Delta v_g^2+2\pi^2 w_0^2}\end{aligned} \quad (6.30)$$

To gain some insight into the results provided by these equations, it is instructive to vary the parameters which are most accessible experimentally. Walkoff angle is set by the phase matching condition of the chosen crystal, and since BBO has the largest phase matching bandwidth of any non-linear material in the visible region, fixing the walkoff angle at 75 mRad. The same is true for the group velocity difference, Δv_g and the nonlinear coefficient, d_{eff}, leaving input pulse width, beam waist at the crystal input and the length of the nonlinear crystal as the readily variable experimental parameters.

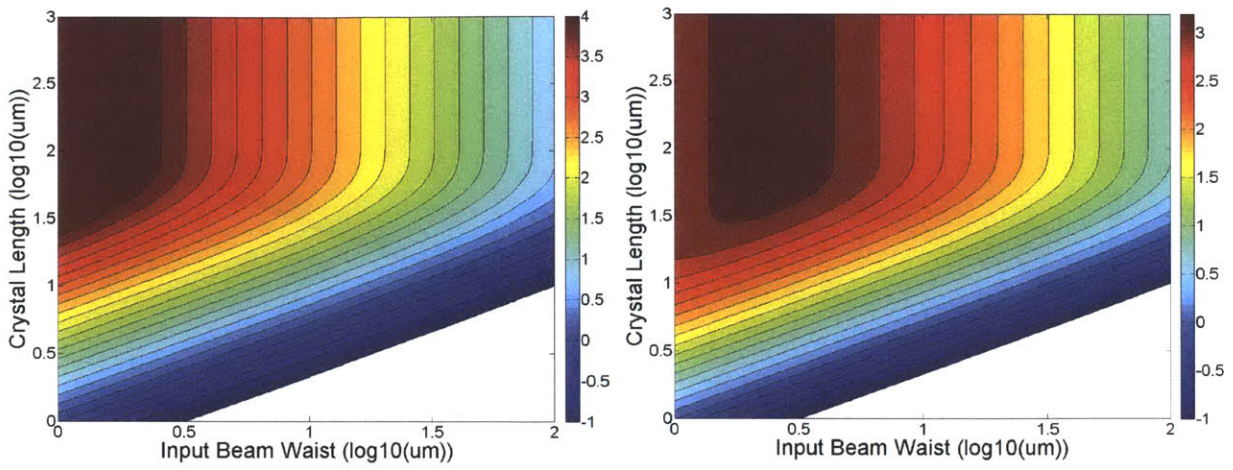

Figure 6.3 – Plots of the difference in converted power between the two arms of the cross correlator. The plot on the left assumes no spatial walkoff while the plot on the right includes the effect of walkoff as described in the text. Units in the z-direction are log10(uW/fs). Both plots assume the 75 mRad walkoff angle for BBO and 1 nJ input pulse energies and 10 fs pulses.

As can be seen in the left hand plot of Fig. 6.2 and 6.3, which plots the difference in converted power in each arm of the cross correlator against both input beam waist and crystal length for the case of no spatial walkoff, the relationship behaves as expected. Making the crystal longer increases the slope of the phase discriminator, and there is no penalty for making the focus of the input beam tighter. In the case which includes spatial walkoff, there is an optimum focal length which maximizes the intensity of the input beams, yet minimizes the impact of the spatial walkoff. For SHG in BBO near 800 nm the optimum focal waist corresponds to an input beam waist of ~10 um for a 10 fs pulse. Interestingly, the optimum values shifts to larger input beam sizes for longer pulses, Figure 6.3. The reason for the shift of the optimal value can be understood directly from the spatial extent of the pulses. At 10 fs, a pulse exists over a distance of 3 μm, which is much less than the effective walkoff distance of ~40 μm. At 100 fs, the pulse exists over a distance comparable to the walkoff dimension, meaning that with a tight enough focus only a fraction of the pulses will be fully overlapped. To ensure full overlap over a longer distance, a looser focus is required. Note, however, that the plot on the right side of Fig. 6.3 is a very smooth function, varying over only 2 dB, so the dependence of the optimal beam waist on input pulse width is a weak effect.

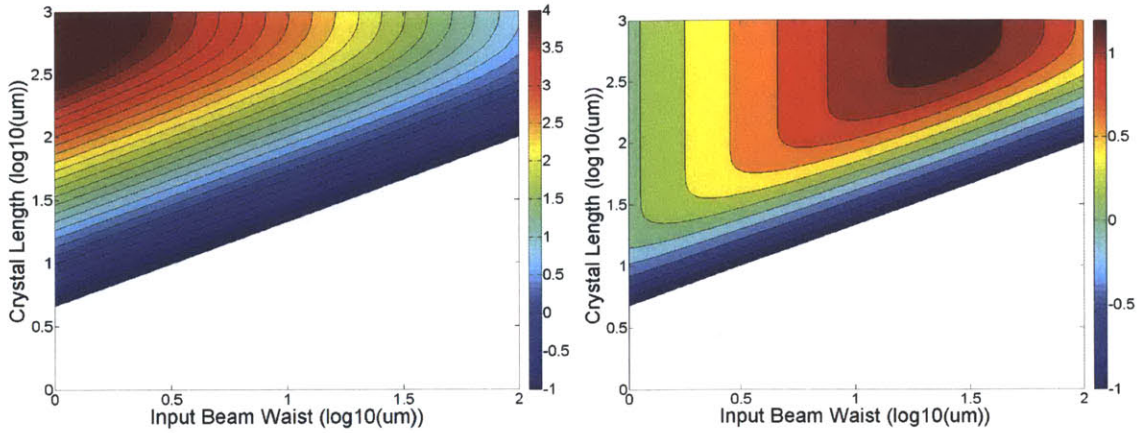

Figure 6.4 – Plots of the difference in converted power between the two arms of the cross correlator. The plot on the left assumes no spatial walkoff while the plot on the right includes the effect of walkoff as described in the text. Units in the z-direction are log10(uW/fs). Both plots assume the 75 mRad walkoff angle for BBO and 1 nJ input pulse energies and 100 fs pulses.

6.3.3 Ultimate measurement sensitivity

Further analysis of the balanced optical cross correlation technique can be made in terms of achievable sensitivity of the method by determining the minimum detectable timing error with respect to both shot noise and electronic noise. Optically referred noise at the photodiode surface is

$$T_e(f) = \frac{1}{\Gamma}\left[P_{shot}^2 + \left(\frac{v_n}{G_v G_T R}\right)^2\right]^{1/2} \tag{6.31}$$

which reports power difference per pulse arrival time difference in *fs/rtHz*, with the amplifier output voltage noise v_n reduced by the circuit voltage gain, G_v, and transimpedance gain, G_T, and photodiode responsivity R. In the ideal case, the phase noise floor of balanced optical cross correlation is set by the shot noise of the incident pulses when the phase locked loop is closed. If the optical portion of the cross correlator has been designed properly, the shot noise level will correspond to an average power equal to the square root sum of the peak converted power from each arm of the cross correlator when the lasers are phase locked together (i.e. output power at $\Delta\tau=0$ for both arms). Depending on how the detector is designed, the crossover from electronic noise to shot noise will occur at different power levels. In Appendix A there is a detailed summary of the design process for such a detector as well as a discussion of the design tradeoffs which occur depending on the goals of the measurement.

For a meaningful comparison, Eq. (6.31) is modified to the form below to report the resulting single sideband white phase noise

$$L_{\phi}(f) = T_e^2(f)\frac{(2\pi f_c)^2}{2} \tag{6.32}$$

Figure 6.4 plots the relationship of Eq.(6.32) to the measurement bandwidth as defined by equation (A.4) and the input pulse energy from the two lasers to the resulting noise floor in dBc/Hz for a 10 GHz carrier. Using the parameters from this experiment of 10 fs pulses, a 400 μm crystal with a 10 μm focus at the face of the input crystal, and assuming a detector output noise level of 1 μV/rtHz is achievable independent of detector configuration, a prediction of the possible measurement sensitivity can be made.

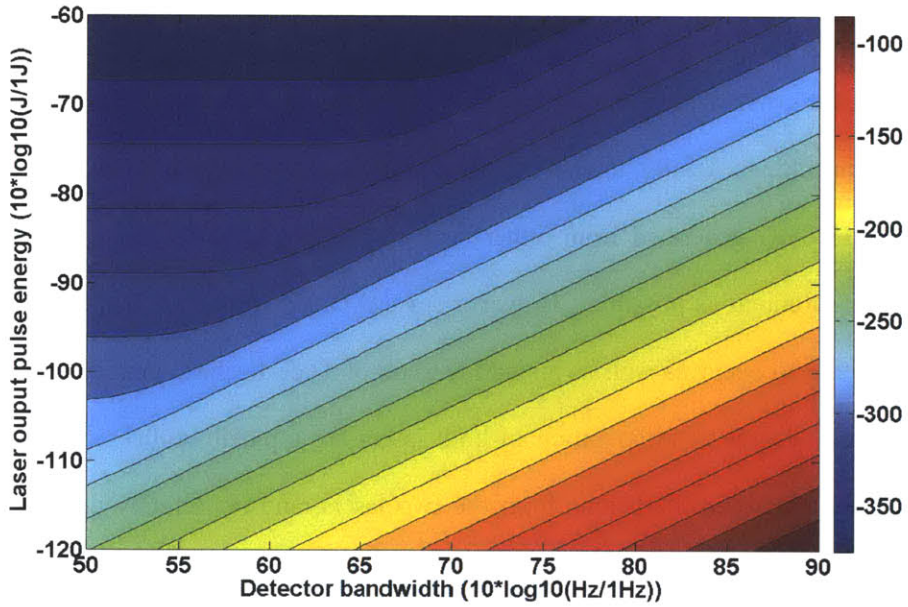

Figure 6.5 – Plot of the predicted noise floor as a function of detector bandwidth and cross correlator input pulse energy, with z-axis units of dBc/Hz. Laser and cross correlator operating parameters assume 6 μm beam waist at the BBO input face, 10 fs pulses, a 400 μm long crystal, 3.9 GHz GBP amplifier with a gain of 25 voltage amplifier as a second stage, 0.35 A/W responsivity photodiodes, and 6 pF effective input capacitance at the transimpedance amplifier inverting input pin. The lower left hand portion of the plot is dominated by the detector noise floor, while the upper left hand corner is shot noise limited.

The noise floor reported in Fig. 6.4 is extremely low and actually operating the measurement system at these low levels would be challenging. One of the main limitations to using a detection system with a sensitivity capable of -210 dBc/Hz or lower is the feedback loop bandwidth necessary to keep the two pulse trains phase locked.

The dynamic range of most high speed detectors is only +/- 2.5 volts, which for a phase error sensitivity of 1 V/fs implies a linear output range of only +/- 2.5 fs. Put another way, the integrated RMS phase error between the pulse trains when they are phase locked together cannot be more than 5 fs, typically 0.5 fs as a maximum to avoid regularly breaking the phase lock. If the phase error signal exceeds the linear region, the effective gain of the loop is reduced resulting in destabilization of the feedback loop due to reduced phase margin. Achieving such a high level of synchronization means significant suppression of the phase noise between the two pulse trains, and since the gain of most feedback loops varies approximately as 1/f to $1/f^2$, feedback gain exceeding 1000 at a frequency of 1 kHz is very challenging to implement using femtosecond lasers (Appendix B).

6.3.4 Misalignment of principal axes

One final aspect of the cross correlation scheme worth mentioning is the extinction ratio between Type-I and Type-II phase matching. Ideally, the BBO crystal is cut such that for a linearly polarized beam, there should be no Type-I SHG generated from either beam. The intent is to remove as much background signal from the measurement as possible. However several factors conspire to allow a finite amount of Type-I phase matching to occur as well as a small amount of Type-II phase matching for a single beam. These factors include, degree of polarization of both lasers are typically 100:1, imperfectly orthogonal polarization alignment between the beams from the two lasers, and imperfectly cut BBO crystals. All three factors combine to create as many as five separate fields to be incident on the photodetector: Type I SHG from both pulse trains individually, Type-II SHG from both pulse trains individually and Type-II from the cross correlation of both pulse trains. The first two fields should be extremely small. The second two however could easily be as much as 1% of the main cross correlation spectrum. These individual Type-II SHG fields will interfere with each other and with the main cross correlation field on the photodiode, generating the beat frequencies seen in Fig. 6.11 at 20, 40 and 60 MHz. While these signals are generally not a problem as their origin is easily identified, they reduce the CMRR of the detector by misaligning the power balance on the detector. Ensuring that the polarizations of the beams

from each laser are as orthogonal as possible is the best solution to minimize the amplitude of these parasitic fields.

6.4 Experimental setup

The experimental setup consisted of two Kerr lens mode-locked Ti:Sapphire lasers, both with repetition rates of 82.6 MHz, using nearly identical optical components. The main differences between the two lasers was a slight difference in the length of the laser crystals (2.2 mm vs 2.28 mm) and corresponding differences in the amount of fused silica used for dispersion compensation, resulting in slightly different optical spectra, Figure 6.7. Both lasers emitted between 100 and 120 mW of power with no apparent dependence on optical output power in the measured results. Output from both lasers was combined in the cross correlator using a broadband dielectric beamsplitter of 3 mm thickness. Prior to the beamsplitter the polarization of one laser is rotated using a pair of silver mirrors in a periscope. The two resulting cross polarized beams were directed into two 400 um long BBO crystals after focusing by 12.7 mm EFL parabolic mirrors. The extraordinary axis of the each BBO crystal was oriented at a 90 deg angle to one another so that each arm of the cross correlator would require a different time offset between the pulses to achieve maximum conversion. Each arm therefore performs a cross correlation between the two input pulses, generating a third pulse at 400 nm with an amplitude and relative phase related to the temporal and spatial overlap of the two pulses in each crystal. Because the slope of the phase error discriminator directly determines the level of the final result of this measurement, the slope was determined both before and after the two pulse trains were phase locked together as well as while the phase lock was closed. Before and after the loop is closed, measurement of the slope is achieved by detuning the repetition rates of the lasers slightly (3 Hz) to allow the pulses to slowly pass through on another performing a repeating

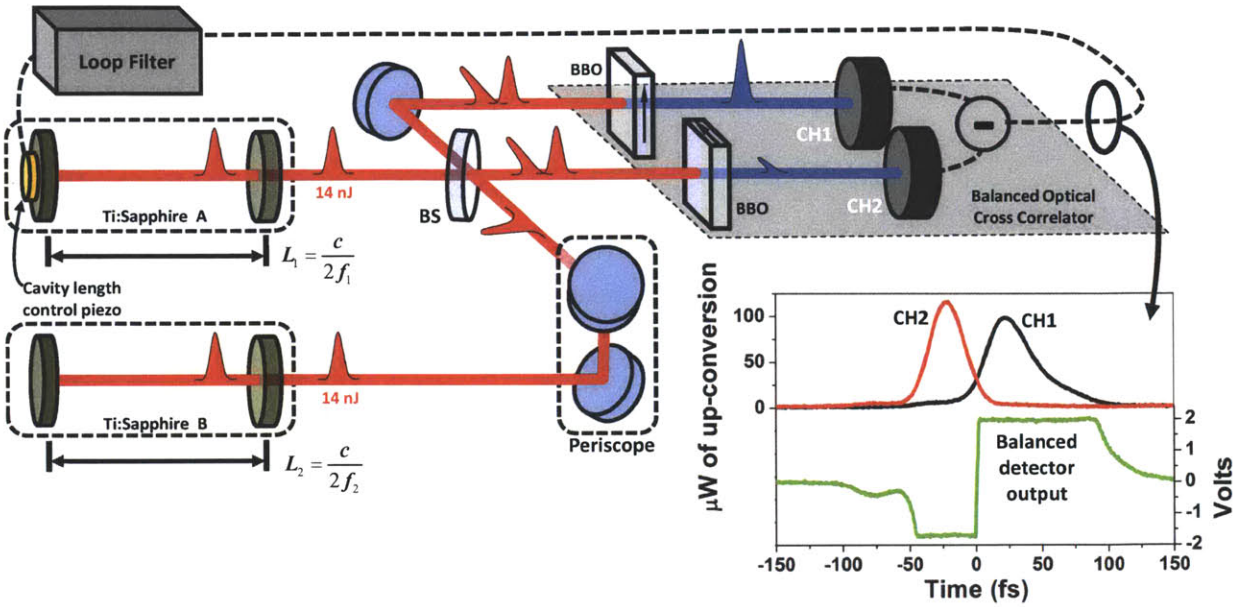

Figure 6.6 -- The output from two nearly identical Ti:Sapphire lasers are spatially overlapped using a beamsplitter (BS). The two resulting beams are composed of orthogonally polarized pulses from both lasers which are focused into two separate 400 um long BBO crystals for Type II second harmonic generation. Orthogonal orientation of the extraordinary axis of the two BBO crystals ensures that equal upconversion efficiency occurs only when the two pulses are exactly overlapped. Peak conversion from each arm of the cross correlator is typically 100 uW, which is collected by a balanced detector to cancel intensity fluctuations of the two lasers. The resulting error signal is characterized by a phase error to voltage conversion of 22.1 kV/Rad, +/- 1.0 kV/Rad for a 10 GHz carrier.

cross correlation and recording the output of the balanced detector using an oscilloscope [128]. When the pulse trains are phase locked together, a small controlled time delay is injected to one of the pulse trains prior to the beamsplitter and coherently detected at the output of the balanced detector using a network analyzer. The mean value determined from these three measurements was 22.1 kV/Rad +/-1.0 kV/Rad, resulting in a measurement uncertainty of +/-0.4 dBc/Hz and +/-0.6 as for the resulting phase and integrated timing error measurements, respectively, Fig. 6.14. The following sections will discuss the two techniques for characterizing the phase error slope discriminator as well as the laser's RIN to phase noise sensitivity.

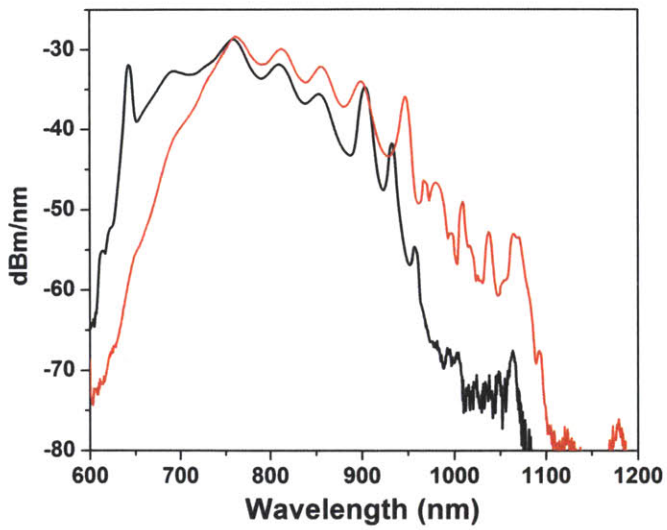

Figure 6.7 -- Optical spectrum from the two 80 MHz Ti:Sapphire lasers. The Fourier transform limited pulse width of both spectra is ~10 fs.

6.5 Characterization of the phase error discriminator slope

A typical characterization trace from the cross correlator is shown in the inset of Figures 6.1 and 6.6 above. The trace is characterized primarily by a very narrow steep slope which occurs when the two pulses from both lasers enter the two crystals at the same time. Slope sensitivities for the cross correlator are typically in excess of 10 kV/Rad, assuming a 10 GHz carrier. The linear range for this high slope region is typically 100 μRadians, again considering a 10 GHz carrier. To measure the frequency spectrum of phase error between the two locked pulse trains, the voltage output from the balanced detector is fed into both a voltage spectrum analyzer to determine the phase error between the lasers and to a servo controller to modify the voltage signal so that it may be used to phase lock the lasers. Phase locking of the two lasers is achieved through length modulation of one of the lasers using a piezo mounted mirror in one of the lasers. The phase error voltage signal was measured using two devices, an Agilent 89410 Vector Signal Analyzer (VSA) for the 100 Hz to 10 MHz frequency range and an Agilent E4407B ESA for the 10 MHz to 90 MHz range.

Because of the alignment sensitivity of the cross correlator, two methods were employed to determine the time error to voltage conversion. Before and after phase locking the two pulse trains together for the actual measurement, the two pulse trains were individually phase locked to two separate

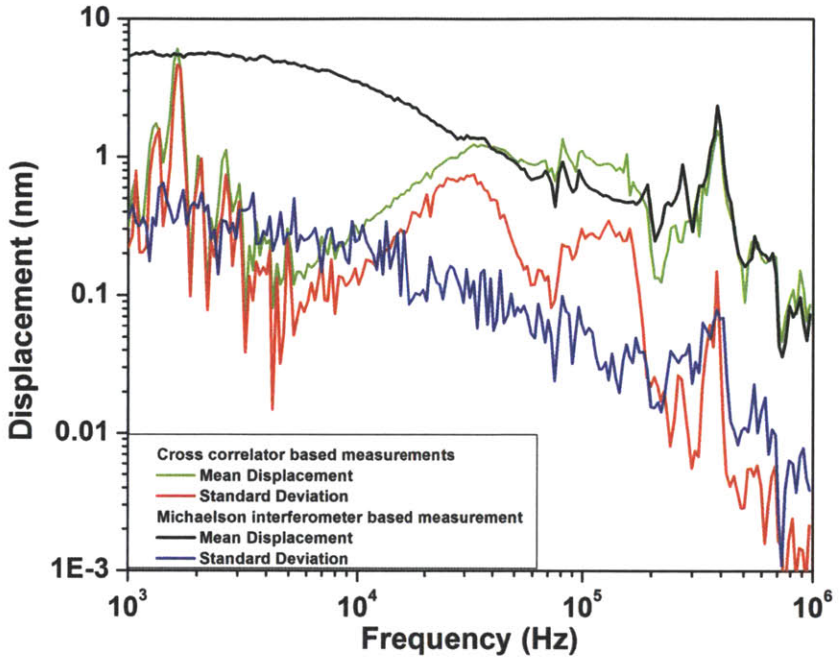

Figure 6.8 -- . Plot of the external piezo mirror displacement as a function of piezo modulation frequency for two different measurement arrangements. Displacement measurements were made using both a Michaelson interferometer and the cross correlator, with the mean and standard deviation of both results plotted for comparison. Both data sets were generated using the same piezo drive voltage.

reference oscillators with a 3 Hz frequency difference. The two reference oscillators were phase locked to one another using the 10 MHz timebase inputs and outputs. The 3 Hz offset allowed the phase difference between the two pulse trains to grow at a controlled rate of 2π, three times per second. Recording the output of the balanced detector on a digital oscilloscope allowed measurement of the cross correlator slope, an example of which is shown in Figure 6.6. Because the portion of the output signal from the balanced detector containing the cross correlator slope was typically only present for 100 ns of the 0.33 s beat frequency period, determination of the cross correlator slope is susceptible to uncompensated phase noise between all of the oscillators involved in the offset lock scheme. Phase noise in a phase locked loop should, however, have zero mean and averaging 3-5 measurements reduced the standard deviation to less than 10%. Regardless, due to the fact that the voltage signal from the balanced

detector requires nearly half of the slew rate of the output amplifier, an online confirmation is in order where the detector is not operating in such an extreme state.

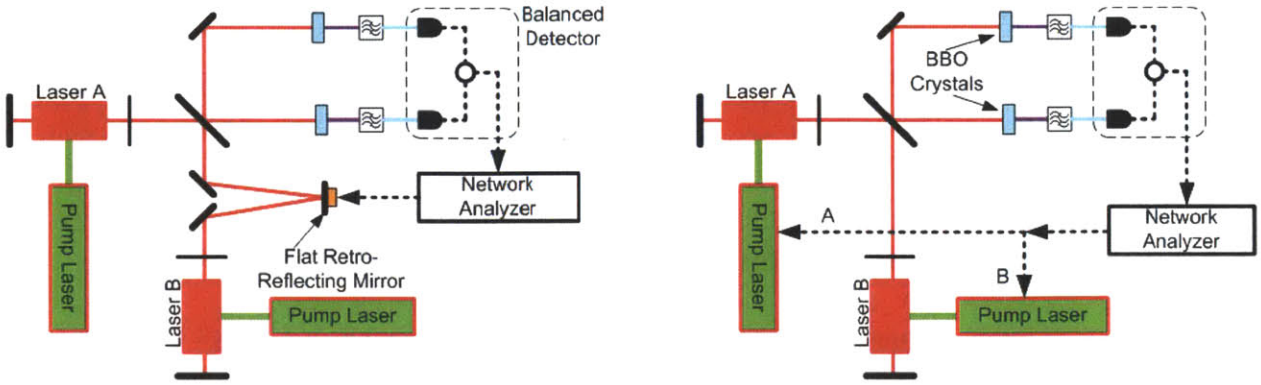

Figure 6.9 – General setup for characterizing phase error discriminator slope (left) and pump RIN to phase error conversion (right). On the left, the output of the network analyzer is used to directly modulate the piezo in this setup. Due to the 50 Ohm output impedance of the analyzer, the unity transformation bandwidth is only about 10 kHz. Careful construction of the piezo and mount allowed resonance free operation to ~300 kHz. On the right, the network analyzer modulates the pump power to both lasers using AOMs. Modulation bandwidth is ~1 MHz, and each pump laser is modulated in turn as described in the text. For both measurements, the pulse trains are locked with the loosest bandwidth possible to maximize the frequency range between the influence of the feedback loop (low frequency limit) or modulation bandwidth high frequency limit).

To check the slope of the cross correlator while the loop was closed and the two pulse trains were phase locked together using the cross correlator as the phase error discriminator, a small time delay between the two pulse trains was introduced prior to combination of the beams at the beamsplitter. A controlled delay was accomplished by mounting a small mirror on a piezoelectric transducer and retroreflecting one of the pulse trains. Calibrating the displacement response of the mirror to a known voltage signal was accomplished using an interferometer. Using the piezo mounted mirror, delays of up to 40 as between the two pulse trains over a frequency range of 1 kHz to 1 MHz were possible. The slope of the cross correlator was confirmed by comparing the mirror displacement reported by the interferometer and that reported by the cross correlator, Figure 6.8. For the result reported here five measurements were made using different gain settings for the phase locked loop to identify which portion of the calibration spectrum was least affected by the loop and therefore would give the best representation of the cross correlator response. The cross correlator slope was determined by selecting a value which minimized the squared difference between the interferometer response and the in-loop measurement over

the frequency range of 60 kHz to 1 MHz. Standard deviation of these three measurements was again less than 10%. The resulting slope used in Fig. 6.14 is the mean of all three measurements (before and after the phase noise measurement using the offset lock, and while the phase lock was closed using the modulation technique), with the standard deviation of each assumed independent and therefore square root summed.

6.6 Characterization of measurement method noise floor

A typical method for measuring the noise floor of an optical detection system is to block the detector at a point in the system which only prevents the signal light from entering the detector. For example, in Fig. 6.9, this would correspond to blocking the output of lasers A and B directly at the laser output. Blocking the measured beam far from the detector has the advantage of including the effect of any ambient light sources in the noise floor measurement, in addition to capturing the noise level of the detector itself. Intensity fluctuations caused by mirror vibrations or air currents or non-linearity in the photodetector are not accounted for using the blocked detector method.

In an attempt to quantify the impact of mirror vibrations and ambient beam pointing errors on the final phase noise measurement, the response of the balanced cross correlator was measured using only one laser pulse train. Measuring the response of the cross correlator using one pulse train as the input should provide an ideal calibration of the system noise spectrum, since any timing or intensity noise from the laser source should be common mode to both arms of the correlator, leaving only environmental perturbations to generate an output signal. The general measurement is described in Fig 6.10. The output of one of the Ti:Sapphire lasers is split into two beams. In one of the beams a periscope is used to rotate the polarization of the pulse train by 90 degrees to simulate the second laser source. The recombined beams are then routed to the cross correlator for analysis. The length of the two beam paths must obviously be kept identical, though length matching is easily achieved using the output of the cross correlator as the length error discriminator. Measurement of the length error spectrum will reveal the desired information about the cross correlator setup.

One challenge of using only one mode-locked laser, is to determine the pulse time arrival to balanced detector output voltage conversion. Since there is only one laser in this experiment, there is no capability to force the two pulses being cross correlated to change their overlap as a function of time as was demonstrated previously. As an alternative, the stage used to keep the two beam paths equal was moved in a controlled way to cross correlate the two pulses. Displacement of the stage was monitored by a second interferometer, with the voltage output of the second interferometer and the output of the balanced detector monitored simultaneously on an oscilloscope while the stage was displaced by hand. The resulting traces are plotted in figure 6.11 and resulted in a slope sensitivity of 405 mV/fs, which is

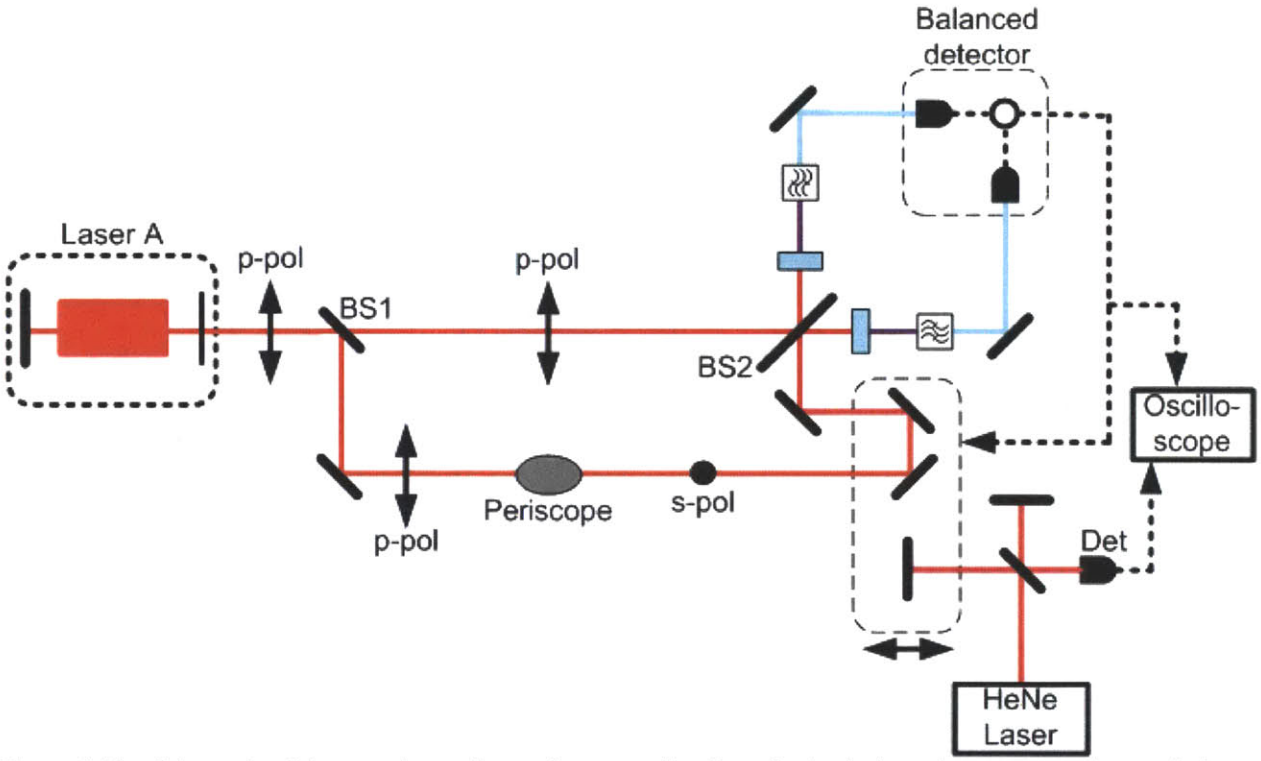

Figure 6.10 – Schematic of the experimental setup for measuring the noise intrinsic to the cross correlator technique. The output of Laser A is split in half at the first beamsplitter, BS1, which is non-polarizing and broadband by way of being a half silvered mirror. One of the two beams remains unchanged while the second beam undergoes polarization rotation by 90 degrees. Polarization rotation is achieved using a periscope, as shown previously in Fig. 6.6; using a periscope introduces no dispersion and is completely achromatic. The two cross polarized beams are recombined on BS2 for entry into the cross correlator setup. The two beam paths are kept at the same length using the feedback loop for the main experiment by controlling a piezo mounted mirror in one arm of the interferometer. The HeNe laser is used in an interferometer to determine the displacement of the delay stage for measurement of the time to voltage conversion of the cross correlator, see text.

somewhat less than what was found when using both lasers. The difference in slope sensitivities is expected however since the power into each crystal has been reduced by a factor of two, and the power levels in each polarization is not exactly equal due to the beamsplitters.

Plotted in Fig 6.12 is the output of the cross correlator with the essentially noiseless pulse train as the input and has several important features. First, because of the low pulse energy used in this experiment, a large transimpedance gain was used which limited the bandwidth of the measurement to just over 1 MHz. The white noise floor at -180 dBc/Hz is due to the electronic noise floor of the detector

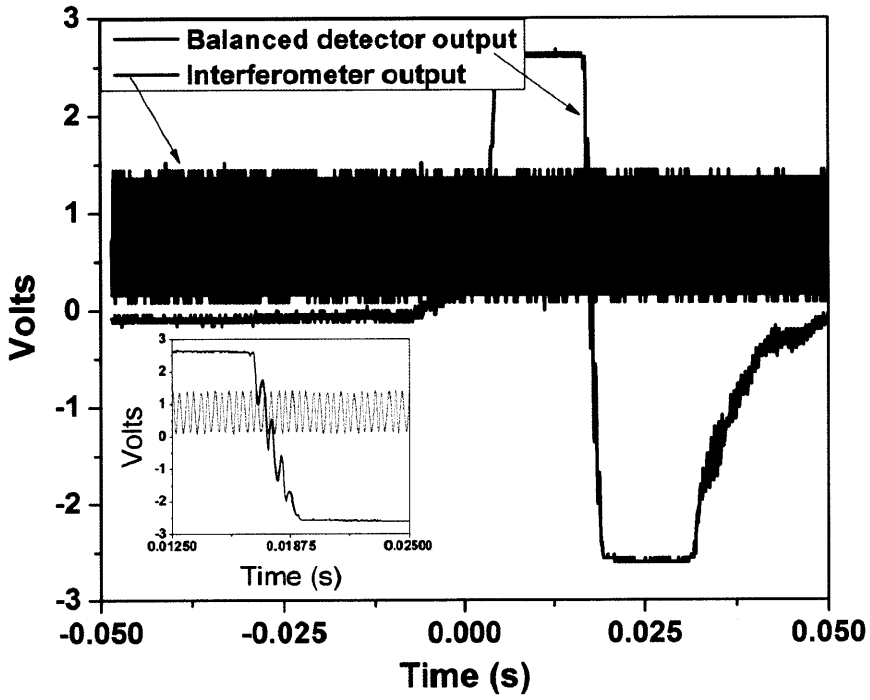

Figure 6.11 – Measurement of cross correlator pulse arrival time error to voltage transfer function. The interferometer output is used to recover the distance traveled by the stage, and thereby the time of arrival delay between the two pulses by a simple conversion assuming a group velocity of c. The inset shows a higher resolution image of the central region near where the cross correlation trace crosses zero volts. The fringes visible in the balanced detector output are likely caused by a slight misalignment of the polarization axis of the two input beams on the BBO crystal, causing a finite amount of Type I SFG in each of the two beams.

which was different from the one used for the main measurement in Fig. 6.14 (New Focus 2107 vs modified Thorlabs 120 as described below). The bandwidth of the feedback loop used for stabilizing the beam paths is estimated to be about 200 Hz from the servo bump. The remaining spectrum between 200

Hz and 10 kHz is environmental noise coupled into the measurement apparatus and converted into timing error by the cross correlator.

It is difficult to draw conclusions from Fig. 6.12 for a few reasons. First, the measurement is actually measuring the environmental noise spectrum which is coupled into both the cross correlator and into two beams which generate the two cross polarized pulse trains from the single input laser pulse train. Ideally this only results in a 3 dB difference, assuming equal contributions from both the cross correlator

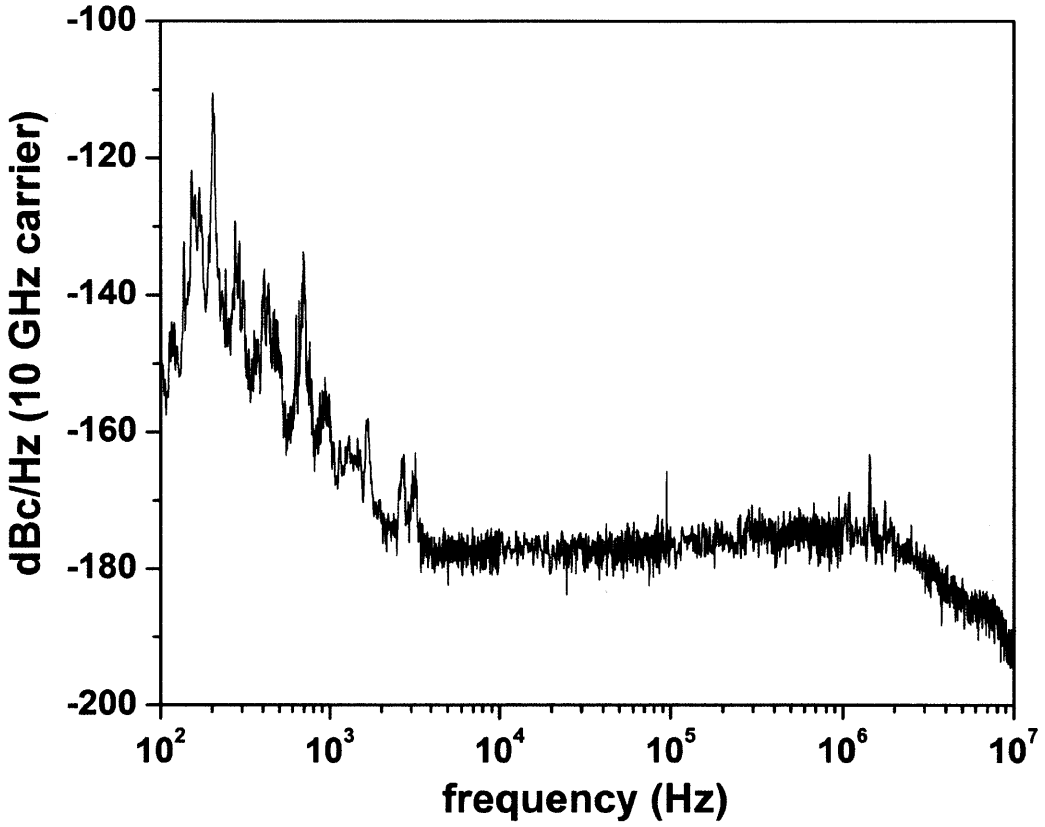

Figure 6.12 – Result from measurement of the cross correlator stability by using the pulse train from one laser which had been split into two pulse trains and recombined as if it were beams from two cross polarized lasers. The white noise floor at -180 dBc/Hz is due to the electronic noise of the photodetector. The bandwidth of the feedback loop is estimated to be 200 Hz.

and split beam paths. Second, the fringes present on the nominally linear central region of the cross correlator calibration trace make confirmation of the time error to voltage conversion uncertain. For a large deflection, the average value of the slope of the central region can be used, though for the small

deflections expected here, the interferometric fringe slope is highly nonlinear. The average value has been used here which may be overly conservative. Because of these uncertainties, Fig 6.12 can only be considered as an upper limit to the intrinsic noise of the measurement setup.

6.7 Characterization of coupling between relative intensity noise and phase noise

The effect of relative intensity noise was determined by a method nearly identical to that described in [129], Fig. 6.9. Controlled modulation of the pump power to each laser was achieved by use of an acousto-optic modulator. Calibration for the degree of modulation of both the pump power and the mode-locked laser output power was achieved by coherent detection of the resulting modulation. Coherent detection of the resulting timing error as measured by the cross correlator and balanced detector

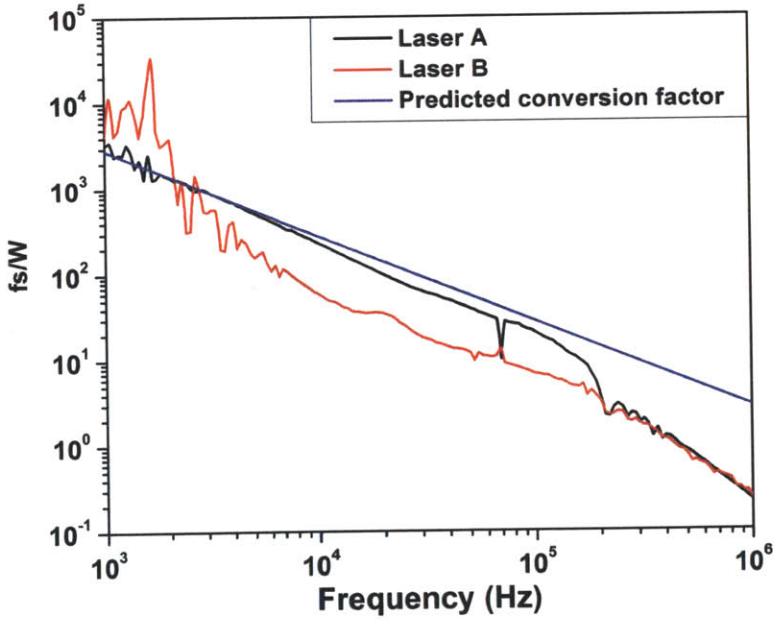

Figure 6.13 – Plot of pump laser intensity modulation to pulse timing shift for each laser. The transfer function has a $1/f$ dependence because the induced time shifts are integrated into frequency errors. The response bandwidth of the Ti:Sapphire gain forces the response to start reducing even faster for frequencies beyond 200 kHz. Both curves have been reconstructed using a simple model of the phase locked loop transfer function. The slight increase in coupling at low frequencies is likely due to a thermal refractive index change of the sapphire crystal caused by pump induced heating.

to determine the effect of pump power modulation on the pulse timing from each laser. Division of the timing error due to pump power modulation amplitude spectrum by the pump power modulation amplitude spectrum yields the frequency dependent conversion factor necessary to convert the measured pump power RIN into pulse train phase noise, Fig. 6.13.

The value of this transfer function can be predicted using the analysis presented in [22]. In that analysis, the self steepening term is treated as a timing shift of the pulse as it circulates in the laser cavity. The resulting expression for the time error spectrum as driven by the pump power RIN spectrum is

$$S_{\Delta t}(f) = \left(\frac{f_R \phi_{NL}}{2\pi^2 f \nu_0} \right)^2 S_P(f) S_{L/P}(f) \qquad (6.33)$$

where f is the offset frequency, f_R is the pulse repetition rate, ϕ_{NL} is the non-linear phase, ν_0 is the carrier frequency, $S_P(f)$ is the pump laser RIN spectrum and $S_{L/P}(f)$ is the frequency dependent optical to optical conversion efficiency. The nonlinear phase term is defined to be

$$\phi_{NL} = n_2 k_0 z I \qquad (6.34)$$

with n_2 as the intensity dependent refractive index, k_0 is the vacuum wavenumber, z taken as two times the Rayleigh range inside the sapphire crystal, and I is the mean pulse intensity inside the laser crystal. Using the above definitions, it can be shown that Fig. 6.13 plots

$$\sqrt{\frac{S_{\Delta t}(f)}{S_P(f)}} = \left(\frac{f_R \phi_{NL}}{2\pi^2 f \nu_0} \right) \sqrt{S_{L/P}(f)} = \frac{1}{f} \frac{2 n_2 P_{avg}}{c \lambda l \tau_p} \sqrt{S_{L/P}(f)} \qquad (6.35)$$

where the definitions for the Rayleigh range and peak intensity have been substituted using P_{avg} as the average laser output power, l as the round trip cavity loss, τ_p as the pulse intensity FWHM, and the laser's center wavelength λ. Using operating points corresponding to that of the two Ti:Sapphire lasers in this experiment of: $Pavg$= 100 mW, τ_p= 10 fs, l= 0.08, n_2=3x10^{-20}cm^2/W and $S_{L/P}(f)$=0.08, results in the predicted conversion factor trace of Fig. 6.13.

Overcoming the RIN to timing error coupling will be a major factor in measuring the real quantum limited timing error of pulse trains generated by Ti:Sapphire lasers. Not only does the RIN contribution to timing error mask the contribution by spontaneous emission, but it also limits the sensitivity of the cross correlator slope which can be used by forcing the cross correlator designer to

satisfy two mutually opposed goals. To allow phase locking, sufficient dynamic range is necessary to ensure the detector output doesn't saturate and reduce the feedback loop gain, destabilizing the feedback loop. Simultaneously the cross correlator output slope must be as steep as possible to ensure that the small phase errors due to spontaneous emission generate a response larger than the intrinsic noise of the detector. The obvious solution to this conflict is to make the pulse train emitted by the lasers more stable especially at low offset frequencies. A promising approach to increasing the stability of the emitted pulse train is to phase lock one comb line of the mode-locked laser's optical spectrum to a cavity-stabilized diode laser as described in [129].

6.8 Discussion of measurement results

The measured spectrum of the phase error between the two Ti:Sapphire lasers is plotted in Fig. 6.14, along with the integrated timing error. The bandwidth of the feedback loop for phase locking the two lasers can be estimated from the servo bump at 30 kHz. Below this frequency the feedback loop is suppressing the phase error spectrum which is dominated mainly by environmental cavity length perturbations. Offset frequencies above 30 kHz show the intrinsic phase noise spectrum between the two lasers until 1 MHz where the phase noise spectrum falls below the noise floor. The large noise spur at 190 kHz is a result of relative intensity noise being converted into phase noise. Confirmation of this dependence, as described above, was accomplished by controlled modulation of both pump lasers in turn and coherent detection of the resulting phase noise using the cross correlator [130], resulting in a conversion factor of 2 Rad/W/f for offset frequencies f, below the relaxation oscillation frequency of each laser, which was 60-100 kHz for these lasers. Using the entire frequency dependent conversion factor and the measured RIN from both pump lasers, one can generate the dotted black curve in Fig. 6.14. The deviation of the measured phase error and phase error predicted by the RIN to phase noise conversion for frequencies beyond 300 kHz is likely caused by the limited common mode rejection ratio of the detector

at both high frequencies and high differential signal levels. The resulting integrated timing error, which covers the entire Nyquist region, is 12.3 as +/-0.6 as with a noise floor contribution of 8.1 as +/-0.4 as. While the phase error for pulse trains from mode-locked lasers are predicted to decrease at a rate of -20 dB/decade, the level of -200 dBc/Hz at 10 kHz offset predicted for the current laser configurations measured here is still too low to allow detection. A noise floor no higher than -240 dBc/Hz at a 1 MHz offset appears to be necessary to observe quantum noise that exceeds the pump RIN induced phase noise.

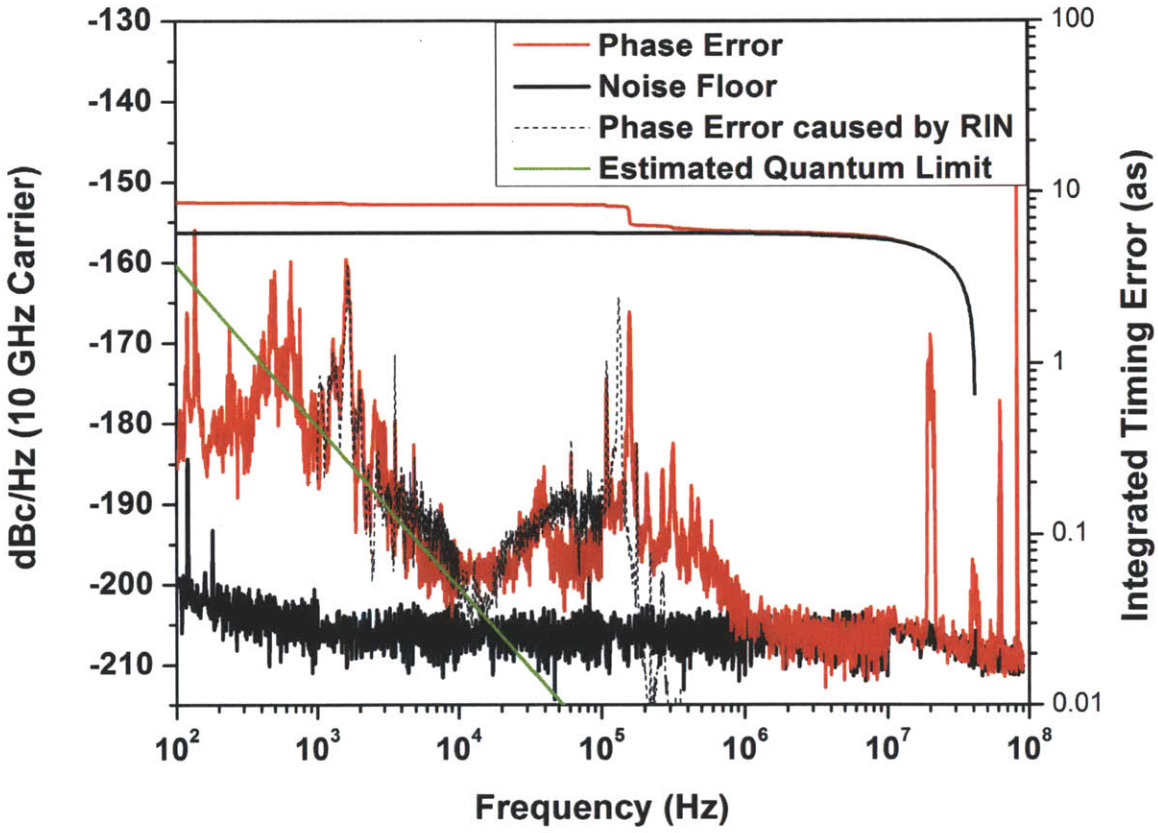

Figure 6.14 -- (a) Spectrum of phase error between two mode-locked Ti:Sapphire laser pulse trains, scaled to a 10 GHz carrier. The result of the optical cross correlator measurement is plotted in red, and in black is the noise floor of the optical cross correlator measurement determined by measuring the output of the balanced detector when blocked. There are four noise spurs at 80 MHz, 60 MHz, 40 MHz, and 20 MHz, none of which are counted towards the integrated timing error of the pulse train. At 80 MHz is the pulse repetition rate of the lasers, f_R; at 20 and 60 MHz is the difference frequency beat between the two laser optical spectra due to their different carrier envelope offset frequencies($f_b = f_{CEO1} - f_{CEO2}$); at 40 MHz is a mixing product between the two f_{CEO} signals and the f_R signal in the photodiodes. In addition, when calculating the integrated timing error from the Nyquist frequency (41.3 MHz) to 100 Hz, the falling response of the detector beyond 20 MHz is corrected to give a white noise floor. The estimated quantum limited phase noise for the lasers measured here, plotted in green, assumes only that the laser cavities have zero dispersion. The corresponding quantum limited integrated timing error does not exceed one attosecond until approximately 200 Hz offset frequency.

6.9 Conclusions and future work

Optical pulse trains from femtosecond mode-locked lasers exhibit the lowest phase noise of any type of oscillator. The estimated spontaneous emission limited phase noise level for a laser with an optical spectrum corresponding to a 5 fs pulse, 1% output coupling, and 125 nJ intracavity pulse energy and no dispersion would be -200 dBc/Hz at a 1 kHz offset frequency. The corresponding integrated timing error would not exceed one attosecond until approximately one Hertz offset frequency. Extremely high speed and precision optical analog to digital conversion as well as ultra-broadband secure communications systems should benefit from such high quality oscillators.

While low noise conversion of the optical pulse trains to electrical signals useful for many applications remains an outstanding problem, the main barrier to realizing the full potential of these low noise oscillators lies in reducing the technical noise contributions from the pump lasers. One possible solution for overcoming the RIN contribution to phase noise in a future measurement would be to pump both Ti:Sapphire lasers with the same pump laser. Using a common pump laser would allow both lasers to experience very nearly the same RIN spectrum. Cancellation of the low frequency differences in the RIN spectrum could be achieved with a scheme similar to that in Figure 6.12. Ensuring good matching of the high frequency RIN spectra (outside the matching bandwidth of Figure 6.12) seen by both lasers will require careful path length matching of the distance from the point where the pump beam is split and each Ti:Sapphire crystal.

Assuming excellent matching of the RIN spectra seen by each laser (>100:1) the conversion factor for each laser of RIN into pulse train phase error will have to be matched. This is a more difficult task as it is not clear how to change the value of the RIN to phase noise conversion factor. An easier task may be to modify the ratio of RIN seen by each laser using the feedback network to minimize the measured RIN induced timing error by manipulating the operating point of the balanced detector.

While measurement of the phase noise between two mode-locked lasers provides excellent information of the noise properties affecting the two lasers, constructing a single laser which emits a low phase noise pulse train is another matter. The low frequency phase noise caused by pump laser RIN and environmental perturbations must be cancelled or prevented. Phase locking one comb line of the Ti:Sapphire's optical spectrum to a single frequency laser which is itself stabilized to a ultra-stable reference cavity could be the ideal arrangement. This method takes advantage of both the reference cavity's low frequency stability and the mode-locked laser's high frequency stability. Ensuring enough feedback bandwidth would still be quite challenging, since the Ti:Sapphire laser has appreciable phase noise due to pump laser RIN out to >200 kHz. Significant suppression of RIN induced phase noise will require a feedback bandwidth of >5 MHz for either a pulse repetition rate stabilization or RIN reduction system. Despite what is essentially a technical difficulty, mode-locked lasers will likely become the low noise oscillator of choice for the most demanding low phase noise applications.

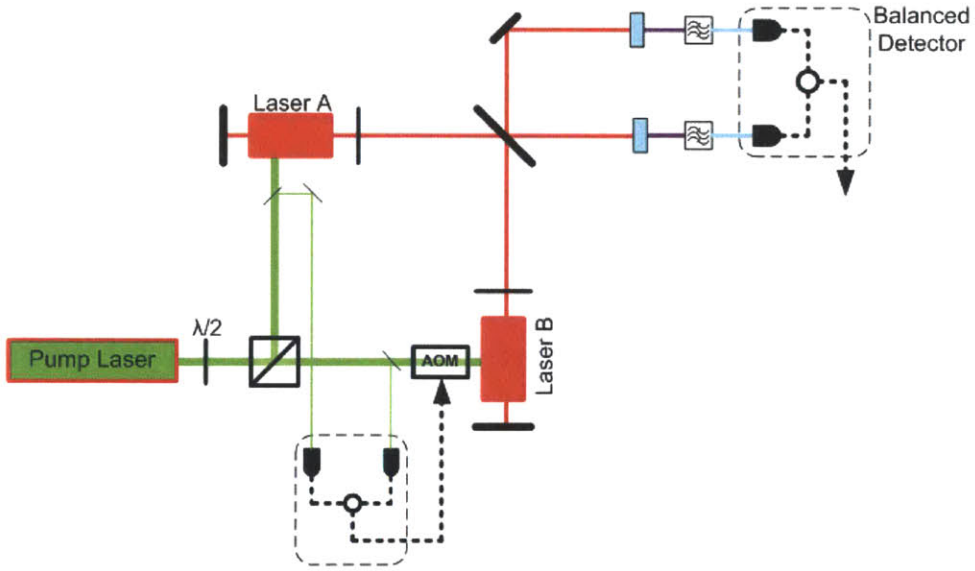

Figure 6.12 – Common pump laser arrangement for reducing the RIN contribution to the measurement of timing error between two Ti:Sapphire lasers. DC band biasing is accomplished using a half wave plate and a polarizing beamsplitter (PBS). High frequency balancing and removal of non common mode power modulations accumulated during propagation between the PBS and the laser crystals (due dust, air currents, etc.) is achieved by correction using balanced detection of the relative power levels of the two beams and either feedforward (pictured) or feedback correction. Further reduction of the influence of the pump laser could be achieved by pre-stabilizing the pump laser intensity prior to the PBS.

THIS PAGE INTENTIONALLY LEFT BLANK

Chapter 7

High Repetition rate lasers: is there life beyond 1 GHz?

7.1 Introduction

For many mode-locked laser applications, including the calibration of astrophysical spectrographs, optical arbitrary waveform generation, precision spectroscopy and two-photon microscopy, increasing the spacing between the comb lines or increasing the repetition rate of the source laser simplifies the design and operation of these systems. Currently the majority of Ti:Sapphire mode-locked lasers are limited to repetition rates of less than 1GHz, with only a few examples operating at higher rates. The current limit for a laser generating an octave spanning spectrum set at 2.16GHz [25]. The highest reported pulse repetition rate is 10GHz [13], though the spectrum of this laser is very far from octave spanning at only 19nm.

This chapter will discuss several of the challenges of scaling the repetition rate, both practically and theoretically. Two lasers with repetition rates greater than 1 GHz were constructed as part of this thesis, the configuration of both lasers and their operating parameters will be reported. The chapter will conclude with some suggestions for overcoming the difficulties identified during this thesis.

7.2 Challenges to increasing the pulse repetition rate

As described in Chapter One, Kerr lens mode-locking relies on non-linear self focusing of the intracavity beam to achieve self amplitude modulation necessary for mode-locking. For generation of octave spanning spectra, there is a further intensity requirement to generate enough self phase modulation for nonlinear broadening of the normal laser output spectrum to an octave. Table 7.1 reports operating parameters for several laser systems as reported in the literature. Direct comparison of the intensity in the Ti:Sapphire crystal for each laser system could be instructive with respect to design of high repetition rate lasers, but such a comparison is difficult as peak intensity is dependent on not only the radius of curvature (ROC) of the focusing mirrors and the pulse energy, but also on the physical alignment of the laser cavity.

A few reasonable assumptions of the operating points for each laser will yield interesting results. Recent simulations of the spatial-temporal dynamics of octave spanning Ti:Sapphire lasers [131] confirms that self amplitude modulation occurs by the traditional soft aperture description, where the spatial Kerr effect forces the Ti:Sapphire beam to improve its overlap with the pump beam to sustain mode-locked operation, as discussed in section 2.2.5. Because the beam size in the Ti:Sapphire crystal is now more well defined, an educated guess can be made about the intensity of the Ti:Sapphire beam in the laser crystal based on the components of the laser cavity (ROC and the index of refraction of sapphire, n_s), as well as the Fourier limited pulse duration of the intracavity spectrum which should occur in the center of the crystal for a ring cavity laser.

A second result from the spatial-temporal simulations is a limit to the peak intensity in the Ti:Sapphire crystal. As the peak intensity in the crystal exceeds 10^{12}W/cm^2, a multi-photon absorption process occurs which generates a plasma in the Ti:Sapphire crystal. The plasma generation process acts as a non-linear loss mechanism, clamping the peak intensity in the laser crystal to a value less than 10^{12}W/cm^2 [131]. By further analyzing the non-linear phase shift in the Ti:Sapphire crystal in the next section of this chapter, a lower bound can also be defined for the peak intensity necessary for octave spanning operation. The peak intensity between these two bounds should be the target operating range

for an octave spanning Ti:Sapphire laser, independent of repetition rate and allow for a better understanding of the power requirements for such a laser.

7.2.1 Pulse energy requirements for octave spanning operation

To determine the lower intensity bound for octave spanning operation, examination of the self phase modulation term is necessary. Repeating the analysis in section 2 Eq. (2.17)

$$\begin{aligned} &\phi = nkz \\ &\Rightarrow \phi = (n_0 + n_2 I)kz \\ &\Rightarrow \omega_{\max} = \tfrac{\partial \phi}{\partial t} = n_2 k \tfrac{\partial I}{\partial t}\Big|_{\max} z \end{aligned} \tag{7.1}$$

where ϕ is the nonlinear phase shift in the sapphire crystal, and n_2 is the nonlinear index of refraction. Defining the intensity of the pulse in the time domain at the center of the crystal at $z=0$ as

$$I(t,0) = \frac{A_0^2}{A_{eff}(0)} \operatorname{sech}\left(\frac{t}{\tau}\right)^2 \tag{7.2}$$

with the pulse energy normalized to the pulse intensity by

$$\omega_p = 2A_0^2 \tau \tag{7.3}$$

Allowing specification of the peak intensity and frequency shift provided by self phase modulation (SPM). To determine the bandwidth of frequency components which are generated, the maximum amplitude of the time derivative of the pulse intensity must be found, which is

$$\tfrac{\partial I}{\partial t} = -\frac{\omega_p}{\tau^2 A_{eff}} \operatorname{sech}\left(\frac{t}{\tau}\right)^2 \tanh\left(\frac{t}{\tau}\right) \tag{7.4}$$

and has maximums at

$$\begin{aligned} &\frac{\partial^2 I}{\partial t^2} = \frac{\omega_p}{2\tau^3 A_{eff}} \left(\cosh\left(2\frac{t}{\tau}\right) - 2\right) \operatorname{sech}\left(\frac{t}{\tau}\right)^4 = 0 \\ &\Rightarrow t_{\max} = \pm \frac{\tau}{2} \cosh(2)^{-1} \end{aligned} \tag{7.5}$$

Substitution of Eq.(7.5) and (7.4) into the result of (7.1) yields

$$\omega_{\max} = n_2 k \frac{E_p}{\tau^2 A_{eff}} \operatorname{sech}\left(\frac{t_{\max}}{\tau}\right)^2 \tanh\left(\frac{t_{\max}}{\tau}\right) z \qquad (7.6)$$

allowing definition of the pulse energy necessary to generate an octave of bandwidth for several different intracavity pulse widths. The assumption of a certain pulse width is equivalent to assuming that the bandwidth generated by the SPM process in a single pass is coupled out from the laser entirely in only a few round trips. This simplifies the dispersion compensation of the laser, by limiting the bandwidth over which extremely linear group delay is necessary. A further assumption of a certain cross sectional area is also necessary, although, again taking the suggestion of [131], a beam waist of 10 um can be assumed without significant loss of accuracy.

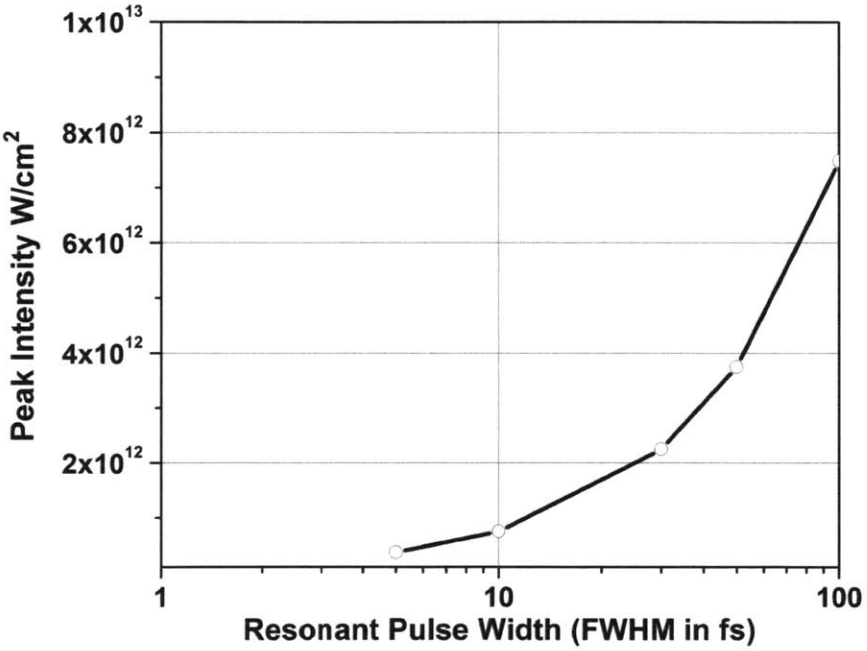

Figure 7.1 – Peak intensity required for generating an octave of bandwidth for several different pulse widths. Since for a given pulse energy, peak intensity is defined, this plot is used to determine the allowable range of pulse widths which will not incur significant loss due to plasma generation. The pulse widths plotted here are those which are resonant in the laser cavity and are not generated through SPM.

Plotted in Fig. 7.1 is the peak intensity in the laser crystal necessary for generating an octave of bandwidth at 800 nm for several different pulse widths. The plasma generation process is proportional to the cube of the peak intensity, so it is likely that an intensity exceeding $2\text{x}10^{12}$ will be heavily absorbed. The resulting loss leaves pulses shorter than 30 fs in the allowable range for generating enough bandwidth

for an octave spanning spectrum at 10 GHz. Figure 7.2 plots the intracavity average power required to achieve the peak intensity values plotted in Fig. 7.1, for repetition rates from 1 to 10 GHz. If a standard output coupling value of 1% is assumed with an additional 1% loss to account for both scattering and absorption loss, an output power of 1 W should be achievable for a cavity which is resonant over a bandwidth corresponding to a 10 fs pulse. Due to the τ^2 scaling of the required pulse energy, moving to even a 30 fs pulse requires that the total cavity loss be reduced by an equivalent amount for a given pumping rate. While ~20 W pump sources exist for Ti:Sapphire lasers, the real hurdle to overcome is the intracavity losses.

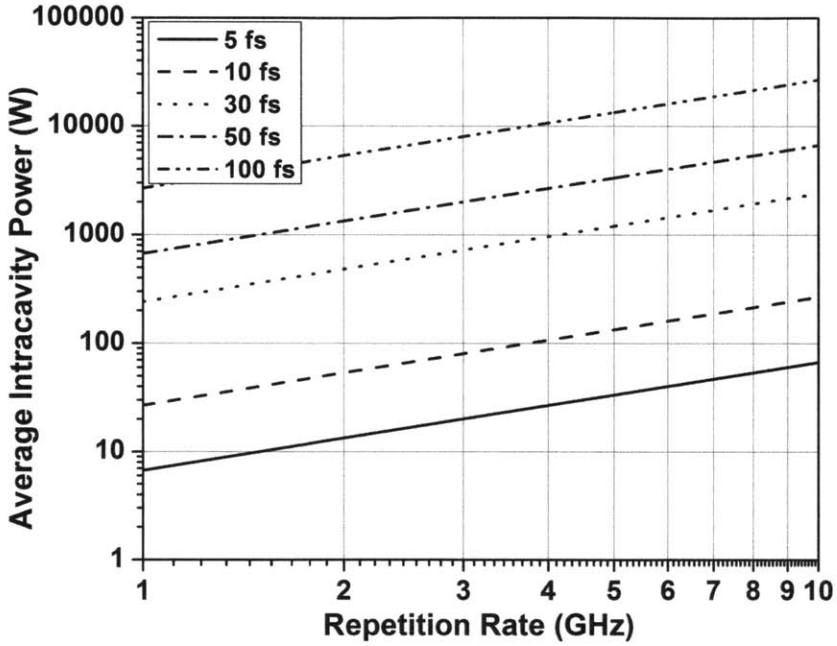

Figure 7.2 – Average intracavity power required to generate an octave of bandwidth through self phase modulation as a function of pulse repetition rate and pulse width. Average intracavity powers exceeding 100 W are challenging to achieve in short pulse lasers.

7.2.2 Literature review of high repetition rate Ti:Sapphire lasers

To reinforce the validity of this analysis, a literature search was performed to determine the operating conditions of narrowband and broadband Ti:Sapphire lasers of several different repetition rates. The results of that search are listed in Table 7.1.

Pump Type and focusing lens	Transform limited intracavity pulse	f-2f beat from laser?	Type	ROC Mirrors	Repetition Rate	Pulse Energy	Total Cavity Loss (~1% intravavity)	Average power	Pump power	Estimated Peak Intensity	Reference
Verdi 30mm	10.9 fs	No(but appears possible)	Ring	3 cm	2.12	14.9 nJ	2% oc	0.95 mW	7.5 W	$3.6x10^{11}$	[93]
Verdi 30mm	7.6 fs	No (but appears possible)	Ring	3 cm	1 GHz	29.6 nJ	2% oc	0.89 mW	7.6 W	$1.0x10^{12}$	[132]
30 mm	36.5 fs	No (narrow band)	Ring (6 mirror)	3 cm	2 GHz	7.5 nJ	1% oc	0.3	3.7	$7.2x10^{10}$	[8]
30 mm	15.8 fs	Yes	Ring	3 cm	1 GHz	40 nJ	2% oc	1.2	10.5	$6.7x10^{11}$	[133]
40 mm Milennia	7.3 fs	Yes	Ring	2.5 cm	2.16 GHz	12.5 nJ	2% oc	0.812	10.5	$4.5x10^{11}$	[25]
30 mm	57 fs	No (narrow band)	Ring	8 mm	10 GHz	3.25 nJ	1% oc	0.65	6.5	$1.3x10^{10}$	[13]
30 mm	132 fs	No (narrow band)	Ring	8 mm	10 GHz	3.5 nJ	2%	1.06	6.5	$1.4x10^{10}$	[13]
30 mm	11.2 fs	Yes	Ring	3 cm	1 GHz	45 nJ	1% oc	0.9	8.5	$9.4x10^{11}$	[66]
30 mm	29 fs	No (narrow band)	Ring	15 mm	5 GHz	7.7 nJ	2% oc	1.15	7.5	$9.3x10^{10}$	[134]
30 mm	8.2 fs	Yes	Ring	3 cm	1 GHz	12 nJ	4%	0.6	10	$4.2x10^{11}$	[50]

Table 7.1 – Summary of recently published broadband and narrowband Ti:Sapphire lasers with pulse repetition rates above 1 GHz.

For the analysis in Figures 7.3 and 7.4, the spectra from the referenced papers were recovered as well as the OC transmission profiles using a simple data retrieval program. Having both the output spectrum and the output coupler transmission data allows recovery of the intracavity pulse width and ultimately the peak intensity in each laser. The data for the output coupler used in Refs [133] and [66] were substituted with a design from Lia Matos's doctoral thesis [89] and which was scaled and shifted to fit the data provided in Ref [66]. The transmission profiles of both optics over the wavelength range provided in Ref [66] are nearly identical when properly scaled. As both optics are likely Bragg reflectors with no attempts at dispersion compensation, the reflectivity outside of the high reflectivity range is likely similar. Further, the spectrum outside of the high reflectivity range where the OC provides more than

90% reflectivity contributes little to the circulating pulse width due to the high loss. For the narrowband lasers listed in Table 7.1, the intracavity spectrum was assumed to be the same as the output spectrum.

The intracavity pulse energies for each laser are determined without accounting for the output coupler and output spectrum shape, i.e. the wavelength dependent loss. An extra 1% of loss was added to all of the output coupler values to account for scattering etc, and an additional 1% loss for spectra which greatly exceeded the output coupler bandwidth to account for the wavelength dependent loss in those cases. The effective cross sectional area of the beam in the Ti:Sapphire crystal is assumed to be the same for all lasers, ~10 um. This is a rough estimate based on the fact that nearly all of the references use 30 mm focal length lenses and most pump lasers have output beams with waists of approximately 1 mm, and is likely the largest source of error in the analysis.

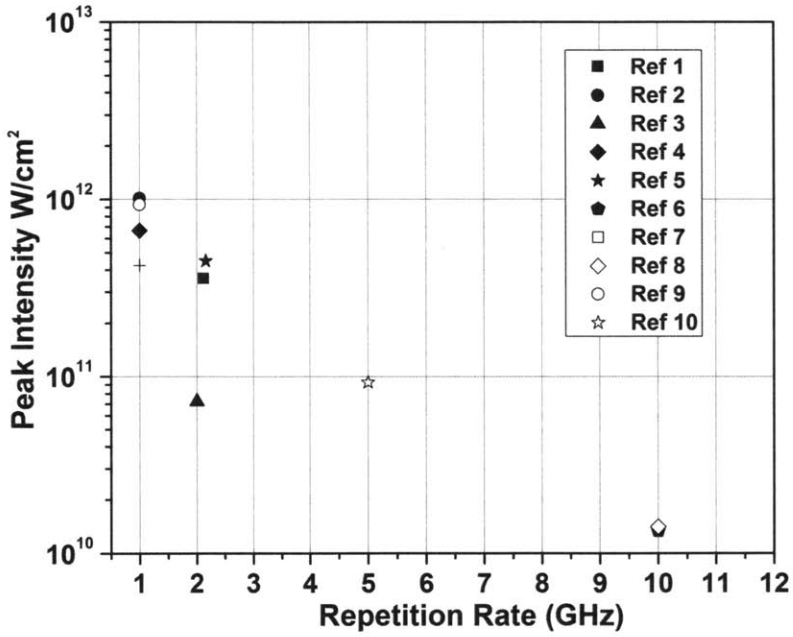

Figure 7.3 – For ten different laser systems from the literature the peak intensity in the Ti:Sapphire crystal was determined using assumptions described in the text. The peak intensity appears to decrease linearly from 10 GHz repetition rate down to about 1.5 GHz, where the plot saturates at 10^{12} W/cm^2.

With the aforementioned assumptions, the plot in Fig. 7.3 is generated, relating the peak intensity in the laser crystal to the repetition rate of the laser in question. Two important points can be drawn from this plot. First, as the pulse repetition rate is reduced from 10 GHz to 1 GHz, the peak intensity increases linearly presumably due to the reduction in pulse repetition rate with an approximately constant average

intracavity power. Second, for the lasers at 1 GHz repetition rate, the peak intensity appears to have saturated at an intensity level of 10^{12} W/cm^2. Continuing the previous trend should have put the peak intensity ~3 times higher, however, such a high intensity would likely result in a tenfold increase in plasma loss. The saturation behavior of the data in Fig. 7.3 lends some support to the previous assumption of a peak intensity limitation of $2x10^{12}$ W/cm^2 used for Fig. 7.1 and 7.2 above.

The second plot of interest is Fig. 7.4 which plots the average power in the laser cavity as a function of repetition rate. Noting that this plot is presented with a linear y-axis, the average intracavity power is nearly constant as a function of pulse repetition rate. Interpretation of Fig. 7.4 is difficult since the lasers plotted here have distinctly different optics and bandwidths. However, if Fig7.4

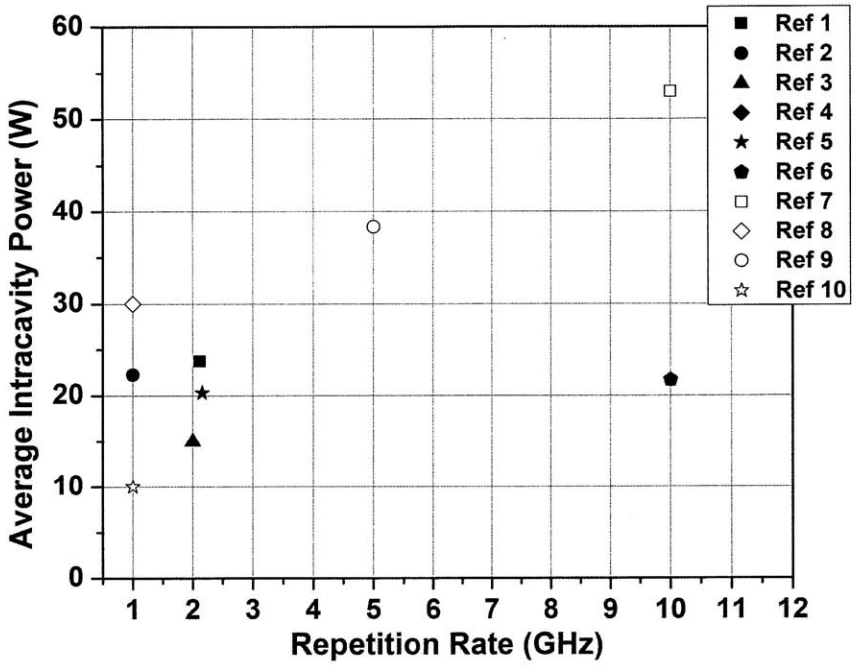

Figure 7.4 – Average intracavity power vs pulse repetition rate for ten references from the literature. Across the reported range of repetition rates, the intracavity power stays within a factor of ten, implying a lower limit to intracavity losses.

is compared with the results in Fig. 7.2, it becomes clear that generating the >100 W of average intracavity power necessary for an octave of bandwidth from a laser with pulses > 8 fs will likely be very difficult. The challenge of generating such a high average power is highlighted by the fact that the result with the highest intracavity power, Ref [13], is a 10 GHz laser with a 1% output coupler. Most likely, a

reduction to a 0.5% output coupler should result in a doubling of the intracavity average power. Further reduction by the factor of 40 necessary to achieve an octave of bandwidth according to Fig. 7.2 is unlikely.

The data presented above highlight the two areas of focus for construction of mode-locked lasers with octave spanning spectra and pulse repetition rates greater than 10 GHz. Reducing the intracavity loss is the most important task. Increasing the amount of pulse energy available for nonlinear broadening of the spectrum by self phase modulation increases the necessary resonant cavity pulse width by a square factor, reducing the dispersion compensated bandwidth. Generating more than 100 W average intracavity power, however, will be challenging considering the results of Fig. 7.4. Without sufficient reduction in intracavity loss, increasing the bandwidth of careful dispersion compensation is the second method for generating an octave of bandwidth at 10 GHz pulse repetition rate. While the corresponding reduction in resonant pulse width is a square factor increase in bandwidth generated by self phase modulation, the increase in complexity and cost for each iteration of chirped mirror design introduces an unwelcome practical aspect to the design process.

The path taken in this thesis has been to combine these approaches. First, a dispersion compensation scheme is devised to allow the laser to operate without additional dispersion compensating elements while simultaneously providing the reflectivity and dispersion compensation bandwidth for a 10 fs pulse. Typically the adjustable dispersion compensating elements are optical quality plates or wedges which are inserted into the intracavity beam at Brewster's angle. Inevitably these optics introduce a finite amount of loss, so their elimination could be key to the success of the project. As an alternative method of allowing some form of dispersion compensating element for the cavity, a wedged Ti:Sapphire crystal is proposed. A tapered crystal could be taller than a standard crystal to allow vertical adjustment of the amount of sapphire material in the cavity, giving a small amount of tuning capability to compensate for manufacturing variances in the chirped mirrors. Time constraints prevented implementation of this second idea; however the approach is still valid.

7.3 Laser design

The physical setup for the 10 GHz laser was chosen to be an x-folded ring type arrangement, Fig. 7.5. A ring cavity configuration was chosen for two reasons; first, the physical size of the laser once constructed will be ~2 times the size of a linear cavity laser of similar repetition rate simply because of the optical path layout of the two types of cavities. Second, a ring type laser offers an advantage by enabling a tighter focusing of the cavity beam in the laser crystal than would be possible with the same ROC mirrors in a confocal cavity configuration. The final physical arrangement used for the 10 GHz laser is shown in Fig 7.5.

In order to minimize the losses internal to the laser cavity, the dispersion compensation scheme was chosen to eliminate the need for extra intracavity elements as discussed in the previous section. During the work for this thesis, two different combinations of optical components were used to successfully construct a mode-locked 10 GHz Ti:Sapphire laser, Table 7.2. The first set of components was a combination of custom designed dispersion compensating mirrors and commercially available optics from Layertec.

	M1	M2	M3	M4	Ti:Sapphire crystal	Focusing lens
Set 1	"green" DCM8, 0.75 cm ROC	"blue" DCM8, 0.75 cm ROC	Layertec high reflector P/N: 100471	Layertec output coupler P/N: 101910	Brewster cut, 2.15 mm GPL	60 mm
Set 2	"green" DCM11, 0.75 cm ROC	"blue" DCM11, 0.75 cm ROC	"green" DCM11, flat	1% INVOC	Brewster cut, 2.28 mm GPL	60 mm

Table 7.2 – optical components used for the two mode-locked Ti:Sapphire lasers with 10 GHz pulse repetition rates reported in this thesis.

The second combination of optics was completely custom designed by the group. The design criteria for this second set of dispersion compensating mirrors was reinforced by the success of the mixed

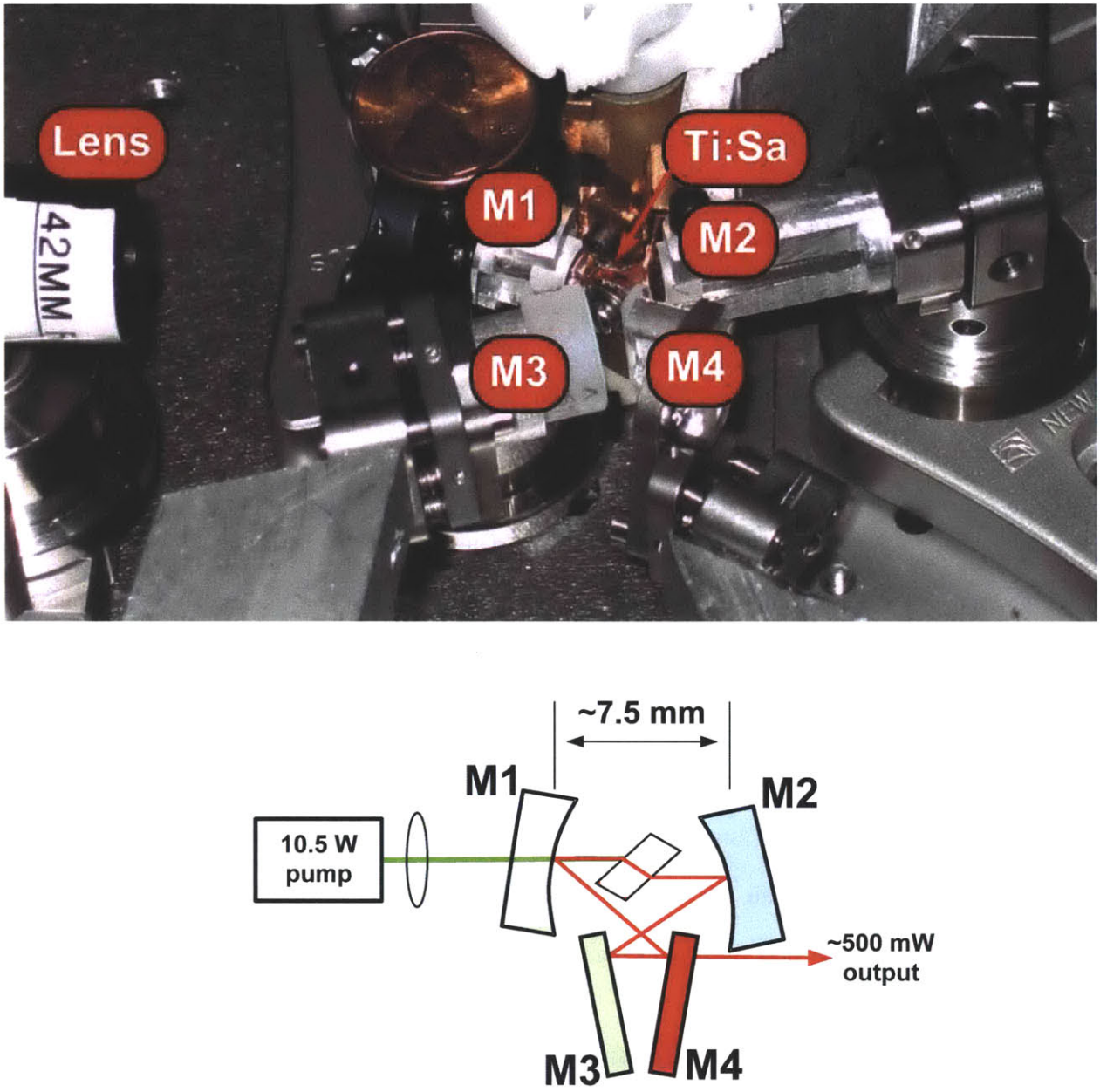

Figure 7.5 – Top - A picture of the laser in a configuration for operation at ~8 GHz. Moving to 10 GHz would require the two flat mirrors to be moved slightly closer together. Bottom – Schematic of the 10 GHz laser discussed in the text. Note the mirror designations discussed in the text and in Table 7.2.

pairs of mirrors used in Set 1. The second set was again designed to completely compensate the dispersion of the sapphire crystal without any extra dispersion compensating elements. With these design criteria in mind Li-Jin Chen designed a pair of dispersion compensating mirrors (generation "DCM11")

where the dispersion of one transit of the Sapphire crystal can be compensated completely by a single pair of dispersion compensating mirrors (mirrors M1 and M2 in Fig. 7.5). The remaining two flat mirrors, M3 and M4, were designed as a copy of M1 and as a gain matched/dispersion matched output coupler respectively. Mirror M3 is simply a plane parallel version of M1, since the DCM11 mirrors are ultimately designed for use in Ti:Sapphire lasers with repetition rates ranging from 80 MHz to 1 GHz, however, their ability to fully compensate for the dispersion of the sapphire crystal with only two reflections.

The reflectivity profile of mirror M4 is designed to have a transmission function that is a scaled version of the Ti:Sapphire gain curve. Frequency dependent output coupling loss which is described by the gain spectrum of the laser material is known as a "gain-matched" output coupler [86]. The general idea is to reduce the amount of self amplitude modulation necessary to start mode-locking by equalizing the net gain in the laser cavity across a wider bandwidth than would normally be the case with standard Bragg type output coupler mirrors. The dispersion on reflection of mirror M4 is designed to compensate the negative dispersion of mirror M4. Again, the general idea is that mirrors M1 and M2 compensate for the dispersion of the sapphire crystal and mirrors M3 and M4 compensate for each other's dispersion as well as the small amount of air dispersion. For the correct length of sapphire crystal, no additional intracavity elements will be necessary, reducing the total intracavity loss.

7.4 Laser operation and characterization

As can likely be guessed from the picture in Fig. 7.5, alignment of a 10 GHz laser is challenging even by the standards of octave spanning Ti:Sapphire lasers. However, once the correct alignment condition was found, and with optics from Set 1, continuous mode-locked operation could be maintained for several hours without the laser in an enclosure. The optics from Set 2 generated a less stable operating condition; the laser could be mode-locked at will, though the laser would drop out of mode-locked operation after only a few minutes. The optical and RF spectrum for operating with optics from Set 1 and Set 2 are

plotted in Fig. 7.6. Output power for Set 1 was 489 mW, and 500 mW for Set 2 with both configurations using 10.5 W of pump power.

Using the same analysis method described above in Section 7.2 and the parameters listed in Table 7.3 a few conclusions can be drawn about the operational state of the current lasers and about what changes should be made for new generations. First, the average power in the laser cavity for both configurations is about the same as the referenced points in Fig. 7.4, indicating that the intracavity loss for both lasers was within a factor of two of what has been achieved in a variety of other laser configurations.

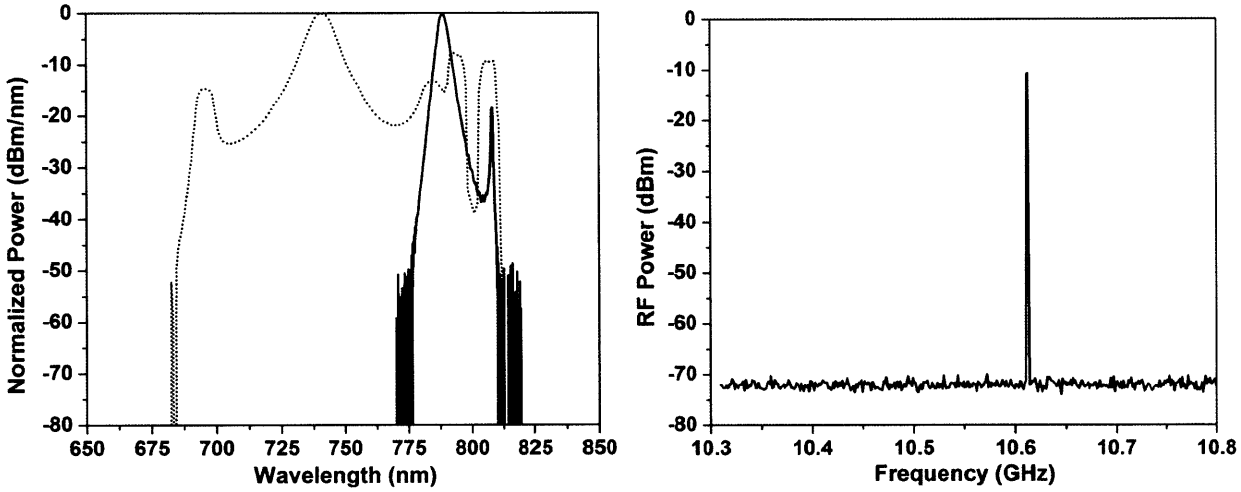

Figure 7.6 – Optical and radio frequency spectra for the two 10 GHz Ti:Sapphire lasers. The optical spectra, left, are plotted in a solid lined for Set 1, while the spectrum for set two is plotted as a dashed line. Set 1 generated a 3.6 nm bandwidth spectrum while Set 2 generated 9.5 nm. The RF spectrum for set one is plotted on the right, while the RF spectrum for Set 2 was not recorded. The repetition rate for Set 2 was measured to be 10.003 GHz.

The peak power was nearly a factor of ten below that achieved in the other configurations (again assuming a 10 μm waist in the sapphire crystal), implying that the dispersion compensation of both of the current configurations was slightly imperfect. In this situation, having a tuning element would likely allow a larger bandwidth of the laser to operate in a low dispersion regime resulting in a broader output spectrum, both due to the resonant pulse , but possibly also due to a finite amount of SPM.

Pump laser type and focusing lens	Transform limited intracavity pulse	f-2f beat possible?	Configuration	ROC Mirrors	Repetition Rate	Pulse Energy	Total Cavity Loss (~1% intravavity)	Average power	Pump power	Estimated Peak Intensity	Reference
Milennia 60 mm	563 fs	No	Ring	0.75 cm	10 GHz	2.5 nJ	1% oc	489 mW	10.5 W	1.2×10^9 W/cm^2	Set 1
Milennia 60 mm	192 fs	No	Ring	0.75 cm	10 GHz	2.5 nJ	1% oc	500 mW	10.5 W	3.6×10^9 W/cm^2	Set2

7.5 Summary and future work

In this section, design criteria for an octave spanning Ti:Sapphire laser with a 10 GHz pulse repetition rate have been developed. These criteria were compared against existing laser systems from the literature and were found to agree well with the published results. Based on these confirmed criteria, two mode-locked Ti:Sapphire lasers operating at 10 GHz were successfully constructed. One was built with commercially available optics and a second was built entirely with custom designed optics. The output power of both lasers was within a factor of two of the only other published 10 GHz mode-locked laser results; however the bandwidth of the lasers constructed during this thesis lasers was only half that of the published results. The difference in bandwidth was traced to the dispersion compensation of both lasers and the lack of an element to allow tuning of the laser dispersion in small amounts.

To circumvent the problem of dispersion compensation and retain the low loss character of the current systems, future high repetition rate lasers should include a dispersion tuning element such as a wedged Ti:Sapphire crystal. Changing the laser cavity arrangement may also provide some benefit since the repetition rate limit with the current setup is at most 12 GHz. The four mirror cavity is extremely challenging to align, although it gives the best advantage for focusing the intracavity beam in the Ti:Sapphire crystal. A three mirror cavity would be a viable option for a laser using a saturable absorber mirror. Such a laser configuration would allow not only higher repetition rates, but also simpler

alignment and self-starting of the mode-locking process. Construction of a saturable absorber mirror which could support octave spanning operation will be extremely challenging.

THIS PAGE INTENTIONALLY LEFT BLANK

Appendix A

Photodetector design

A.1 Introduction

For the majority of measurements which are undertaken, commercially available photodetectors are more than adequate. Occasionally though, a slight modification to an existing detector or a completely separate design will be in order. This section will summarize some general guidelines for constructing balanced photodetectors as well as two limitations of the balanced photodetection technique.

A.2 Balanced transimpedance amplifier design guide

Perhaps the first driving requirement for any detector is how much gain and bandwidth is needed. Referring to Fig. A.1, the output of the transimpedance amplifier (TIA) can be expressed as

$$V_o = (V_+ - V_-)A \tag{A.1}$$

$$V_o = -V_- A = i\frac{AR_F}{1+R_F sC} - V_o\frac{A}{1+R_F sC} \tag{A.2}$$

$$\frac{V_o}{i} = \frac{-AR_F}{A+1+R_F sC} \tag{A.3}$$

which is a standard result [135]. Defining $A = a/s$ as the gain bandwidth product (GBP) in the frequency region near unity gain, the bandwidth of the circuit is

$$f_{3dB} = \sqrt{\frac{GBP}{2\pi R_F C}} \tag{A.4}$$

giving a useful expression linking several design parameters together. Depending on how much transimpedance gain is needed, the next step might be determining the noise characteristics of this circuit.

In the case of needing both high transimpedance gain and high bandwidth, a low noise voltage amplifier is in order as a second stage, Fig A.1. Depending on the application, very large transimpedance gain will limit the available optical dynamic range due to the limited dynamic range of the detector output. An example of an application where extremely high conversion factors (>100kV/W) from a two stage circuit is useful is the measurement undertaken in chapter 6 of this thesis. In that measurement the phase locked loop keeps the DC value of the detector output near zero, only allowing fluctuations outside the loop bandwidth to generate significant output signals.

Low noise design of such a two stage circuit requires a careful distribution of gain. The ideal distribution with respect to meeting both the bandwidth and transimpedance gain goals is to only use as much voltage gain as is necessary to allow the corresponding reduction in transimpedance gain to satisfy the bandwidth requirements of the circuit. Since the TIA is the only stage which can distinguish between signal and noise, it is the stage which will have the most effect on the final signal to noise ratio and should thereby have as much gain as possible. Once the gain has been set for both the TIA and voltage amplifier, analysis of the noise in each stage can be completed. Reference [136] has an exceptionally clear description of how to account for noise contributions from both the op-amp and the gain setting resistors. Note that the only noise contribution which needs to be considered from the photodiode is the shot noise from the photocurrent, as Johnson noise currents due to the shunt resistance of the photodiode are typically far smaller than the input current noise from the op-amp.

Finally, choosing which op-amp(s) to use for a new detector can be an overwhelming task. Between the five or six major semiconductor manufacturers there are thousands of different amplifiers, at least 10% of which are suitable for use in a transimpedance amplifier. Beyond the guideline of gain bandwidth product in Eq. (A.4), the following are a few other useful comparison points.

- The type of transistor used in the input stage of the op-amp will have the largest bearing on the level of input current and voltage noise that the amplifier exhibits. Bipolar junction transistor (BJT) based input stages will have very low voltage noise (<1nV/rtHz) and field effect transistor

(FET) based input stages can have very low input current noise (<1 fA/rtHz). Neither type has extremely low levels of both current and voltage noise.

- Input capacitance of op-amp input terminals is important because it adds to the capacitance of the photodiode, C_D, seen by the TIA input terminal, Fig A.1. The network formed by the input and photodiode capacitance and the feedback capacitance in parallel with R_F will determine the peaking and noise gain of the circuit response. An excellent description of noise gain appears in [137], but briefly this is the increase in the circuit noise floor at high frequencies due to an increase in circuit gain. At high frequencies if the impedance of C_D falls faster than C_F, the amplifier gain will rise until the GBP of the amplifier is reached. Unfortunately, op-amps with input stages composed of FETs tend to have larger input capacitances than BJT based amplifiers. As a result, FET input op amps will have the lowest white noise floor, and unless properly compensated (usually at the expense of bandwidth) they will exhibit peaking and significant noise gain at high frequencies.
- So far all discussions have assumed the use of voltage feedback op-amps. Current feedback op-amps can be used as well, as they tend to have even higher bandwidths than the best voltage feedback op-amps. Unfortunately the input voltage and current noise is typically also much higher, usually enough to negate the bandwidth advantage.

With respect to physical construction, when dealing with high speed semiconductors (>50 MHz), special construction considerations should be made. While not the most aesthetically pleasing method, constructing the circuit on a plain copper clad board is the best method for ensuring success. This type of construction minimizes stray capacitances and offers an excellent low impedance ground plane to mount components on for shielding from external noise sources and reducing the chance for unintended feedback paths. Reference [138] has over 100 pages of excellent discussion and diagrams on how to construct, measure and debug high speed circuitry.

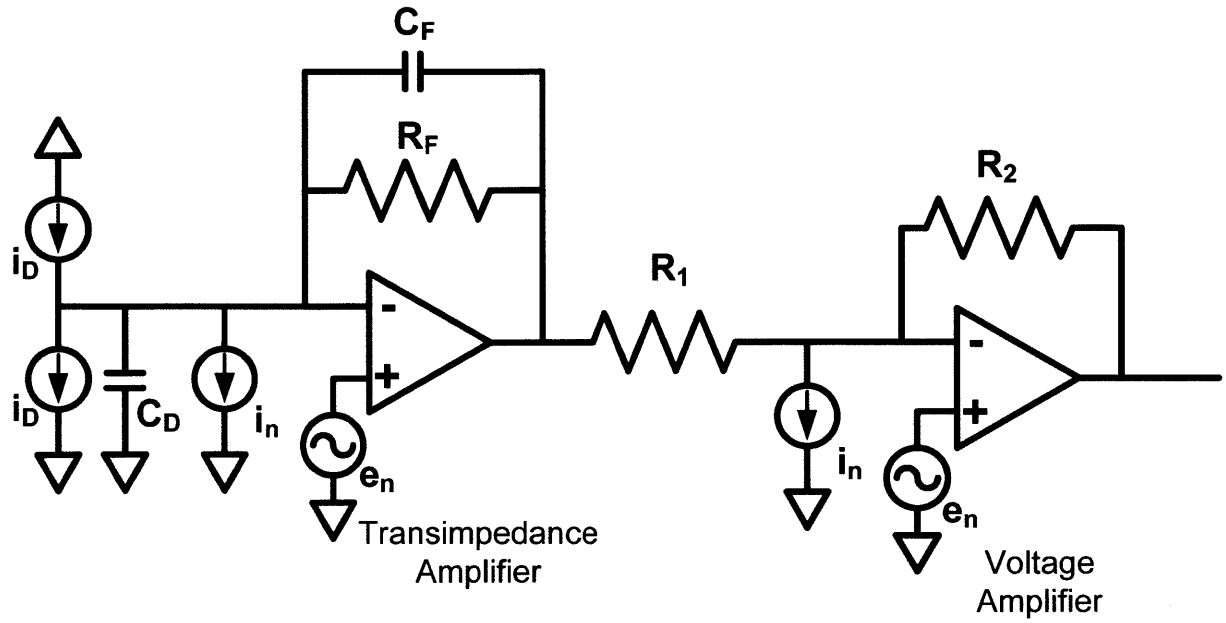

Figure A.1 -- Generic schematic of a balanced detector consisting of a transimpedance stage followed by a voltage amplifier stage. Intrinsic noise sources for the op-amps are shown as current and voltage noise sources e_n and i_n. the capacitance element C_D contains the photodiode capacitance as well as the input capacitance of the op-amp.

A.3 Limitations of balanced detection

Balanced detection is a commonly used measurement method because it offers the opportunity to reject unwanted signals impressed on the interrogating beam before reaching the experiment. Typically "noise" some sort of intensity noise in the laser source or power fluctuation caused by propagation of the beam to the part of the experiment which will perform the desired modulation. Cancellation occurs because both photodetectors measure the exact same signal, except for the desired modulation on one beam or ideally differential modulation on both beams, Fig 5.3. The ratio of differential signal output to the output due to signals present on both channels is the common mode rejection ratio (CMRR). Rejection of common mode signal occurs because ideally the phase and amplitude of photocurrent fluctuations are equal, so no signal voltage is generated at the amplifier output. There are limitations to the amount of common mode cancellation which is achievable, two which are particularly applicable to the experiment in chapter 6 are degradation of the CMRR due to the differential signal level and phase mismatch between otherwise common mode signals on both arms of the detector.

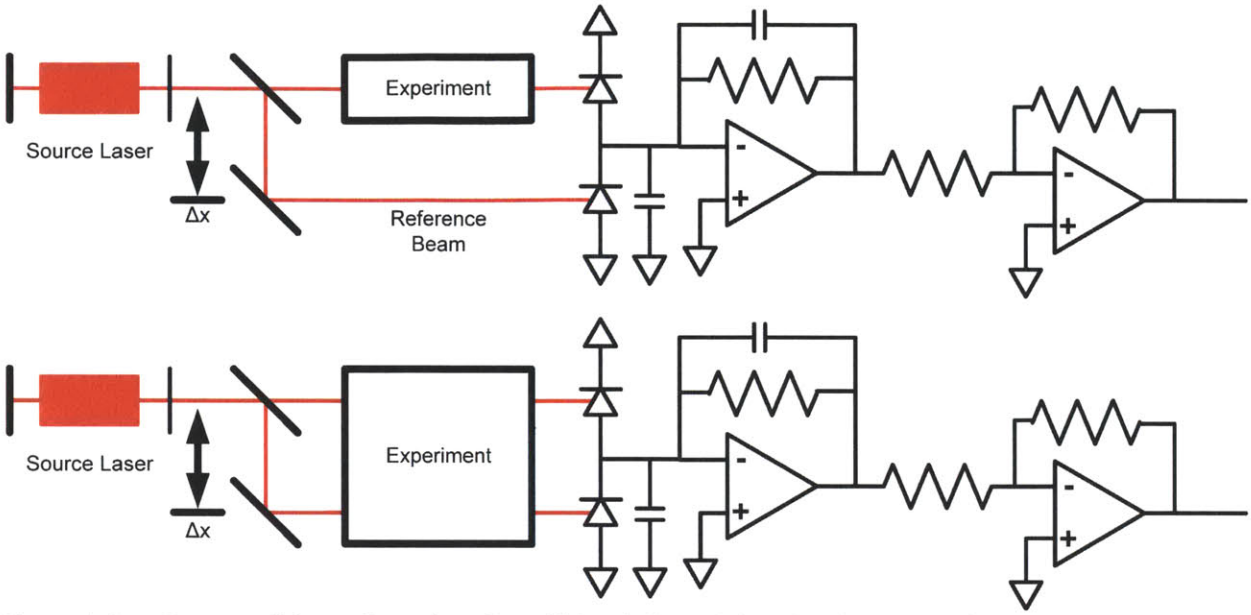

Figure A.2 -- Two possible configurations for utilizing balanced detection in an experimental setup. The upper setup is essentially the same as many simple setups, with the exception of the reference beam. The presence of the second beam allows cancellation of intensity fluctuations in the laser which occur prior to the beamsplitter. This is similar to a Hobbs type detector [139]. In the lower setup, the experiment spans both the main beam and the reference beam. In this second arrangement the signal from the experimental setup can be fully differential such that the signal in the two channels is opposite. Modulating both beams offers the additional possibility of removing errors in the signal which are common to both channels. Both setups suffer from the same difference in path length between the beamsplitter and the detector, limiting the total CMRR available as the frequency of noise processes increase. See text and Figure A.3.

A.3.1 Effect of differential signal level

To eliminate signals common to both arms of the detector, the phase and amplitude of the "common mode" signal must be the same on both photodiodes. To have an output other than zero, the balanced detector must have different optical power levels on the two photodiodes. Depending on how a particular noise source scales with signal level, this unbalance can change the CMRR as a function of the differential signal level. Defining the photocurrent in each of the two diodes

$$I_1 = I_{1DC} + i_1 + \delta i_1 + \alpha I_1 \qquad \text{(A.5)}$$

$$I_2 = I_{2DC} + i_2 + \delta i_2 + \alpha I_2 \qquad \text{(A.6)}$$

where I_{jDC} is the large signal DC component, i_j is the desired small signal modulation, δi_j is a strictly additive noise process accumulated after the beamsplitter in Fig. A.2, and αI_1 and αI_2 are fractional noise

processes described as the RIN of the source laser. The balanced detector subtracts these two photocurrents to yield

$$I_1 - I_2 = I_{1DC} + i_1 + \delta i_1 + \alpha I_1 - I_{2DC} - i_2 - \delta i_2 - \alpha I_2 \qquad \text{(A.7)}$$

If the output of the balanced detector is used as error point in a control loop, the output of the balanced detector must have zero mean on the timescale corresponding to the phase locked loop bandwidth, requiring $I_{1DC}=I_{2DC}$. Assuming a nearly 50/50 power split on the photodetectors, the balanced detector voltage output will be

$$V_o = (I_1 - I_2) R G_T = \left[(i_1 - i_2) + (\delta i_1 - \delta i_2) + \alpha (i_1 - i_2 + \delta i_1 - \delta i_2) \right] R G_T \quad \text{(A.8)}$$

with photodiode responsivity R and transimpedance gain G_T. In the ideal case, only the first term on the right side of Eq. (A.8) is non-zero. However, because there must be a non-zero output for both the control loop to work and to make a measurement of the differential signal outside the bandwidth of the feedback loop, all terms in Eq.(A.8) are non zero. Because of the requirement for a non-zero output, the CMRR can be redefined as an Effective CMRR, as the ratio of the desired differential term and those terms which are either undesired or caused by what should be a common mode source

$$ECMRR = \frac{(i_1 - i_2)}{(\delta i_1 - \delta i_2) + \alpha (i_1 - i_2) + \alpha (\delta i_1 - \delta i_2)} \approx \frac{(i_1 - i_2)}{(\delta i_1 - \delta i_2) + \alpha I_{DC} \sqrt{2}} \quad \text{(A.9)}$$

where $\alpha (I_1 - I_2) \approx 0$ by virtue of the feedback loop. The resulting expression emphasizes the need for a small differential signal to maintain good RIN suppression by the balanced detector. Estimations of the ECMRR for a given measurement should be made by determining the integrated voltage error during a given measurement period (integrating from the detector bandwidth to the RBW or inverse duration of a time trace for signals which are fast Fourier transformed) and dividing by what would be the DC voltage level of either channel without balancing.

$$e_n = \sqrt{\int_{RBW}^{DetBW} S_V(f)\, df} \qquad \text{(A.10)}$$

$$ECMRR = \frac{e_n}{V_{DC}} \qquad \text{(A.11)}$$

This new ECMRR can be applied to known fractional noise spectra to predict their contribution to the final signal output.

A.3.2 Effect of length mismatch for common mode signals

The second contributor to a limited CMMR is unequal path lengths for each arm of the experiment between the beamsplitter and the detector. Cancellation of common mode signals requires that both the amplitude and phase of the common mode signals be equal at the balanced detector. Using the small angle approximation the phase error at the detector can be defined as

$$\delta\varphi = 2\pi \frac{\Delta x}{c} f \qquad \text{(A.12)}$$

where Δx is the difference in path length between the two arms and f is the measurement frequency of interest. Using Eq.(A.12) and assuming equal signal amplitudes at the two photodetectors, the resulting rejection of the common mode signal is plotted in Fig. 5.4 plots Eq.(A.12) for several values of Δx.

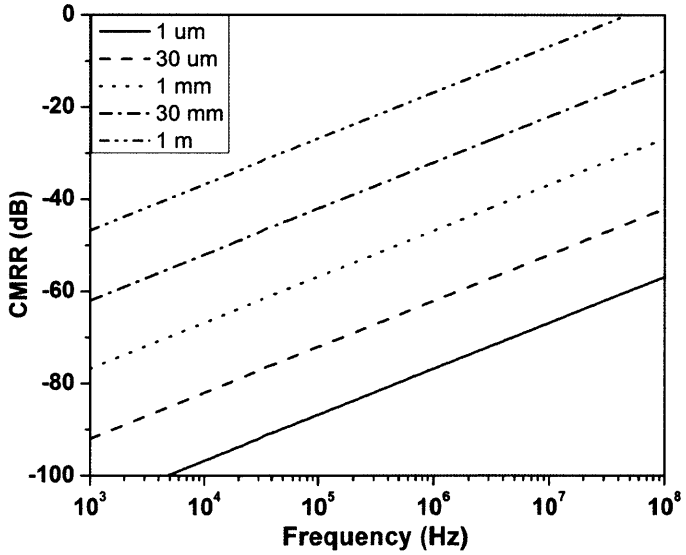

Figure A.3 -- Plot of maximum possible common mode rejection ratio as a function of frequency for several different differential distances, Δx, as depicted in Figure A.2.

THIS PAGE INTENTIONALLY LEFT BLANK

Appendix B

Piezo mounted mirrors for optical cavity length stabilization

B.1 Introduction

Laser cavity length stabilization is an extremely important part of frequency comb system design. The following is a review of theoretical and empirical conclusions for control of frequency comb systems, specifically repetition rate control systems which are necessary for stabilizing the frequency spacing of the comb lines in the optical spectrum of a mode-locked laser. To control the repetition rate, the length of the optical cavity must be controlled, which can be achieved several ways, the most common method being to mount one of the laser cavity mirrors on a piezoelectric transducer as the main feedback element in a phase locked loop. Design criteria for the piezo mirror support as well as design of driver circuits appropriate for capacitive loads are discussed. A brief introduction to control theory is also included. Far more in depth analysis can be found in the works of Gardner [140] and Best [141], to cite only two in a rich field of study.

B.2 Basic control theory

Phase locked loops are no different from any other control problem. There are details regarding how to detect the phase error between two oscillators, and how to implement a control signal to send to the oscillator, but these problems can be generalized to any controlled system. The general control problem is drawn in Fig. B.1, where all practical details have been abstracted away. The output signal, *R(t)*, is

ideally exactly the same as the input signal *C(t)*, with the impulse response of the intervening system and sensor response represented by *G(s)* and *H(s)*, respectively.

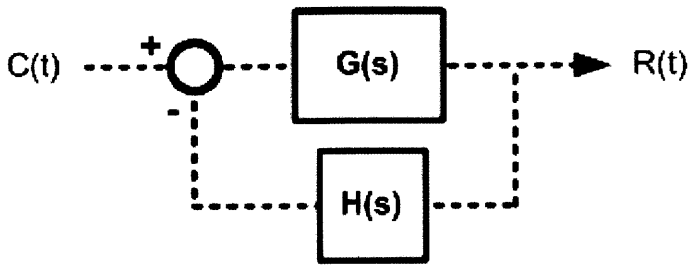

Figure B.1 – Generic feedback system diagram. *C(t)* is the input signal which one would like the output signal, *R(t)*, to match. *G(s)* is known as the plant or forward path gain, and *H(s)* is known as the sensor or the backward path gain. Systems which can be abstracted to this level are easily represented by Black's formula as described in the text.

The response of such a system can be characterized using Black's formula, which relates the output of a feedback system to its input through the two gain blocks as

$$\frac{R(s)}{C(s)} = \frac{G(s)}{1+G(s)H(s)} \tag{B.1}$$

The product, *G(s)H(s)* in the denominator is known as the loop transmission, *L(s)*, and it determines the range of frequencies over which the output will faithfully follow the input as well as the stability of the overall system. Good tracking, $R(t) \approx C(t)$, occurs when the product *L(s)* is large, and stability is assured as long as *L(s)* doesn't approach -1. The impact of the magnitude and phase of L(s) is more readily apparent when written as

$$\frac{R(s)}{C(s)} = \frac{G(s)}{1+|L(s)|\exp(i\angle L(s))} \tag{B.2}$$

Both the tracking and stability conditions are best assessed by inspection of a frequency domain plot of *L(s)*, Fig. B.2. In the two example plots for *L(s)*, both systems have large gain at low frequencies, however the gain of the two systems is very different at high frequencies. As the gain of the system described by the dotted line falls at high frequency, the phase is still far from -180°, preventing a positive or nearly positive feedback situation. The system described by the solid line however has a bit too much

frequency independent gain such that when the loop transmission phase crosses -180, the gain is only a slightly larger than unity, causing an uncontrolled enhancement in the loop response. For this particular example, the uncontrolled response can be prevented by either lowering the system gain, or by changing the system response so the phase at the desired unity gain frequency is much smaller than -180°.

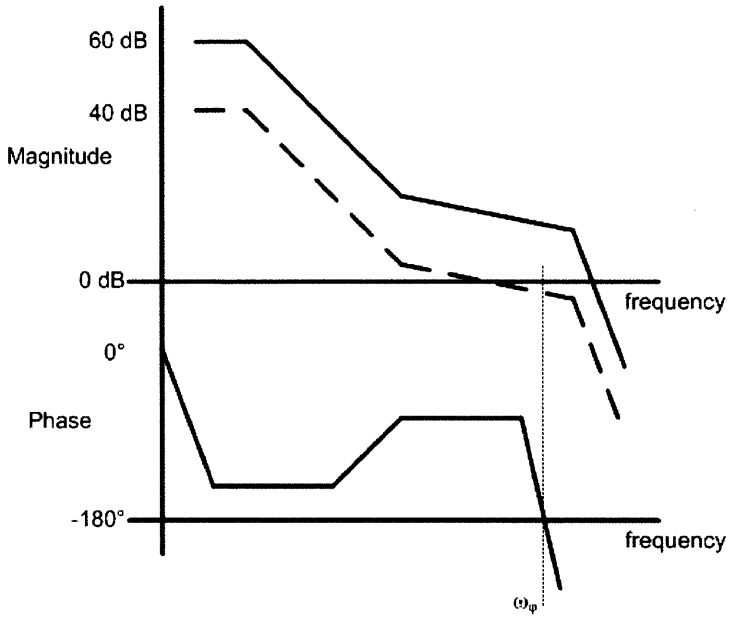

Figure B.2 – Bode plot of a hypothetical system with two different levels of frequency independent gain. The phase response of the system is the same in both cases, but the system is only stable in the configuration depicted by the dotted line. The slight reduction in frequency independent gain causes the system response to become unstable near ω_ϕ.

The important result from this analysis is twofold. First, characterization of the frequency domain characteristics of the feedback loop as carefully as possible and over as wide of a bandwidth as possible will allow optimization of the feedback loop limiting factors. Second, ensure that L(s) doesn't approach -1 within the bandwidth of interest by increasing the bandwidth of response of the lowest bandwidth components in the feedback loop and eliminating any time delays in the loop. In repetition rate control systems for mode-locked lasers, the lowest bandwidth component is the piezo mounted mirror.

B.3 Piezo mirror system

The most commonly encountered method for controlling the repetition rate of mode-locked lasers is to mount one of the laser cavity mirrors on a small piezoelectric transducer. Displacing one of the cavity mirrors both minimizes the optical dispersion added to the laser due to the length stabilization system and generally gives the largest feedback bandwidth. Other methods are possible for fiber laser systems using intracavity electro-optic phase modulators, but this is only possible due to the much reduced optical bandwidth of those lasers [142]. The piezo mirror system, Fig.B.3, is composed of four pieces: the mirror, piezo, the mount which holds the piezo and mirror, and the circuit used to drive the piezo. As the piezo mirror systems described here will operate on only a rather low voltage (+/-15 V) with very small piezos (5x5x2mm typically), with a total dynamic range usually only about 100 nm before deformation or tilting of the piezo mirror will adversely affect the laser operation. Generally the limited dynamic range is overcome by using a second piezo with much longer travel and much lower bandwidth to cancel larger cavity length fluctuations (up to 10 μm) which occur on much longer timescales (minutes).

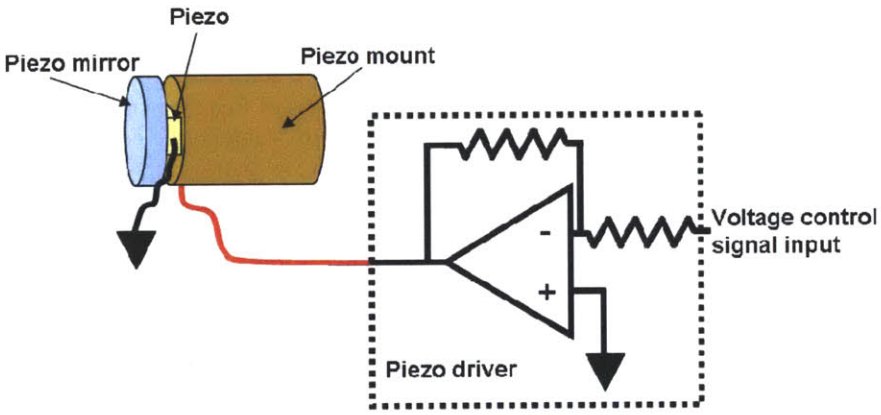

Figure B.3 -- Schematic of the piezo mirror system.

B.4 Piezo driver

The piezo driver as described here is based on a low voltage, high current (< 60v) op amp (OPA551, OPA552, etc.) operational amplifier. It is possible to build a fast, high voltage(+/- 150v) piezo drivers,

however for practical reasons such circuits are more complex and more expensive. As discussed in the section on feedback theory, the main problem to be overcome for all components in the feedback path is the time delay in signal propagation from input to output. In the frequency domain a time delay is manifested as a phase delay which will reduce the stability and bandwidth of the feedback system. The problem in this section is to generate a circuit which will control the voltage across the piezo used to displace one of the cavity mirrors with minimal time delay.

The most accurate way to model the electrical response of a piezo is as a RLC circuit to account for the capacitance of the dielectric, inertia of the physical structure, as well as any internal or external resistances. However, doing so presumes use of the piezo in a range where the resonance frequency is important. Since near resonance the phase and magnitude response of the piezo (both electrical and dimensional) change quite quickly, it is best to avoid this frequency range. By avoiding the resonance, it is reasonable to treat the piezo as a pure capacitance.

By driving a purely capacitive load, a rather common solution is to put a small resistance at the output of the driver before the capacitive load, Fig. B.4(D). This stabilizes the circuit by creating a first order response between the input voltage to output voltage transfer function. While the circuit is stable, it is also usually slow because optimization of the output resistor value is either not done or not understood. To understand why using this configuration works and how to optimize it, a model of the circuit should be constructed. Fig. B.4 gives progressively more complicated models of the op amp's circuit including the output resistance of the op amp, the capacitive load of the piezo and finally the stabilizing load resistor. Fig. B.4(C) allows understanding of why simply attaching a capacitive load to an op amp can destabilize the circuit.

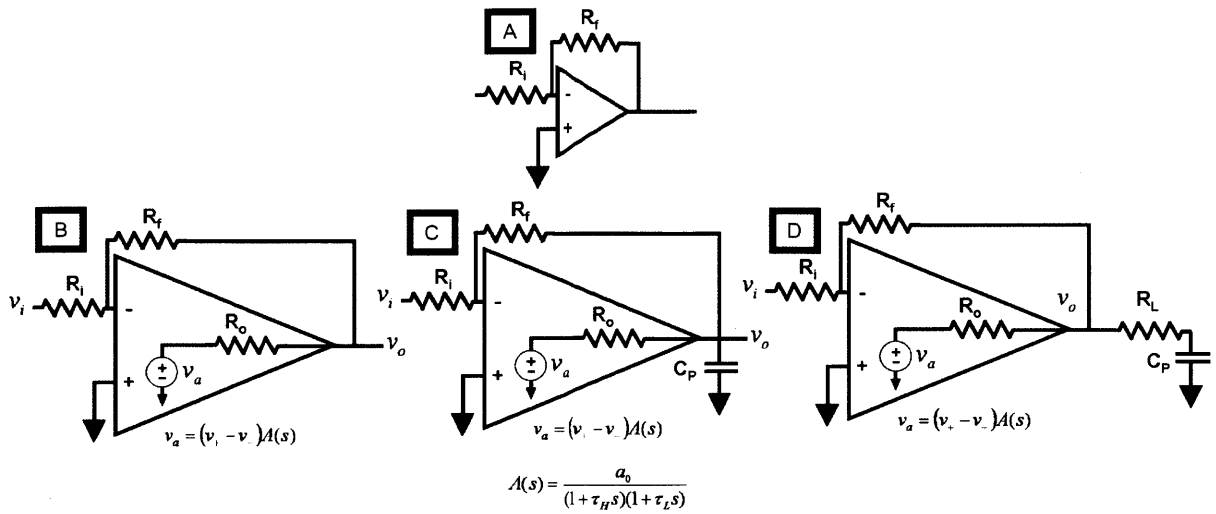

Figure B.4 -- Three levels of piezo driver complexity. A – Generic inverting configuration with little meaningful detail. R_i and R_f are the input and feedback resistors. B - More complete model of op amp operating circuit including output resistance and internal transfer function. A(s) will be best modeled by a two pole system (τ_H and τ_L) with high DC gain *a0* which captures both the tendency for instability from capacitive loads and the non-infinite gain and resulting non-zero error signal. C - Similar to case B except now the capacitive load of a piezo is included. D - Lag compensated piezo driver with external stabilizing resistor R_L.

Normally the equation for the output voltage of the op amp is written as,

$$v_a = (v_+ - v_-)\,A(s) \qquad \text{(B.3)}$$

and since the amplifier is in an inverting configuration another equation is used to describe the voltage at the inverting input as a function of both the input and output voltages

$$v_- = v_i(Z_{id}) + v_a(Z_{od}) \qquad \text{(B.4)}$$

where $Z_{id,od}$ is the impedance divider network from the input and output voltage sources of the op amp, v_i and v_a to the inverting input. The result, while not terribly complex, hides the role of the output resistance in destabilizing the system. The same result can be obtained in a more understandable way by making the reasonable assumption that the output resistance *Ro* of the op amp and the load resistance *RL* should be much smaller than both the input and feedback resistors, *Ri* and *Rf* in Fig.2 allowing the op amp circuit to be drawn as shown in Fig. B.5, where *H(s)* can be recognized as a low pass filter. Drawing the feedback loop for the circuit in Fig. B.5, the solution for *L(s)* determines the circuit stability and bandwidth.

The loop transmission of the circuit of the resulting circuit is plotted in Fig. B.6, where it is possible to determine from the total phase at high frequency that the system transfer function v_o/v_i,

contains three poles. Generally in systems similar to the one described in Fig. B.5, the second pole will determine where the phase crossover point is and therefore the stability of the system. The second pole is generated by the output resistance of the op amp and the load capacitance of the piezo. Unless the load capacitance is very small (< 100pF) the op amp will be unstable or will have an oscillating response due to the small phase margin.

To prevent oscillation, the most common solution is to put a small resistor at the output of the op amp as shown in Fig. B.4(D). The addition of the output resistor changes *H(s)* from a low pass filter to a passive lag filter where the response of *H(s)* for frequencies above $1/2\pi R_L C_P$ is purely resistive so that the piezo driver behaves like a two pole system which can never be unstable. The type of response the circuit gives will however be a function of the frequency at which the lag filter makes its transition, Fig. B.7. While it seems that the problem is solved, one caution is warranted. The resistor value chosen will only provide stable control of the piezo voltage for capacitances equal to or greater to the capacitance that the circuit was designed for.

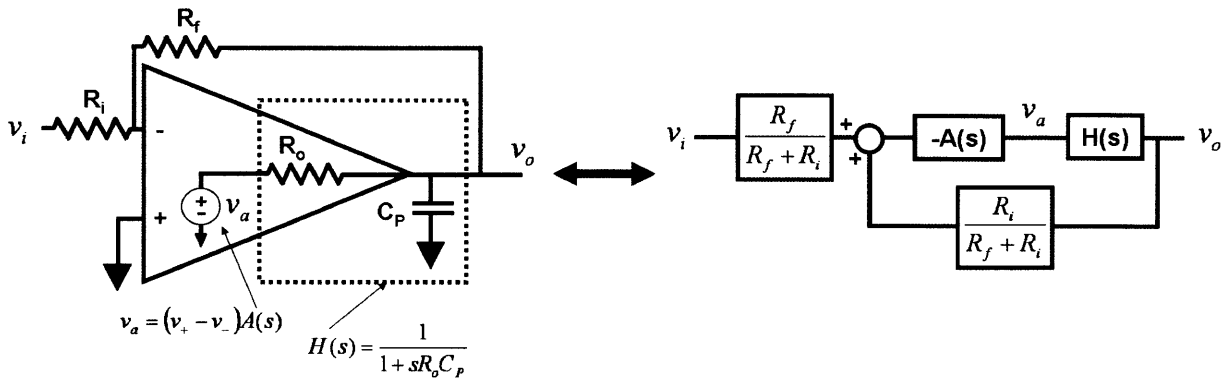

Figure B.5 -- Because of the large difference in impedance between *Ro* and the *Rf* + *Ri* combination, it is possible to separate the effect of the low pass filter formed by *Ro* and C_P from the rest of the feedback network. By making this separation, drawing the block diagram of the system becomes both simple and general.

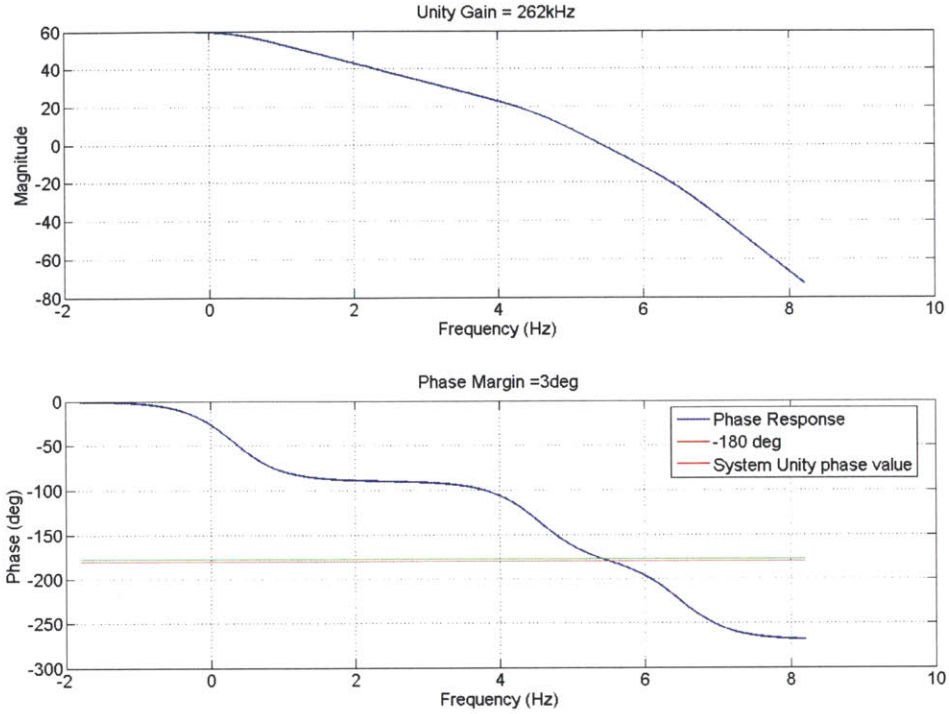

Figure B.6 -- Loop transmission of the capacitively loaded op amp. Note that there are three poles, where the high and low frequency poles are determined by the op amps transfer function and the middle pole is generated by the output resistance and load capacitance. As a result, the phase margin is only 2 deg which will not allow for a controllable response.

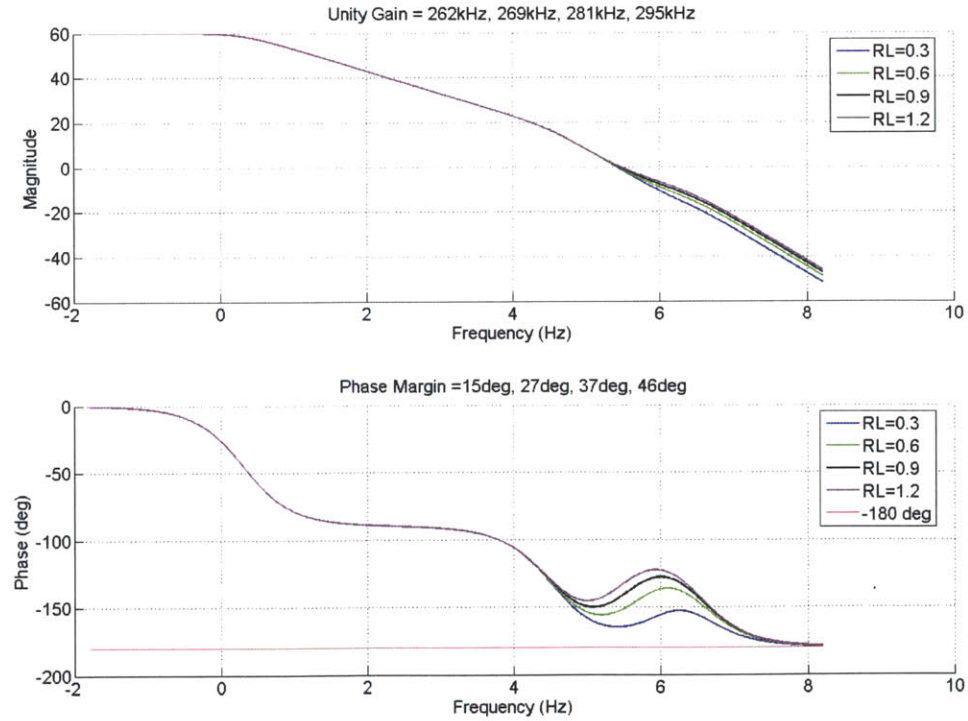

Figure B.7 -- Loop transmission of the capacitively loaded op amp with lag compensation. Note that there are still three poles, however a zero has been added to the system such that the overall phase response is only -180 deg. More importantly, the minimum phase margin can be varied by tuning the value of the load resistor.

B.5 Piezo mirror and piezo mount design

Design of the piezo mount and selection of the mirror to be mounted on the piezo have the largest influence on the final response of the repetition rate control system. The mirror design is rather straightforward, although the design of the mount is somewhat subtle and will require the bulk of this section. The section will conclude with a note about adhesive attachment of the mirror to the piezo and the piezo to the mount.

The mirror should be made as small as is practical for the optics portion of the setup. Reducing the mirror diameter will reduce the mass of the mirror and subsequently the force (piezo voltage) required to displace the mirror at a given speed. With the reduction in mass in mind, the mirror thickness should not be less than ~1 mm since thinner substrates are both difficult to polish , and subject to deformation due to stress from any dielectric coating and from the glue used to mount the mirror to the piezo.

The purpose of the piezo mount is to resist the force applied by the piezo so that the majority of that force is utilized in displacing the mirror. The mass of the piezo is limited though, by the requirement to keep the resonance frequency of the mount outside the desired feedback bandwidth. The piezo will be excited by a broadband signal from the feedback loop, but ideally the mount is assumed to be a completely solid mass and only the spring constant of the piezo must be considered with respect to possible vibration modes. It turns out that the vibration modes of the mount itself are the dominant contributors, and the physical shape of the resulting mount as well as the materials of construction are quite important.

For simplicity of analysis, a cylindrical shape is assumed, as in Fig. B.3. For an oscillating point load applied near the cylindrical axis, there are three dominant vibrating modes: A compression mode, a Bessel type mode and a bending mode due to off axis placement of the piezo and mirror on the face of the mount. The compression mode is a density wave which travels at the speed of sound in the material. Speed of sound is defined as

$$c_s = \sqrt{\frac{E}{\rho}} \tag{B.5}$$

with E as the modulus of elasticity, or Young's modulus, and the material density ρ. Using the same relation as in optics, the frequency of the first compression mode as a function of the rod's length L can be found using

$$f_c = \frac{c_s}{2L} \tag{B.6}$$

The lowest order bending mode is determined by assuming a beam with cylindrical cross section that is free (unsupported) at both ends [143]

$$f_b = \frac{1}{2\pi}(\beta_1 L)^2 \sqrt{\frac{EI}{\rho L^4}} \tag{B.7}$$

with I as the area moment of inertia of the beam and $(\beta L)^2$ as a parameter related to the boundary condition, which in this case takes a value of 22.4. According to Fig. B.8, the bending mode has the lowest

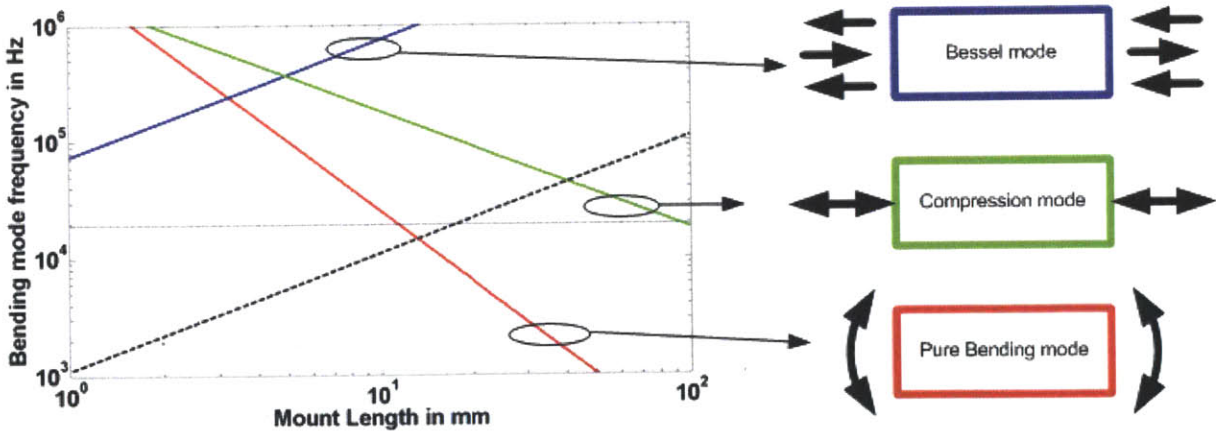

Figure B.8 – Diagram of bending modes and the frequencies of the lowest vibrating mode for a ½" diameter copper rod. The dotted line represents the mass of the cylinder as a function of the cylinder length, and the straight line at 20 kHz is represents 30 times the mass of the piezo mirror. The mount length where the goal mass and the rods actual mass intersect is the desired piezo length. In this case a resonance should be expected at a frequency of ~200 kHz.

frequency of all three of the modes considered in the frequency range of interest. Fortunately, excitation of the bending mode requires the piezo and mirror to be attached to the face of the cylindrical mount away from the center. Careful centering of the mirror and piezo can reduce or eliminate excitation of this mode. The lowest order Bessel mode is approximated by a bending mode across the plane of the piezo mounting face.

$$f_B = \frac{9L}{r^2}\sqrt{\frac{E}{\pi\rho}} \tag{B.8}$$

with r as the radius of the cylindrical mount. The stiffness of the mount when excited from the center face of the mount is very high, and thereby the lowest vibrating mode frequency is also very high, and the Bessel mode need not be considered except for very thin mounts.

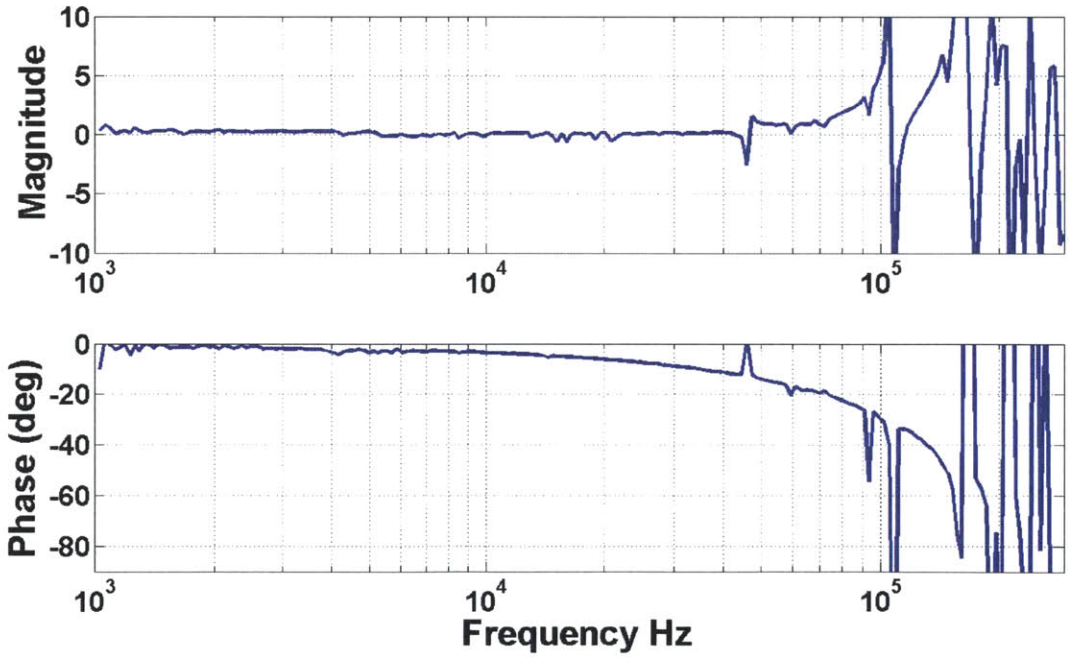

Figure B.9 – Measured response function of the piezo designed using methods described in Appendix B. Note the prominent resonance at 100 kHz as predicted by the analysis in this section. The small zero-pole doublet resonance 45 kHz is likely from deformation of the mirror.

The response of the piezo used in chapter 3 of this thesis was designed using the described design method, with the result of the design calculations used for Fig. B.8. Plotted in Fig. B.9 is the result of a response measurement made using the technique described in Appendix B.6. The result of that

characterization agrees very well with the predictions of Fig. B.8., specifically, there is a prominent resonance at 100 kHz as predicted by the calculation for the lowest order compression mode.

While the above analysis accurately predicts the frequency of a resonance in the piezo response function, the resonance itself can be a problem for the feedback loop. The first resonance in Fig. B.9 represents a nearly 10 dB enhancement of the piezo response, which can force a significant reduction in feedback loop bandwidth to ensure that *L(s)* does not approach -1 at that frequency. Methods for dealing with these resonances include filling the mount with some sort of damping material to reduce the amount of stored energy in the mount at resonance [144].

Finally, while no carefully controlled experiments have been made to compare different types of adhesive, all piezo mirrors constructed in this thesis were assembled using CrystalBond brand adhesive, which is a thermal adhesive, which melts at about 150 C and hardens to a crystalline structure. Certain epoxies may perform as well or better, however CrystalBond offers the opportunity to re-set previously glued optics in case of error or redesign simply by reheating the piece with no apparent loss of holding strength. Best results are achieved when using the absolute minimum amount of adhesive.

B.6 Characterizing the piezo mirror system

Measurement of the piezo mirror system transfer function can be achieved in a few different ways (electrical drive impedance of piezo mirror, direct measurement of piezo voltage, etc.), though direct measurement of the mirror displacement as a function of applied voltage will arguably give the most unambiguous result. To measure the voltage to mirror displacement transfer function, the piezo mirror system should be installed in a Michaelson interferometer similar to the one depicted in Fig.6. Biasing the arm length imbalance so that the central fringe detected by the photodiode is at the half intensity point and driving the piezo mirror system with a small amplitude swept sine wave signal, the piezo mirror transfer function can be directly measured.

A few details of Fig.6 should be highlighted, first is the requirement that all of the components outlined in gray should be mounted on their own small breadboard. Further, the breadboard should be

placed on at minimum a thin piece of rubber or preferably a very dense foam to isolate the setup from large amplitude vibrations of the larger table which will make the measurement unnecessarily difficult. Some small amount of isolation is generally necessary even if an air isolated optical table is used as the workspace. The defocusing lens is used to enable easier

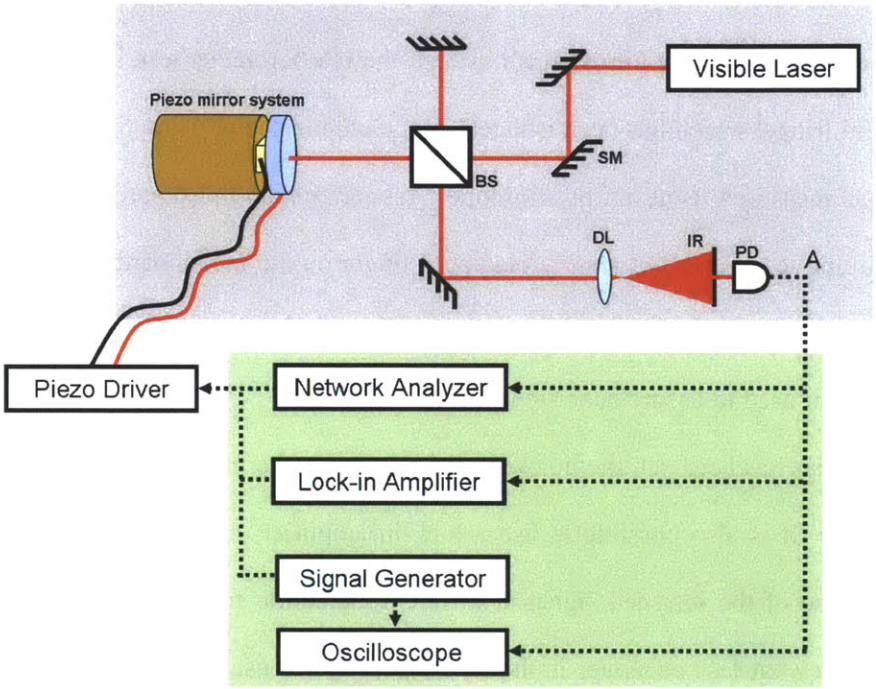

Figure B.10 -- Schematic of the optical and electrical layout of a piezo mirror system response measurement. All of the components out- lined in gray should be located on their own small breadboard separate from the main workspace. The area in green outlines simultaneously three different possible methods for recovering the piezo mirror system response. SM-silver mirror, DL-Defocusing mirror, IR-Circular iris, BS-Non-polarizing 50/50 beamsplitter, PD-Photodiode, A-location where piezo driver should be connected for measurement system calibration.

isolation of the central fringe of the interference pattern on to the active area of the photodiode. Fringe selection is further enhanced by using a circular iris again to ensure that the only light reaching the photodiode active area is from the central fringe of the interference pattern. Care should be taken to avoid back reflections into the laser as this will destabilize the laser with an increase in intensity noise. The visible laser should also be reasonably narrow band (< 3 nm) to allow good fringe contrast, though bandwidth is usually only an issue with inexpensive laser diodes.

Measurement of the response can be recorded several different ways, however prior to any measurement a calibration should be made to remove the effect of the piezo driver, cabling delays, etc.

Calibration can be achieved by, Fig.6, connecting the output of the piezo driver directly to the cable which would normally connect to the photodiode. For both the reference measurement and the measurement of the piezo mirror system, the parameters of interest are the phase and amplitude of the signal returned from the photodiode cable at point A with respect to the signal which excited the system minus any static offsets. The assumption is that the system should have a unity transfer function at DC. To make the measurement of the piezo mirror system the interferometer arm imbalance should be adjust so that the central fringe, which has been isolated on the photodetector using the circular iris, is at its half intensity point as measured using an oscilloscope. Air currents and unsuppressed vibrations will likely cause the bias to move around, but simply placing a finger on the breadboard should allow control over the bias point which should be visually monitored throughout the measurement regardless of the measurement system used to ensure consistent system response.

Once the bias has been set, the quickest and easiest way to measure the system response is to use a network analyzer. It is also possible to use a lock-in amplifier, making several measurements of the amplitude and phase of the returned signal at different excitation frequencies to map out the response. Finally, while somewhat less accurate, it should be possible to use a common signal generator and an oscilloscope to recover the amplitude and phase of the returned signal with respect to the excitation signal. The last method is somewhat undesirable as it is quite slow and prone to errors especially with respect to the phase measurement since it requires the experimenter to manually recover the phase of two time domain waves by measuring a small time delay between two smooth functions on the oscilloscope screen. Accurate measurements are possible, though the repeatability of the results are highly dependent on the user whereas the previous two methods are much less dependent of user skill and patience.

Measurement of the response from 1 kHz to 1 MHz is enough to completely characterize most systems. Attempting to measure the system response at excitation frequencies lower than 1 kHz is problematic because the system must simultaneously cancel the effect of environmental noise and excite the system at the same range of frequencies, making separation of the signal from the noise very difficult. As for excitation amplitudes, use only enough to generate a clean measurement signal. There are two

reasons for using small amplitude drive signals, first, it is important to only record the linear response of the systems and minimizing the excitation amplitude should minimize the contribution of any non-linear terms. Second, when the mode-locked laser's repetition rate is locked, the piezo will generally only see an AC error signal amplitude of <100mV or less, so characterizing the system with a 5 volt signal is not representative of the final operating condition.

Once the amplitude and phase of both the reference response, X(s), and the measured piezo, piezo driver and mirror response, Y(s), have been measured over the desired range of excitation frequencies, determining the piezo transfer function is simply a matter of taking a ratio of the two results.

$$H_{piezo}(s) = \frac{Y(s)}{X(s)} \tag{B.9}$$

Similarly the phase response can be recovered from

$$\phi_H = \phi_Y - \phi_X \tag{B.10}$$

THIS PAGE INTENTIONALLY LEFT BLANK

Appendix C

Frequency Metrology

C.1 Introduction

Characterization of frequency combs requires understanding of some basic phase and frequency noise definitions. Understanding how these representations are related and how they change when multiplying, dividing the frequency of a signal of interest is especially important. A clear understanding is of particular importance when selecting a stabilization scheme for a particular frequency comb application. This section will review some basic representations of noise properties of high quality oscillators. Official definitions from the IEEE are described very concisely in Ref [145].

C.2 Basic representations

In this discussion, an oscillator will refer to any electrical or optical signal which has a regular, repeating waveform, the lowest harmonic of which will be used to characterize the stability of the oscillator. With these assumptions, the electric field, or voltage signal of such an oscillator can be written as [146]

$$E(t) = E_0 \sin\left(2\pi\nu_0 t + \phi(t)\right) \qquad \text{(C.1)}$$

where E_0 is the wave amplitude, ν is the average frequency and $\phi(t)$ is the time dependent phase fluctuations. Amplitude fluctuations have been neglected since in high quality oscillators the phase/frequency noise spectrum is much larger than the amplitude noise spectrum. The instantaneous frequency of the oscillator is

$$\nu = \nu_0 + \frac{1}{2\pi}\frac{\partial\phi(t)}{\partial t} \tag{C.2}$$

and the normalized fractional frequency deviation is

$$y(t) = \frac{1}{2\pi\nu_0}\frac{\partial\phi(t)}{\partial t} \tag{C.3}$$

Using the autocorrelation theorem for Fourier Transforms [147] the two sided power spectrum of the fractional frequency fluctuations can be defined as

$$S_y(f) = \int \langle y(t)y(t)^* \rangle e^{-i\omega t} dt \tag{C.4}$$

Substituting (C.3) gives the relationship between the phase and frequency noise spectra

$$S_\phi(f) = \frac{\nu_0^2}{f^2} S_y(f) \tag{C.5}$$

which are both frequency domain representations of the phase or frequency noise of the oscillator. Typically S_y and S_ϕ are used to describe phase and frequency noise over an offset frequency range of 100 mHz to several megahertz. For phase and frequency noise at even smaller offset frequencies, the generally accepted method is to use the Allan deviation [148].

The Allan deviation is a measure of the average fractional change in frequency of an oscillator as a function of the averaging time. Using Eq.(C.3) the average fractional change in frequency for the n^{th} measurement period of duration T can be defined as

$$\overline{y(T_n)} = \frac{1}{T}\int_{T_n}^{T_{n+1}} y(t)\,dt \tag{C.6}$$

Averaging over many successive averaging periods as an approximation of many identical oscillators simultaneously gives

$$\sigma_y(T) = \left\langle \frac{1}{2}\left[\overline{y(T_{n+1})} - \overline{y(T_n)}\right]^2 \right\rangle^{1/2} \tag{C.7}$$

Since only a finite number of measurements can be made, Eq.(C.7) is typically approximated as

$$\sigma_y(T)=\left[\frac{1}{2(M-1)}\sum_{i=1}^{M-1}\left[y(T_{n+1})-y(T_n)\right]^2\right]^{1/2} \quad \text{(C.8)}$$

where the summation is made over M cycles. There are several subtleties to using this representation, many of which are well described in [147].

The Allan Deviation and frequency domain phase and frequency noise representations are related through a window function which describes the Allan deviation averaging period

$$\sigma_y{}^2(T)=\frac{2}{\nu_0^2(\pi T)^2}\int_0^\infty S_y(f)\frac{\sin^4(\pi fT)}{f^2}df=\frac{2}{\nu_0{}^4(\pi T)^2}\int_0^\infty f^2S_\varphi(f)\sin^4(\pi fT)df \quad \text{(C.9)}$$

with the window function for the Allan deviation as

$$|W_A|=\frac{\sqrt{2}}{\pi fT}\sin^2(\pi fT) \quad \text{(C.10)}$$

C.3 Frequency comb example

When stabilizing a frequency comb, it is important to realize the implications of choosing a reference oscillator at one frequency over another. As a simple example, consider stabilization of the optical spectrum of a Ti:Sapphire laser to a "low phase noise" quartz crystal oscillator. The pulse repetition rate of the laser to be stabilized is ~1 GHz, and the optical frequency of a particular comb line of interest is a ~100 THz. In this example, the pulse repetition rate is ν_0 and the optical frequency is ν_n, so the instantaneous optical frequency can be defined as

$$\nu_n=N\nu_0+\frac{N}{2\pi}\frac{\partial(t)}{\partial t} \quad \text{(C.11)}$$

and the fractional frequency deviation as

$$y_n(t)=\frac{N}{2\pi N\nu_0}\frac{\partial(t)}{\partial t} \quad \text{(C.12)}$$

noting that in equation (C.12) that the fractional frequency fluctuations are being described in terms of the new frequency requiring that S_y remain constant over frequency translation, though S_ϕ will not as shown below

$$S_{\phi N}(f) = \frac{N^2 \nu_0^2}{f^2} S_y(f) \qquad \text{(C.13)}$$

The obvious implication of Eq. (C.13) result is that measurements using frequency combs which can be averaged for several seconds will likely have a much less stringent stabilization requirement than those which require low phase noise in the optical spectrum.

Going back to the example, and defining the stability of the quartz crystal as characterized by an Allan deviation of 10^{-9} on a 10 s timescale and phase noise of -120 dBc/Hz at 1kHz offset. From the results of (C.12) and (C.13), the 100 THz comb line needed for the experiment will also have a fractional frequency stability of 10^{-9} on a 10 s timescale, though the phase noise at the 1 kHz offset frequency will have increased by a factor of 10^{10} to -20 dBc/Hz. Depending on the application of the resulting comb, such a large increase in phase noise may not be an issue. If phase noise is still a problem, three options are possible: reduce the feedback bandwidth of the phase locked loop which stabilizes the pulse repetition rate to the quartz oscillator, find a better reference oscillator or use a different stabilization scheme.

Bibliography

1. A. D. Ludlow, T. Zelevinsky, G. K. Campbell, S. Blatt, M. M. Boyd, M. H. G. de Miranda, M. J. Martin, J. W. Thomsen, S. M. Foreman, J. Ye, T. M. Fortier, J. E. Stalnaker, S. A. Diddams, Y. Le Coq, Z. W. Barber, N. Poli, N. D. Lemke, K. M. Beck, and C. W. Oates, "Sr lattice clock at 1 x 10(-16) fractional uncertainty by remote optical evaluation with a Ca clock," Science **319**, 1805-1808 (2008).
2. T. Steinmetz, T. Wilken, C. Araujo-Hauck, R. Holzwarth, T. W. Hansch, L. Pasquini, A. Manescau, S. D'Odorico, M. T. Murphy, T. Kentischer, W. Schmidt, and T. Udem, "Laser Frequency Combs for Astronomical Observations," Science **321**, 1335-1337 (2008).
3. C.-H. Li, A. J. Benedick, P. Fendel, A. G. Glenday, F. X. Kärtner, D. F. Phillips, D. Sasselov, A. Szentgyorgyi, and R. L. Walsworth, "A laser frequency comb that enables radial velocity measurements with a precision of 1 cm s(-1)," Nature **452**, 610-612 (2008).
4. D. A. Braje, M. S. Kirchner, S. Osterman, T. Fortier, and S. A. Diddams, "Astronomical spectrograph calibration with broad-spectrum frequency combs," European Physical Journal D **48**, 57-66 (2008).
5. M. T. Murphy, T. Udem, R. Holzwarth, A. Sizmann, L. Pasquini, C. Araujo-Hauck, H. Dekker, S. D'Odorico, M. Fischer, T. W. Hansch, and A. Manescau, "High-precision wavelength calibration of astronomical spectrographs with laser frequency combs," Monthly Notices of the Royal Astronomical Society **380**, 839-847 (2007).
6. Z. Jiang, C.-B. Huang, D. E. Leaird, and A. M. Weiner, "Optical arbitrary waveform processing of more than 100 spectral comb lines," Nat Photon **1**, 463-467 (2007).
7. A. Ehlers, I. Riemann, S. Martin, R. Le Harzic, A. Bartels, C. Janke, and K. Konig, "High (1 GHz) repetition rate compact femtosecond laser: A powerful multiphoton tool for nanomedicine and nanobiotechnology," Journal of Applied Physics **102**, 014701 (2007).
8. A. Bartels, T. Dekorsy, and H. Kurz, "Femtosecond Ti : sapphire ring laser with a 2-GHz repetition rate and its application in time-resolved spectroscopy," Optics Letters **24**, 996-998 (1999).
9. S. A. Diddams, M. Kirchner, T. Fortier, D. Braje, A. M. Weiner, and L. Hollberg, "Improved signal-to-noise ratio of 10 GHz microwave signals generated with a mode-filtered femtosecond laser frequency comb," Opt. Express **17**, 3331-3340 (2009).
10. J. E. Stalnaker, S. A. Diddams, T. M. Fortier, K. Kim, L. Hollberg, J. C. Bergquist, W. M. Itano, M. J. Delany, L. Lorini, W. H. Oskay, T. P. Heavner, S. R. Jefferts, F. Levi, T. E. Parker, and J. Shirley, "Optical-to-microwave frequency comparison with fractional uncertainty of 10-15," Applied Physics B: Lasers and Optics **89**, 167-176 (2007).
11. S. A. Diddams, A. Bartels, T. M. Ramond, C. W. Oates, S. Bize, E. A. Curtis, J. C. Bergquist, and L. Hollberg, "Design and control of femtosecond lasers for optical clocks and the synthesis of low-noise optical and microwave signals," Ieee Journal of Selected Topics in Quantum Electronics **9**, 1072-1080 (2003).
12. J. J. McFerran, E. N. Ivanov, A. Bartels, G. Wilpers, C. W. Oates, S. A. Diddams, and L. Hollberg, "Low-noise synthesis of microwave signals from an optical source," Electronics Letters **41**, 650-651 (2005).
13. A. Bartels, D. Heinecke, and S. A. Diddams, "Passively mode-locked 10 GHz femtosecond Ti:sapphire laser," Opt. Lett. **33**, 1905-1907 (2008).
14. P. W. Roth, A. J. Maclean, D. Burns, and A. J. Kemp, "Directly diode-laser-pumped Ti:sapphire laser," Opt. Lett. **34**, 3334-3336 (2009).
15. P. W. Roth, A. J. Maclean, D. Burns, and A. J. Kemp, "Direct diode-laser pumping of a mode-locked Ti:sapphire laser," Opt. Lett. **36**, 304-306 (2011).
16. H. N. Chapman, P. Fromme, A. Barty, T. A. White, R. A. Kirian, A. Aquila, M. S. Hunter, J. Schulz, D. P. DePonte, U. Weierstall, R. B. Doak, F. R. N. C. Maia, A. V. Martin, I. Schlichting, L.

Lomb, N. Coppola, R. L. Shoeman, S. W. Epp, R. Hartmann, D. Rolles, A. Rudenko, L. Foucar, N. Kimmel, G. Weidenspointner, P. Holl, M. Liang, M. Barthelmess, C. Caleman, S. Boutet, M. J. Bogan, J. Krzywinski, C. Bostedt, S. Bajt, L. Gumprecht, B. Rudek, B. Erk, C. Schmidt, A. Homke, C. Reich, D. Pietschner, L. Struder, G. Hauser, H. Gorke, J. Ullrich, S. Herrmann, G. Schaller, F. Schopper, H. Soltau, K.-U. Kuhnel, M. Messerschmidt, J. D. Bozek, S. P. Hau-Riege, M. Frank, C. Y. Hampton, R. G. Sierra, D. Starodub, G. J. Williams, J. Hajdu, N. Timneanu, M. M. Seibert, J. Andreasson, A. Rocker, O. Jonsson, M. Svenda, S. Stern, K. Nass, R. Andritschke, C.-D. Schroter, F. Krasniqi, M. Bott, K. E. Schmidt, X. Wang, I. Grotjohann, J. M. Holton, T. R. M. Barends, R. Neutze, S. Marchesini, R. Fromme, S. Schorb, D. Rupp, M. Adolph, T. Gorkhover, I. Andersson, H. Hirsemann, G. Potdevin, H. Graafsma, B. Nilsson, and J. C. H. Spence, "Femtosecond X-ray protein nanocrystallography," Nature **470**, 73-77 (2011).

17. F. Schotte, M. Lim, T. A. Jackson, A. V. Smirnov, J. Soman, J. S. Olson, G. N. Phillips, M. Wulff, and P. A. Anfinrud, "Watching a Protein as it Functions with 150-ps Time-Resolved X-ray Crystallography," Science **300**, 1944 -1947 (2003).
18. M. Lewenstein, P. Balcou, M. Y. Ivanov, A. L'Huillier, and P. B. Corkum, "Theory of high-harmonic generation by low-frequency laser fields," Physical Review A **49**, 2117 (1994).
19. A. Gordon and F. Kärtner, "Scaling of keV HHG photon yield with drive wavelength," Opt. Express **13**, 2941-2947 (2005).
20. E. N. Ivanov and M. E. Tobar, "Low phase-noise sapphire crystal microwave oscillators: current status," Ultrasonics, Ferroelectrics and Frequency Control, IEEE Transactions on **56**, 263-269 (2009).
21. H. A. Haus and A. Mecozzi, "Noise of mode-locked lasers," Quantum Electronics, IEEE Journal of **29**, 983-996 (1993).
22. R. Paschotta, "Noise of mode-locked lasers (Part II): timing jitter and other fluctuations," Appl Phys B **79**, (2004).
23. E. N. Ivanov, J. J. McFerran, S. A. Diddams, and L. Hollberg, "Noise properties of microwave signals synthesized with femtosecond lasers," in *Frequency Control Symposium and Exposition, 2005. Proceedings Of the 2005 IEEE International* (2005), pp. 932-936.
24. E. N. Ivanov, S. A. Diddams, and L. Hollberg, "Experimental study of noise properties of a Ti:sapphire femtosecond laser," Ultrasonics, Ferroelectrics and Frequency Control, IEEE Transactions on **50**, 355-360 (2003).
25. L.-J. Chen, A. J. Benedick, J. R. Birge, M. Y. Sander, and F. Kärtner, "Octave-spanning, dual-output 2.166 GHz Ti:sapphire laser," Opt. Express **16**, 20699-20705 (2008).
26. J. N. Eckstein, A. I. Ferguson, and T. W. Hänsch, "High-Resolution Two-Photon Spectroscopy with Picosecond Light Pulses," Phys. Rev. Lett. **40**, 847 (1978).
27. H. Schnatz, B. Lipphardt, J. Helmcke, F. Riehle, and G. Zinner, "First Phase-Coherent Frequency Measurement of Visible Radiation," Phys. Rev. Lett. **76**, 18 (1996).
28. T. W. Hänsch, "A proposed sub-femtosecond pulse synthesizer using separate phase-locked laser oscillators," Optics Communications **80**, 71-75 (1990).
29. T. Haensch, "A Passion for Precision,"Srockholm University (December 8, 2005).
30. H. R. Telle, G. Steinmeyer, A. E. Dunlop, J. Stenger, D. H. Sutter, and U. Keller, "Carrier-envelope offset phase control: A novel concept for absolute optical frequency measurement and ultrashort pulse generation," Applied Physics B: Lasers and Optics **69**, 327-332 (1999).
31. S. A. Diddams, D. J. Jones, J. Ye, S. T. Cundiff, J. L. Hall, J. K. Ranka, R. S. Windeler, R. Holzwarth, T. Udem, and T. W. Hansch, "Direct link between microwave and optical frequencies with a 300 THz femtosecond laser comb," Physical Review Letters **84**, 5102-5105 (2000).
32. D. J. Jones, S. A. Diddams, J. K. Ranka, A. Stentz, R. S. Windeler, J. L. Hall, and S. T. Cundiff, "Carrier-envelope phase control of femtosecond mode-locked lasers and direct optical frequency synthesis," Science **288**, 635-639 (2000).
33. T. Udem, J. Reichert, R. Holzwarth, and T. W. Hansch, "Absolute optical frequency measurement of the cesium D-1 line with a mode-locked laser," Physical Review Letters **82**, 3568-3571 (1999).

34. J. K. Ranka, R. S. Windeler, and A. J. Stentz, "Visible continuum generation in air-silica microstructure optical fibers with anomalous dispersion at 800 nm," Opt. Lett. **25**, 25-27 (2000).
35. J. Stenger, H. Schnatz, C. Tamm, and H. R. Telle, "Ultraprecise Measurement of Optical Frequency Ratios," Phys. Rev. Lett. **88**, 073601 (2002).
36. M. Zimmermann, C. Gohle, R. Holzwarth, T. Udem, and T. W. Hansch, "Optical clockwork with an offset-free difference-frequency comb: accuracy of sum- and difference-frequency generation," Optics Letters **29**, 310-312 (2004).
37. S. A. Diddams, T. Udem, J. C. Bergquist, E. A. Curtis, R. E. Drullinger, L. Hollberg, W. M. Itano, W. D. Lee, C. W. Oates, K. R. Vogel, and D. J. Wineland, "An Optical Clock Based on a Single Trapped 199Hg+ Ion," Science **293**, 825-828 (2001).
38. H. A. Haus, J. G. Fujimoto, and E. P. Ippen, "Structures for additive pulse mode locking," J. Opt. Soc. Am. B **8**, 2068-2076 (1991).
39. J. P. Gordon and R. L. Fork, "Optical resonator with negative dispersion," Opt. Lett. **9**, 153-155 (1984).
40. R. Szipöcs, K. Ferencz, C. Spielmann, and F. Krausz, "Chirped multilayer coatings for broadband dispersion control in femtosecond lasers," Opt. Lett. **19**, 201-203 (1994).
41. F. X. Kärtner, U. Morgner, R. Ell, T. Schibli, J. G. Fujimoto, E. P. Ippen, V. Scheuer, G. Angelow, and T. Tschudi, "Ultrabroadband double-chirped mirror pairs for generation of octave spectra," Journal of the Optical Society of America B-Optical Physics **18**, 882-885 (2001).
42. J. R. Birge and F. X. Kärtner, "Phase distortion ratio: alternative to group delay dispersion for analysis and optimization of dispersion compensating optics," Opt. Lett. **35**, 2469-2471 (n.d.).
43. R. Y. Chiao, E. Garmire, and C. H. Townes, "Self-Trapping of Optical Beams," Phys. Rev. Lett. **13**, 479 (1964).
44. M. J. Ablowitz, *Solitons and the Inverse Scattering Transform* (SIAM, 1981).
45. M. Y. Sander, E. P. Ippen, and F. X. Kärtner, "Carrier-envelope phase dynamics of octave-spanning dispersion-managed Ti: sapphire lasers," Opt. Express **18**, 4948-4960 (2010).
46. L. Matos, O. D. Mücke, J. Chen, and F. X. Kärtner, "Carrier-envelope phase dynamics and noise analysis in octave-spanning Ti:sapphire lasers," Opt. Express **14**, 2497-2511 (2006).
47. F. X. Kärtner, "6.977 Course notes, Spring 2005," (2005).
48. F. L. Walls and A. Demarchi, "RF Spectrum of a Signal after Frequency Multiplication; Measurement and Comparison with a Simple Calculation," Instrumentation and Measurement, IEEE Transactions on **24**, 210-217 (1975).
49. F. Quinlan, G. Ycas, S. Osterman, and S. A. Diddams, "A 12.5 GHz-spaced optical frequency comb spanning > 400 nm for near-infrared astronomical spectrograph calibration," Review of Scientific Instruments **81**, 063105-9 (2010).
50. A. Benedick, D. Tyurikov, M. Gubin, R. Shewmon, I. Chuang, and F. X. Kärtner, "Compact, Ti:sapphire-based, methane-stabilized optical molecular frequency comb and clock," Opt. Lett. **34**, 2168-2170 (2009).
51. S. M. Foreman, A. Marian, J. Ye, E. A. Petrukhin, M. A. Gubin, O. D. Mucke, F. N. C. Wong, E. P. Ippen, and F. X. Kärtner, "Demonstration of a HeNe/CH4-based optical molecular clock," Optics Letters **30**, 570-572 (2005).
52. O. D. Mucke, R. Ell, A. Winter, J. W. Kim, J. R. Birge, L. Matos, and F. X. Kärtner, "Self-referenced 200 MHz octave-spanning Ti : sapphire laser with 50 attosecond carrier-envelope phase jitter," Optics Express **13**, 5163-5169 (2005).
53. M. A. Gubin, D. A. Tyurikov, A. S. Shelkovnikov, E. V. Kovalchuk, G. Kramer, and B. Lipphardt, "Transportable He-Ne/Ch4 Optical Frequency Standard and Absolute Measurements of Its Frequency," Ieee Journal of Quantum Electronics **31**, 2177-2182 (1995).
54. M. A. Gubin and E. D. Protsenko, "Laser frequency standards based on saturated-dispersion lines of methane," Quantum Electronics **27**, 1048-1062 (1997).
55. T. M. Fortier, J. Ye, S. T. Cundiff, and R. S. Windeler, "Nonlinear phase noise generated in air-silica microstructure fiber and its effect on carrier-envelope phase," Opt. Lett. **27**, 445-447 (2002).

56. T. M. Ramond, S. A. Diddams, L. Hollberg, and A. Bartels, "Phase-coherent link from optical to microwave frequencies by means of the broadband continuum from a 1-GHz Ti : sapphire femtosecond oscillator," Optics Letters **27**, 1842-1844 (2002).
57. R. Jason Jones, J.-C. Diels, J. Jasapara, and W. Rudolph, "Stabilization of the frequency, phase, and repetition rate of an ultra-short pulse train to a Fabry-Perot reference cavity," Optics Communications **175**, 409-418 (2000).
58. R. J. Jones and J. C. Diels, "Stabilization of femtosecond lasers for optical frequency metrology and direct optical to radio frequency synthesis," Physical Review Letters **86**, 3288-3291 (2001).
59. R. W. P. Drever, J. L. Hall, F. V. Kowalski, J. Hough, G. M. Ford, A. J. Munley, and H. Ward, "Laser phase and frequency stabilization using an optical resonator," Applied Physics B: Lasers and Optics **31**, 97-105 (1983).
60. E. D. Black, "An introduction to Pound–Drever–Hall laser frequency stabilization," Am. J. Phys. **69**, 79 (2001).
61. J. Chen, J. W. Sickler, P. Fendel, E. P. Ippen, F. X. Kärtner, T. Wilken, R. Holzwarth, and T. W. Hansch, "Generation of low-timing-jitter femtosecond pulse trains with 2 GHz repetition rate via external repetition rate multiplication," Optics Letters **33**, 959-961 (2008).
62. M. J. Thorpe, K. D. Moll, R. J. Jones, B. Safdi, and J. Ye, "Broadband cavity ringdown spectroscopy for sensitive and rapid molecular detection," Science **311**, 1595-1599 (2006).
63. R. Holzwarth, T. Udem, T. W. Hansch, J. C. Knight, W. J. Wadsworth, and P. S. J. Russell, "Optical frequency synthesizer for precision spectroscopy," Physical Review Letters **85**, 2264-2267 (2000).
64. T. Rosenband, D. B. Hume, P. O. Schmidt, C. W. Chou, A. Brusch, L. Lorini, W. H. Oskay, R. E. Drullinger, T. M. Fortier, J. E. Stalnaker, S. A. Diddams, W. C. Swann, N. R. Newbury, W. M. Itano, D. J. Wineland, and J. C. Bergquist, "Frequency Ratio of Al+ and Hg+ Single-Ion Optical Clocks; Metrology at the 17th Decimal Place," Science **319**, 1808-1812 (2008).
65. S. M. Foreman, K. W. Holman, D. D. Hudson, D. J. Jones, and J. Ye, "Remote transfer of ultrastable frequency references via fiber networks," Review of Scientific Instruments **78**, 021101 (2007).
66. T. M. Fortier, A. Bartels, and S. A. Diddams, "Octave-spanning Ti : sapphire laser with a repetition rate > 1 GHz for optical frequency measurements and comparisons," Optics Letters **31**, 1011-1013 (2006).
67. R. Ell, U. Morgner, F. X. Kärtner, J. G. Fujimoto, E. P. Ippen, V. Scheuer, G. Angelow, T. Tschudi, M. J. Lederer, A. Boiko, and B. Luther-Davies, "Generation of 5-fs pulses and octave-spanning spectra directly from a Ti : sapphire laser," Optics Letters **26**, 373-375 (2001).
68. G. Cerullo, S. De Silvestri, V. Magni, and L. Pallaro, "Resonators for Kerr-lens mode-locked femtosecond Ti:sapphire lasers," Opt. Lett. **19**, 807-809 (1994).
69. V. Magni, G. Cerullo, S. D. Silvestri, and A. Monguzzi, "Astigmatism in Gaussian-beam self-focusing and in resonators for Kerr-lens mode locking," J. Opt. Soc. Am. B **12**, 476-485 (1995).
70. D. Huang, M. Ulman, L. H. Acioli, H. A. Haus, and J. G. Fujimoto, "Self-focusing-induced saturable loss for laser mode locking," Opt. Lett. **17**, 511-513 (1992).
71. T. Brabec, P. F. Curley, C. Spielmann, E. Wintner, and A. J. Schmidt, "Hard-aperture Kerr-lens mode locking," J. Opt. Soc. Am. B **10**, 1029-1034 (1993).
72. T. Brabec, C. Spielmann, P. F. Curley, and F. Krausz, "Kerr lens mode locking," Opt. Lett. **17**, 1292-1294 (1992).
73. V. Magni, G. Cerullo, and S. De Silvestri, "ABCD matrix analysis of propagation of gaussian beams through Kerr media," Optics Communications **96**, 348-355 (1993).
74. V. Magni, G. Cerullo, and S. De Silvestri, "Closed form gaussian beam analysis of resonators containing a Kerr medium for femtosecond lasers," Optics Communications **101**, 365-370 (1993).
75. X. G. Huang and M. R. Wang, "Analytical design for Kerr-lens mode locking of compact solid-state lasers," Optics Communications **158**, 322-330 (1998).
76. A. E. Siegman, *Lasers* (University Science Books, 1986).

77. H. A. Haus, *Waves and Fields In Optoelectronics* (Prentice-Hall, 1984).
78. D. E. Spence, P. N. Kean, and W. Sibbett, "60-Fsec Pulse Generation from a Self-Mode-Locked Ti-Sapphire Laser," Optics Letters **16**, 42-44 (1991).
79. H. Kogelnik, E. Ippen, A. Dienes, and C. Shank, "Astigmatically compensated cavities for CW dye lasers," Quantum Electronics, IEEE Journal of **8**, 373-379 (1972).
80. A. Penzkofer, M. Wittmann, M. Lorenz, E. Siegert, and S. Macnamara, "Kerr lens effects in a folded-cavity four-mirror linear resonator," Opt Quant Electron **28**, 423-442 (1996).
81. Y. Chen, F. X. Kärtner, U. Morgner, S. H. Cho, H. A. Haus, E. P. Ippen, and J. G. Fujimoto, "Dispersion-managed mode locking," J. Opt. Soc. Am. B **16**, 1999-2004 (1999).
82. F. X. Kärtner, N. Matuschek, T. Schibli, U. Keller, H. A. Haus, C. Heine, R. Morf, V. Scheuer, M. Tilsch, and T. Tschudi, "Design and fabrication of double-chirped mirrors," Optics Letters **22**, 831-833 (1997).
83. "McMaster Carr company - Acoustical foam/Lead absorber-barriers - Part No. 53995T34," (n.d.).
84. J. Kim, J. Chen, J. Cox, and F. X. Kärtner, "Attosecond-resolution timing jitter characterization of free-running mode-locked lasers," Opt. Lett. **32**, 3519-3521 (2007).
85. M. S. Kirchner and S. A. Diddams, "Grism-based pulse shaper for line-by-line control of more than 600 optical frequency comb lines," Opt. Lett. **35**, 3264-3266 (2010).
86. L.-J. Chen, M. Y. Sander, and F. X. Kärtner, "Kerr-lens mode locking with minimum nonlinearity using gain-matched output couplers," Opt. Lett. **35**, 2916-2918 (2010).
87. U. Morgner, "Erzeugung kürzester Laserpulse im nahen Infraroten," (2001).
88. R. Kienberger, M. Hentschel, M. Uiberacker, C. Spielmann, M. Kitzler, A. Scrinzi, M. Wieland, T. Westerwalbesloh, U. Kleineberg, U. Heinzmann, M. Drescher, and F. Krausz, "Steering Attosecond Electron Wave Packets with Light," Science **297**, 1144 -1148 (2002).
89. L. M. de Matos, "Octave-spanning lasers for optical metrology applications," http://dspace.mit.edu/handle/1721.1/34389.
90. S. T. Cundiff and J. Ye, "Colloquium: Femtosecond optical frequency combs," Reviews of Modern Physics **75**, 325 (2003).
91. T. Steinmetz, T. Wilken, C. Araujo-Hauck, R. Holzwarth, T. Hänsch, and T. Udem, "Fabry–Pérot filter cavities for wide-spaced frequency combs with large spectral bandwidth," Applied Physics B: Lasers and Optics **96**, 251-256 (2009).
92. M. S. Kirchner, D. A. Braje, T. M. Fortier, A. M. Weiner, L. Hollberg, and S. A. Diddams, "Generation of 20 GHz, sub-40 fs pulses at 960 nm via repetition-rate multiplication," Opt. Lett. **34**, 872-874 (2009).
93. G. T. Nogueira, B. W. Xu, Y. Coello, M. Dantus, and F. C. Cruz, "Broadband 2.12 GHz Ti : sapphire laser compressed to 5.9 femtoseconds using MIIPS," Optics Express **16**, 10033-10038 (2008).
94. A. Bartels, D. Heinecke, and S. A. Diddams, "10-GHz Self-Referenced Optical Frequency Comb," Science **326**, 681- (2009).
95. A. Sandage, "The change of redshift and apparrent luminosity of galaxies due to the deceleration of selected expanding universes," The Astrophysical Journal **136**, 319-333 (1962).
96. A. Loeb, "Direct Measurement of Cosmological Parameters from the Cosmic Deceleration of Extragalactic Objects," The Astrophysical Journal **499**, L111-L114 (1998).
97. S. Osterman, S. Diddams, M. Beasley, C. Froning, L. Hollberg, P. MacQueen, V. Mbele, and A. Weiner, "A proposed laser frequency comb-based wavelength reference for high-resolution spectroscopy," in *Techniques and Instrumentation For Detection Of Exoplanets III* (SPIE, 2007), Vol. 6693, p. 66931G-9.
98. T. Wilken, C. Lovis, A. Manescau, T. Steinmetz, L. Pasquini, G. L. Curto, T. W. Hänsch, R. Holzwarth, and U. Th, "High-precision calibration of spectrographs," Monthly Notices of the Royal Astronomical Society: Letters **405**, L16-L20 (n.d.).
99. F. Bouchy, F. Pepe, and D. Queloz, "Fundamental photon noise limit to radial velocity measurements," A&A **374**, 733-739 (2001).

100. C.-H. Li, A. G. Glenday, A. J. Benedick, G. Chang, L.-J. Chen, C. Cramer, P. Fendel, G. Furesz, F. X. Kärtner, S. Korzennik, D. F. Phillips, D. Sasselov, A. Szentgyorgyi, and R. L. Walsworth, "In-situ determination of astro-comb calibrator lines to better than 10 cm s(-1)," OPTICS EXPRESS **18**, 13239-13249 (2010).
101. J. W. Brault, "High precision fourier transform spectrometry: The critical role of phase corrections," Microchimica Acta **93**, 215-227 (1987).
102. L.-J. Chen, G. Chang, C.-H. Li, A. Glenday, A. J. Benedick, D. F. Phillips, R. L. Walsworth, and F. X. Kärtner, "High-Finesse Dispersion-Free Cavities for Broadband Filtration of Laser Comb Lines," in *International Conference On Ultrafast Phenomena* (Optical Society of America, 2010), p. TuF1.
103. J. R. Birge and F. X. Kärtner, "Design of Optimal Dispersive Mirrors for Femtosecond Enhancement Cavities and Compressors by Minimizing Phase Distortion Power," in *Conference On Lasers and Electro-Optics/International Quantum Electronics Conference*, OSA Technical Digest (CD) (Optical Society of America, 2009), p. CThDD1.
104. S. Diddams and J.-C. Diels, "Dispersion measurements with white-light interferometry," J. Opt. Soc. Am. B **13**, 1120-1129 (1996).
105. G. Furesz, "Design and application of high resolution and multiobject spectrographs: Dynamical studies of open clusters," University of Szeged, (2008).
106. F. Wildi, F. Pepe, B. Chazelas, G. Lo Curto, and C. Lovis, "A Fabry-Perot calibrator of the HARPS radial velocity spectrograph: performance report," in (2010), p. 77354X-77354X-11.
107. G. Chang, C.-H. Li, D. F. Phillips, R. L. Walsworth, and F. X. Kärtner, "Toward a broadband astro-comb: effects of nonlinear spectral broadening in optical fibers," Opt. Express **18**, 12736-12747 (2010).
108. D. M. Fritz, D. A. Reis, B. Adams, R. A. Akre, J. Arthur, C. Blome, P. H. Bucksbaum, A. L. Cavalieri, S. Engemann, S. Fahy, R. W. Falcone, P. H. Fuoss, K. J. Gaffney, M. J. George, J. Hajdu, M. P. Hertlein, P. B. Hillyard, M. Horn-von Hoegen, M. Kammler, J. Kaspar, R. Kienberger, P. Krejcik, S. H. Lee, A. M. Lindenberg, B. McFarland, D. Meyer, T. Montagne, É. D. Murray, A. J. Nelson, M. Nicoul, R. Pahl, J. Rudati, H. Schlarb, D. P. Siddons, K. Sokolowski-Tinten, T. Tschentscher, D. von der Linde, and J. B. Hastings, "Ultrafast Bond Softening in Bismuth: Mapping a Solid's Interatomic Potential with X-rays," Science **315**, 633 -636 (2007).
109. A. M. Lindenberg, J. Larsson, K. Sokolowski-Tinten, K. J. Gaffney, C. Blome, O. Synnergren, J. Sheppard, C. Caleman, A. G. MacPhee, D. Weinstein, D. P. Lowney, T. K. Allison, T. Matthews, R. W. Falcone, A. L. Cavalieri, D. M. Fritz, S. H. Lee, P. H. Bucksbaum, D. A. Reis, J. Rudati, P. H. Fuoss, C. C. Kao, D. P. Siddons, R. Pahl, J. Als-Nielsen, S. Duesterer, R. Ischebeck, H. Schlarb, H. Schulte-Schrepping, T. Tschentscher, J. Schneider, D. von der Linde, O. Hignette, F. Sette, H. N. Chapman, R. W. Lee, T. N. Hansen, S. Techert, J. S. Wark, M. Bergh, G. Huldt, D. van der Spoel, N. Timneanu, J. Hajdu, R. A. Akre, E. Bong, P. Krejcik, J. Arthur, S. Brennan, K. Luening, and J. B. Hastings, "Atomic-Scale Visualization of Inertial Dynamics," Science **308**, 392 -395 (2005).
110. A. B. Wöhri, G. Katona, L. C. Johansson, E. Fritz, E. Malmerberg, M. Andersson, J. Vincent, M. Eklund, M. Cammarata, M. Wulff, J. Davidsson, G. Groenhof, and R. Neutze, "Light-Induced Structural Changes in a Photosynthetic Reaction Center Caught by Laue Diffraction," Science **328**, 630 -633 (2010).
111. R. H. Walden, "Analog-to-digital converter survey and analysis," Selected Areas in Communications, IEEE Journal on **17**, 539-550 (1999).
112. J. P. Gordon and H. A. Haus, "Random walk of coherently amplified solitons in optical fiber transmission," Opt. Lett. **11**, 665-667 (1986).
113. H. A. Haus and E. P. Ippen, "Group velocity of solitons," Opt. Lett. **26**, 1654-1656 (2001).
114. T. Udem, R. Holzwarth, and T. W. Hansch, "Optical frequency metrology," Nature **416**, 233-237 (2002).

115. A. Ozawa, J. Rauschenberger, C. Gohle, M. Herrmann, D. R. Walker, V. Pervak, A. Fernandez, R. Graf, A. Apolonski, R. Holzwarth, F. Krausz, T. W. Hansch, and T. Udem, "High Harmonic Frequency Combs for High Resolution Spectroscopy," Physical Review Letters **100**, 253901-4 (2008).
116. P. B. Corkum and F. Krausz, "Attosecond science," Nat Phys **3**, 381-387 (2007).
117. F. Krausz and M. Ivanov, "Attosecond physics," Reviews of Modern Physics **81**, 163-72 (2009).
118. J. Kim and F. X. Kärtner, "Attosecond-precision ultrafast photonics," Laser & Photon. Rev. **4**, 432-456 (2010).
119. E. N. Ivanov, D. Mouneyrac, J.-M. Le Floch, M. E. Tobar, and D. Cros, "Precise phase synchronization of a cryogenic microwave oscillator," Rev. Sci. Instrum. **81**, 064702 (2010).
120. R. Paschotta, "Noise of mode-locked lasers (Part I): numerical model," Appl Phys B **79**, (2004).
121. E. N. Ivanov, L. Hollberg, and S. A. Diddams, "Analysis of noise mechanisms limiting frequency stability of microwave signals generated with a femtosecond laser," in *Frequency Control Symposium and PDA Exhibition, 2002. IEEE International* (2002), pp. 435-441.
122. A. Bartels, S. A. Diddams, C. W. Oates, G. Wilpers, J. C. Bergquist, W. H. Oskay, and L. Hollberg, "Femtosecond-laser-based synthesis of ultrastable microwave signals from optical frequency references," Opt. Lett. **30**, 667-669 (2005).
123. J. Kim and F. X. Kärtner, "Microwave signal extraction from femtosecond mode-locked lasers with attosecond relative timing drift," Opt. Lett. **35**, 2022-2024 (2010).
124. E. N. Ivanov, M. E. Tobar, and R. A. Woode, "Microwave interferometry: application to precision measurements and noise reduction techniques," Ultrasonics, Ferroelectrics and Frequency Control, IEEE Transactions on **45**, 1526-1536 (1998).
125. T. R. Schibli, J. Kim, O. Kuzucu, J. T. Gopinath, S. N. Tandon, G. S. Petrich, L. A. Kolodziejski, J. G. Fujimoto, E. P. Ippen, and F. X. Kärtner, "Attosecond active synchronization of passively mode-locked lasers by balanced cross correlation," Opt. Lett. **28**, 947-949 (2003).
126. A. Bartels, S. A. Diddams, T. M. Ramond, and L. Hollberg, "Mode-locked laser pulse trains with subfemtosecond timing jitter synchronized to an optical reference oscillator," Optics Letters **28**, 663-665 (2003).
127. X. Ma, L. Liu, and J. Tang, "Timing jitter measurement of transmitted laser pulse relative to the reference using type II second harmonic generation in two nonlinear crystals," Opt. Express **17**, 19102-19112 (2009).
128. R. P. Scott, C. Langrock, and B. H. Kolner, "High-dynamic-range laser amplitude and phase noise measurement techniques," Selected Topics in Quantum Electronics, IEEE Journal of **7**, 641-655 (2001).
129. T. M. Fortier, M. S. Kirchner, F. Quinlan, J. Taylor, J. C. Bergquist, T. Rosenband, N. Lemke, A. Ludlow, Y. Jiang, C. W. Oates, and S. A. Diddams, "Photonic Generation of Ultrastable Microwave Signals," 1101.3616 (2011).
130. T. D. Mulder, R. P. Scott, and B. H. Kolner, "Amplitude and envelope phase noise of amodelocked laser predicted from itsnoise transfer function and the pumpnoise power spectrum," Opt. Express **16**, 14186-14191 (2008).
131. L.-J. Chen, "Discussions regarding LJC's ongoing spatio-temporal simulations," (2011).
132. G. T. Nogueira and F. C. Cruz, "Efficient 1 GHz Ti : sapphire laser with improved broadband continuum in the infrared," Optics Letters **31**, 2069-2071 (2006).
133. A. Bartels and H. Kurz, "Generation of a broadband continuum by a Ti : sapphire femtosecond oscillator with a 1-GHz repetition rate," Optics Letters **27**, 1839-1841 (2002).
134. A. Bartels, R. Gebs, M. S. Kirchner, and S. A. Diddams, "Spectrally resolved optical frequency comb from a self-referenced 5 GHz femtosecond laser," Optics Letters **32**, 2553-2555 (2007).
135. X. Ramus, "Transimpedance Considerations for High-Speed Operational Amplifiers," (2009).
136. Texas Instruments, "Noise Analysis in Operational Amplifier Circuits," (2007).
137. L. Smith and D. H. Sheingold, "Noise and Operational Amplifier Circuits, Analog Devices, AN-358," (n.d.).

138. J. Williams, "High Speed Amplifier Techniques - A Designer's Companion for Wideband Circuitry," (1991).
139. P. C. D. Hobbs, "Ultrasensitive laser measurements without tears," Appl. Opt. **36**, 903-920 (1997).
140. F. M. Gardner, *Phaselock Techniques*, 3rd ed. (John Wiley, 2005).
141. R. E. Best, *Phase-Locked Loops: Design, Simulation, and Applications*, 6th ed. (McGraw-Hill, 2007).
142. E. Baumann, F. R. Giorgetta, J. W. Nicholson, W. C. Swann, I. Coddington, and N. R. Newbury, "High-performance, vibration-immune, fiber-laser frequency comb," Opt. Lett. **34**, 638-640 (2009).
143. W. T. Thomson, *Theory Of Vibration With Applications*, 4th ed. (Chapman & Hall, 1993).
144. T. C. Briles, D. C. Yost, A. Cingöz, J. Ye, and T. R. Schibli, "Simple piezoelectric-actuated mirror with 180 kHz servo bandwidth," Opt. Express **18**, 9739-9746 (n.d.).
145. Standards Coordinating Committee 27, "IEEE Standard Definitionsof Physical Quantities forFundamental Frequency and TimeMetrology—Random Instabilities," (2008).
146. F. L. Walls, "Phase noise issues in femtosecond lasers," in *Laser Frequency Stabilization, Standards, Measurement, and Applications* (SPIE, 2001), Vol. 4269, pp. 170-177.
147. S. T. Dawkins, J. J. McFerran, and A. N. Luiten, "Considerations on the measurement of the stability of oscillators with frequency counters," Ultrasonics, Ferroelectrics and Frequency Control, IEEE Transactions on **54**, 918-925 (2007).
148. J. A. Barnes, A. R. Chi, L. S. Cutler, D. J. Healey, D. B. Leeson, T. E. McGunigal, J. A. Mullen, W. L. Smith, R. L. Sydnor, R. F. C. Vessot, and G. M. R. Winkler, "Characterization of Frequency Stability," IEEE Transactions on Instrumentation and Measurement **IM-20**, 105-120 (1971).